Accuracy and efficiency in numerical river modelling

Platzek, Frank

ACCURACY AND EFFICIENCY IN NUMERICAL RIVER MODELLING

INVESTIGATING THE LARGE EFFECTS

OF

SEEMINGLY SMALL NUMERICAL CHOICES

FRANK W. PLATZEK

NOVEMBER 2017

ACCURACY AND EFFICIENCY
IN
NUMERICAL RIVER MODELLING

PROEFSCHRIFT

ter verkrijging van de graad van doctor
aan de Technische Universiteit Delft;
op gezag van de Rector Magnificus prof. ir. K.Ch.A.M. Luyben;
voorzitter van het College voor Promoties,
in het openbaar te verdedigen op
dinsdag 14 november 2017 om 15:00 uur.

door

Frank Wouter PLATZEK

Ingenieur in de luchtvaart en ruimtevaart,
Technische Universiteit Delft, Nederland
geboren te 's Gravenhage, Nederland

This page is intentionally left blank

ABSTRACT

A river engineer is challenged with the task of setting up an appropriate model for a certain application. The model needs to provide suitable answers to the questions asked (i.e. be effective) and needs to do this within the available time (i.e be efficient). To set up such a model with sufficient accuracy and certainty, a modeller needs to fully understand all processes that determine the flow patterns and the flow resistance. These encapsulate both the physical processes, such as bottom friction and turbulent mixing, as well as the unwanted, 'numerical processes', due to discretization errors and grid effects. Unfortunately, these errors can be considerably large and can greatly influence model results.

To quantify the effects of numerical inaccuracies on the flow patterns and resistance (or backwater) in a river, several building blocks of the governing flow equations were analysed. In particular for moderate resolutions, where a part of the geometrical variation in a river is captured on the grid, the influence of the momentum advection scheme and the turbulence model on the model results increases. For these modelling aspects, certain common methods were therefore analyzed concerning their accuracy, efficiency and convergence properties, for grid resolutions applied in practical engineering work.

The common consensus is that the backwater in river models is dominated by bottom friction and that momentum advection only has a local effect on the water levels and flow patterns. However, in this work, it is demonstrated that the artificial backwater contribution from the momentum advection approximation can be of the same order of magnitude as the bottom friction contribution, depending on the advection scheme. First this is shown using a one-dimensional (1D) analysis and then it is verified using 1D and two-dimensional (2D) numerical experiments with a wavy bed, with emerged and submerged groynes and finally for an actual river. For each test, the backwater contribution of three basic first-order and two second-order accurate advection schemes are computed and compared. The size of this contribution is found to be largely determined by the conservation/constancy properties of the scheme and to a lesser extent by the order of the scheme.

Of course, the bottom friction forms the most important contribution to the total backwater. In 2D models, the bottom friction computation is considered to be straightforward, in particular when applying the newly-developed subgrid method by Casulli and Stelling [51] and Stelling [219]. However, for three-dimensional (3D) hydrodynamic models, the computation is more complicated due to the vertical structure of the flow. Most 3D river models apply the popular σ-layering, where the grid nicely follows the bed and free-surface. At present, z-layer models are seldomly applied in river computations, because they suffer from the problem of inaccurate and discontinuous bottom shear stress representation, commonly assumed to arise due to the staircase bottom representation. At higher grid resolution, where more features of the topography are represented on the grid, a terrain-following coordinate system such as the σ-layering can result in a strong distortion of the grid. This is avoided using a z-layer discretization. Additionally, the latter discretization could be very efficient for river applications, due to the fact that excessive vertical resolution is avoided in shallow areas, such as floodplains.

For this purpose, the discretized equations for the z-layer model are analyzed and the cause of the inaccuracies is clearly shown to come from the emergence of thin near-bed layers. Based on this analysis, a new method is presented that significantly reduces the errors and the grid dependency of the results. The method consists of a near-bed layer-remapping and a modified near-bed discretization of the $k - \varepsilon$ turbulence model. The applicability of the approach is demonstrated for uniform channel flow, using a schematized 2D vertical (2DV) model and for the flow over a bottom sill using the Delft3D modeling system (Deltares [69]).

Finally a new modelling strategy is presented for improving the efficiency of computationally intensive flow problems in environmental free-surface flows. The approach combines the recently developed semi-implicit subgrid method by Casulli and Stelling (Casulli [46], Casulli and Stelling [51], and Stelling [219]) with a hierarchical-grid solution strategy. The method allows the incorporation of high-resolution data on subgrid scale to obtain a more accurate and efficient hydrodynamic model. The subgrid method improves the efficiency of the hierarchical grid method by providing better solutions on coarse grids. The method is applicable to both steady and unsteady flows, but it is particularly useful in river computations with steady boundary conditions. There, the combined hierarchical grid-subgrid method reduces the computational effort to obtain a steady

state with factors up to 43. For unsteady models, the method can be used for efficiently generating accurate initial conditions and further dynamic computations on high-resolution grids. Additionally, the method provides automatic insight in grid convergence. The efficiency and applicability of the method is demonstrated using a schematic test for the vortex shedding around a circular cylinder and a real-world case study on the Elbe River in Germany.

SAMENVATTING

Een rivierbouwkundig ingenieur heeft de uitdagende taak een geschikt model op te zetten voor een bepaalde toepassing. Het model dient treffende antwoorden te leveren op de gestelde vragen (i.e. doelmatig te zijn) en dient dit te doen binnen de beschikbare tijd (i.e. efficient te zijn). Om zulk een model met voldoende nauwkeurigheid en zekerheid op te zetten, moet een modelleur volledige kennis hebben van alle processen die de stromingspatronen en -weerstand bepalen. Deze bevatten zowel de fysische processen, zoals bodemwrijving en turbulente uitwisseling, als ook de ongewenste, 'numerieke processen', die onstaan door discretisatiefouten en roostereffecten. Helaas kunnen deze numerieke fouten aanzienlijk zijn en de resultaten sterk beïnvloeden.

Om het effect van de numerieke onnauwkeurigheden op de stromingspatronen en -weerstand (of opstuwing) in een rivier te quantificeren, zijn verschillende bouwstenen van de stromingsvergelijkingen geanalyseerd. Specifiek voor gematigd fijne resoluties waar een deel van de geometrievariatie in de rivier op het rooster gevat wordt, neemt de invloed van het advectieschema en van het turbulentiemodel op de resultaten toe. Met betrekking tot deze modelleeraspecten zijn enkele regelmatig toegepaste methoden geanalyseerd, betreffende hun nauwkeurigheid, efficiëntie en convergentiegedrag, voor roosterresoluties zoals deze in de praktijk worden gebruikt.

De gemeenschappelijke consensus is dat de opstuwing in riviermodellen wordt bepaald door de bodemwrijving en dat advectie van impuls slechts een lokaal effect levert op de waterstanden en stroombeelden. Echter, in dit werk wordt aangetoond dat de kunstmatige bijdrage aan de opstuwing door de advectiediscretisatie van dezelfde orde van grootte kan zijn als de bodemwrijvingsbijdrage, afhankelijk van het gekozen advectieschema. Dit wordt eerst gerealiseerd middels een één-dimensionale (1D) analyse en vervolgens geverifieerd met 1D en twee-dimensionale (2D) numerieke experimenten, met een hobbelende bodem, met om- en overstroomde kribben en ten slotte voor een echte rivier. Voor iedere test, worden de opstuwingsbijdragen van drie eerste-orde en twee tweede-orde nauwkeurige advectieschema's berekend en vergeleken. Het blijkt dat de grootte van deze bijdrage voornamelijk bepaald wordt door de behouds/constantheids-

eigenschappen van het schema en in mindere mate door de orde van nauwkeurigheid van het schema.

Natuurlijk vormt de bodemwrijving de belangrijkste bijdrage aan de totale opstuwing. In 2D modellen wordt de bodemwrijvingsberekening als relatief eenvoudig beschouwd, in het bijzonder wanneer de onlangs ontwikkelde subgrid methode van Casulli en Stelling [51] en Stelling [219] gebruikt wordt. Voor drie-dimensionale (3D) hydrodynamische modellen is deze berekening echter gecompliceerder door de vertikale structuur van de stroming. Veel 3D riviermodellen passen de populaire σ-lagen discretisatie toe, waarbij het rooster netjes de bodem- en het vrije water oppervlak volgt. Z-lagen modellen worden zelden voor riviertoepassingen ingezet, vanwege de onnauwkeurige en discontinue weergave van de bodemwrijving, waarvan aangenomen wordt dat deze ontstaat door de *trapjesbodem*. Bij hogere roosterresolutie, waar meer details van de topografie op het rooster worden afgebeeld, kan een terrein-volgend coordinatensysteem zoals het σ-lagen model, tot een sterke vervorming van het rooster leiden. Dit wordt vermeden middels een z-lagen discretisatie. Bovendien zou een z-lagen model een zeer efficiënte methode kunnen bieden voor riviermodellen, door het vermijden van overmatige vertikale resolutie in ondiepe delen, zoals het winterbed.

Om deze reden worden de stromingsvergelijkingen voor het z-lagen model geanalyseerd en wordt aangetoond dat de reden van de onnauwkeurigheden ligt in het ontstaan van dunne lagen bij de bodem. Op basis van deze analyse wordt een nieuwe methode gepresenteerd die een significante reductie van de fouten en roosterafhankelijkheid van de oplossing brengt. De methode bestaat uit een laagdikte-aanpassing bij de bodem en een lokaal gemodificeerde discretisatie van het $k - \varepsilon$ turbulentiemodel. De toepasbaarheid van de methode word gedemonstreerd aan de hand van een uniforme kanaalstroming, met een schematisch 2D vertikaal (2DV) model en voor de stroming over een bodemhobbel met het Delft3D modelleersysteem (Deltares [69]).

Ten slotte wordt een nieuwe modelleerstrategie gepresenteerd om de efficientie van rekenintensieve stromingsproblemen met een vrij wateroppervlak te verbeteren. Deze strategie combineert de recent ontwikkelde semi-impliciete subgrid methode van Casulli en Stelling (Casulli [46], Casulli en Stelling [51] en Stelling [219]) met een oplosmechanisme op hierarchische roosters. De methode maakt het mogelijk hoge resolutie data op subgrid schaal in het model op te nemen om een nauwkeuriger en efficien-

ter model te verkrijgen. De subgrid methode verbeterd de efficientie van de hierarchische rooster methode, door betere resultaten op de grovere roosters te leveren. De methode is bruikbaar voor zowel stationaire an dynamische stromingsproblemen, maar is voornamelijk bruikbaar voor problemen met stationaire randvoorwaarden. Daar reduceert de gecombineerde hierarchische-rooster-subgrid-methode de rekentijd om een stationaire toestand de verkrijgen met factoren tot 43. For dynamische problemen kan de methode gebruikt worden om efficient nauwkeurige initiële condities te genereren en dynamisch verder te rekenen op hoge-resolutie roosters. Bovendien levert de methode automatisch inzicht in roosterconvergentie. De efficientie en toepasbaarheid van de methode wordt aangetoond met een schematische test voor wervelloslating rond een cylinder en middels een daadwerkelijke toepassing aan de rivier de Elbe in Duitsland.

ZUSAMMENFASSUNG

Eine der wichtigsten und herausfordernsten Aufgabenstellung eines Flussbauingenieurs zur Bearbeitung seiner Anwendungen ist die korrekte Wahl eines geeigneten Modells. Das Modell soll treffende Antworten zu den gestellten Fragen liefern (i.e. effektiv sein) und das innerhalb der verfügbarer Zeit (i.e. effizient sein). Um solch ein Modell mit ausreichender Genauigkeit und Zuverlässigkeit aufzubauen, braucht ein Modellierer vollständige Kenntnisse von den Prozessen die die Strömung und deren Widerstand bestimmen. Diese beinhalten sowohl die physikalischen Prozesse, wie Sohlreibung und Turbulenter Austausch, als auch die ungewünschten, 'numerischen Prozesse', welche durch Diskretizierungsfehler and Gittereffekte entstehen. Bedauerlicherweise können solche Fehler sehr gross sein mit entsprechendem Einfluss auf die Modellergebnisse.

Um die Effekte der einzelnen numerischen Ungenauigkeiten auf das Strömungsverhalten und -Widerstand (Stauwirkung) in einem Fluss zu quantifizieren, werden verschiedene Bausteine der Strömungsgleichungen analysiert. Insbesondere für verhältnismäßig grobe Gitter, wo ein Teil der Geometrievariation im Fluss auf dem Netz erfasst wird, nimmt der Einfluss des Advektionsschemas und des Turbulenzmodells auf die Modellergebnisse zu. Im Rahmen diesen Modellieraspekten, sind einige häufig benutzte Verfahren analysiert worden Bezüglich ihrer Genauigkeit, Effizienz und Konvergenzeigenschaften, für Gitterauflösungen aus der Anwendungspraxis.

Der allgemeine Konsensus ist daß die Stauwirkung in Flussmodellen hauptsächlich bestimmt wird durch Sohlreibung und daß Advection von Impuls nur einen Lokalen Effekt auf die Wasserspiegellagen und Strömungsverhältnissen hat. In dieser Arbeit, wird allerdings gezeigt daß die künstliche (numerische) Stauwirkung durch das Advektionsschema von der gleichen Grössenordnung sein kann als der Beitrag der Sohlreibung, abhängig vom Advektionsschema. Dies wird erst gezeigt anhand einer eindimensionaler (1D) Analyse und danach bestätigt mittels 1D und zweidimensionaler (2D) numerischen Beispielen für die Strömung über eine wellende Sohle, mit umströmten und überströmten Buhnen und letztendlich für ein wirkliches Flussbeispiel. Für jeden Test, wird für drei einfache

erster-Ordnung Upwind-Verfahren und zwei zweiter-Ordnung Verfahren, der numerischer Beitrag des Advektionsschematas an die Stauwirkung berechnet und verglichen. Es stellt sich heraus daß die Größe dieses Beitrags hauptsächlich bestimmt wird durch die Erhaltungs/Unveränderlichkeitseigenschaften des Schemas und nur zum geringeren Teil durch den Ordnung des Schemas.

Natürlich kommt der wichtigste Beitrag an der Stauwirkung von der Sohlreibung. In 2D Modellen, kann die Sohlreibung relativ unkompliziert berechnet werden, ins besondere wenn der neu-entwickelte Subgrid Ansatz von Casulli und Stelling [51] und Stelling [219] benutzt wird. Für drei-dimensionale (3D) hydrodynamische Modelle, allerdings, ist die Berechnung komplizierter durch die vertikale Struktur der Ströming. Viele 3D Flussmodelle verwenden das populäre σ-Schichten Modell, wo das Gitter die Topographie und die freie Oberfläche folgt. Z-Schichtverfahren werden heutzutage selten benutzt für Flussanwendungen, wegen ungenauer und unstetiger Berechnung der Sohlschubspannung, von dem angenommen wird daß es auftritt durch die gestufte Abbildung der Sohle. Bei feinerem Gitterauflösung, bei denen mehr Details der Topographie auf dem Netz abgebildet werden können, kann ein Topographie-folgendes Koordinatensystem wie das des σ-Modells zu einer starke Verformung des Rechennetzes führen. Mitttels einer z-Schicht Diskretisierung kann dies umgehen werden. Zusätzlich könnte eine z-Schicht Diskretisierung sehr effizient sein für Flussanwendungen, dadurch daß unnötig hohe vertikale Auflösung vermieden werden kann in flache Teilgebieten wie z.B. auf dem Vorland.

Aus diesem Grund, sind die discretisierte Gleichungen für das z-Schicht Modell analysiert worden und ist eindeutig bestimmt daß die Gründe der Ungenauigkeiten kommen durch das Entstehen von dünnen Schichten an der Sohle. Basierend auf dieser Analyse, wird ein neuer Ansatz vorgestellt der die Fehler und Gitterabhängikeit der Ergebnissen erheblich reduziert. Der Ansatz enhält eine geänderte sohlnahe Schichtverteilung und eine angepasste sohlnahe Diskretisierung des $k - \varepsilon$ Turbulenzmodells. Die Anwendbarkeit dieses Ansatzes wird mit einem 2D vertikales (2DV) Modell nachgewiesen anhand einer uniformen Kanalströmungs und mit dem Delft3D Modelliersystem (Deltares [69]) für die Strömung über eine Sohlschwelle.

Zum Schluss wird eine neue Modellierstrategie zur Effizienzsteigerung rechenintensiver Simulationen von Flüssen vorgestellt. Der Ansatz kombi-

niert einen erst vor kurzem entwickelten semi-impliziten Subgrid-Ansatz von Casulli und Stelling (Casulli [46], Casulli und Stelling [51] und Stelling [219]) mit einer auf hierarchischen Netzen basierenden Stategie, deren Kombination eine sinnvolle Berücksichtigung von hoch-aufgelösten Geländeinformationen – auch auf gröberen Netzen – erlaubt und zur Genauigkeits- und Effizienzsteigerung hydro-numerischer Flussmodelle. Der Subgrid-Ansatz verbessert den Effizienz des hierarchischen-Gitter Ansatzes, durch genauere Lösungen auf gröberen Netzen. Diese Herangehensweise ist sowohl im stationären als auch im instationären Fall verwendbar, spezifisch aber für Flussanwendungen mit stationären Randbedingungen wird die Effizienz erhebig verbessert. Es wird gezeigt, dass der *Hierarische Gitter-Subgrid-Ansatz* im dem Fall zu einer bis zu 43-fachen Verringerung der Rechenzeiten führen kann. Für instationäre Modellen, kann das Verfahren benutzt werden mit hoher Effizienz genaue Anfangsbedingungen zu generieren für weiter dynamische Berechnungen auf hoch-aufgelösten Netzen. Quasi gratis hinzu bekommt man eine einfache und sehr schnelle Methode für Gitterkonvergenzstudien. Es wird die Effizienz und Anwendbarkeit des Ansatzes sowohl für ein schematisches Beispiel als auch ein reales Flussmodell der Elbe in Deutschland aufgezeigt.

ACKNOWLEDGEMENTS

I thank Vincenzo Casulli for explaining numerical hydrodynamics and the subgrid method with unprecedented clarity and for making the UnTRIM workshop in Trento a delight each year.

Last but not least, I would like to express my endless thanks to my parents and to Manu for their patience, support, love and understanding during the past years and to Mara, Kennet and Maarten for both delaying and speeding up the finalization of this thesis.

<div align="right">

Frank Platzek
Delft, 2017

</div>

"Shallow Water"
(inspired by "Hallelujah" as performed by Leonard Cohen / Jeff Buckley)

A river, a lake, an estuary
A channel, an ocean, the deep blue sea
You can use Navier-Stokes, but please don't bother
'Cause the depth is usually much smaller than
The length over which you will model them
And you can simply use shallow water

Shal–low wa–ter, shal–low wa–ter
Shal–low wa–ter, shal–low wa–a–a–a–a–a–ter

The advection terms should be handled with care
A central method will not get you there
You must use an upwind scheme, or just don't bother
An explicit method might not be stable
Implicitness will let you be able
To use larger time steps for your shallow water

Shal–low wa–ter, shal–low wa–ter
Shal–low wa–ter, shal–low wa–a–a–a–a–a–ter

But what's the method of which you dream
Is it called the Eulerian-Lagrangian scheme?
It will always be more stable than the others
Just trace along the Lagrangian track
And get your advected velocities back
But will you have your stable shallow water?

Shal–low wa–ter, shal–low wa–ter
Shal–low wa–ter, shal–low wa–a–a–a–a–a–ter

The pressure terms in momentum conservation
and the velocities in the free-surface equation
They will couple one equation to the other
The celerity will suffer from extradition
From the Courant-Friedrichs-Levy condition
And you will have your stable shallow water!

Shal–low wa–ter, shal–low wa–ter
Shal–low wa–ter, shal–low wa–a–a–a–a–ter

Frank Platzek,
Trento, Italy,
February 2011,
after being positively 'brainwashed' during the Winter School on Advanced
Numerical Methods for Free-Surface Hydrodynamics.

CONTENTS

LIST OF FIGURES

LIST OF TABLES

LIST OF RESEARCH QUESTIONS

In this thesis the following research questions are answered, to improve the accuracy and efficiency of present-day river models and to offer a river engineer more certainty in setting up a model. Behind each question, the page number is indicated where the answer to the question can be found.

The answers to these questions are also summarized in the general conclusions in Chapter 5.

INTRODUCTION

1.1 NUMERICAL RIVER MODELLING

1.1.1 *Background*

Many of the world's major cities have been built along rivers for their many purposes. Rivers allow shipping, provide drinking water or cooling water for power plants, form ecological habitats and room for recreational activities, but perhaps most importantly, they carry water from precipitation and snowmelt to the seas and oceans, forming an important chain in the natural water cycle and a first natural prevention against flooding. However, rivers have a limited capacity, and with climate change, the frequency and severity of floods has increased (see e.g. Milly et al. [156]), underlining the need for adequate measures and flood level predictions, particularly in combination with increasing population density (e.g. Kundzewicz et al. [127] and Strauss, Kulp, and Levermann [223]).

River engineers are, therefore, challenged with the task of performing urgent flood forecasts in case of high water or strong precipitation, but equally important with that of planning, construction, maintenance and evaluation of river training works. Worldwide, costly and time-consuming projects are executed, e.g. for maintaining fairway depth for shipping, for protecting surrounding areas and their inhabitants from flooding, for optimizing sediment management or restoring ecological systems and habitats along the river banks.

Such projects involve the construction or modification of groynes, weirs and parallel dams, the dredging of sediments, the channelling or restoration of rivers and measures for bank protection. Expensive field campaigns and laboratory tests are set up and executed to obtain the required data and to verify the effects of taken measures.

Particular river training measures that have been under investigation the last decade are the *lowering or streamlining of groynes*. It is expected that by lowering or streamlining (i.e. reducing the groyne slope, mostly on the downstream side) the groynes, the flow experiences less resistance during

Figure 1: Lowering the groynes in the River Waal. Source:
https://beeldbank.rws.nl, Rijkswaterstaat, Ruimte voor de Rivier.

high water stages, when the groynes are submerged, and that flood levels can be reduced and the conveyance capacity of the river can be increased. The question remains how large these effects will be. In 2009, a pilot project was executed to quantify the effect of lowering the groynes in the River Waal, a branch of the Rhine River in the Netherlands (see Figure 1). Over a stretch of 10 km, 70 groynes were lowered and a monitoring project was started to measure the effects on both the hydro- and morphodynamics in the river (Busnelli et al. [37]). After this, another 390 groynes were lowered over approximately 70 km and several parallel dams were constructed over a distance of 10 km.

However, before such measures or construction works are realized, they are commonly tested and optimized using numerical models, allowing the river engineer to consider different options and geometries, varying the relevant parameters that influence the effectiveness of the measure: e.g. the river discharge, the channel geometry, vegetation resistance, soil character-

istics or meteorological effects. To allow adequate and prompt measures, accurate and efficient predictions are required, putting increasingly strong requirements on the quality of the applied models and methods.

Traditionally, and mostly due to limitations on computational resources, river models either concern one-dimensional (1D) models, or coarse two-dimensional (2D) models, where only the global geometric features (banks and bends) of the channel are captured on the computational grid, often with limited resolution. Smaller features, such as hydraulic structures (e.g. weirs, groynes, dikes, sluice gates), or bed forms, are commonly included through parameterizations or by increased roughness coefficients, see e.g. Cunge, Holly, and Verwey [65] for a review of classical approaches in hydraulic engineering. However, there has been a change in the demands on numerical river modelling over the past decades. Numerical models shifted from mostly 1D to 2D or even three-dimensional (3D) models, with increasing resolution, because policy-makers ask not only for water level predictions and discharge distributions, but demand detailed results including accurate velocity fields, based on models including more and more of the governing physical processes at higher and higher resolution, see. e.g Lane et al. [129] and Uijttewaal [234].

Unfortunately, for most reach-scale river applications (10–100 km length), computational grids still do not resolve all geometric features, due to limitations in computational resources. With the increased demands on the numerical models, the common trade-off between accuracy and efficiency has become even more important than before. River modelling is now performed at scales and resolutions, where processes have become important, which could be neglected (or parameterized) in the past. Within this new scope, some of the common assumptions and commonly-applied building blocks of numerical river models need to be reconsidered.

1.1.2 *On accuracy and efficiency*

Accuracy

In research on the accuracy of certain methods, often accuracy in a mathematical sense is meant, referring to the order of accuracy or convergence, see e.g. Richtmyer and Morton [195]. This type of accuracy says something about the rate with which numerical errors diminish with grid refinement, often assuming that solutions are smooth and that the forcing of the prob-

lem is well-resolved. When related to the development of methods for flow problems, such texts mostly concern the construction of higher-order methods, where *higher* often means *higher than second order*. However, as mentioned above, the order of accuracy only has a meaning when the forcing of the problem is well-resolved. For environmental flow problems, such as river flows, this would mean that the geometry must be well-resolved compared to the solution, which is seldomly the case. Therefore, considering the accuracy in environmental flow problems only in the mathematical sense as in Richtmyer and Morton [195] is not sufficient. The accuracy should also be considered with a more pragmatic approach as opted for by Haile and Rientjes [92] and Vreugdenhil [243, 244], where a solution is considered *accurate* when the variation in the results due to uncertain parameters becomes small and an engineer or policy maker can have confidence in the results, taking into account the accuracy and uncertainty of the data used for input, calibration and validation.

Of course, an increased mathematical accuracy formally decreases the numerical errors made in the approximations, increasing the confidence in the results and can, therefore, also be strived for. Developments in the direction of higher-order methods concern among others (Weighted) Essentially Non-Oscillatory (ENO/WENO) methods, e.g. Jiang and Shu [113], Noelle, Xing, and Shu [171], Shu [212], Xing [256], and Xing and Shu [257], Discontinuous Galerkin (DG) finite element methods, e.g. Dumbser and Casulli [73], Kubatko, Westerink, and Dawson [126], and Ringler et al. [196], and research in the field of Large-Eddy Simulation (LES), e.g. Cevheri, McSherry, and Stoesser [57], Kang et al. [116], and Rodi, Constantinescu, and Stoesser [200]. A review and comparison of several higher-order WENO finite difference/finite volume and Discontinuous Galerkin methods is given in Xing and Shu [258]. These approaches have been demonstrated to achieve higher-order accuracy for certain academic benchmark cases. However, for real river cases, with variable topography in combination with wetting and drying, such methods have not yet been applied and the gain in accuracy is still to be demonstrated. Additionally, such methods often come at higher computational costs and accuracy means little to an engineer without efficiency. Only a method that is both accurate and efficient provides a modeller or engineer with an *effective* computation.

Efficiency

The concept of efficiency embellishes two components: doing things fast and only doing the necessary things. Doing things fast can be achieved through efficient solution techniques or better hardware (and corresponding, suitably-parallelized software).

Different types of efficient solution strategies were developed over the years. Alternating Direction Implicit (ADI) methods and approaches building on these (see e.g. Leendertse [135] and Stelling [217]) were developed more than 40 years ago, but are still hard to beat when it comes to combined accuracy and efficiency. The semi-implicit solution technique for coupled (shallow-water) equations developed by Casulli [44] does not perform the directional splitting as in ADI, yet reduces the size of the algebraic system of equations that is to be solved iteratively and thereby considerably reduces the computational effort.

Besides the solution strategy, many methods were developed that apply some form of multi-resolution approach, where different components of the solution process are handled on different resolutions or scales. Examples are *multigrid* methods (Brandt [27, 28], Hackbusch [91], Nabi et al. [165], Trottenberg, Oosterlee, and Schüller [232], and Zhou et al. [267]), *multiscale* methods (Bresch, Klein, and Lucas [29], Lamby, Müller, and Stiriba [128], Lee, Zhou, and Tchelepi [134], Müller and Stiriba [163], and Sagout, Deck, and Terracol [204]), *(adaptive) local grid refinement* (Berger, LeVeque, and Mandli [15], Berger and Colella [16], Brandt [27], Hess [99], Liang et al. [141], Mitchell and Fulton [158], Stelling [219], and Trottenberg, Oosterlee, and Schüller [232]), *coarse-grid projection* (Lentine, Zheng, and Fedkiw [138]), *nested-grid* modelling (Baranya, Olsen, and Józsa [10]), *coupling of models with different resolutions* (Fringer, McWilliams, and Street [83]), or *hp-adaptivity* in finite element methods (Kubatko, Westerink, and Dawson [126]).

Combinations of these approaches, where a semi-implicit method is combined with an approach involving multiple resolutions can be found in Casulli [46, 47], Casulli and Stelling [51], Lentine, Zheng, and Fedkiw [138], Stelling [219], and Volp, Prooijen, and Stelling [240].

In recent years, a number of works have extended such multi-resolution approaches or made combinations of the aforementioned methods to further improve the efficiency and applicability, e.g. using MPI or GPU parallelization, applications on unstructured grids, Algebraic Multigrid (AMG),

application to the Navier-Stokes equations, Large Eddy Simulation (LES) or Immersed Boundary Methods (IBM), see e.g. Kang et al. [116], Kashyap et al. [117], Lv et al. [144], McAdams, Sifakis, and Teran [148], and Tai and Zhao [227].

The work by Lentine, Zheng, and Fedkiw [138], originating from the field of realistic animation and visualization, involves a coarse-grid projection, where a part of the flow problem is set up on a high-resolution grid and another part on a coarser grid. The equations are then solved on the coarse grid, after which a projection is required to finally obtain the remaining part of the solution on the higher resolution grid. This work concerns the simulation of smoke, but the developed method appears to be generally applicable.

The second way to obtain fast computations is by allocating improved hardware. The increase in computational power that we have seen over the past decades has stagnated due to power consumption and heat production limitations on processor units. Further performance increase is mostly achieved through parallel computing. Parallel computations on many-cores (100-10000) are being performed ever more often (e.g. Dietrich et al. [71]). However, the performance of such simulations is not yet sufficient for reach-scale LES or Direct Numerical Simulation (DNS). Moreover, the hardware required for such computations will not be available to most (river) engineers in the foreseeable future.

As mentioned at the start of this section, a different way to improve the efficiency is by only doing the necessary things. Of course, local grid refinement is already an example of this, but there are many ways to avoid spending time on unnecessary computations. One such an approach is related to the so-called *spin-up problem*, referring to the length of spin-up times to obtain adequate starting conditions for forecast simulations. Particularly in ocean-climate models, where obtaining the global equilibrium state may involve computational periods in the order of 1000 years (see. e.g. Bernsen [17], this is an important issue. However, also for high-resolution river models, where flow patterns of different scales are present, the spin-up time may take a considerable part of the total computation time, due to the limited damping and longer travel distances of both initial waves and waves interacting with the resolved topography.

1.1.3 *On the computational grid and resolving the geometry*

The computational grid

Traditionally, river models were 1D and the grid consisted of a network of branches with prescribed cross-sections. With the emergence of 2D models, grids became either rectangular with staircase boundaries or curvilinear grids were applied to follow the river banks and bends. Nowadays, structured (rectangular, curvilinear), block-structured, locally-refined, unstructured and even adaptive or moving grids are commonly applied, see e.g. Biron et al. [20], Conroy, Kubatko, and West [63], Gassmann [87], Holleman, Fringer, and Stacey [104], Ii and Xiao [108], Kang, Borazjani, and Sotiropoulos [115], Kirkpatrick, Armfield, and Kent [121], Liang and Borthwick [140], Rosatti, Cesari, and Bonaventura [202], Sinha [213], Wenneker [248], and Zelicourt et al. [264].

Grid generation has become a scientific field and an art form for itself. Many commercial and free software packages are available, see e.g. Owen [175] and Schneiders [206] for an overview. Yet what is the most suitable type of grid depends on many factors: the problem to be solved, the required accuracy and efficiency, the range of spatial scales in the available data, etc. It is well-known that the grid structure can have a significant effect on the computational results. The reader is referred to Ferziger and Perić [77], Hirsch [100, Chapters 6 and 4.3] and Versteeg and Malalasekera [239, Chapter 11] and the references therein for a review on the use of different grid structures. An important conclusion is that higher-order schemes can easily loose an order of accuracy on non-uniform or unstructured grids.

The structure and resolution of the computational grid are often chosen based on the geometry that is to be represented. For certain data-scarse applications, the input data then needs to be downscaled or interpolated to the computational grid. In other situations, where more data is available, the input data (e.g. the geometry) needs to be upscaled or averaged to the grid. For this reason, the grid and the input data are connected. This is particularly critical for the specification of the geometry.

Resolving the geometry

High-resolution data is becoming ever more available through improved remote-sensing techniques, e.g. Cobby, Mason, and Davenport [62], Dot-

tori, Baldassarre, and Todini [72], Rabus et al. [192], and Westaway, Lane, and Hicks [249]. The use of such high-resolution geometric data was recognized to be of key importance for accurate river modelling by a large number of researchers, e.g. Bates and Roo [11], Bates et al. [12], Biron et al. [20], Capart et al. [41], Casas et al. [42], Casas et al. [43], Cea and Vázquez-Cendón [55], Defina [67], Fu and Hodges [85], Hardy et al. [96], Hodges [101], Horritt, Bates, and Mattinson [105], Hunter et al. [106], Lane et al. [129–131], Marks and Bates [147], McMillan and Brasington [153], Nicholas and Mitchell [168], Olsen and Stokseth [172], Sanders, Schubert, and Gallegos [205], Schumann, Andreadis, and Bates [208], and Yu and Lane [261, 262].

In recent years a number of works have appeared where the river geometry was resolved with a higher resolution (i.e. with grid sizes < 10 m), capturing the most important geometric scales. For short river reaches (e.g. < 10 km) this was performed by e.g. Abad et al. [1], Baranya and Jozsa [9], Constantinescu [64], Jia, Xu, and Wang [111], Kang et al. [116], Lane et al. [129, 130], MacWilliams [145], McCoy [149], Paz et al. [180], Stoesser et al. [222], Tritthart and Gutknecht [230], and Williams et al. [251].

High-resolution computations for reach-scale applications (> 10 km) are seldomly found in the literature. One exception is (Patzwahl (2011), pers. comm.), where a 3D non-hydrostatic UnTRIM model (Casulli and Walters [52], Casulli and Zanolli [53], and Jankowski [110]) was setup for a 70 km stretch of the Danube river, with a 3 m resolution in the main channel and 5–10 m resolution on the floodplains. The computations were executed on 192 computational cores. This application is close to the limit of the current possibilities in numerical river modelling (see also Appendix A).

However, because most modellers and engineers do not have such resources available, much research was invested in developing some intelligent form of upscaling, often based on a cell porosity, to include the effect of high-resolution *subgrid* variability of the geometry in coarse-grid models, see e.g. Bates and Roo [11], Bates et al. [12], Biron et al. [20], Capart et al. [41], Casas et al. [42], Casas et al. [43], Cea and Vázquez-Cendón [55], Defina [67], Fu and Hodges [85], Hardy et al. [96], Hodges [101], Horritt, Bates, and Mattinson [105], Hunter et al. [106], Lane et al. [129–131], Marks and Bates [147], McMillan and Brasington [153], Neal, Schumann, and Bates [166], Nicholas and Mitchell [168], Olsen and Stokseth [172], Sanders, Schubert, and Gallegos [205], Schumann, Andreadis, and Bates [208], and Yu and Lane [261, 262]. Some of such approaches make a dis-

tinction between channels and floodplains, allowing the bottom friction to act differently in the (deeper) channels and on the (shallower or dry) flood-plains, see e.g. Neal, Schumann, and Bates [166]. These methods have all been shown to greatly improve the results of coarse-grid computations.

A new subgrid[1] method based on *integration* over subgrid topography was recently developed by Casulli and Stelling (Casulli [46], Casulli and Stelling [51], and Stelling [219]). The method has been demonstrated to allow computing on relatively coarse grids, applying higher-resolution topographical and land-use data on subgrid scale, without averaging or upscaling the measured data to lumped values, but instead by integrating over this data within computational cells. An important feaure of this method is that wetting and drying is considered in a non-linear fashion, providing a more stable reproduction of the wet-dry interface and resulting in a more accurate volume representation, as demonstrated in Casulli [46], Casulli and Stelling [51], and Stelling [219].

Traditionally, numerical river models are assumed to be dominated by a balance between pressure gradient and bottom friction (see e.g. McGahey, Samuels, and Knight [152]). However, at grid resolutions where the topography is (partly) resolved and velocity gradients and turbulence generated by these topographical features are captured on the grid, other terms such as momentum advection and turbulent diffusion become more important in the governing flow equations. For this range of grid resolutions, there is a need to address the accuracy of the approximation/discretization of these terms, in particular for river computations, to meet the requirements on the accuracy of the applied numerical models.

1.1.4   *On turbulence modelling and momentum advection*

Turbulence modelling

For river models on finer computational grids, turbulence becomes important. The exchange between high-velocity regions and still-water zones and

---

1 Here the term *subgrid* is not to be confused with the terminology used in turbulence models, although it has a similar meaning. In the mentioned subgrid methods, the term subgrid refers to quantities which are included at a resolution finer than the computational grid, just as in the Sub-Grid-Scale (SGS) models known in turbulence modelling. The difference with the terminology as it is used in turbulence modelling, is that in Casulli and Stelling's subgrid method, certain quantities are actually known on subgrid resolution and included in the model by integrating over subcells.

the emergence of vortices can be captured on the grid. The Reynolds numbers in rivers are so high that the flow can be considered fully turbulent (e.g. Rodi [199]). Only a very thin part of the boundary layer is in the laminar range. This part is, however, seldomly resolved by the computational grid. A Direct Numerical Simulation (DNS) of a river would involve all turbulence scales and would not require a turbulence model. Such simulations are not feasible in practice and will remain so for quite some time in the future (Rodi [199]). Thus, for common numerical river models with limited resolution, turbulence modelling is required to include the effect of turbulent fluctuations and mixing that is not represented on the grid (both in space and time).

Depending on the application, the scale of the problem and the amount of detail required to answer the engineering/research question, different turbulence approaches/models are applied in river computations. For commonly applied moderate resolutions, river models are based on Reynolds-averaging, leading to the Reynolds-Averaged Navier-Stokes (RANS) equations or after applying the hydrostatic pressure assumption, the Shallow-Water Equations (SWE). In RANS models, either simple algebraic (zero-equation) turbulence models, such as Prandtl's mixing-length model (Prandtl [190]), which after averaging over the vertical approximately leads to the Elder model (Elder [75]), or one- or two-equation turbulence models, such as the $k - \varepsilon$ (Jones and Launder [114] and Rodi [198]) or the $k - \omega$ model (Wilcox [250]) are applied.

For more detailed investigations at higher-resolutions, Large-Eddy Simulation (LES) is applied. Also in the river engineering community, LES is gaining popularity as can be seen from recent applications, such as Cevheri, McSherry, and Stoesser [57], Constantinescu [64], Kang et al. [116], Kashyap et al. [117], McCoy, Weber, and Constantinescu [151], Rodi, Constantinescu, and Stoesser [200], Sagout, Deck, and Terracol [204], and Van Balen, Uijttewaal, and Blanckaert [237]. In LES, the Smagorinsky model (Smagorinsky [214]) is often applied as subgrid-scale turbulence model. It should be noted that a similar approach derived from Prandtl's mixing length concept (sometimes combined with Elder's model) is regularly applied in RANS models (see e.g. Wu, Wang, and Chiba [255]).

Different turbulence models are thus applied at different resolutions, but the effect or meaning of the turbulence model also changes with the grid resolution, as already noted by Madsen, Rugbjerg, and Warren [146]. In coarse 2D models, the turbulence model is often only used to introduce

some mixing/diffusion and to damp nonlinear build-up of energy on the smallest resolved scales (so-called $2\Delta x$ waves). In high resolution 3D computations, the aim of the turbulence model is to represent the turbulent momentum exhange and transfer of turbulent energy across different scales (the energy cascade, see. e.g. Nieuwstadt [169] and Pope [189]). A recent overview of the applicabilty of different turbulence models is given by Rodi [199].

One important remark on turbulence modelling needs to be made. In engineering practice, the notions of *turbulence* and *turbulence modelling* are often erroneously assumed to be directly related and even used as synonyms. Turbulence is a physical process, referring to mixing due to (chaotic) vortical motion, causing energy and momentum transfer across different scales of motion (the energy cascade). Turbulence modelling is an approach to include the effect of certain missing processes on smaller scales. In RANS modelling, it is used for solving the closure problem introduced in the governing equations due to spatial and temporal (Reynolds-)averaging. In LES it is used for adding the necessary dissipation at scales smaller than the grid resolution. In the Navier-Stokes equations, no "turbulence term" is present, only molecular diffusion. The Reynolds stresses that emerge from the averaging, originate from the nonlinear momentum-advection term, as also noted e.g. in Hirsch [100] and Rodi, Constantinescu, and Stoesser [200]. The fact that these terms are then transformed to a viscous term through an eddy-viscosity coefficient (Boussinesq approximation), unfortunately results in the fact that researchers and modellers focus on the computation of the eddy viscosity using a turbulence model and on the associated diffusion or mixing that is then modelled. Turbulence itself is, however, not a viscous process, but a chaotic vortical process. Only at the smallest scales the viscous effects become dominant. The vortical motion comes from momentum advection. The author therefore underlines that one cannot perform turbulence modelling, without considering the momentum-advection approximation and its properties (accuracy, momentum/energy conservation, numerical diffusion). The relative importance of the turbulence model and the momentum-advection scheme strongly depends on the chosen grid resolution and the geometrical and temporal scales of a particular flow problem. An example of research which aims to exploit this connection between the advection scheme and the turbulence model can be found in the field of Implicit LES (ILES) models see e.g. Boris et al. [26], Grinstein, Fureby, and DeVore [90], and Rodi, Constantinescu, and Stoesser [200].

Momentum advection

Advection is an important component in many applications, including atmospheric/meteorologic predictions, pollutant transport, ocean modelling, and also in Computational Fluid Dynamics (CFD) applications for the design of aircraft, cars or ships. For this purpose, the development of accurate and efficient advection schemes has been an important research topic for many decades. Early developments concerned finite difference approximations to the linear and nonlinear advection/transport equation, focusing on numerical accuracy, stability and consistency and formed the basis of all modern Eulerian schemes, see e.g. Boris and Book [25], Forester [80], Fromm [84], Godunov [89], Lax and Wendroff [132], Leonard [139], Richtmyer and Morton [195], Roache [197], Stelling [217], and Van Leer [238] and the references therein.

Nowadays, advection schemes are developed within many contexts, depending on the application (and the background of the researcher). Schemes can be based on finite difference, finite volume, finite element or spectral methods, concern linear or nonlinear advection, Eulerian, Lagrangian or mixed approaches, low-order or higher-order methods, involve limiters or filters or specific (e.g. ENO/WENO) reconstructions for maintaining positive and non-oscillatory solutions and can have different conservation properties for momentum, energy, vorticity or enstrophy. To the author's knowledge no work in literature is known where all possible approaches are compared. Nevertheless, some excellent reviews can be found in Kent et al. [118], Rood [201], Thompson [228], and Waterson and Deconinck [246].

The advection of momentum is a nonlinear term in contrast to advection of a scalar such as temperature or a tracer. Therefore, the development of higher harmonics and the (possible) build up of energy at shorter scales/wave lengths must be taken into account when considering momentum advection.

To avoid treatment of the nonlinearity and emergence of the Courant criterion for stability, Eulerian-Lagrangian methods were developed, where the advection term is included in the material derivative, which is then approximated directly (i.e. local and advective acceleration together) using a Lagrangian tracking algorithm, see e.g. Casulli and Cheng [50], Ham, Pietrzak, and Stelling [94], Jankowski [110], Lentine, Grétarsson, and Fed-

kiw [137], Lin and Rood [142], Rosatti, Cesari, and Bonaventura [202], Staniforth and Côté [216], Wang, Zhao, and Fringer [245], and Zhao [266]).

New developments within standard Eulerian advection schemes for momentum transport are mostly found in the direction of ENO/WENO schemes, Riemann-solvers and Discontinuous Galerkin approaches, in particular for unstructured grids. Most of the works focus on the respresentation of discontinuous solutions (shocks, dambreaks) for certain benchmark cases (see .e.g Caleffi and Valiani [38], Caleffi, Valiani, and Li [39], Dumbser and Casulli [73], Kubatko, Westerink, and Dawson [126], Noelle, Xing, and Shu [171], Ricchiuto [194], Ringler et al. [196], Toro and Garcia-Navarro [229], Xing [256], Xing and Shu [257], and Xing and Shu [258]. To the author's knowledge, no reporting is available in literature on the application of such approaches for real-world environmental flow situations with complex geometry and wetting and drying.

Adhering to the directional/transporting character of advection, often some form of *upwind* discretization is applied for obtaining stable approximations. This inclusion of an upwind term causes the emergence of numerical errors, commonly in the form of numerical diffusion or dispersion (depending on the order of accuracy of the approximation). All the aforementioned works in this section aim at reducing these errors, while maintaining stable solutions. The link between this numerical diffusion and the modelling of turbulent diffusion by a turbulence model was established by researchers working in the field of Implicit LES (ILES), as mentioned already above, see e.g. Boris et al. [26], Grinstein, Fureby, and DeVore [90], and Rodi, Constantinescu, and Stoesser [200].

Overviews of many different advection schemes and approaches can be found in Durran [74], Ferziger and Perić [77], Hirsch [100], LeVeque [133], and Versteeg and Malalasekera [239]. A recent example concerning the effect of discretization errors in the advection scheme on the accuracy in ocean models can be found in Mohammadi-Aragh et al. [160] and similarly for the accuracy in atmospheric studies in Schroeder, Schlünzen, and Schimmel [207].

1.1.5 *On wetting and drying*

Rivers have banks or levees on both sides, often with connected floodplains, and sometimes with urban areas or other economical property, which are all prone to flooding during high water levels. In general, the water level

will move, making wetting and drying an indispensible component of a numerical river model.

The accurate and, above all, robust representation of wetting and drying has been a long-term challenge as can be seen from the many papers on the topic, see e.g. Atzeni et al. [6], Balzano [7], Begnudelli and Sanders [14], Brufau and García-Navarro [30], Bunya et al. [33], Capart et al. [41], Defina [67], Hof and Vollebregt [102], Liang and Borthwick [140], Molinaro, Di Fillippo, and Ferrari [162], Ricchiuto [194], and Yu and Lane [261]. In many of these approaches, some form of a flooding/drying threshold is introduced to (temporarily) exclude dry cells or cell edges from participating in the solution. Also, very often oscillations and large velocity variations were identified near the wet/dry interface due to the vanishing water depth.

Using the subgrid topography approach of Casulli and Stelling (Casulli [46], Casulli and Stelling [51], Sehili, Lang, and Lippert [209], Stelling [219], and Volp, Prooijen, and Stelling [240]), already mentioned in section 1.1.3, these variations and oscillations are greatly reduced or diminished due to the nonlinear treatment of the volume (or continuity) equation. The method was mostly tested on schematic cases and estuarine applications involving friction-dominated flow over large shallow areas. The effectivity of the approach for river or channel flow was only considered in Stelling [219], for the flow through a 180° bend with a dry inner bank.

1.1.6 *On model dimensionality and other topics*

Model dimensionality

As mentioned in section 1.1.1, river models traditionally concerned 1D or coarse 2D models, resolving only the global geometric features on the computational grid. Lane et al. [129] compared 2D and 3D model results for the flow in a river confluence and found that 2D and 3D model schematisations react differently to geometry and roughness variations. The confidence in model results and the predictive capabilities were higher for the 3D model, despite limitations due to the need for accurate boundary condition specification.

The choice in model dimensionality will likely be determined by the size of the domain that is to be modelled, the foreseen grid resolution and the available computational resources. Therefore, for large-scale applications (> 100 km), 1D and coarse 2D models will probably still be used in the

next decades. However, higher resolution 2D and 3D models may become feasible due to increased computational resources and improved (geometric) data resolution and quality.

Three-dimensional modelling is already common practice in other scientific and engineering fields, e.g. coastal, ocean or lake modelling, atmospheric computations, but also in the aerospace and automotive industry. In the river modeling community, the application of 3D models gained in popularity approximately twenty years ago, where researchers started applying 3D models to simulate detailed local flow phenomema near hydraulic structures, such as groynes or weirs and in bends, see e.g. Abad et al. [1], Baranya and Jozsa [9], Fischer-Antze et al. [78], Hardy et al. [97], Jia, Xu, and Wang [111], Kashyap et al. [117], Lane et al. [129], Lege, Alexy, and Kellermann [136], Nihei, Kato, and Sato [170], Patzwahl, Jankowski, and Lege [179], Van Balen, Uijttewaal, and Blanckaert [237], and Wu, Rodi, and Wenka [254].

With the emergence of three-dimensional river models, the vertical discretization, the turbulence model and (wall/bottom) boundary conditions require more attention. Traditionally, either a σ- or z-layer discretization has been applied in the vertical. When applying a σ-layering, one has the advantage that the grid nicely follows the topography and that all cells have neighbours, allowing for relatively straightforward discretizations. However, disadvantages are that 1) for steeper topography, e.g. near groynes and banks, the sigma-transformation suffers from the so-called *hydrostatic inconsistency*, see e.g. Haney [95], Mesinger [154], and Stelling and Van Kester [221] and 2) that excessive vertical resolution is applied in shallower areas, e.g. on the floodplains, reducing the efficiency of the model. On the other hand, geopotential z-layer models have simple horizontal discretizations and can handle steep slopes without difficulty (disregaring the invalidity of the hydrostatic pressure assumption near such slopes), but they do not follow the topography and free-surface and, therefore, the discretization requires special attention near these boundaries. A well-known example is the computation of the bed shear stress on the staircase bottom boundary, which causes problems (see e.g. Bijvelds [18] and Pietrzak et al. [184]).

Other topics

Several unmentioned topics are also relevant in numerical river modelling. These topics concern among others, *river morphodynamics* (see e.g. Mewis [155], Nabi et al. [165], Ottevanger [173], Sukhodolov, Uijttewaal, and Engelhardt [224], Volp et al. [241], Volp [242], Wu [253], Yossef [259], and Yossef and Vriend [260]), *flow in bends* (e.g. Blanckaert and Graf [22], Blanckaert et al. [23], Jia et al. [112], Mewis [155], Ottevanger [173], Ottevanger and Balen [174], Syme [225], Tritthart and Gutknecht [230], and Van Balen, Uijttewaal, and Blanckaert [237]), the effect of *vegetation* (see e.g. Ali [4], Baptist et al. [8], Defina and Bixio [68], Fischer-Antze et al. [78], Galema [86], Huthoff [107], Nepf [167], Shields, Coulton, and Nepf [211], and Wu [253]) and *non-hydrostatic* modelling (e.g. Ai and Jin [3], Altinakar, Miglio, and Leupi [5], Busnelli [36], Casulli [45], Casulli and Zanolli [53], Cea, Stelling, and Zijlema [54], Constantinescu [64], Fringer, Gerritsen, and Street [82], Hervouet and Jankowski [98], Jankowski [109, 110], Tritthart and Gutknecht [230], Ullmann [236], Wols [252], Zhao [266], and Zijlema and Stelling [268]). Since other researchers have spent considerable effort to improve the accuracy and efficiency of the numerical approaches for these issues, and to limit the scope of the present work, they are left out of the scope of this thesis.

1.2   CHALLENGES FOR TODAY'S RIVER MODELLER

1.2.1   *Setting up an appropriate model*

In section 1.1, several important aspects of numerical river modelling were briefly addressed. For today's river modeller, the question remains:

> *"How to set up an appropriate model for my application?"*

where in the present thesis, *appropriate* means sufficiently accurate for answering the research or engineering question with confidence in model results and sufficiently efficient for providing these answers within the available amount of time.

Numerous very general and robust modelling systems are available worldwide for modelling free-surface (river) flows. Commonly, the choice for a river modeller is limited to those system(s) that is/are available within his/her institution or company. The choice is either between different mod-

els, or between different methods within the models (grid structure, turbulence model, advection scheme, etc.). Modelling systems are most often based on finite difference, finite volume or finite element discretizations. Each of these approaches has its own advantages and disadvantages when it comes to accuracy, efficiency, conservation (of mass, momentum, energy and transported constituents) and robustness/stability.

At moderate resolutions, where the topography is partly resolved and resulting velocity gradients are represented on the computational grid (the scope of this thesis), the choices for an adequate turbulence model and advection scheme for momentum transport become important. Of course, also the grid type and the actual resolution, in particular in relation to the scales of the geometry are known to influence the results (see section 1.1.3). Since not all available systems are able to model 3D flows, an important criterion for choosing a certain modelling system, is the model dimensionality (see section 1.2.6). Another deciding factor can be the implemented wetting and drying algorithm, in particular when flooding scenarios are to be simulated, but also when (quasi-)stationary solutions are sought in a partially-wet domain. In the remainder of this section, these topics are briefly considered, illustrating the important – and often difficult – choices a river engineer is faced with in setting up a numerical model.

1.2.2   *Choosing the grid type*

Some modelling systems are based on a certain grid type (e.g. structured quadrilaterals *or* unstructured triangles) and others offer hybrid discretizations, sometimes even offering penta- or hexagonal cells/elements. Just as with the vertical layering types, each grid type has its own advantages and disadvantages and no type of grid has been found to yield systematically improved results for a wide range of applications (see e.g. Ferziger and Perić [77]). In general, it can be said that higher-order accuracy is more easily achieved on structured grids than on unstructured grids, at least for finite difference and finite volume schemes and that transitions in grid structure (e.g. from quadrilateral to triangles) locally reduce the accuracy of the approximations. Finite element discretizations achieve their order within elements and therefore the order of the scheme can be achieved irrespective of the grid structure.

Unstructured or locally-refined grids offer the possibility to better approximate the domain geometry. On the other hand, with the emergence of

subgrid (topography) methods as those developed by the references mentioned in section 1.1.3 and in particular by the integral method from Casulli [46], Casulli and Stelling [51], Stelling [219], and Volp, Prooijen, and Stelling [240], the need to follow the geometry with the computational grid may be relaxed as the topography is automatically resolved on subgrid level (see also chapter 4). With this new method, the modeller also obtains some more flexibility in the choice of the computational grid resolution.

1.2.3   *Choosing the grid resolution*

As mentioned before, the grid resolution not only determines the level of detail of the model results, but it also determines which other model settings or components are important (e.g. the turbulence model, the advection scheme, non-hydrostatic modelling). The choice for a certain grid resolution is, however, mostly determined by the size of the model domain and the available computational resources.

To illustrate how the size of the model domain, the grid resolution and the computational (CPU) time are related and to provide some insight in what grid resolution is feasible with present-day resources, a schematic analysis was performed to estimate the required CPU times for simulating a river stretch with the following characteristic dimensions:

- length L of 100 km,

- width W of 1 km.

Within the analysis, river computations have been categorized in two classes: either as short-term (often steady-state) or long-term (often dynamic) runs, where the former mostly focuses on obtaining water levels for ship navigation or establishing dike heights and the latter aims at gaining insight in long-term flooding frequency or river morphodynamics.

Making certain assumptions on the applied computational model and grid, the time step size and flow characteristics, a relation was established relating the total CPU time to the grid size Δx, for both classes of computations (see Appendix A for more details on the analysis). For a typical range in model efficiency, a bandwidth of feasible computations can be established, both with and without parallel computations, for the two classes of river computations. This is illustrated in Figure 2, which shows a double logarithmic plot of the two relations, where the range of model efficiency
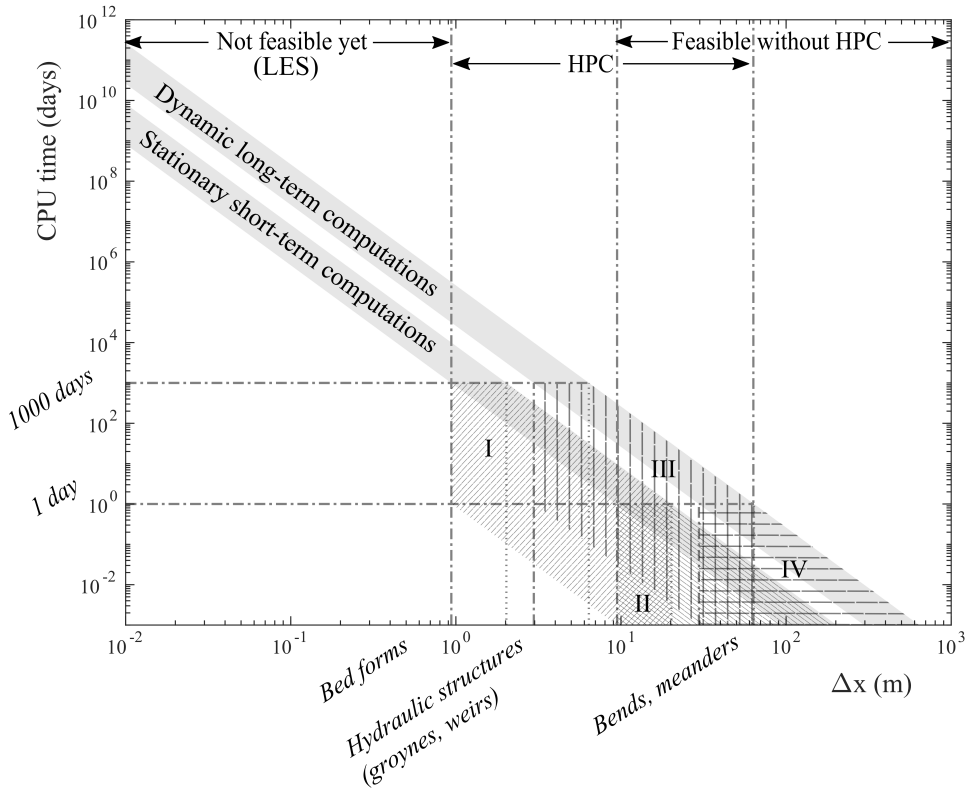
Figure 2: Schematic representation of the increase in CPU time with increasing resolution. The shaded area represents a representative bandwidth of model efficiency. The hatched regions I–IV indicate the ranges of feasible computations with and without parallel High Performance Computing (HPC).

is represented by the two shaded bands (one bandwidth for the short-term and one for the long-term computations). From the figure one can directly see what CPU times would be approximately necessary to perform computations at a certain grid resolution. Of course, CPU times can be reduced by parallel computing.

As an indication of feasible grid resolutions, two characteristic CPU times have been chosen: the first for a one-day computation, below which all computations are feasible without parallel High-Performance Computing (HPC) and one for a 1000-day CPU time, indicating the range of computations that is feasible when HPC resources are available, assuming a maximum parallel speed-up of 1000 (resulting again in a CPU time of

one day or less). It can be seen that – depending on the model efficiency – there is an overlap of the different feasability regions. For clarity, four regions have been indicated:

Region I : (hatched southwest-northeast) indicates the most performant range of short-term computations, where computational times up to 1000 days are accelerated using parallel HPC to around one day (parallel speed-up factors of up to 1000 required). These computations are not feasible without HPC. The region is bounded approximately between grid sizes $1 < \Delta x < 20$ m, where the bandwidth of short-term computations then indicates the computational times without parallel speed up.

Region II : (hatched southeast-northwest) indicates the range of short-term computations feasible also without HPC. Simulations in this region are feasible using grid sizes of approximately $\Delta x > 10$ m, where the bandwidth of short-term computations then indicates the computational times corresponding to a certain grid size.

Region III : (hatched vertically) indicates the range of long-term computations feasible only with HPC (serial CPU times up to 1000 days). The region lies between approximately $3 < \Delta x < 60$ m, where now the bandwidth of long-term computations indicates the computational times without parallel speed up.

Region IV : (hatched horizontally) indicates the range of long-term computations feasible also without HPC. These simulations are feasible with grid sizes of approximately $\Delta x > 30$ m, where the bandwidth of short-term computations again indicates the computational times corresponding to a certain grid size.

As can be seen from Figure 2, the grid resolution required for resolving all geometric scales (bed forms, hydraulic structures, bends, etc.) is often not feasible. There appears to be a gap between *required* and *feasible* grid resolutions. In the choice for an adequate grid resolution, a modeller, therefore, often has to decide which processes and scales are to be represented on the computational grid and which are to be included using some type of subgrid parameterization. For this reason, the choice for the grid resolution is not straightforward and often the final resolution is chosen after

a number of preliminary computations, where the grid size is varied to determine the influence on the results.

The figure indicates that all computations with grid sizes $\Delta x < 1$ m (termed LES computations in the figure) are not feasible yet for large-scale river computations, even with parallel computing. In particular for dynamic, long-term computations, this will most likely remain so for quite some time in the future, unless there is a considerable increase in computational performance or a change in the way the topography is discretized in a numerical model, e.g. using the subgrid method by Casulli [46], Casulli and Stelling [51], and Stelling [219].

It is to be noted that actual grid convergence studies are often difficult, both due to the nonlinearity of the governing equations and due to the fact that also the geometry resolution often changes with the grid. When smaller scales are represented on the grid, different processes with different (turbulent) characteristics may emerge, causing the results not to 'converge' with grid refinement. This, however, has nothing to do with the formal convergence properties of the method. Nevertheless, such grid refinement studies often aid in choosing the correct grid resolution and in gaining confidence in model results.

1.2.4 *Choosing a turbulence model*

As mentioned in section 1.1.4, different turbulence models are applied at different model resolutions. Whether a mixing length approach, an Elder model, $k - \varepsilon$, $k - \omega$ or an LES approach is appropriate for an application, depends on the aim of the computation. Is the aim to model the effect of additional mixing due to increased bottom friction in shallower areas in a steady-flow application? Then the Elder model may suffice. Is the aim to model vortex shedding from the tip of a groyne? Then a model that includes the transport (advection) of turbulent kinetic energy, such as the $k - \varepsilon$ or $k - \omega$ model or perhaps a high-resolution LES is required.

An additional complication in shallow-water flow models, is the anisotropy of horizontal and vertical scales. The limited vertical extent, compared to the horizontal dimensions, causes the emergence of *quasi-two-dimensional* coherent structures/eddies (see e.g. McCoy, Constantinescu, and Weber [150], Prooijen, Booij, and Uijttewaal [191], Uijttewaal [234], Uijttewaal, Lehmann, and Mazijk [235], and Weitbrecht, Socolofsky, and Jirka [247]. For this purpose, in 2D computations, sometimes specific depth-

averaged turbulence models (see. e.g. Bijvelds [18], Bijvelds, Kranenburg, and Stelling [19], Rastogi and Rodi [193], and Wu, Wang, and Chiba [255] are applied and in 3D applications, different horizontal and vertical turbulence models are used, e.g. by Bijvelds [18].

At the presently-applied higher resolutions, we are now somewhere inbetween RANS and LES modelling. A part of the energy transfer and momentum exchange is resolved on the grid (both in space and in time), representing the turbulent energy cascade. However, not all relevant scales are well-represented and the applicability of the different available turbulence models may need to be revisited for this range of resolutions. One can question whether the methods developed 40–60 years ago, such as the $k - \varepsilon$ (Jones and Launder [114] and Rodi [198]) and Smagorinsky model (Smagorinsky [214]), are valid for the present spatial and temporal scales, including the resolved topography.

However, the turbulence model is not the initiator of turbulence. With insufficient grid resolution – even with a sophisticated turbulence model – no turbulent flow structures will develop, since the required amount of energy cannot accumulate on the smaller scales due to nonlinear interactions. For this purpose, the choice for a specific turbulence model cannot be made without at least thinking about, but preferably quantifying to some extent, the numerical diffusion from the momentum advection scheme (for the chosen grid resolution), as discussed in the next section and in section 1.1.4).

1.2.5 *Choosing a momentum advection scheme*

Turbulent structures are generated by momentum advection. Therefore, in a numerical model, the properties of the advection scheme determine the scales of the turbulent structures that are generated and the amount of energy that is present at the smallest scales that can be represented on the grid. This is a very delicate balance: on the one hand, this energy forms the basis of the emergence of larger turbulent structures/eddies and on the other hand, this energy needs to be suitably dissipated to avoid the unphysical build-up of energy on this scale.

Schemes that do not dissipate enough (e.g. central schemes), therefore, show oscillations when nonlinear interactions cause steepening of a signal. Conversely, schemes that dissipate too much (e.g. first-order upwind

schemes) allow less energy build-up on the smallest scales, and therefore require finer grids to show the initiation of turbulent eddies.

The importance of the choice for an adequate advection scheme (if one has the choice), is sometimes underestimated. The effect of the advection scheme on model results can often best be demonstrated by switching off the advection term. The effect can be compared to the hydrostatic pressure assumption in 3D computations. Due to this assumption, where the vertical acceleration (incl. advection) terms are omitted, the acceleration of the fluid in the vertical becomes 'free', i.e. the flow can accelerate over an obstacle without requiring energy to do so. Therefore, in hydrostatic computations, no vertical recirculation will be found (unless other discretization errors cause the flow to separate from the bottom). Similarly, when switching off the (horizontal) advection terms, any horizontal acceleration will become 'free', i.e. the flow can pass around any obstacle (e.g. a groyne), without detaching – because it can freely accelerate – and no horizontal recirculation will be found. This can easily be verified using numerical tests.

Therefore, the emergence of turbulence is strongly related to the properties of the advection scheme. How the energy is dissipated at the grid scale should be determined by the turbulence model. However, as mentioned above, the advection scheme also has discretization errors, often acting as a (numerical) diffusion term. The total amount of diffusion or dissipation is, therefore determined by both the advection scheme and the turbulence model. They cannot be considered separately, as was also noticed by researchers in the field of Implicit Large-Eddy Simulation (ILES), see e.g. Boris et al. [26], Grinstein, Fureby, and DeVore [90], and Rodi, Constantinescu, and Stoesser [200].

1.2.6 *Choosing the model dimensionality*

As mentioned in section 1.1.6, most present-day river models concern 2D depth-averaged models. The choice for a 3D model, may be required when vertical flow variation is expected, e.g. for the flow over steep topography or hydraulic structures, for the flow in (strong) bends, for flows with temperature or salinity stratification or in case of strong wind effects. With this choice, it should be noted that in reality the topography may be gradually-varying, but that due to the projection on a grid, it may become locally steep.

Common 3D models either apply a σ- or a z-layering, or some combination in the vertical (see e.g. Bijvelds [18]). The choice for a certain layering type will depend e.g. on the steepness of the topography, the relative extent of the main channel and the floodplains and on the required efficiency. When a 3D model is considered for an application, also the turbulence model (and possible ansitropic treatment of the horizontal and vertical, see section 1.2.4) may need to be revisited and one may need to reconsider the hydrostatic pressure assumption and think about applying a non-hydrostatic model.

1.2.7 *General remarks*

Depending on the aim of a certain project, the focus can be more on accuracy or more on efficiency. This will ultimately determine the choices described in the previous sections. Experimenting with different options and visually inspecting the results cannot be avoided. In particular when limited validation data is available, an important issue is the confidence in model results. With all the different options and settings available, one can only get confidence in the model results by investigating the effect of the different options, preferably in combination with different grid resolutions.

For a river engineer or modeller, the challenge is obtaining an overview of the applicability of the different available models and methods, such that not all possible combinations of settings and options need to be investigated for a certain application. For this purpose, today's river engineer needs to have a strong background in physics and numerics and a level of understanding of the applied methods that is comparable to that of the developer of the simulation system. In the remainder of this thesis, it will become clear that many of the different components are interconnected and that the choices listed in the preceeding sections can seldomly be made without considering the other aspects. To aid the modeller to some extent, a list of questions is provided here, that can help in setting up a numerical river model:

1. Are three-dimensional processes expected to play a role, either due to vertical recirculation behind obstacles or in bends, or due to wind effects?

2. Is steep topography present in the model? Here it is to be noted that the topography may be gradually-varying in the continuous repre-

sentation, but that it may be considered steep in the discrete representation on the grid.

3. Which processes/scales are represented on the grid and which are to be handled by turbulence models or other subgrid approaches?

4. How can the grid be constructed, such that all obstacles are properly represented, that either steer or block the flow or significantly limit the flow cross-section?

5. Are dynamic turbulent processes, e.g. vortex shedding, anticipated?

6. What type of momentum advection schemes are available and is there any experience as to how much numerical diffusion is to be expected from them?

7. Are the anticipated spatial and temporal resolutions more in the range of RANS or LES?

By carefully giving these questions some thought before setting up a model, a considerable time can be saved in changes to that model afterwards, based on (unexpected) results from preliminary model runs.

1.3 AIM OF THE THESIS

The primary aim of this thesis is to identify and develop methods suitable for accurate and efficient 2D and 3D river computations. Here, a method is considered accurate when it adequately predicts the total flow resistance and the corresponding water levels, needed for flooding and ship navigation studies, as these are considered the most important aims in river engineering.

To obtain accurate predictions, the model needs to have sufficient resolution, where certain key topographical features (e.g. groynes) are resolved. However, for efficiency, the grid needs to be as coarse as possible, conform the gap between *required* and *feasible* grid resolution as introduced in section 1.2.3. This gap is to be addressed by investigating the possibility to develop an efficient solution algorithm based on the subgrid method from Casulli [46], Casulli and Stelling [51], and Stelling [219], for effectively simulating quasi-steady river flow.

1

As mentioned in the previous sections, at topography-resolving resolutions, other terms in the governing equations become important. For this purpose, the accuracy of several commonly-applied methods both for momentum advection and for turbulent diffusion is reviewed, with a focus on relatively coarse, but geometry-resolving grid resolutions.

For 3D river (flooding) computations, the use of a z-layer model offers a gain in efficiency by avoiding the use of excessive vertical resolution in shallow areas. For this purpose, particular attention is paid to resolving the well-known problem of accurate representation of bed shear stress and vertical turbulent profiles in 3D z-layer models for rivers, addressed in section 1.1.6.

A secondary aim is to create some awareness for the sometimes *large effects* of certain *seemingly small* choices for a river modeller (as expressed by the subtitle of the present thesis). In particular, the artificial backwater effect due to the momentum advection scheme in 2D computations and the effect of the vertical layering and the turbulence model on the bed shear stress and vertical flow structure in 3D computations is investigated. For this purpose, chapters 2 through 4 have titles that express the combination of specific modelling choices and their corresponding physical aspects.

Based on these aims, the research questions of the thesis were formulated. They can be found in section *Research questions*.

1.4   SCOPE OF THE THESIS

The work in this thesis concerns numerical approximations for free-surface flows, with a focus on low-land and inland river flows, i.e. with mild slopes and without salinity transport or tidal influence. The considerations in this work are particularly of interest for quasi-steady applications, where the accuracy of the time integration is of subordinated importance.

For practical purposes, the focus of this work is on computations with a *limited* grid resolution, for which the performance of the considered methods is investigated. By limited grid resolution, a resolution is meant where the important geometrical (or flow) features are resolved using a moderate number of grids cells (commonly between one and ten cells).

The investigations for z-layer models in Chapter 3 are not restricted to river applications and also apply to oceanographic or estuarine modelling, although the bottom shear stress and the effect of the bottom boundary layer on the vertical profiles is less important for such applications (see e.g.

Kleptsova, Pietrzak, and Stelling [123] and Kleptsova, Stelling, and Pietrzak [124]).

The investigations in this thesis involve finite volume and finite difference methods on staggered grids, with a semi-implicit time integration method, where the horizontal advection and diffusion terms are discretized explicitly and both the free-surface gradient and the bottom friction term are discretized implicitly in the momentum equations (see e.g. Casulli [44], Casulli and Cattani [48], Casulli and Stelling [51], and Stelling [219]). This choice was made as it is the author's opinion that this is the best compromise between accuracy and efficiency at moderate grid resolution. For simplicity, we only apply structured grids, both horizontally and vertically (layered, σ- or z-layering). However, the concepts from Chapter 3 are also applicable to horizontally unstructured grids.

1.5 OUTLINE OF THE THESIS

In this thesis we discuss a number of important computational ingredients of numerical river modelling. First in Chapter 2, we address the advection scheme for momentum transport and investigate to what extent it has a numerical/artificial contribution to the backwater in rivers. In this chapter, research questions 1 and 2 are answered. Next, in Chapter 3, we discuss the development of an accurate and efficient 3D z-layer model for river applications. Here we consider the bottom shear stress computation and the vertical turbulence model and how its implementation details can affect the development of the bottom boundary layer and the vertical profiles of e.g. velocity and turbulent eddy viscosity in river models. The representation of the bottom shear stress and the effect of the layering distribution on the accuracy of the results is investigated in combination with the $k - \varepsilon$ turbulence model. Here, research questions 3 and 4 are answered.

Third, in Chapter 4, we present a new solution strategy for the efficient simulation of quasi-steady river flow, applying an approach that combines a recently developed semi-implicit subgrid method (Casulli [46], Casulli and Stelling [51], and Stelling [219]) with a hierarchical-grid solution strategy. The method allows the incorporation of high-resolution data on subgrid scale to obtain a more accurate and efficient hydrodynamic model. Additionally, the method provides automatic insight in grid convergence, by supplying the modeller with computational results on a sequence of (hi-

1

erarchically) refined grids. This chapter answers research questions 5 and 6.

The thesis is finalized in Chapter 5 by summarized answers to the *Research questions*, followed by the general conclusions and an outlook to further possible research.

THE ADVECTION SCHEME AND THE BACKWATER

This chapter is accepted for publication as Platzek et al. [188]: "River computations: artificial backwater from the momentum advection scheme" in the Journal of Hydraulic Research.

The established method for determining dike heights and dimensioning river training structures is to assess the resulting backwater by numerical modelling. The common consensus is that bottom friction determines the backwater and that momentum advection only has a local effect. We demonstrate that the numerical/artificial backwater contribution from the momentum advection approximation can be of the same order of magnitude as the bottom friction contribution, depending on the advection scheme. This is realized using a one-dimensional analysis and verified using a set of one- and two-dimensional test problems including a wavy bed case, flow over emerged and submerged groynes and finally an actual river. We compare first- and second-order accurate advection schemes and compute their artificial contribution to the backwater, for a range of practically-feasible grid resolutions. The tests demonstrate that the conservation/constancy properties of the scheme determine the size of this contribution, rather than the order of the scheme.

2.1 INTRODUCTION

In many countries worldwide, costly river engineering projects aim at verifying the dike heights for flood protection or at dimensioning of river training structures (e.g. groynes) for ship navigation and bank protection. In such projects, the backwater needs to be determined with great certainty and accuracy, mostly by one- and two-dimensional numerical modelling. The backwater arises due to energy losses, commonly assumed to come

2

from bottom friction and turbulent dissipation. However, computer models suffer from numerical errors, which reduce the accuracy of the solution. Such errors mostly originate from the advection approximation for momentum transport, due to its nonlinearity. Here, one might ask: *Do these errors also affect the backwater?*

Most research on the numerical accuracy of advection schemes in shallow-water models is conducted using Godunov methods with Riemann solvers, see Toro and Garcia-Navarro [229] for an overview. These approaches are particularly suited for capturing of shocks or discontinuities, e.g. in dambreak flows or hydraulic jumps. For accurate (quasi-)steady flow predictions over variable topography these schemes require being *well-balanced*, meaning that the flux terms and the source terms need to balance each other in the momentum equations, see e.g. Caleffi and Valiani [38], Caleffi, Valiani, and Li [39], Noelle, Xing, and Shu [171], and Ricchiuto [194] for some recent papers on this topic. These works succesfully illustrate the accuracy, conservation and convergence properties of the applied methods using a number of commonly accepted academic test cases for such local phenomena (dambreak, flow over a bump, interacting shocks, etc.). However, many of these applications apply high-resolution grids, where the relevant (topographical) features are sufficiently resolved.

When considering large-scale river applications, with limited grid resolution (with respect to the topopgraphy), the local accuracy of the model and the capturing of possible discontinuities is often not feasible and also not the most critical issue. More important is the representation of the total energy loss in the system – resulting in the backwater – and the prediction of areas with increased velocity and bottom shear stress, e.g. for morphodynamic predictions. There may be locations in a model where one might expect energy losses in reality, but where the model lacks the required resolution to accurately represent the flow patterns causing them, e.g. for the flow over obstacles such as weirs or groynes. For this purpose, the numerical accuracy of the model needs to be investigated differently by focusing on the total flow resistance (physical and numerical).

To the authors' knowledge very few works have considered the numerical errors in this way. Canestrelli and Toro [40] investigated a FORCE-type centred momentum advection scheme and found that different implementations of the scheme showed considerable differences in the backwater in a river reach, due to numerical diffusion from the advection discretization. This matches the findings of Stelling and Duinmeijer [220], who ex-

2

amined a number of advection schemes, with different conservation/constancy properties, and showed how the head loss varies for the flow over sudden expansions, contractions and over a weir.

In this work, we continue these considerations and provide a new interpretation of discretization errors in numerical river modelling, introducing the concept of *artificial backwater*. We focus on real-world, quasi-steady river applications with complex geometry, using feasible grid resolution for engineering practice. The aim of this work is to determine the artificial contribution to the backwater and its dependence on the momentum advection approximation, for river applications with variable topography. We establish expressions for the contribution to the global backwater from errors in the advection scheme through an analysis of the steady inviscid momentum equation, also called the backwater or Bélanger equation, see e.g. Chanson [58, 59].

The results from this analysis are confirmed using a sequence of tests with flow over variable topography. A set of test problems was defined that increases in complexity towards a real-world case study of a 17 km stretch of the Elbe river in Germany. Applying a vertically-integrated, two-dimensional model, we perform three schematic, actually one-dimensional (1D) tests, investigating the effect of a wavy bed, as well as two schematic two-dimensional (2D) tests with flow around and over groynes, and finally the case study of the Elbe river itself. In order to diminish errors due to the grid structure, we consider simple rectangular grids, allowing us to compare the effect of the advection scheme, exclusively.

In section 2.2, we introduce the investigated momentum advection schemes, for which we analyse the artificial backwater contributions using a 1D analysis in section 2.3. We describe the test cases in section 2.4 and present the results in section 2.5. We end with a discussion and conclusions in sections 2.6 and 2.7.

2.2 MOMENTUM ADVECTION DISCRETIZATIONS

The modelling systems used for real-world river applications are often based on (semi-)implicit, staggered grid, finite-difference methods: e.g. POM (Blumberg and Mellor [24]), UnTRIM (Casulli and Walters [52]), Suntans (Fringer, Gerritsen, and Street [82]), Delft3D (Deltares [69], MIKE 21 (DHI [66]) and HEC-RAS (Brunner [31]). Due to the implicit treatment of the pressure terms, the Courant number for stability is only based on the

flow velocity u and not on the wave celerity $c = \sqrt{gH}$. For this reason – for low-Froude number, quasi-steady river computations – these approaches allow the application of relatively large time steps and suffer from numerical diffusion that only scales with u and not with $u \pm c$.

The (nonlinear) momentum advection schemes in the aforementioned models are often extensions/combinations of several basic upwind schemes. In this section, we present a number of such schemes, which have been chosen for their different properties and complexities. The schemes have been implemented and tested in a two-dimensional, depth-averaged shallow-water solver (Platzek et al. [187]). For the present investigations, the contributions due to horizontal diffusion, Coriolis and wind are neglected. The momentum and continuity equations then read:

$$\frac{\partial u}{\partial t} + u\frac{\partial u}{\partial x} + v\frac{\partial u}{\partial y} + g\frac{\partial \zeta}{\partial x} + \frac{\gamma \,|U|\, u}{H} \;=\; 0 \tag{1}$$

$$\frac{\partial v}{\partial t} + u\frac{\partial v}{\partial x} + v\frac{\partial v}{\partial y} + g\frac{\partial \zeta}{\partial y} + \frac{\gamma \,|U|\, v}{H} \;=\; 0 \tag{2}$$

$$\frac{\partial \zeta}{\partial t} + \frac{\partial \,(Hu)}{\partial x} + \frac{\partial \,(Hv)}{\partial y} \;=\; 0 \tag{3}$$

where u and v are the depth-averaged velocities in the x- and y-directions; ζ is the free-surface position; H is the total water depth defined as $H = \zeta - h$, where h is the bed level; t represents time; g is the gravitational acceleration and γ is the bottom friction coefficient, computed using e.g. a Chézy, Manning or Nikuradse roughness formulation and $|U| = (u^2 + v^2)^{1/2}$.

The equations are discretized on a uniform Cartesian grid, with grid sizes Δx and Δy. The grid has I cells in the x-direction and J cells in the y-direction. We use a C-grid administration (staggered positioning of variables), i.e. the water level ζ is specified in cell centres and the velocity components u and v at cell edges (see Fig. 3 for a 1D representation). $\Omega_{i,j}$ is the cell at position (i, j), where i and j are the indices in x and y-direction, respectively, with $i = 1, 2, \ldots, I$; $j = 1, 2, \ldots, J$. We discretize the momentum equation (1) for each cell edge $\Gamma_{i+1/2,j}$ using a semi-implicit time discretization where the advection term is treated explicitly and both the free-surface

2

gradient and the bottom friction term are discretized implicitly (see e.g. Casulli [44] and Casulli and Cattani [48]):

$$\frac{u_{i+1/2,j}^{n+1} - u_{i+1/2,j}^{n}}{\Delta t} + Fu_{i+1/2,j}^{n} + g\frac{\zeta_{i+1,j}^{n+1} - \zeta_{i,j}^{n+1}}{\Delta x}$$
$$+ \frac{\gamma_{i+1/2,j}^{n}}{H_{i+1/2,j}^{n}}\left|U_{i+1/2,j}^{n}\right|u_{i+1/2,j}^{n+1} = 0 \tag{4}$$

where n is the time level and Δt is the time step size. On the uniform rectangular grid, the central discretization for the pressure gradient in (4) is second-order accurate. The depth in the velocity point $H_{i+1/2}^{n}$ used in the friction term is also approximated using central averaging. The operator $Fu_{i+1/2,j}^{n}$ contains the explicit discretization of the momentum advection term and is the subject of the present investigation. The momentum equation in the y-direction (2) is discretized similarly.

We investigate the effect on the backwater of three first-order and two second-order accurate discretizations for the advective operator Fu (and Fv):

(1) First-order upwind   (FOU)
(2) First-order upwind, momentum conservative   (FOU-MC-E)
(3) First-order upwind, with energy-head constancy   (FOU-EHC)
(4) Second-order upwind   (SOU)
(5) Second-order upwind, momentum conservative   (SOU-MC-E)

For brevity, only the discretization of the longitudinal advection term $u\partial u/\partial x$ as in a 1D model (leaving out the cross-advection term $v\partial u/\partial y$) is presented. Similar expressions hold for the discretization of Fv in two dimensions. The three first-order schemes can be written in the following general form:

$$Fu_{i+1/2,j}^{n} = u_{i+1,j}^{+}\frac{u_{i+3/2,j}^{n} - u_{i+1/2,j}^{n}}{\Delta x} + u_{i,j}^{-}\frac{u_{i+1/2,j}^{n} - u_{i-1/2,j}^{n}}{\Delta x} \tag{5}$$

The definition of the advective velocities $u_{i+1,j}^{+}$ and $u_{i,j}^{-}$ determines the properties of the scheme.

a) Finite difference   b) Finite volume
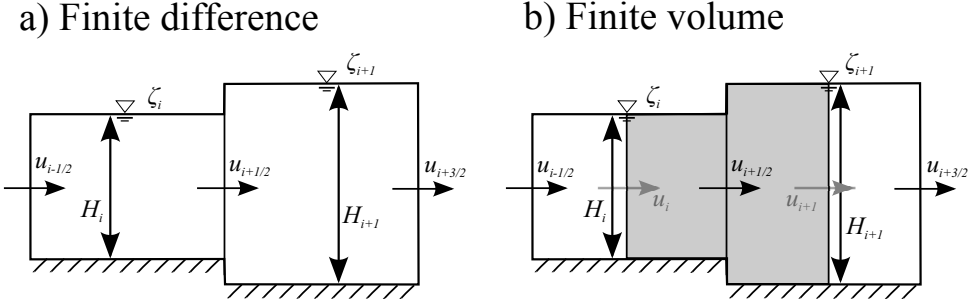
Figure 3: The staggered 1D stencil with water level ζ and total depth H in the cell centres and velocity u and at the edges. a): the finite difference stencil. b): the finite volume stencil with the velocity volume (grey area) and the cell centre velocities u_i (grey vectors).

2.2.1   *First order upwind (FOU)*

This is the simplest upwind discretization. The advection term is computed using (5), where the advective velocities are simply taken first-order upwind:

$$u^+_{i+1,j} = \begin{cases} 0 & \text{if} \quad u^n_{i+1/2,j} \geq 0 \\ u^n_{i+1/2,j} & \text{if} \quad u^n_{i+1/2,j} < 0 \end{cases} \tag{6}$$

$$u^-_{i,j} = \begin{cases} u^n_{i+1/2,j} & \text{if} \quad u^n_{i+1/2,j} > 0 \\ 0 & \text{if} \quad u^n_{i+1/2,j} \leq 0 \end{cases} \tag{7}$$

For positive flow direction ($u^n_{i+1/2,j} > 0$), insertion of these advective velocities in (5) results in:

$$Fu^n_{i+1/2,j} = u^n_{i+1/2,j} \frac{u^n_{i+1/2,j} - u^n_{i-1/2,j}}{\Delta x} \tag{8}$$

2.2.2   *First order upwind, momentum conservative (FOU-MC-E)*

In this discretization, that was introduced in Stelling and Duinmeijer [220], a conservative finite volume formulation is rewritten to a simple finite difference method with the same properties. The method was extended to unstructured grids based on the work by Perot [181] in Kramer and Stelling [125] and applied and further developed in Kernkamp et al. [119] and Kleptsova, Pietrzak, and Stelling [123]. It was applied in combination with

high-resolution subgrid topography by Stelling [219] (on quadtree grids) and Volp, Prooijen, and Stelling [240]. With the chosen semi-implicit temporal discretization, it can only be demonstrated to be momentum conservative on a discrete level for stationary conditions. It is derived by rewriting the advection term from (1) into:

$$u\frac{\partial u}{\partial x} = \frac{1}{H}\left(\frac{\partial\left(qu\right)}{\partial x} - u\frac{\partial q}{\partial x}\right) \tag{9}$$

where $q = Hu$ is the specific discharge. Discretizing for edge $\Gamma_{i+1/2,j}$ at time level n, we get:

$$Fu_{i+1/2,j}^n = \frac{1}{\overline{H}_{i+1/2,j}^n}\left(\frac{\overline{q}_{i+1,j}^x u_{i+1,j}^* - \overline{q}_{i,j}^x u_{i,j}^*}{\Delta x} - u_{i+1/2,j}\frac{\overline{q}_{i+1,j}^x - \overline{q}_{i,j}^x}{\Delta x}\right) \tag{10}$$

where

$$\overline{q}_i^x,j = \frac{1}{2}\left(q_{i-1/2,j}^x + q_{i+1/2,j}^x\right)$$
$$= \frac{1}{2}\left(H_{i-1/2,j}^* u_{i-1/2,j}^n + H_{i+1/2,j}^* u_{i+1/2,j}^n\right) \tag{11}$$

$$\overline{H}_{i+1/2,j}^n = \frac{1}{2}\left(H_{i,j}^n + H_{i+1,j}^n\right) \tag{12}$$

$$H_{i+1/2,j}^* = \begin{cases} \zeta_{i,j}^n - h_{i+1/2,j}^n & \text{if } u_{i+1/2,j}^n \geq 0 \\ \zeta_{i+1,j}^n - h_{i+1/2,j}^n & \text{if } u_{i+1/2,j}^n < 0 \end{cases} \tag{13}$$

$$u_{i,j}^* = \begin{cases} u_{i-1/2,j}^n & \text{if } u_{i-1/2,j}^n + u_{i+1/2,j}^n \geq 0 \\ u_{i+1/2,j}^n & \text{if } u_{i-1/2,j}^n + u_{i+1/2,j}^n < 0 \end{cases} \tag{14}$$

For flow in the positive x-direction, this simplifies to the following advection term:

$$u\frac{\partial u}{\partial x}\bigg|_{i+1/2}^n = \frac{q_{i-1/2,j}^x + q_{i+1/2,j}^x}{H_{i,j}^n + H_{i+1,j}^n}\frac{u_{i+1/2}^n - u_{i-1/2}^n}{\Delta x} \tag{15}$$

The advective velocities in (5) for this scheme are thus computed as:

$$u_{i+1,j}^+ = \begin{cases} 0 & \text{if } u_{i+1/2,j}^n + u_{i+3/2,j}^n \geq 0 \\ \frac{q_{i+1/2,j}^x + q_{i+3/2,j}^x}{H_{i,j}^n + H_{i+1,j}^n} & \text{if } u_{i+1/2,j}^n + u_{i+3/2,j}^n < 0 \end{cases} \tag{16}$$

$$u_{i,j}^- = \begin{cases} \frac{q_{i-1/2,j}^x + q_{i+1/2,j}^x}{H_{i,j}^n + H_{i+1,j}^n} & \text{if } u_{i-1/2,j}^n + u_{i+1/2,j}^n > 0 \\ 0 & \text{if } u_{i-1/2,j}^n + u_{i+1/2,j}^n \leq 0 \end{cases} \tag{17}$$

where $q_{i+1/2,j}^x = Q_{i+1/2,j}^n/\Delta y$ is the specific discharge in x-direction. The detailed derivation can be found in Stelling and Duinmeijer [220].

2

2.2.3 *First order upwind, with energy-head constancy (FOU-EHC)*

This discretization was also introduced in Stelling and Duinmeijer [220] and applied in Kramer and Stelling [125] and Platzek et al. [187]. The advection is again expressed as (5), and the advective velocities are computed as:

$$
u^{+}_{i+1,j} = \begin{cases} 0 & \text{if} \quad u^{n}_{i+1/2,j} + u^{n}_{i+3/2,j} \geq 0 \\ -\frac{1}{2}\left(u^{n}_{i+1/2,j} + u^{n}_{i+3/2,j}\right) & \text{if} \quad u^{n}_{i+1/2,j} + u^{n}_{i+3/2,j} < 0 \end{cases} \quad (18)
$$

$$
u^{-}_{i,j} = \begin{cases} \frac{1}{2}\left(u^{n}_{i-1/2,j} + u^{n}_{i+1/2,j}\right) & \text{if} \quad u^{n}_{i-1/2,j} + u^{n}_{i+1/2,j} > 0 \\ 0 & \text{if} \quad u^{n}_{i-1/2,j} + u^{n}_{i+1/2,j} \leq 0 \end{cases} \quad (19)
$$

For positive flow direction ($u^{n}_{i+1/2,j} > 0$), insertion of these advective velocities in (5) results in:

$$
\begin{aligned}
Fu^{n}_{i+1/2,j} &= \frac{u^{n}_{i-1/2,j} + u^{n}_{i+1/2,j}}{2} \frac{u^{n}_{i+1/2,j} - u^{n}_{i-1/2,j}}{\Delta x} \\
&= \frac{\frac{1}{2}\left(u^{n}_{i+1/2,j}\right)^{2} - \frac{1}{2}\left(u^{n}_{i-1/2,j}\right)^{2}}{\Delta x}
\end{aligned} \quad (20)
$$

Combined with a central discretization of the pressure gradient, this scheme keeps the energy head $\zeta_{i,j} + u^{2}_{i-1/2,j}/(2g)$ (note the shifted indices) constant along streamlines without introducing any backwater. The analysis in section 2.3 and the numerical tests in section 2.4 confirm this property.

2.2.4 *Second-order upwind (SOU)*

This scheme is the extension of the first order upwind scheme in section 2.2.1, based on inclusion of an extra term from the Taylor series expansion. It cannot be written in the general form of the first-order schemes (5). Instead the discretization reads:

$$
\begin{aligned}
Fu^{n}_{i+1/2,j} = -\frac{1}{\Delta x} \Big[&u^{*}_{i+1,j}\left(u^{n}_{i+5/2,j} - 4u^{n}_{i+3/2,j} + 3u^{n}_{i+1/2,j}\right) \\
&+ u^{*}_{i,j}\left(3u^{n}_{i+1/2,j} - 4u^{n}_{i-1/2,j} + u^{n}_{i-3/2,j}\right) \Big]
\end{aligned} \quad (21)
$$

2

with advective velocities u_{i+1}^* and u_i^*:

$$u_{i+1,j}^* = \begin{cases} 0 & \text{if} \quad u_{i+1/2,j}^n \geq 0 \\ u_{i+1/2,j}^n & \text{if} \quad u_{i+1/2,j}^n < 0 \end{cases} \tag{22}$$

$$u_{i,j}^* = \begin{cases} u_{i+1/2,j}^x & \text{if} \quad u_{i+1/2,j}^n > 0 \\ 0 & \text{if} \quad u_{i+1/2,j}^n \leq 0 \end{cases} \tag{23}$$

This scheme can be shown to be second-order accurate in space on a regular grid.

2.2.5 *Second order upwind, momentum conservative (SOU-MC-E)*

The scheme from section 2.2.2 can be improved by using second-order accurate interpolation with a slope limiter (see e.g. Stelling and Duinmeijer [220]), to compute both the upwind value for $u_{i,j}^*$ at the cell centre and the water level $\zeta_{i+1/2,j}^*$ needed at the cell face to compute the total depth $H_{i+1/2}$. In practice, the slope limiter makes sure that the scheme reduces to first order when there is large local variation of the gradients. In the end, only the computation of the upwind expressions for $H_{i+1/2,j}^n$ and for $u_{i,j}^*$ is modified:

$$H_{i+1/2,j}^n = \zeta_{i+1/2,j}^* - h_{i+1/2,j}^n \tag{24}$$

$$\zeta_{i+1/2,j}^* = \begin{cases} \zeta_{i,j}^n + \frac{1}{2}\psi\left(r_+^\zeta\right)\left(\zeta_{i,j}^n - \zeta_{i-1,j}^n\right) & \text{if} \quad u_{i+1/2,j}^n \geq 0 \\ \zeta_{i+1,j}^n - \frac{1}{2}\psi\left(r_-^\zeta\right)\left(\zeta_{i+2,j}^n - \zeta_{i+1,j}^n\right) & \text{if} \quad u_{i+1/2,j}^n < 0 \end{cases} \tag{25}$$

$$r_+^\zeta = \frac{\zeta_{i+1,j}^n - \zeta_{i,j}^n}{\zeta_{i,j}^n - \zeta_{i-1,j}^n} \quad , \quad r_-^\zeta = \frac{\zeta_{i+1,j}^n - \zeta_{i,j}^n}{\zeta_{i+2,j}^n - \zeta_{i+1,j}^n} \tag{26}$$

$$u_{i,j}^* = \begin{cases} u_{i-1/2,j}^n + \\ \quad \frac{1}{2}\psi\left(r_+^u\right)\left(u_{i-1/2,j}^n - u_{i-3/2,j}^n\right) & \text{if} \quad u_{i-1/2,j}^n + u_{i+1/2,j}^n \geq 0 \\ u_{i+1/2,j}^n - \\ \quad \frac{1}{2}\psi\left(r_-^u\right)\left(u_{i+3/2,j}^n - u_{i+1/2,j}^n\right) & \text{if} \quad u_{i-1/2,j}^n + u_{i+1/2,j}^n < 0 \end{cases} \tag{27}$$

$$r_+^u = \frac{u_{i+1/2,j}^n - u_{i-1/2,j}^n}{u_{i-1/2,j}^n - u_{i-3/2,j}^n} \quad , \quad r_-^u = \frac{u_{i+1/2,j}^n - u_{i-1/2,j}^n}{u_{i+3/2,j}^n - u_{i+1/2,j}^n} \tag{28}$$

For the evaluation of the limiter function ψ many variants are known from the literature, see e.g. Zhang et al. [265]. We have implemented and tested several (MinMod, Van Leer, Koren, Monotonized Central, etc.), but the Min-Mod limiter showed the least restriction on the time step for stability and is applied in the present work:

$$\psi\left(r^u\right) = \max\left(0, \min\left(1, r^u\right)\right) \tag{29}$$

For the water levels ζ the expression is defined accordingly.

2.3   ADVECTION SCHEME ANALYSIS

The differential and intregral forms of the governing equations are strictly energy-conservative and – when no discontinuities are present – this should not be affected by the momentum advection term. Unfortunately, discretization errors in the advection scheme lead to numerical diffusion. Here, we analyse the momentum equation (4) and determine the artificial contribution to the backwater due to these discretization errors. For simplicity, we only analyse the three first-order accurate schemes from section 2.2. We restrict ourselves to steady, inviscid, 1D flow and consider only flow in the positive direction ($u > 0$).

The FOU and FOU-EHC scheme are strict finite difference schemes, whereas the FOU-MC-E scheme is derived from a finite volume scheme (see also Fig. 3). For the purpose of performing a general analysis for the three schemes, we define left (L) and right (R) velocities as follows:

$$\begin{aligned} \text{FOU / FOU-EHC}: \quad & u_L = u_{i-1/2}, \quad u_R = u_{i+1/2} \\ \text{FOU-MC-E}: \quad & u_L = u_i, \quad u_R = u_{i+1} \end{aligned} \tag{30}$$

where we leave the actual definition of the cell centre velocities u_i and u_{i+1} open. The water levels for all three schemes are defined as $\zeta_L = \zeta_i$ and $\zeta_R = \zeta_{i+1}$. In this way, the schemes can be written in a general form and (4) reduces to (dropping the time level n since we have assumed a steady state):

$$(\alpha u_L + (1-\alpha)u_R)\frac{u_R - u_L}{\Delta x} + g\frac{\zeta_R - \zeta_L}{\Delta x} = 0 \tag{31}$$

with coefficient α:

$$\begin{aligned} \text{FOU}: \quad & \alpha = 0 \\ \text{FOU-EHC}: \quad & \alpha = \tfrac{1}{2} \\ \text{FOU-MC-E}: \quad & \alpha = u_R/(u_L + u_R) \end{aligned} \tag{32}$$

where the expression for α for the FOU-MC-E scheme was obtained using the definition $q = Hu$, providing $\alpha = H_L/(H_L + H_R) = u_R/(u_L + u_R)$.

Now we integrate the momentum equation over all cells in the x-direction and scale with g to obtain an expression with the dimension of the energy head ([m]):

$$M = \frac{\Delta x}{g} \sum_{i=1}^{I} \left\{ (\alpha u_L + (1 - \alpha)u_R) \frac{u_R - u_L}{\Delta x} + g\frac{\zeta_R - \zeta_L}{\Delta x} \right\} \tag{33}$$

where M is the integral of the momentum equation, which can be rewritten as $M = \Delta H + \Delta H^{ADV}$ (where ADV denotes the chosen advection scheme), to give the backwater ΔH in terms of the energy head $\zeta + u^2/(2g)$:

$$
\begin{aligned}
M &= \frac{1}{g} \sum_{i=1}^{I} \left\{ \left(g\zeta_L + \frac{1}{2}u_L^2 \right) - \left(g\zeta_R + \frac{1}{2}u_R^2 \right) \right\} \\
&+ \frac{1}{g} \sum_{i=1}^{I} \left\{ \left(\frac{1}{2} - \alpha \right) u_L^2 + \left(\frac{1}{2} - \alpha \right) u_R^2 + (2\alpha - 1) u_L u_R \right\}
\end{aligned}
\tag{34}
$$

where the first term on the right is a conservative discretization of the gradient of the energy head which does not contribute to the backwater. The term on the second line forms the artificial backwater contribution from the advection term. We can inspect its value for different α. It can easily be seen that for FOU-EHC scheme (with $\alpha = 1/2$), the total head loss is zero: $\Delta H^{ADV} = \Delta H^{FOU-EHC} = 0$ and the advection term has no contribution to the backwater, as was expected for this scheme.

For $\alpha = 0$ (the FOU scheme), the backwater contribution ΔH becomes:

$$\Delta H^{FOU} = \frac{1}{2g} \sum_{i=1}^{I} (u_L - u_R)^2 \tag{35}$$

which is identical to the sum of all Carnot losses over the channel (without contraction/expansion coefficient), see e.g. Chanson [58]. This term is quadratic and therefore, the artificial backwater contribution from advection for the FOU scheme is always positive.

The same analysis can be done for the FOU-MC-E scheme. Inserting α from (32) in (34) and rearranging, we obtain:

$$\Delta H^{FOU-MC-E} = \frac{1}{2g} \sum_{i=1}^{I} \frac{(u_L - u_R)^3}{u_L + u_R} \tag{36}$$

We can compare the sign and size of (36) and (35) by computing the ratio λ between the local artificial head loss for the FOU-MC-E and FOU scheme:

$$\lambda_{i+1/2} = \frac{\Delta H_{i+1/2}^{FOU-MC-E}}{\Delta H_{i+1/2}^{FOU}} = \frac{u_L - u_R}{u_L + u_R} \tag{37}$$

Since we assumed positive flow direction, this ratio is always smaller than 1 and therefore the backwater from the FOU-MC-E scheme is always less than that from the FOU scheme. Moreover, the ratio is positive for $u_L > u_R$, i.e. for expansions and it is negative for $u_L < u_R$, i.e. for contractions. In other words, for local contractions, the FOU-MC-E advection scheme gives a negative contribution to the backwater, i.e. the advection term causes an erroneous increase in energy head, as already recognized by Kramer and Stelling [125] and Stelling and Duinmeijer [220] for the flow over sudden contractions (flow over a saw-tooth bottom and over a weir).

In line with Kramer and Stelling [125] and Stelling and Duinmeijer [220], one can conclude that for (strong) local contractions with sudden flow variation, the hydrostatic pressure assumption is not valid and equation (4) should be applied with care. In such flow situations, switching locally between the FOU-EHC (at contractions) and the FOU-MC-E scheme (elsewhere), provides more physically correct results.

2.4 NUMERICAL EXPERIMENTS

We now aim to verify the findings from section 2.3 using numerical experiments and quantify the contribution to the backwater or total head loss due to the advection discretization for the flow over variable topography. As a reference, we take an existing numerical model for a stretch of the Elbe river, between the German cities of Lauenburg and Geesthacht (Platzek et al. [187]). From this model, we construct a series of tests with increasing complexity, that schematically represents the geometrical variation along the river stretch: the overall bed slope, bed forms and groynes (leaving bends outside the present investigation). We obtain three schematic 1D tests, two schematic 2D tests and the actual river case study:

1. Uniform channel flow along a constant slope (1D)

2. Flow over a wavy bed without bottom friction (1D)

3. Flow over a sloped wavy bed with bottom friction (1D)

4. Flow over a sloped wavy bed with bottom friction and emerged groynes (2D)

5. Flow over a sloped wavy bed with bottom friction and submerged groynes (2D)

6. Case study: Elbe river from Lauenburg to Geesthacht (2D)

The topography and water levels for the five schematic tests are depicted in Fig. 4. For each test, the channel has a length $L = 1000$ m and width $W = 240$ m. At the upstream boundary a discharge $Q = 960$ m$^3/s$ is prescribed. At the downstream boundary the water level is fixed at $\zeta = 8$ m, which is also the initial condition. The initial flow velocity is $u = v = 0$ m/s. We define a reference bottom height $h_{ref} = 4$ m on which all different geometry variations are superpositioned. In all schematic tests, except for the uniform channel flow test, the channel bottom contains bed forms, which are described by a cosine function in the longitudinal x-direction. The bottom profile with the bed forms is described by the function:

$$h_b(x,y) = h_{ref} + A_b\cos(f_b x) \tag{38}$$

where $h_b(x,y)$ is the bottom height (positive upwards) and A_b is the wave/bed form amplitude. The frequency f_b determines the length of the 'bed forms' and is defined as $f_b = 2\pi n_b/L$, where n_b is the number of bed forms within the domain (see Table 1).

For the groyne tests (tests 4 and 5), seven cosine-shaped groynes – extending over half of the channel width – are superpositioned on top of the sloped wavy bottom, i.e. the main channel and groyne fields have the bottom geometry containing the bed forms from test 3. The length of the groyne fields L_{gf} was chosen to be 130 m (from groyne crest to groyne crest). At the position of the groynes, the topography is described by:

$$h_g(x,y) = h_{ref} + A_b\cos(f_b x) + A_g(1 + \cos(f_g(x - x_{gs}))) \tag{39}$$

where A_g is the groyne amplitude (half of the height) and x_{gs} is the x-coordinate where the cosine of each groyne starts. The frequency f_g follows from the chosen 'width of the groyne' W_g and is defined as $f_g = 2\pi/W_g$. The geometrical parameters of all the tests are presented in Table 1.

For all five schematic tests and all five advection schemes, we apply four recursively finer grids, to investigate the convergence properties and grid dependency of the schemes:

2
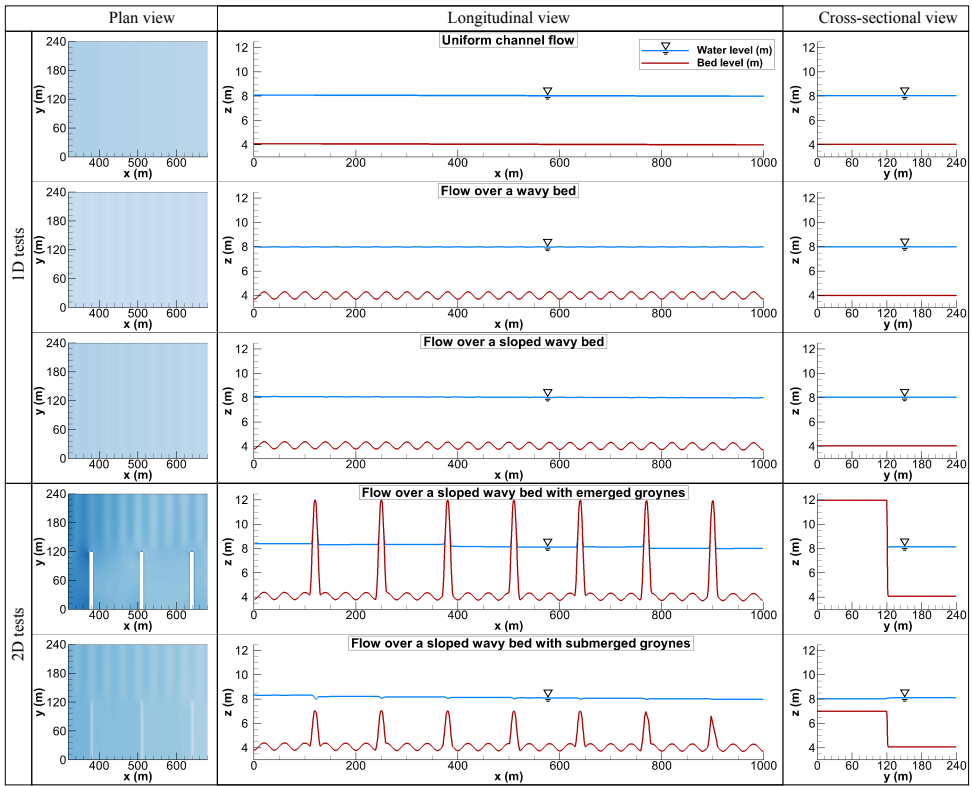
Figure 4: Plan view of water level (left), longitudinal view (middle) and cross-sectional view (right) of geometry and water level for tests 1–5. Longitudinal section taken at y = 60 m. Lateral cross-section taken x = 510 m.

1. Δx = 10 m (4 cells per bed form)

2. Δx = 5 m (8 cells per bed form)

3. Δx = 2.5 m (16 cells per bed form)

4. Δx = 1.25 m (32 cells per bed form)

For the Elbe river test, also 4 recursively finer resolutions ranging from Δx = 16 m to Δx = 2 m are applied.

For all tests, the time step is determined dynamically based on a prescribed Courant number $C = |u^{max}|\Delta t/\Delta x$ and the maximum flow velocity u^{max}. For the first-order schemes, the Courant number was fixed at C = 0.7 and for the second-order schemes at C = 0.2, for maintaining stable solutions. The maximum Froude number $F^{max} = u/\sqrt{gH}$ was also determined,

Table 1: Topography definitions for the five schematic tests. [a] The maximum Froude number $F^{max} \approx 1$ at the most upstream groyne for the submerged groyne case.

Test	L (m)	W [m]	h_{ref} (m)	i_b (-)	C_z ($\sqrt{m}$/s)	n_b (-)	L_b (m)	A_b (m)	n_g (-)	W_g (m)	A_g (m)	L_{gf} (m)	F^{max} (-)
					Parameter								
1	1000	240	4	10^{-4}	50	0	0	0	0	0	0	0	0.16
2	1000	240	4	0	∞	25	40	0.3	0	0	0	0	0.17
3	1000	240	4	10^{-4}	50	25	40	0.3	0	0	0	0	0.17
4	1000	240	4	10^{-4}	50	25	40	0.3	7	20	4	130	0.36
5	1000	240	4	10^{-4}	50	25	40	0.3	7	20	1.5	130	0.7^{a}

yielding subcritical flow for all cases (see Table 1). Only for the submerged groyne case, the flow locally becomes critical, with $\mathsf{F}^{\max} \approx 1$ at the first groyne, see section 2.5.5.

2.4.1 Uniform channel flow

For this test, the channel described above has a bottom slope $i_b = 1 \times 10^{-4}$ m/m (see Table 1), sloping from $z = 4.1$ m to $z = 4$ m (h_{ref}), giving the channel an equilibrium depth of $H^{eq} = 4$ m. Combined with a Chézy bottom roughness $C_z = 50$ m$^{1/2}$/s, this results in a flow velocity $u = C_z\sqrt{Hi_b} = 1$ m/s, which matches the boundary condition described above. For this test, the advection term should be zero.

2.4.2 Flow over a wavy bed

As described above, the channel bottom is described by a series of 25 cosines (wave length $L_b = 40$ m) forming a wavy bed in the longitudinal x-direction (see Table 1). The amplitude of the bed forms is $A_b = 0.3$ m, causing the total water depth to vary approximately from $H = 3.7$ to 4.3 m. In the lateral y-direction, the bottom is constant. There is no general slope in the bed and the bottom friction is switched off: $\gamma = 0$. The bottom topography is shown in Fig. 4.

For the steady and inviscid flow over a smooth bottom at low Froude numbers the analytical solution can be computed based on the principles of mass and momentum conservation. For this simple flow situation, the momentum equation reduces to the Bernoulli equation upon integration (formally along a streamline):

$$u\frac{\partial u}{\partial x} + g\frac{\partial \zeta}{\partial x} = 0 \Rightarrow \tag{40}$$

$$\frac{1}{2}u^2 + g\zeta = E \tag{41}$$

where E is the integration constant, being the total (kinetic + potential) energy (divided by the density) in the system. It can be determined using the continuity equation and the boundary condition: $E = g\zeta_{BC} - \frac{1}{2}(q/H_{BC})^2$, where ζ_{BC} is the water level prescribed e.g. at the downstream boundary and H_{BC} is its corresponding total water depth. This system of equations can be reduced to a single equation by substituting the steady 1D continuity equation $u = Q/(WH) = q/H$ into the Bernoulli equation. After some

algebra one ends up with the following cubic relation for the unknown total water depth $H = H(x)$, depending also on the bottom topography $h = h(x)$ (see e.g. also Ricchiuto [194]):

$$H^3 + \left(h - \frac{E}{2g}\right) H^2 + \frac{q^2}{2g} = 0 \tag{42}$$

This equation can be solved e.g. using Cardano's formula, or iteratively using Newton iterations. The solution for u is then obtained from $u = q/H$. The expressions for H and u are lengthy and therefore omitted, but as can be expected, they show an alternating wavy pattern. For this test, it is important that there should be no energy losses (zero bottom friction) and therefore no global backwater. The water level at the entrance of the channel should also be at $\zeta = 8$ m. Any backwater in the experiment must come from numerical dissipation.

2.4.3 Flow over a sloped wavy bed with bottom friction

In this test the uniform channel flow (with bottom friction) and the inviscid wavy bed test are combined. The bottom topography for the sloped wavy bed test is the same as for the wavy bed case, except for an additional downward slope of $i_b = 1 \times 10^{-4}$. Additionally, the bed friction is set to $C_z = 50$ m$^{1/2}$/s. The test settings are summarized in Table 1. The reference solution for this test was obtained by a step method integrating the momentum equation (now including bottom friction) from the downstream boundary upwards.

2.4.4 Flow over a sloped wavy bed with emerged groynes

In this test, we add groynes to the sloped channel with wavy bed. Seven schematic groynes (described by cosine waves), with a groyne width in stream-wise direction $W_g = 20$ m are added. The groynes extend over half of the channel width, i.e. the groynes are 120 m long and the groyne heads are cut vertically. The groyne fields between the groynes have a length $L_{gf} = 130$ m (from groyne crest to groyne crest). In this first test, the groynes have a height of 8 m (twice the cosine amplitude of the groyne $A_g = 4$ m) and are therefore emerged, see Table 1 and Figure 4.

2.4.5   *Flow over a sloped wavy bed with submerged groynes*

For this test, only the cosine amplitude (half of the height) of the groynes is modified. The groynes are now 3 m high (A_g = 1.5 m) and therefore approximately 1 m submerged. All other parameters for this test are identical to the emerged groynes test of the previous section, see Table 1. The topography and water level is displayed in Fig. 4.

By comparing the results of the emerged and the submerged groynes case, one can investigate the effect of *lowering the groynes*, an important topic of discussion for river maintenance and flood protection issues (see e.g. Busnelli et al. [37]).

2.4.6   *The Elbe River from Lauenburg to Geesthacht*

The final test is the case study from which we derived the schematic tests. It concerns a reach of the Elbe River between the cities of Lauenburg and Geesthacht in Germany, which is approximately 17 km long and – including the floodplains – 2.5 km wide (see Fig. 25). The stretch contains natural bed forms with similar characteristics as the wavy bed cases and it contains groynes which are emerged near the bank and submerged near the groyne tip, for the chosen discharge. All parameters for this test were taken from Platzek et al. [187].

2.5   RESULTS

For each of the tests described in section 2.4, for all five advection schemes and the four specified grid resolutions, we compute the contributions from bottom friction and the advection scheme to the total backwater, and the behaviour of these contributions with grid refinement. The different contributions to the backwater are computed numerically in the same way as for the analysis in section 2.3, i.e. by integrating the corresponding terms (pressure, advection, bottom friction) over the length of the channel and scaling with g. For the 2D tests, an additional averaging over the width of the channel is performed. We express the backwater or head loss ΔH at the inflow boundary in % of the backwater due to bottom friction over the same channel length. For test 2, with only bed forms and no bottom friction, the (analytical) backwater due to bottom friction from test 3 is used
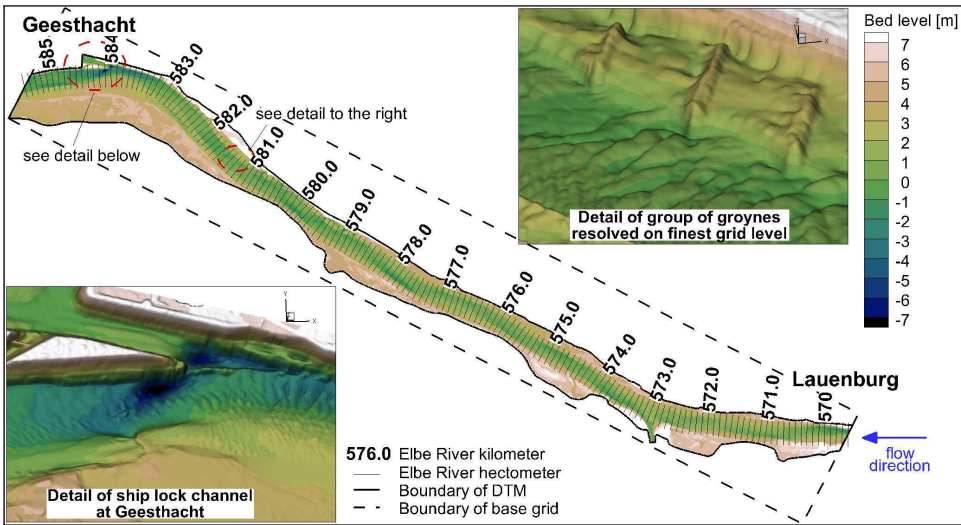
Figure 5: The Elbe River model: Digital Terrain Model (DTM) (2x2 m) for the Elbe River between the city of Lauenburg and the weir at Geesthacht. The 3D detail figures of the topography are ten times vertically exaggerated, compared to the horizontal scale. Copyright © 2016 John Wiley & Sons, reprinted with permission from Platzek et al. [187].

as a reference. For the two groyne tests and for the Elbe river case no analytic solution is available and the head loss from the runs with the smallest backwater is taken as the reference ΔH^{ref}.

We have seen from the analysis in section 2.3, that the artificial backwater contribution from the momentum advection discretization can be positive or negative. For this purpose, we have chosen the backwater (or upstream water level difference) as the error norm and not a strictly-positive mathematical error norm (e.g. L_∞, L_1 or L_2), as it would not show the difference between a positive or negative backwater effect. To illustrate the order of convergence for tests 2 and 3 (where an analytical solution is available), we compute the L_∞ norm and the convergence rates p based on the L_1 norm of the water level:

$$
p^l = \frac{\log\left(\frac{L_1^{l-1}}{L_1^l}\right)}{\log(2)}, \quad \text{for} \quad l = 2, 3, \ldots, l^{\max}
\tag{43}
$$

2

with

$$L_1^l = \frac{1}{I^l} \sum_{i=1}^{I^l} \left(\zeta_i^l - \zeta_i^{analytic} \right) \tag{44}$$

where l is the grid level within the convergence study and I^l is the number of grid cells in x-direction on grid l. The convergence rate then gives the order of the scheme: $O(\Delta x^p)$.

2.5.1 *Uniform channel flow*

In this test, bottom friction causes the water level to be sloped downward along the channel from $\zeta = 8.1$ m to $\zeta = 8$ m, resulting in a constant total water depth $H = 4$ m. Any deviation must come from errors made in the advection discretizaton or from the boundaries. The largest deviation of the water level at the upstream boundary, i.e. the numerical head loss or backwater, over all four resolutions, drops from -5 $\times$ 10^{-4} m ($\Delta x = 10$ m) to -5 $\times$ 10^{-5} m. For the backwater $\Delta H = 10$ cm over the length of the channel, this is a spurious contribution of -0.5 to -0.05 % due to discretization errors. No significant differences were found between the different advection schemes. For this test, it can therefore be concluded that – as expected – advection plays no significant role, and only bottom friction causes the backwater.

2.5.2 *Flow over a wavy bed*

For this test, the bottom friction is zero, but the bed level varies, causing gradual flow variation (due to the Bernoulli effect), which should occur without energy losses. As a reference for this test we take the backwater one would have over the same channel length, when bottom friction would be applied (see section 2.5.3). Due to the additional resistance of the flow accelerations over the wavy bed, this backwater amounts to 10.22 cm (instead of the 10 cm for the uniform channel flow). Figure 6a shows the upstream head loss (or backwater) for the five advection schemes and the four grid resolutions. There is only a contribution from the advection term, as the bottom friction is zero. It can be seen that depending on the advection scheme, the numerical head loss can be as high as 36 % of the backwater due to bottom friction, amounting to an artificial (additional) backwater of

2
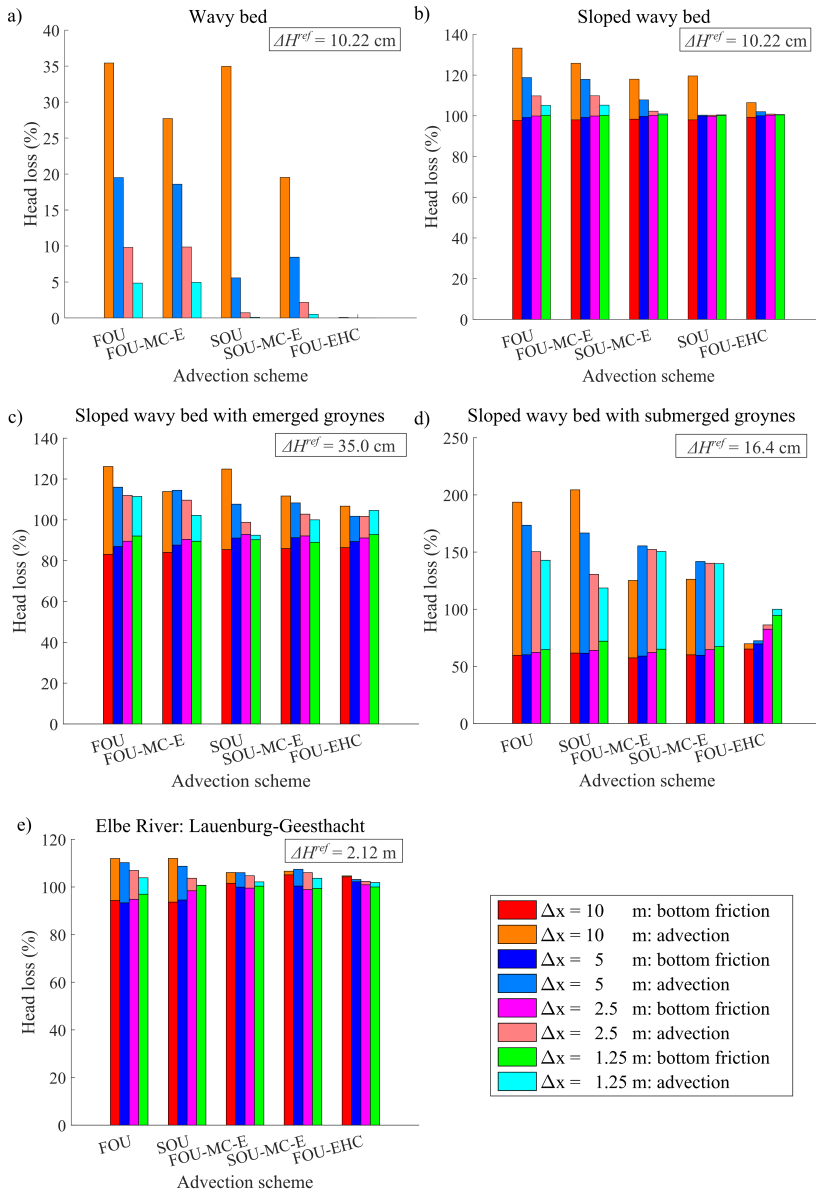
Figure 6: Percentual head loss for test cases 2–6, for all five advection schemes and all four grid resolutions. Displayed is the total head loss as a sum of the head loss due to bottom friction and the head loss due to advection for: a) flow over a wavy bed; b) flow over a sloped wavy bed; c) flow over a sloped wavy bed with emerged groynes; d) flow over a sloped wavy bed with submerged groynes; e) the Elbe River from Lauenburg to Geesthacht. The reference head losses ΔH^{ref} are also included.

3.6 cm. As was demonstrated using the analysis in section 2.3, the FOU-EHC scheme shows (almost) no backwater. The very small backwater on the coarsest grid (0.1 %) comes exclusively from the downstream boundary, due to a discrepancy in discretely representing the exact bed level at the boundary. Over the channel there is no additional build-up of the backwater. As expected, the second-order schemes perform somewhat better than their first-order counterparts. This can also be verified using the L_∞ norms and convergence rates given in Table 2.

2.5.3 *Flow over a sloped wavy bed*

Now we investigate to which extent the results from the previous test are also valid when combined with bottom friction (and a channel slope). For this test, the bed level variations interact with the quadratic bottom friction, resulting in a theoretical backwater and reference head loss of ΔH^{ref} = 10.22 cm (obtained using numerical integration of the equations on a Δx = 0.00125 m grid). Figure 6b shows the total percentual upstream head loss $100 \times (\zeta_{upstream} - \zeta_{upstream}^{ref})/\Delta H^{ref}$ consisting of contributions both from the bed friction and from the advection term, for the different advection schemes and the four resolutions. The maximum head loss of 132 % corresponds to 13.7 cm total head loss, instead of the 10.22 cm (100 %) for the analytic solution. The results for the five schemes correspond to those of the previous test.

From these results one can conclude that the common consensus that numerical river models are dominated by a *global* balance between pressure gradient and bottom friction (in the momentum equation) is not completely valid, due to the artificial backwater contribution from the advection approximation. For moderately coarse grids and for many advection schemes, the contribution of the advection term to the balance is of the same order as the backwater due to bottom friction. For the *local* balance in the momentum equation, the contribution from the advection term is even more dominant, as can be seen from Fig. 7, where we plotted the distribution along the channel centreline of the different acceleration terms in the momentum equation (summing up to zero), for the sloped wavy bed test, where we even reduced the bed form amplitude A_b to only 5 cm.

For completeness, the L_∞ norms and the convergence rates for this test have been included in Table 2. It can be seen that the inclusion of bottom

Table 2: L_∞ norms and convergence rates p for the different advection schemes, for tests 2 and 3 (flow over a wavy bed and over a sloped wavy bed).

Advection scheme	Grid resolution Δx (m)	Test 2: wavy bed		Test 3: sloped wavy bed	
		L_∞ norm (m)	Convergence rate p	L_∞ norm (m)	Convergence rate p
FOU	10	4.2×10^{-2}	-	4.0×10^{-2}	-
	5	2.3×10^{-2}	0.98	2.2×10^{-2}	0.97
	2.5	1.2×10^{-2}	1.06	1.1×10^{-2}	1.05
	1.25	5.7×10^{-3}	1.05	5.6×10^{-3}	1.04
FOU-MC-E	10	3.4×10^{-2}	-	3.3×10^{-2}	-
	5	2.2×10^{-2}	0.75	2.1×10^{-2}	0.75
	2.5	1.1×10^{-2}	0.99	1.1×10^{-2}	0.98
	1.25	5.8×10^{-3}	1.03	5.7×10^{-3}	1.02
FOU-EHC	10	6.1×10^{-3}	-	6.4×10^{-3}	-
	5	3.1×10^{-3}	0.93	3.3×10^{-3}	0.93
	2.5	1.6×10^{-3}	0.98	1.6×10^{-3}	0.98
	1.25	7.9×10^{-4}	0.99	8.4×10^{-4}	0.99
SOU	10	3.7×10^{-2}	-	3.6×10^{-2}	-
	5	6.1×10^{-3}	2.92	6.1×10^{-3}	2.87
	2.5	8.9×10^{-4}	2.79	9.5×10^{-4}	2.72
	1.25	2.3×10^{-4}	2.12	1.9×10^{-4}	2.17
SOU-MC-E	10	2.6×10^{-2}	-	2.5×10^{-2}	-
	5	1.0×10^{-2}	1.45	1.0×10^{-2}	1.43
	2.5	2.6×10^{-3}	2.02	2.6×10^{-3}	1.96
	1.25	6.3×10^{-4}	2.10	6.6×10^{-4}	1.95

2
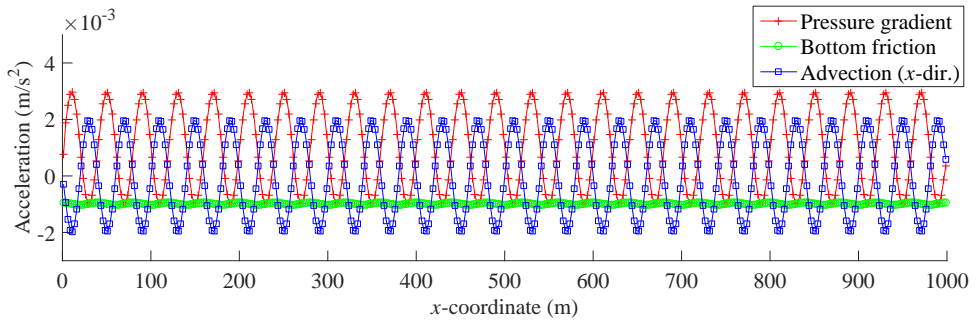
Figure 7: Different acceleration terms in the momentum equation along the channel centreline for the sloped wavy bed test with a reduced bed form amplitude A_b = 0.05 m.

friction has little effect on the convergence rates and that the targeted accuracy is attained by the second-order approximations.

2.5.4 *Flow over a sloped wavy bed with emerged groynes*

In this test, groynes are added to the test from section 2.5.3. The groynes have a height of 6 m above the bed and are therefore emerged. We now inspect the effect of such groynes on the backwater and more specifically, the dependency on the advection scheme. The total head loss again has two contributions: bottom friction and advection. Figure 6c shows the percentual head loss for the five schemes. As no analytical solution is available for this test, we have taken the advection scheme with the least total head loss at the upstream boundary as the reference: ΔH^{ref} = 35 cm, as computed by the FOU-EHC scheme on the Δx = 1.25 m grid (corresponding to a percentual head loss $\Delta H = 100$ %). A 20 % head loss in the figure thus corresponds to 7 cm of additional head loss on top of the 35 cm.

From the figure three things can be noted. First, one can see that with an increased head loss due to advection, the head loss due to bottom friction decreases. Second, the convergence behaviour of the schemes is different. In particular the FOU-EHC scheme shows very little variation over the grids. Finally, it appears that the different schemes converge to different solutions. In particular the fine-grid results of the FOU and SOU scheme differ from the results of the other three schemes.

The switch from a first- to a second-order advection scheme shows moderate influence on the backwater. The effect on the flow velocity and on the
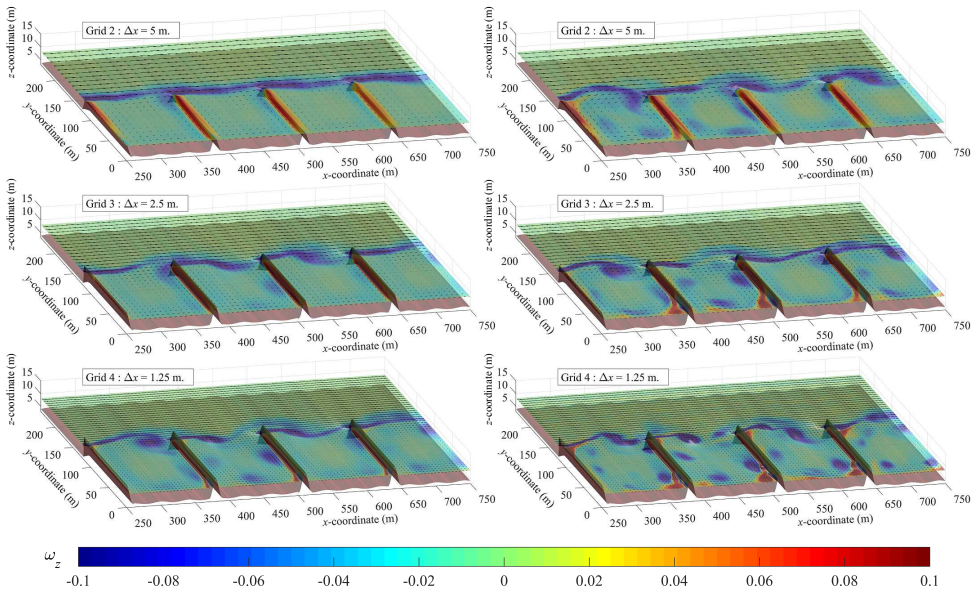
Figure 8: Flow around emerged groynes: z-component of the vorticity $\vec{\omega}$ $[s^{-1}]$ around groynes 5, 6 and 7, superimposed on the free surface level, for the FOU-MC-E (left) and SOU-MC-E (right) advection scheme, for the three finest grids.

emergence of turbulent eddies is much greater. In Fig. 8, the z-component of the vorticity $\vec{\omega} = \vec{\nabla} \times \vec{u}$ is displayed as projected on the free surface, for the FOU-MC-E and SOU-MC-E schemes for the three finest grids. It can be seen that with the first-order scheme, vortex shedding is much less pronounced than with the second-order scheme, in particular on the coarser grids.

2.5.5 *Flow over a sloped wavy bed with submerged groynes*

In this test, the groynes from the previous test are lowered such that they become submerged. The maximum Froude number for this case occurs at the groyne crest near the groyne head. Depending on the chosen advection scheme (and the resulting backwater) we obtain $F^{max} \approx 0.7$. Only at the first groyne, the flow becomes critical with $F^{max} \approx 1$, see also Table 1. This is due to the fact that a uniform discharge is specified over the whole width of the upstream boundary, resulting in a higher specific discharge over the first groyne.

Figure 6d shows the percentual head loss for the different advection schemes and grid resolutions. The reference solution for this test was taken to be the solution obtained with the FOU-EHC scheme on the finest grid resolution with $\Delta x = 1.25$ m, with a total head loss of 16.4 cm, corresponding to a 100 % head loss in the figure. This means that the 277 % head loss in the figure – as obtained using the FOU scheme on the coarsest grid, gives a total head loss of 45.4 cm, i.e. an additional backwater of 29 cm over 1000 m of channel length, due to the advection discretization.

Again, we can deduce several things from the figure. First, the head losses for this test are much larger than for the previous tests. Second, it can be seen that on the finer grids the FOU, FOU-MC-E and SOU-MC-E schemes provide similar head losses $\Delta H \approx 140 - 150$ %. We know that – in reality – vertical recirculation zones emerge behind the groynes, dissipating energy. This mechanism is, of course, not incorporated in our 2D, depth-averaged model. In civil engineering methods, these losses are commonly parameterized using Carnot losses for sudden expansions (see e.g. Chanson [58]). From the analysis in section 2.3, we know that the FOU scheme gives exactly the Carnot loss for any (discrete) velocity variation. It appears that both momentum conservative schemes also tend towards this result. Additionally, it can be noted that these two schemes also show relatively little dependence on the grid resolution.

Finally, it can be seen that the FOU-EHC scheme provides a reduction in the backwater for the coarser grids. From the analysis, we know that the scheme does not give any head losses related to the velocity gradients. Therefore, the backwater is much less than for the other schemes. The increase in head losses with increased grid resolution, most likely comes from the better representation of the local accelerations over the groynes and therefore the increased bottom friction contribution. The advection contribution only varies between 4 and 8 % over the grids. The FOU-MC-E scheme gives a significantly larger backwater than the FOU-EHC scheme and depending on the resolution a larger or smaller backwater than the FOU scheme (conform the results from section 2.3). It can also be seen that it shows relatively little variation over the range of grid resolutions.

By comparing the results with the test with emerged groynes, one can investigate the effect of lowering the groynes in a river section (see e.g. Busnelli et al. [37]). Computing the difference in water levels for the two flow situations, for the different advection schemes and grid resolutions, the effect of lowering the groynes can be found to be in the range of 9–

2

23 cm. Considering the fact that often river engineering projects involve man-induced modifications which result in water level changes of several centimeters to decimeters and that the river engineers commonly need to provide water level predictions with an accuracy below 5 cm, this result can be considered worrying.

2.5.6 *Case study: Elbe River from Lauenburg to Geesthacht*

Finally, we consider the actual case study from which we deduced the schematic tests and their topographical characteristics. Again, we apply all five advection schemes on the four grid resolutions, and inspect the differences in the total backwater at the upstream boundary. From Fig. 6e one can see that the variation in total head loss over the schemes is less than for the schematic cases: the contribution from the bottom friction is more dominant for this case. Nonetheless, the maximum difference of 10.4 % (of a total backwater of 2.12 m over 17 km) corresponds to a water level difference of 22 cm, from which one can again conclude that the uncertainty due to the advection scheme is quite significant. This needs to be counteracted by a reduced bottom friction, which may modify the flow patterns, specifically in shallow areas, reducing the reliability and applicability of the model, in particular for possible morphodynamic computations, relying on accurate bottom shear stress predictions.

However, the variation over the grids for the two momentum-conservative schemes and for the FOU-EHC scheme is relatively small, rendering them more reliable than the FOU and SOU schemes. It can thus be concluded that the order of the scheme is not the essential property for an advection scheme to be accurate and reliable in river applications for backwater assesSment.

2.6 DISCUSSION

It was shown that, for quasi-steady river flow over variable topography, the *local balance* in the momentum equation is dominated by the pressure gradient and advection term and not by the pressure gradient and bottom friction. Due to the errors in the advection scheme, even the contribution to the *global balance* may be substantial, depending on the chosen advection scheme and grid resolution. Therefore, the common consensus that

numerical river models are dominated by a balance between pressure (or free-surface) gradient and bottom friction is often invalid. Already for relatively small bottom variations, the global contribution to the backwater due to inaccuracies of the advection scheme may be of the same order of magnitude as that from bottom friction.

The effect of numerical errors on the energy head and backwater was investigated from an integral viewpoint. A more local approach (per cell/edge) is applied in research on energy-balanced schemes over (discontinuous) topography, see e.g. Bruwier et al. [32], Fjordholm, Mishra, and Tadmor [79], Murillo and García-Navarro [164], and Tadmor and Zhong [226]. A comparison of both approaches may yield interesting similarities and offer new insights in the effectivity of the different discretizations near bottom discontinuities.

We applied a range of practically-feasible grid resolutions, capturing the geometrical variation with a very limited number of cells, as the computational resources are often limited for large-scale river applications. In comparison with classical test cases such as the "*subcritical flow over a bottom bump*", we considered a series of such bumps (and groynes), to allow for an accumulation of the possible numerical/artificial backwater that is introduced by the errors in the advection discretization.

The backwater effect for the flow over bed forms and influenced by groynes was studied. However, as any variation of the bathymetry may lead to artificial advection effects, it is very likely that this is also the case for the flow through bends, where similar investigations could be realized (e.g. Blanckaert [21], Blanckaert and Graf [22], Stelling [219], and Van Balen, Uijttewaal, and Blanckaert [237]). Also, in this study we restrict ourselves to quasi-steady flow with stationary boundary conditions. As can be seen from the presented results, the findings from this work also apply for mildly instationary flow situations.

In the present work a number of basic advection schemes were tested. It may be of interest to also apply other advection approximations to the presented set of test cases, inspired by a real-world river application, with the focus on the head loss and backwater. Additionally, the investigations from this work can be realized on unstructured (triangular) or locally-refined grids, where the discretization errors from the advection scheme will interact with errors from the grid structure.

2

2.7 CONCLUSIONS

We provided a new interpretation of discretization errors in numerical river models, introducing the concept of artificial backwater. The artificial/numerical backwater effect due to the momentum advection approximation was quantified for three first-order advection schemes using a 1D analysis and verified using a sequence of 2D numerical experiments for the same schemes and for two second-order accurate extensions.

We demonstrated that a scheme designed for maintaining constant energy head, can indeed compute the flow over variable topography with minimal energy losses. It was also shown that – in agreement with the conclusions from Kramer and Stelling [125] and Stelling and Duinmeijer [220] – the artificial backwater for the momentum-conservative scheme cannot be controlled. The scheme gives an energy loss (positive backwater contribution) at expansions and an energy gain (negative backwater contribution) for contractions. However, the momentum-conservative scheme yields a smaller artificial backwater than the non-conservative (standard) first-order upwind (FOU) scheme.

This answers research question 1.

These findings are confirmed by the numerical experiments, where the contributions to the global backwater from bottom friction and from the advection scheme have been computed. The scheme with energy-head constancy indeed shows very little to no backwater, but unfortunately shows this property also for flows where losses might be expected, such as for the flow over groynes. The non-conservative first-order upwind scheme was found to cause an artificial backwater effect that could be as high as 35% of the backwater due to bottom friction. In agreement with the 1D analysis, the momentum-conservative scheme shows less backwater than the FOU scheme.

Tests with the second-order extensions of the schemes – show that the non-conservative second-order scheme does converge faster than the FOU scheme, but on coarser grids, the backwater is equal or even larger than with the FOU scheme. First-order advection schemes that adhere to physical principles, such as momentum conservation or energy-head constancy along streamlines, give less artificial backwater than a higher-order scheme that does not adhere to such principles.

This answers research question 2.

For the flow over and around groynes, the total head loss for the different advection schemes and resolutions varies with as much as a factor two, corresponding to several decimeters of water level difference. The lower-

2

ing of the groynes resulted in a decrease in water levels in the range of 9–23 cm, depending on the advection scheme and the grid resolution, rendering these choices very relevant in engineering projects.

At present, most river computations employ relatively coarse grids, where the topography is resolved with limited resolution and the size of the artificial backwater considerably depends on the chosen advection scheme. From the semi-implicit, staggered grid, finite difference/finite volume schemes investigated in the present work – for such low-resolution computations – the authors recommend the use of a momentum-conservative first-order scheme or a scheme with energy-head constancy, for their efficiency and insensitivity to the grid resolution. Only for higher resolutions – where accurate flow patterns need to be resolved (e.g. including vortex shedding) – a second-order momentum-conservative scheme is recommended.

3

THE TURBULENCE MODEL AND THE VERTICAL FLOW STRUCTURE

Three-dimensional hydrodynamic *z*-layer models, which are used for simulating the flow in rivers, estuaries and oceans, suffer from an inaccurate and often discontinuous bottom shear stress representation, due to the staircase bottom. We analyze the governing equations and clearly show the cause of the inaccuracies. Based on the analysis, we present a new method that significantly reduces the errors and the grid dependency of the results. The method consists of a near-bed layer-remapping and a modified near-bed discretization of the $k - \varepsilon$ turbulence model. We demonstrate the applicability of the approach for uniform channel flow, using a schematized two-dimensional vertical model and for the flow over a bottom sill using the Delft3D modeling system.

3.1 INTRODUCTION

Three-dimensional (3D) hydrodynamic models, such as POM (Blumberg and Mellor [24]), UnTRIM (Casulli and Walters [52]), SUNTANS (Fringer, Gerritsen, and Street [82]), Delfin (Ham, Pietrzak, and Stelling [93]) and Delft3D (Deltares [69]), are applied to simulate the flow in rivers, oceans, estuaries and lakes, to predict flooding, aid in ship navigation and sediment management and to study morphology and water quality. For such applications the vertical structure of the flow – including possible stratification – is of key importance. Specifically the river modeling community has only relatively recently started applying 3D models to simulate the

3
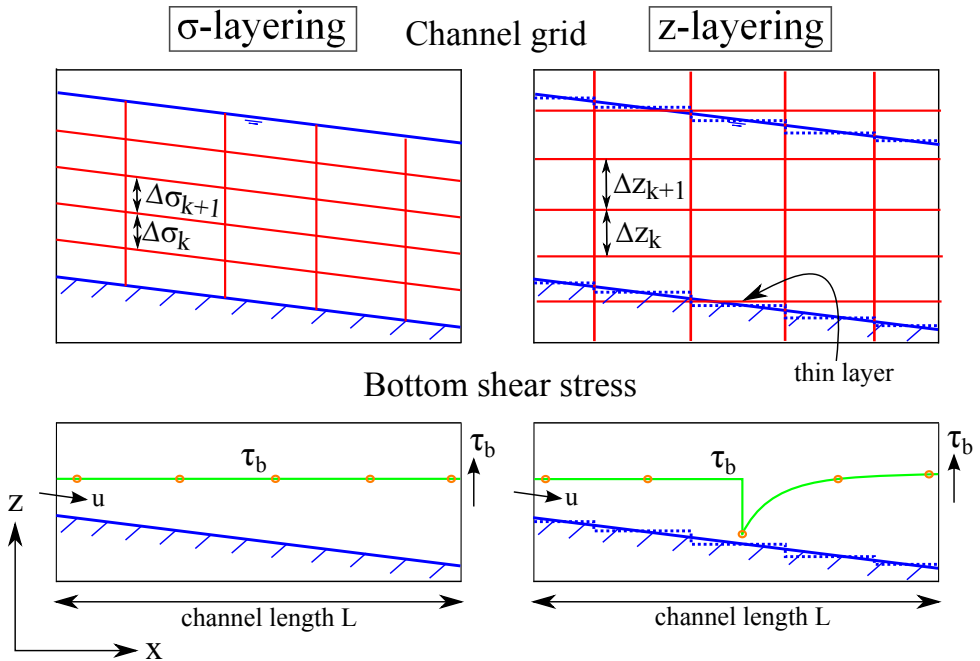
Figure 9: Vertical grid structure and bottom shear stress for uniform channel flow, using the σ-layer grid (left) and the z-layer grid (right).

flow in bends and near hydraulic structures such as groynes or weirs (see e.g. Hardy et al. [97], Lane et al. [129], Lege, Alexy, and Kellermann [136], Nihei, Kato, and Sato [170], Patzwahl, Jankowski, and Lege [179], and Wu, Rodi, and Wenka [254]).

For the vertical discretization in 3D models, commonly either terrain-following σ-layers, as introduced by Phillips [182], or strictly horizontal, geopotential z-layers are used (Figure 9). Using σ-layers, the grid follows the bottom and free surface, allowing the relatively simple application of boundary conditions. However, problems with *hydrostatic consistency* arise when modeling the flow above steep bottom slopes, in particular for stratified flow (e.g. Haney [95], Mesinger [154], and Stelling and Van Kester [221]). Additionally, σ-models provide excessive resolution in shallow areas and the layering can even become singular with zero depth, posing difficulties in simulating wetting and drying.

Conversely, the z-layer discretization allows simple horizontal discretizations for pressure, advection and diffusion and it efficiently handles shallow areas. However, the bottom and free-surface boundaries are repre-

sented as 'staircases', see Figure 9. Even using a partial- or shaved-cell approach (see e.g. Adcroft, Hill, and Marshall [2] and Pacanowski and Gnanadesikan [176]), these boundaries cause problems. Firstly, inadequate treatment of advection introduces implicit form drag along staircase boundaries (e.g. Beckmann and Döscher [13], Chen [60], Ezer and Mellor [76], Kleptsova, Stelling, and Pietrzak [124], and Song and Chao [215]). Secondly, thin layers – occurring when the bottom or free surface crosses a layer interface – cause discontinuities in velocity and shear stress, see Figure 9. Wilcox [250] reported this problem for non-uniform grid spacing near boundaries, i.e. also for σ-models. These problems were considered e.g. by Bijvelds [18], Chen [60], Stelling [218], and Tseng and Ferziger [233], but we did not find proof that the proposed approaches provide accurate results on relatively coarse, non-uniform grids, when combined with a sophisticated vertical turbulence model.

Similar considerations hold for Immersed Boundary Methods (IBMs). In such methods, the boundary arbitrarily cuts through the grid, forming an *immersed boundary*. The effect of this boundary on the flow can then be incorporated in the governing equations in a number of ways. One common approach is to use ghost-cells, situated outside the boundary. The boundary condition is then transferred from the actual boundary to the ghost cell using interpolation (Mittal and Iaccarino [159] and Tseng and Ferziger [233]). Another approach is to apply cut-cells, where large ratios in cell size can occur near the boundary. This problem is very similar to the problem of thin layers in z-layer models. In IBMs, the small-cells problem was addressed e.g. by Kirkpatrick, Armfield, and Kent [121] and Seo and Mittal [210].

Specifically for fluvial applications, the application of z-layers offers a considerable decrease in computational time, due to the efficient treatment of shallow (floodplain) areas, using a limited number of layers. However, the resistance effect of the bottom boundary layer in these shallow areas – also over variable topography – must be adequately represented using the relatively coarse vertical resolution. This is a known problem for z-layer models and severely limits the application of these models, especially in combination with morphodynamics. We therefore aim at accurate representation of bottom shear stress and vertical shear in z-layers, specifically with limited grid resolution.

We first give a general description of the 3D models to which this work applies. We then identify the cause of the erroneous variation of the bottom

shear stress and velocity in z-layer models with a staircase bottom, by analyzing a schematic one-dimensional vertical (1DV) model with an algebraic turbulence model, applicable to uniform channel flow. From this analysis we propose a near-bottom layer-remapping that significantly reduces the discretization errors that cause the erroneous variation.

Additionally, based on numerical experiments with the $k - \varepsilon$ turbulence model, we present a modified near-bottom discretization of the vertical diffusion terms in the $k - \varepsilon$ turbulence model. We test the methods for uniform channel flow using a width-averaged 2D vertical (2DV) model and for the flow over a bottom sill using the Delft3D modeling system, both using the $k - \varepsilon$ turbulence model. We show that the dependency of the results on the near-bed grid structure in z-layer models is greatly reduced and the accuracy of the vertical profiles greatly improved using the new method.

3.2 MATHEMATICAL MODEL

We consider a 3D z-layer model, applicable to modeling rivers, estuaries and oceans, as e.g. UnTRIM (Casulli and Walters [52]), SUNTANS (Fringer, Gerritsen, and Street [82]), Delfin (Ham, Pietrzak, and Stelling [93]) and Delft3D (Deltares [69]). These models differ foremost in the time integration, advection scheme and wetting and drying algorithms. For our analysis of the bottom shear stress and vertical profiles, these differences are not important. For simplicity we assume a hydrostatic pressure, but the new methods presented in this paper also apply to non-hydrostatic models.

3.2.1 *Continuous model*

The 3D model consists of the momentum equations in x- and y-direction (omitting buoyancy for simplicity):

$$\frac{\partial u}{\partial t} + u\frac{\partial u}{\partial x} + v\frac{\partial u}{\partial y} + w\frac{\partial u}{\partial z} - fv =$$
$$-g\frac{\partial \zeta}{\partial x} + \frac{\partial}{\partial x}\left(\nu_h\frac{\partial u}{\partial x}\right) + \frac{\partial}{\partial y}\left(\nu_h\frac{\partial u}{\partial y}\right) + \frac{\partial}{\partial z}\left(\nu\frac{\partial u}{\partial z}\right) \tag{45}$$

$$\frac{\partial v}{\partial t} + u\frac{\partial v}{\partial x} + v\frac{\partial v}{\partial y} + w\frac{\partial v}{\partial z} + fu =$$
$$-g\frac{\partial \zeta}{\partial y} + \frac{\partial}{\partial x}\left(\nu_h\frac{\partial v}{\partial x}\right) + \frac{\partial}{\partial y}\left(\nu_h\frac{\partial v}{\partial y}\right) + \frac{\partial}{\partial z}\left(\nu\frac{\partial v}{\partial z}\right) \tag{46}$$

where u, v, and w are the velocity components in x-, y- and z-directions, respectively, t represents time, ζ is the free-surface level, ν_h and ν are the horizontal and vertical eddy viscosities, f is the Coriolis parameter and g is the gravitational acceleration. We note that commonly ν refers to the molecular viscosity and ν_t to the turbulent eddy viscosity. For brevity, we have used ν in the rest of this work.

Omitting sources for simplicity, the continuity equation reads:

$$\frac{\partial u}{\partial x} + \frac{\partial v}{\partial y} + \frac{\partial w}{\partial z} = 0 \tag{47}$$

After vertical integration and using kinematic relations at the free surface and bottom, (47) can be rewritten to the free-surface equation:

$$\frac{\partial \zeta}{\partial t} + \frac{\partial}{\partial x}\left(\int_{-d}^{\zeta} u dz\right) + \frac{\partial}{\partial y}\left(\int_{-d}^{\zeta} v dz\right) = 0 \tag{48}$$

where d is the bottom depth (positive downwards from the reference level).

Neglecting wind shear, the bottom and free-surface boundary conditions for (45)-(46) are:

$$\nu\frac{\partial u}{\partial z}\bigg|_{z=-d} = |U_*|u_* \quad , \quad \nu\frac{\partial v}{\partial z}\bigg|_{z=-d} = |U_*|v_* \tag{49}$$

$$\nu\frac{\partial u}{\partial z}\bigg|_{z=\zeta} = 0 \qquad , \quad \nu\frac{\partial v}{\partial z}\bigg|_{z=\zeta} = 0 \tag{50}$$

where u_* and v_* are the shear velocities, which can be determined e.g. based on a Chézy or Manning formulation. We define u_* and v_* based

on the assumption of the logarithmic law of the wall for fully-developed turbulent flow:

$$u_* = \frac{\kappa u^+}{\ln\left(\frac{z^+}{z_0}+1\right)} \quad , \quad v_* = \frac{\kappa v^+}{\ln\left(\frac{z^+}{z_0}+1\right)} \tag{51}$$

$$|U_*| = \frac{\kappa U^+}{\ln\left(\frac{z^+}{z_0}+1\right)} \tag{52}$$

where u^+ and v^+ are velocities at a height z^+ from the bottom, $U^+ = ((u^+)^2 + (v^+)^2)^{1/2}$ and z_0 is the roughness height, which is commonly defined as $z_0 = k_s/30$, where k_s is known as Nikuradse's equivalent sand roughness. Parameter z_0 (or k_s) is often used as primary calibration parameter.

To complete the 3D model, we need turbulence closures to compute the eddy viscosities ν_h and ν. For simplicity, we assume ν_h to be constant. To obtain accurate vertical profiles for a wide range of applications, we apply the standard $k - \varepsilon$ turbulence model (Jones and Launder [114]) to compute the vertical eddy viscosity ν. For the model to be numerically stable, it is essential that ν is strictly positive. Mohammadi and Pironneau [161] (p. 56–57 and 65–66) show that under the assumptions made to derive the differential form of the $k - \varepsilon$ model, the model has strictly positive solutions.

In the $k - \varepsilon$ model, ν is computed from the turbulent kinetic energy k and its dissipation rate ε:

$$\nu = c_\mu \frac{k^2}{\varepsilon} \tag{53}$$

where c_μ is an empirical constant. The unknowns k and ε are computed using two separate transport equations. The 3D k- and ε-equations read:

$$\frac{\partial k}{\partial t} + u\frac{\partial k}{\partial x} + v\frac{\partial k}{\partial y} + w\frac{\partial k}{\partial z} - \frac{\partial}{\partial z}\left(\frac{\nu}{\sigma_k}\frac{\partial k}{\partial z}\right) - P_k + \varepsilon = 0 \tag{54}$$

$$\frac{\partial \varepsilon}{\partial t} + u\frac{\partial \varepsilon}{\partial x} + v\frac{\partial \varepsilon}{\partial y} + w\frac{\partial \varepsilon}{\partial z} - \frac{\partial}{\partial z}\left(\frac{\nu}{\sigma_\varepsilon}\frac{\partial \varepsilon}{\partial z}\right) - P_\varepsilon + \varepsilon_\varepsilon = 0 \tag{55}$$

where:

$$P_k = \nu \left[\left(\frac{\partial u}{\partial z} \right)^2 + \left(\frac{\partial v}{\partial z} \right)^2 \right] \tag{56}$$

$$P_\varepsilon = c_{1\varepsilon} \frac{\varepsilon}{k} P_k = c_{1\varepsilon} c_\mu k \left[\left(\frac{\partial u}{\partial z} \right)^2 + \left(\frac{\partial v}{\partial z} \right)^2 \right] \tag{57}$$

$$\varepsilon_\varepsilon = c_{2\varepsilon} \frac{\varepsilon^2}{k} \tag{58}$$

are the production rate of k, the production rate of ε and the dissipation rate of ε, respectively. We have neglected the horizontal diffusion terms as they are commonly very small compared to the other terms (Bijvelds [18]) and also because the advection terms will be discretized using the dissipative (but stable and positive) first order upwind scheme. Adding the horizontal diffusion terms would lead to excessive horizontal dissipation (Kester [120]).

In the absence of wind shear, Dirichlet boundary conditions for the $k - \varepsilon$ model are (see e.g. Rodi [198]):

$$\begin{aligned} k|_{z=-d} &= \frac{|U_*|^2}{\sqrt{c_\mu}} & , & \quad \varepsilon|_{z=-d} &= \frac{|U_*|^3}{\kappa z_0} & , & \quad \nu|_{z=-d} &= \kappa |U_*| z_0 \\ k|_{z=\zeta} &= k_{bg} & , & \quad \varepsilon|_{z=\zeta} &= \varepsilon_{bg} & , & \quad \nu|_{z=\zeta} &= \nu_{bg} \end{aligned} \tag{59}$$

where κ is the von Kármán constant and k_{bg}, ε_{bg} and ν_{bg} are background values that account for some background turbulence, of which we assume it is always present. The background value for ν satisfies (53). In our tests we used $k_{bg} = 1.0e^{-5} \mathrm{m}^2/\mathrm{s}^2$, $\varepsilon_{bg} = 9.0e^{-7} \mathrm{m}^2/\mathrm{s}^3$ and $\nu_{bg} = 1.0e^{-5} \mathrm{m}^2/\mathrm{s}$. We also use these values as initial conditions for the $k - \varepsilon$ model.

One could also apply Neumann-type boundary conditions for k and ε as e.g. done by Burchard and Petersen [35] and Burchard, Deleersnijder, and Stoyan [34] (see section 3.6).

The constants in the $k - \varepsilon$ model are (Rodi [198]):

$$\begin{aligned} c_\mu &= 0.09, & c_{1\varepsilon} &= 1.44, & c_{2\varepsilon} &= 1.92, \\ \sigma_k &= 1.0, & \sigma_\varepsilon &= 1.3 \end{aligned} \tag{60}$$

3.2.2   Discretized model

We discretize the equations on a structured C-grid (staggered positioning of variables). For simplicity, we assume a constant grid spacing Δx and Δy.

3

Our considerations mostly concern the vertical discretizations, rendering them also applicable to curvilinear or unstructured C-grid models. We use a semi-implicit formulation as used e.g. in UnTRIM and SUNTANS, but a combination of our method with e.g. an ADI-type time integration as in Delft3D is also feasible as demonstrated in section 3.5. The vertical eddy viscosity ν is defined in w-points, i.e. at the layer interfaces. The discretized momentum and free-surface equations read:

$$
\frac{u_{i+1/2,j,k}^{n+1} - u_{i+1/2,j,k}^{n}}{\Delta t} + Fu_{i+1/2,j,k}^{n} - fv_{i+1/2,j,k}^{n} =
$$

$$
-g\frac{\zeta_{i+1,j}^{n+1} - \zeta_{i,j}^{n+1}}{\Delta x}
$$

$$
+\frac{1}{\Delta z_{i+1/2,j,k}^{n}}\left(\nu_{i+1/2,j,k+1/2}^{n}\frac{u_{i+1/2,j,k+1}^{n+1} - u_{i+1/2,j,k}^{n+1}}{\Delta z_{i+1/2,j,k+1/2}^{n}}\right.
$$

$$
\left.-\nu_{i+1/2,j,k-1/2}^{n}\frac{u_{i+1/2,j,k}^{n+1} - u_{i+1/2,j,k-1}^{n+1}}{\Delta z_{i+1/2,j,k-1/2}^{n}}\right) \tag{61}
$$

$$
\frac{v_{i,j+1/2,k}^{n+1} - v_{i,j+1/2,k}^{n}}{\Delta t} + Fv_{i,j+1/2,k}^{n} + fu_{i,j+1/2,k}^{n} =
$$

$$
-g\frac{\zeta_{i,j+1}^{n+1} - \zeta_{i,j}^{n+1}}{\Delta y}
$$

$$
+\frac{1}{\Delta z_{i,j+1/2,k}^{n}}\left(\nu_{i,j+1/2,k+1/2}^{n}\frac{v_{i,j+1/2,k+1}^{n+1} - v_{i,j+1/2,k}^{n+1}}{\Delta z_{i,j+1/2,k+1/2}^{n}}\right.
$$

$$
\left.-\nu_{i,j+1/2,k-1/2}^{n}\frac{v_{i,j+1/2,k}^{n+1} - v_{i,j+1/2,k-1}^{n+1}}{\Delta z_{i,j+1/2,k-1/2}^{n}}\right) \tag{62}
$$

$$\frac{\zeta_{i,j}^{n+1} - \zeta_{i,j}^n}{\Delta t}$$

$$+ \frac{1}{\Delta x} \left[\sum_{k=m_{i+1/2,j}}^{k=M_{i+1/2,j}^n} \Delta z_{i+1/2,j,k}^n u_{i+1/2,j,k}^{n+1} \right.$$

$$\left. - \sum_{k=m_{i-1/2,j}}^{k=M_{i-1/2,j}^n} \Delta z_{i-1/2,j,k}^n u_{i-1/2,j,k}^{n+1} \right]$$

$$+ \frac{1}{\Delta y} \left[\sum_{k=m_{i,j+1/2}}^{k=M_{i,j+1/2}^n} \Delta z_{i,j+1/2,k}^n v_{i,j+1/2,k}^{n+1} \right.$$

$$\left. - \sum_{k=m_{i,j-1/2}}^{k=M_{i,j-1/2}^n} \Delta z_{i,j-1/2,k}^n v_{i,j-1/2,k}^{n+1} \right] = 0 \qquad (63)$$

where i, j and k are the indices corresponding to the x-, y- and z-direction, m is the bottom layer index, M^n is the free-surface layer index at time level n and Fu and Fv contain the explicitly discretized advection and horizontal diffusion terms. The advection terms can be approximated e.g. using a conservative upwind scheme as in Kleptsova, Stelling, and Pietrzak [124] or an Eulerian-Lagrangian scheme (e.g. Casulli and Cheng [49] and Ham, Pietrzak, and Stelling [94]).

After computing the new free-surface levels ζ and the new horizontal velocities u and v from (61)-(63), the vertical velocities are computed recursively upwards from the bottom, using the discrete continuity equation:

$$w_{i,j,k+1/2}^{n+1} = w_{i,j,k-1/2}^{n+1}$$

$$+ \frac{1}{\Delta x} \left(\Delta z_{i-1/2,j,k}^n u_{i-1/2,j,k}^{n+1} - \Delta z_{i+1/2,j,k}^n u_{i+1/2,j,k}^{n+1} \right)$$

$$+ \frac{1}{\Delta y} \left(\Delta z_{i,j-1/2,k}^n v_{i,j-1/2,k}^{n+1} - \Delta z_{i,j+1/2,k}^n v_{i,j+1/2,k}^{n+1} \right)$$

$$\text{for} \quad k = m, m+1, \ldots, M^n - 1 \qquad (64)$$

where the vertical velocity at the bottom $w_{i,j,m-1/2}^{n+1}$ is zero.

The bottom and free-surface boundary conditions for (61) and (62) are given by (again neglecting wind shear):

$$v^n_{i+1/2,j,m-1/2} \frac{u^{n+1}_{i+1/2,j,m} - u^{n+1}_{i+1/2,j,m-1}}{\Delta z^n_{i+1/2,j,m-1/2}} = |U_*|\, u_*$$

$$= r_x \left| U^n_{i+1/2,j,m} \right| u^{n+1}_{i+1/2,j,m} \tag{65}$$

$$v^n_{i,j+1/2,m-1/2} \frac{v^{n+1}_{i,j+1/2,m} - v^{n+1}_{i,j+1/2,m-1}}{\Delta z^n_{i,j+1/2,m-1/2}} = |V_*|\, v_*$$

$$= r_y \left| V^n_{i,j+1/2,m} \right| v^{n+1}_{i,j+1/2,m} \tag{66}$$

$$v^n_{i+1/2,j,M^n+1/2} \frac{u^{n+1}_{i+1/2,j,M^n+1} - u^{n+1}_{i+1/2,j,M^n}}{\Delta z^n_{i+1/2,j,M^n+1/2}} = 0 \tag{67}$$

$$v^n_{i,j+1/2,M^n+1/2} \frac{v^{n+1}_{i,j+1/2,M^n+1} - v^{n+1}_{i,j+1/2,M^n}}{\Delta z^n_{i,j+1/2,M^n+1/2}} = 0 \tag{68}$$

where r_x and r_y are the Taylor coefficients, which we determine from the logarithmic law of the wall:

$$r_x = \frac{\kappa^2}{\ln^2 \left(\frac{\Delta z^n_{i+1/2,j,m}}{2z_0} + 1 \right)} \tag{69}$$

$$r_y = \frac{\kappa^2}{\ln^2 \left(\frac{\Delta z^n_{i,j+1/2,m}}{2z_0} + 1 \right)} \tag{70}$$

and where:

$$\left| U^n_{i+1/2,j,m} \right| = \sqrt{\left(u^n_{i+1/2,j,m} \right)^2 + \left(v^n_{i+1/2,j,m} \right)^2} \tag{71}$$

$$\left| V^n_{i,j+1/2,m} \right| = \sqrt{\left(u^n_{i,j+1/2,m} \right)^2 + \left(v^n_{i,j+1/2,m} \right)^2} \tag{72}$$

Eqs. (69)-(70) follow when u^+ and v^+ are taken as the velocities in the bottom layer, i.e at $z^+ = \Delta z^n_m/2$, in (51). We note that – in contrast to (52) – due to the staggering, $|U_*|$ and $|V_*|$ are now different, because they concern absolute velocities in different positions on the grid.

The model is completed by the discretized $k - \varepsilon$ turbulence model. We define k and ε at the layer interfaces, in correspondence with ν. The placement of ν at the layer interfaces avoids vertical averaging of the viscosity

in the horizontal momentum equations (61)-(62), but instead requires such averaging in the k- and ε-equations. This leads to inaccuracies, specifically near the bottom (see section 3.4).

To maintain positive solutions for k and ε, we use Patankar's linearization of the sink terms in the k- and ε-equations (Patankar [178]). This linearization can be justified as follows. The dissipation ε is defined as $\varepsilon = k^{3/2}/l = \sqrt{k}k/l$, where l is a turbulent length scale. In writing an expression for ε^{n+1}, this form suggests a linearization like Patankar's:

$$\varepsilon^{n+1} = \frac{\sqrt{k^n}k^{n+1}}{l^n} = \frac{\varepsilon^n k^{n+1}}{k^n} \tag{73}$$

The discrete $k - \varepsilon$ model then reads:

$$\frac{k_{i,j,k+1/2}^{n+1} - k_{i,j,k+1/2}^{n}}{\Delta t} + Fk_{i,j,k+1/2}^{n}$$

$$-\frac{1}{\Delta z_{i,j,k+1/2}^{n}} \left(\frac{v_{i,j,k+1}^{n}}{\sigma_k} \frac{k_{i,j,k+3/2}^{n+1} - k_{i,j,k+1/2}^{n+1}}{\Delta z_{i,j,k+1}^{n}} \right.$$

$$\left. - \frac{v_{i,j,k}^{n}}{\sigma_k} \frac{k_{i,j,k+1/2}^{n+1} - k_{i,j,k-1/2}^{n+1}}{\Delta z_{i,j,k}^{n}} \right)$$

$$-(P_k)_{i,j,k+1/2} + \underbrace{\frac{k_{i,j,k+1/2}^{n+1}}{k_{i,j,k+1/2}^{n}}\varepsilon_{i,j,k+1/2}^{n}}_{\text{Patankar's linearization}} = 0 \tag{74}$$

$$\frac{\varepsilon_{i,j,k+1/2}^{n+1} - \varepsilon_{i,j,k+1/2}^{n}}{\Delta t} + F\varepsilon_{i,j,k+1/2}^{n}$$

$$-\frac{1}{\Delta z_{i,j,k+1/2}^{n}} \left(\frac{v_{i,j,k+1}^{n}}{\sigma_\varepsilon} \frac{\varepsilon_{i,j,k+3/2}^{n+1} - \varepsilon_{i,j,k+1/2}^{n+1}}{\Delta z_{i,j,k+1}^{n}} \right.$$

$$\left. - \frac{v_{i,j,k}^{n}}{\sigma_\varepsilon} \frac{\varepsilon_{i,j,k+1/2}^{n+1} - \varepsilon_{i,j,k-1/2}^{n+1}}{\Delta z_{i,j,k}^{n}} \right)$$

$$-c_{1\varepsilon}\frac{\varepsilon_{i,j,k+1/2}^{n}}{k_{i,j,k+1/2}^{n}} (P_k)_{i,j,k+1/2}$$

$$+ \underbrace{c_{2\varepsilon}\frac{\varepsilon_{i,j,k+1/2}^{n}}{k_{i,j,k+1/2}^{n}}\varepsilon_{i,j,k+1/2}^{n+1}}_{\text{Patankar's linearization}} = 0 \tag{75}$$
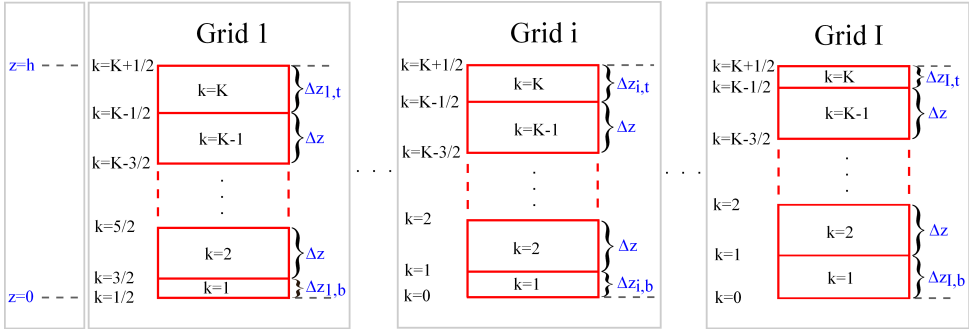
Figure 10: Three different vertical grid distributions for the 1DV example, where all layers have thickness Δz, except for the layers containing the bottom or free surface.

where:

$$
v_{i,j,k}^n = \frac{\left(v_{i,j,k+1/2}^n + v_{i,j,k-1/2}^n\right)}{2} \tag{76}
$$

$$
(P_k)_{i,j,k+1/2} = \frac{v_{i,j,k+1/2}^n}{4} \left(
\begin{array}{c}
\left(\dfrac{u_{i-1/2,j,k+1}^n - u_{i-1/2,j,k}^n}{\Delta z_{i-1/2,j,k+1/2}^n}\right)^2 \\[2ex]
+ \left(\dfrac{u_{i+1/2,j,k+1}^n - u_{i+1/2,j,k}^n}{\Delta z_{i+1/2,j,k+1/2}^n}\right)^2 \\[2ex]
+ \left(\dfrac{v_{i,j-1/2,k+1}^n - v_{i,j-1/2,k}^n}{\Delta z_{i,j-1/2,k+1/2}^n}\right)^2 \\[2ex]
+ \left(\dfrac{v_{i,j+1/2,k+1}^n - v_{i,j+1/2,k}^n}{\Delta z_{i,j+1/2,k+1/2}^n}\right)^2
\end{array}
\right) \tag{77}
$$

and where $Fk_{i,j,k+1/2}^n$ and $F\varepsilon_{i,j,k+1/2}^n$ contain the advection terms, which we discretize using an explicit first order upwind scheme, see Bijvelds [18].

The boundary conditions for the $k - \varepsilon$ model (neglecting wind shear) are given by (59). After computing k and ε, the eddy viscosity v is obtained from (53).

3.3   INFLUENCE OF THE STAIRCASE BOTTOM

Three-dimensional z-layer models as described in section 3.2, suffer from an inaccurate and often discontinuous bottom shear stress representation,

due to the staircase approximation of the bottom. More specifically, the discontinuities in velocities and bottom shear stress occur at locations where the bottom crosses a layer interface, introducing a thin layer. We have analyzed the governing equations and will clearly show that the errors are caused by inaccuracy of the central discretization of the vertical diffusion term in the horizontal momentum equations (61)-(62), near the bottom.

3.3.1 *Problem analysis for uniform channel flow*

To identify the cause of the inaccuracies and discontinuities in bottom shear stress and vertical profiles of horizontal velocity in z-layer models, we consider uniform channel flow, for which we know the analytical solution. Omitting advection, horizontal diffusion, Coriolis, lateral effects, the transient term and variation of the pressure gradient, the momentum equation in x-direction (61) reduces to a 1DV model:

$$\frac{\partial}{\partial z}\left(\nu\frac{\partial u}{\partial z}\right) = g\frac{\partial \zeta}{\partial x} = -\frac{(u_*)^2}{h} \quad \text{for} \quad 0 \leq z \leq h \tag{78}$$

where h is the total water depth and where we have assumed the bottom to be at $z = 0$.

For uniform channel flow, we know that ν varies parabolically in the vertical as prescribed by an algebraic turbulence model based on the mixing-length concept (Prandtl [190]):

$$\nu(z) = \kappa u_* \left(z + z_0\right)\left(1 - \frac{z}{h}\right) \tag{79}$$

The model is completed with the bottom and free-surface boundary conditions in the x-direction from (49)-(50). Solving the set (78)-(79) analytically leads to the well-known logarithmic velocity profile:

$$u(z) = \frac{u_*}{\kappa}\ln\left(\frac{z}{z_0} + 1\right) \tag{80}$$

However, in discretizing and solving our equations we make errors, which reduce the accuracy of the solution. The size of the errors depends on the grid distribution and the existence of possible thin layers.

3.3.2   *Discretization*

We investigated to what extent the discrete problem resembles the continuous problem. For C-grids, (78) is commonly approximated as in (61):

$$\frac{1}{\Delta z_k} \left(\nu_{k+1/2} \frac{2\left(u_{k+1} - u_k\right)}{\left(\Delta z_{k+1} + \Delta z_k\right)} \right.$$
$$\left. - \nu_{k-1/2} \frac{2\left(u_k - u_{k-1}\right)}{\left(\Delta z_k + \Delta z_{k-1}\right)} \right) = -\frac{\left(u_*\right)^2}{h} \tag{81}$$

Inserting the bottom boundary condition (65), yields the following expression for (81) in the layer containing the bottom ($k = m$). For simplicity we assumed $m = 1$:

$$\frac{1}{\Delta z_1} \left(\nu_{3/2} \frac{2\left(u_2 - u_1\right)}{\left(\Delta z_2 + \Delta z_b\right)} - \left(u_*\right)^2 \right) = -\frac{\left(u_*\right)^2}{h} \tag{82}$$

where $\Delta z_b = \Delta z_1$ is the thickness of the layer containing the bottom. For a relatively smooth bed – as can be assumed for uniform channel flow – in principle, a no-slip boundary condition could be applied at the bottom. This, however, requires extreme vertical resolutions to accurately represent the boundary layer (see section 3.6).

From (82) – evaluating $\nu_{3/2}$ using (79) – we obtain an expression for u_2:

$$u_2 = u_1 + \frac{u_*}{\kappa} \frac{\left(\Delta z_2 + \Delta z_b\right)}{2\left(\Delta z_b + z_0\right)} \tag{83}$$

which can be verified to be equal to:

$$u_2 = u_1 + \Delta z_{3/2} \frac{\tau_{3/2}}{\nu_{3/2}} = u_1 + \Delta z_{3/2} \left(\frac{\partial u}{\partial z}\right)_{3/2} \tag{84}$$

where $\tau = \nu \partial u / \partial z$ is the shear stress. In other words, the velocity in the second layer from the bed, is computed using a linear approximation of the vertical gradient in horizontal velocity at the interface between the two near-bed layers.

The near-bottom velocity u_1 is obtained by evaluating the law of the wall at the height of the first velocity point above the bottom:

$$u_1 = \frac{u_*}{\kappa} \ln \left(\frac{\Delta z_b}{2 z_0} + 1 \right) \tag{85}$$
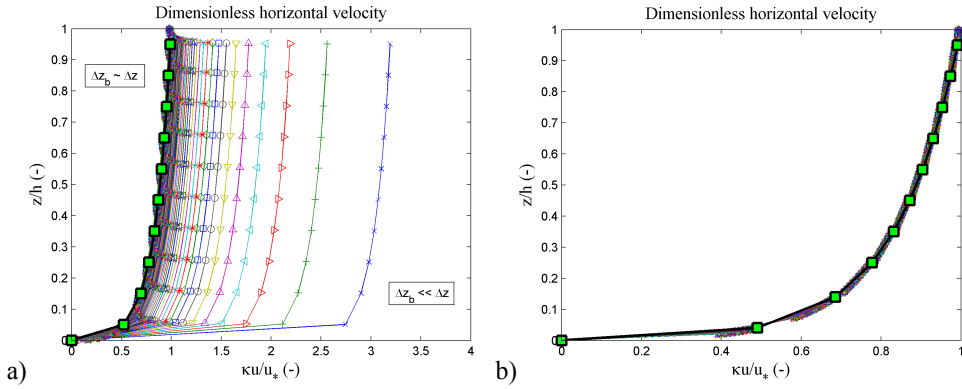
Figure 11: Dimensionless velocity profiles obtained for the 1DV model with algebraic turbulence model, for the $I = 100$ different vertical grid distributions (all with $K = 10$ layers); a) Original layering; b) Near-bed layering modified to minimize the local truncation error ($\alpha = 0.402$ in this case). The analytical solution is included as the thick black line with green square markers. Note the different velocity scales.

which exactly corresponds to the analytical logarithmic solution given by (80). If the velocity approximation in (83) contains errors, these errors must therefore come from the linear approximation of the vertical velocity gradients, which vary as $\partial u / \partial z \sim \partial / \partial z \left(\ln(z) \right) = 1/z$.

3.3.3 Solution accuracy

We investigated the accuracy of (83) and its dependency on the local grid structure, by computing the velocity profiles for $I = 100$ different vertical grid layerings, having a constant layer thickness Δz, except for the bottom layer, which has a thickness $\Delta z / I < \Delta z_{i,b} < \Delta z$, where i is now the grid counter (see Figure 10). For this example we chose $z_0 / h = 0.002$ and applied $K = 10$ layers, in all simulations. The resulting velocity profiles for the $I = 100$ different vertical grid distributions are given in Figure 11a.

The figure shows significant errors for those vertical grid distributions that have relatively small values of near-bed layer thickness $\Delta z_{i,b}$. The errors are particularly large near the bottom, but the effect is clearly noticeable over the complete water column. It suggests that this local error is responsible for the overall inaccuracy. Due to the fact that we used the analytical
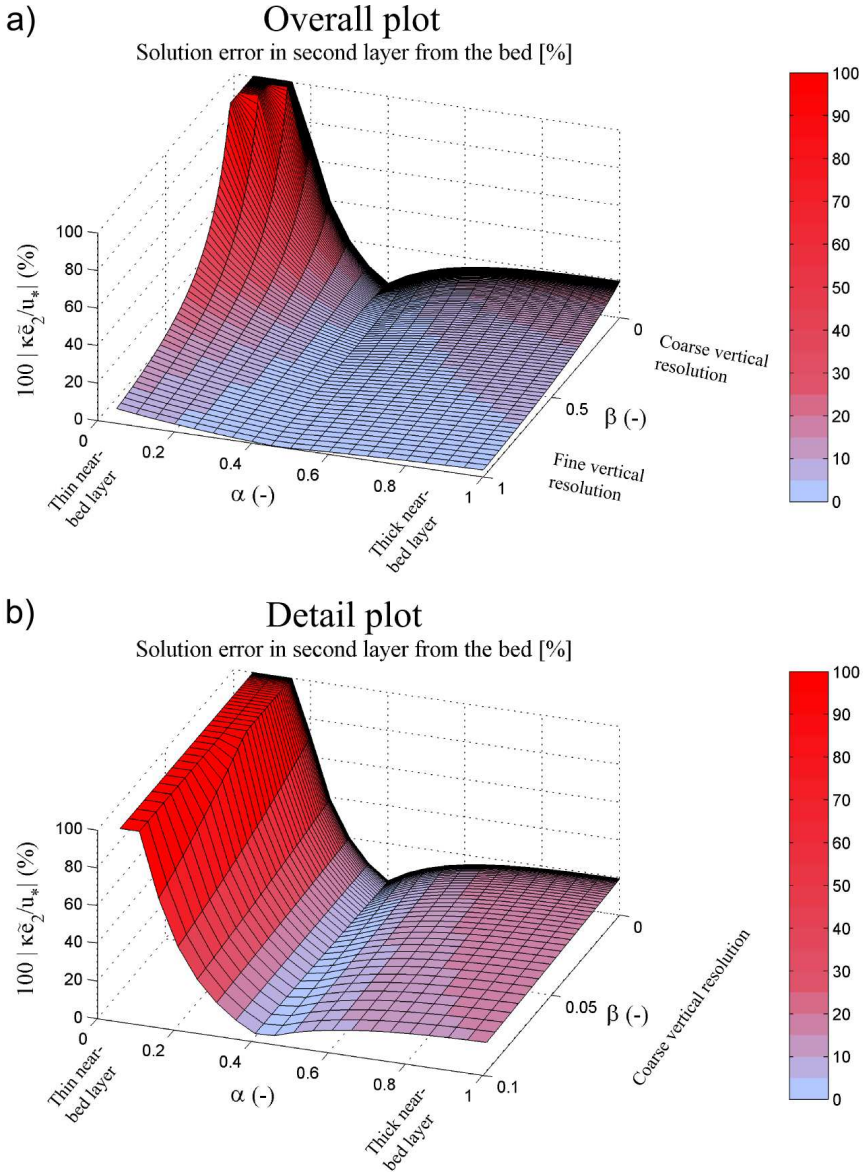
Figure 12: Percentual, absolute, dimensionless local solution error $100\,|\kappa\tilde{e}_{i,2}/u_*|$ as a function of near-bed layer-thickness ratio $\alpha = \Delta z_{i,b}/\overline{\Delta z}_{i,b}$ and 'roughness height ratio' $\beta = z_0/\overline{\Delta z}_{i,b}$; a) Overall plot for range $0 < \alpha < 1$ and $0 < \beta < 1$; b) Detail plot for $\beta < 0.1$ (coarse vertical resolution).

solution for u_1, the solution error of u_2 is precisely the local truncation error $\tilde{e}$ in the second layer from the bottom:

$$\tilde{e}_{i,2} = u_{i,2}^{analytic} - u_{i,2}^{numeric} \tag{86}$$

or using (80), (85) and (83):

$$\tilde{e}_{i,2} = \frac{u_*}{\kappa} \left[\ln \left(\frac{2\Delta z_{i,b} + \Delta z + 2z_0}{\Delta z_{i,b} + 2z_0} \right) - \frac{\Delta z + \Delta z_{i,b}}{2 \left(\Delta z_{i,b} + z_0 \right)} \right] \tag{87}$$

We see that $\tilde{e}_{i,2}$ depends on the layer thickness of the two near-bed layers, on u_* and on z_0. We can gain more insight in the behavior of $\tilde{e}_{i,2}$ by defining the sum of the two near-bed layer thicknesses $\overline{\Delta z_{i,b}} = \Delta z_{i,b} + \Delta z$ and by writing $\Delta z_{i,b} = \alpha \overline{\Delta z_{i,b}} = \alpha / \left(1 - \alpha \right) \Delta z$ and $z_0 = \beta \overline{\Delta z_{i,b}}$. Substituting these expressions in (87), we obtain:

$$\tilde{e}_{i,2} = \frac{u_*}{\kappa} \left[\ln \left(\frac{1 + \alpha + 2\beta}{\alpha + 2\beta} \right) - \frac{1}{2 \left(\alpha + \beta \right)} \right] \tag{88}$$

In Figure 12a, we have plotted the dimensionless, absolute percentual error $(100 \left| \kappa \tilde{e}_{i,2} / u_* \right|)$ for grid distributions ranging from relatively thin near-bed layers to relatively thick near-bed layers ($0 < \alpha < 1$) and for the range from coarse vertical resolutions to fine vertical resolutions ($0 < \beta < 1$). When $\beta \uparrow 1$, we have a very fine vertical resolution ($\overline{\Delta z_{i,b}} \approx z_0$) and when $\beta \downarrow 0$ we have a coarse vertical resolution ($\overline{\Delta z_{i,b}} >> z_0$). Since most applications have limited vertical resolution, we included a detail plot in Figure 12b, showing the error for small values of β. Several conclusions can be drawn from the figure:

1. For $0.4 \leq \alpha \leq 0.5$ the error is smallest, with limited dependency on β.

2. For α smaller than $\alpha \approx 0.3$, the error grows very rapidly (in absolute sense) for coarse vertical resolutions.

3. Even for moderately fine vertical resolutions, e.g. $\beta = 0.2$ ($\overline{\Delta z_{i,b}} = 5z_0$), the error is significant for small α, i.e. for large ratios in near-bed layer thickness.
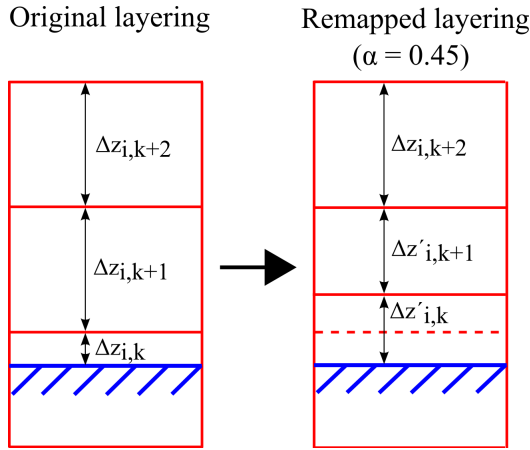
Figure 13: Remapping of the two near-bed layers to a layering with $\alpha = 0.45$ in a 1DV grid.

This answers research question 3.

To obtain small discretization errors for a large range of α, we would require very high vertical resolution ($\overline{\Delta z_{i,b}} < \sim 2z_0$), which we consider not feasible. We therefore investigate the option of modifying the grid near the bottom to obtain an α that provides small discretization errors in the velocity approximation, for a large range of β, i.e. both for coarse and fine vertical resolution. To obtain $0.4 < \alpha < 0.5$, we must modify the near-bottom layering to a layering where the bottom layer thickness $\Delta z_b = \alpha / (1 - \alpha) \Delta z$. Such a local remapping/remeshing is illustrated for $\alpha = 0.45$ in Figure 13. The remapping ensures that no large ratios in layer thinkness occur near the bottom.

We can find the locally-optimal ratio α for the grid layer distribution near the bottom to obtain a zero truncation error, from the following equation:

$$\ln \left(\frac{1 + \alpha + 2\beta}{\alpha + 2\beta} \right) - \frac{1}{2(\alpha + \beta)} = 0 \tag{89}$$

which is easily solved by Newton iteration.

Figure 11b shows the drastic improvement of the results, when we use the optimal α with $\tilde{e}_{i,2} = 0$ ($\alpha \approx 0.402$ for $z_0/h = 0.002$) to modify the near-bed layer thickness to $\Delta z'_{i,b} = \alpha (\Delta z_{i,b} + \Delta z)$. The velocity profiles are very similar to the analytical solution and show almost no dependency on the grid structure. We can conclude that reducing the discretization error in the second layer from the bottom, improves the complete vertical profile.

One might suggest avoiding modification of the mesh and attempting to improve the approximation of the near-bed velocity gradients using higher-order approximations. We did not pursue this, for a number of reasons. Firstly, we focus on coarse grids, limiting the application of larger stencils. Secondly, we consider the boundary layer, where the solution varies strongly, reducing the applicability of higher-order schemes. And thirdly, higher-order methods only provide more accurate results on smooth grids (Hoffman [103]). The use of higher-order discretizations within cells or elements, as in a finite element framework, may be worth investigating. This, however, requires the specification of higher-order derivatives in the boundary conditions.

3.4 ACCURATE PROFILES FOR THE $k - \varepsilon$ TURBULENCE MODEL

In section 3.3, we analyzed the truncation errors when using an algebraic (mixing-length) turbulence model and demonstrated that the numerical approximation of the vertical profile of horizontal velocity is very sensitive to the vertical grid structure near the bottom. Applying the standard central scheme to approximate the vertical diffusion term, results in significant truncation errors for large ratios in near-bed layer thickness. The errors can be greatly reduced by remapping the two near-bed layers using an optimal layer thickness ratio α obtained from (89). Here we demonstrate that to obtain accurate vertical profiles using the more widely applicable $k - \varepsilon$ turbulence model, the near-bed discretization of the vertical diffusion terms in the k- and ε-equations requires careful attention.

3.4.1 Solution accuracy for the $k - \varepsilon$ turbulence model

Using the reduced 1DV model, presented in section 3.3, but now coupled to the $k - \varepsilon$ model to compute ν, we computed profiles of u, ν, k and ε for the 100 different 1D vertical grid layerings (section 3.3.2). The profiles are depicted in Figure 14 (all with $K = 10$ layers), showing the effect of the near-bed vertical layering. In the figure, we included profiles obtained using a model with $K = 1000$ layers, as a reference solution. From the figure we notice that the negative effect of the large ratios in near-bed layer thickness is slightly less pronounced for the 1DV $k - \varepsilon$ model than for the algebraic turbulence model, but variability of the profiles is still clearly visible. The

reduced effect can be attributed to the fact that the eddy viscosity is now coupled to the velocity and therefore also acts upon the strong velocity gradients that emerge due to the large truncation errors, i.e. the errors are smoothed out.

3.4.2   *Improved discretization for the $k - \varepsilon$ turbulence model*

For the model with mixing-length turbulence, we found that modifying the near-bed layering using $\alpha = 0.4 - 0.5$, could minimize the truncation error and the variation of the velocity profiles. Conversely, for the model with $k - \varepsilon$ turbulence, we found from numerical experiments that using a near-bed equidistant layering ($\alpha = 0.5$), leads to the smallest dependency of the results on the grid layering. We attribute this to the $\partial\varepsilon/\partial z$-term in the ε-equation and the $(\partial u/\partial z)^2$-terms in the production terms in both the k- and ε-equation. In the bottom boundary layer, these terms are (theoretically) proportional to $1/(z + z_0)^2$, which becomes large for thin bottom layers and moreover, the discrete (linear) approximations of these terms become inaccurate for large ratios in near-bed layer thickness. These discrete approximations show the least sensitivity when an equidistant layering is applied near the bottom. Therefore, the remapping to a near-bed equidistant layering with $\alpha = 0.5$ is applied throughout the remaining part of this paper. We stress that the near-bed layering is modified for all terms in the equations, not only for the vertical diffusion and bottom shear stress computation.

Figure 15 shows the improved profiles for u, v, k and ε, obtained using the model with $k - \varepsilon$ turbulence when a modified near-bed layer thickness $\Delta z'_{i,b} = \alpha (\Delta z_{i,b} + \Delta z)$ is used, with $\alpha = 0.5$ (again we chose $z_0/h = 0.002$).

Our numerical experiments have shown that applying an α, computed by minimizing the local truncation error using (89) reduces the variability of u with the vertical layer distribution, but it does not lead to optimal results. This can be understood, considering that the $k - \varepsilon$ model does not lead to the 'analytical' profiles for u and v (valid for the mixing-length model) and also that the vertical diffusion term of ε and the production terms in both the k- and ε-equation show the near-singular behavior near the bottom, described above.

Due to the described behavior of the aforementioned terms, the specification of the Dirichlet boundary conditions (59) in the $k - \varepsilon$ model is often not sufficient. For this reason, many researchers have turned to Neumann-type
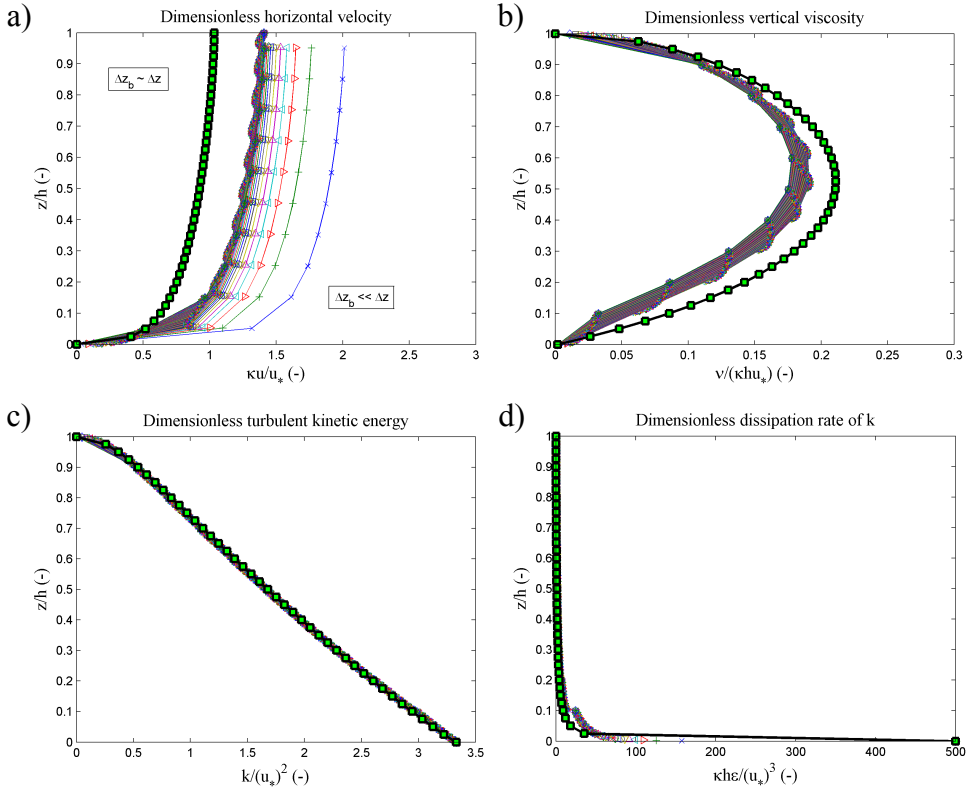
Figure 14: Dimensionless vertical profiles obtained for the uniform channel flow using the $k - \varepsilon$ turbulence model for the $I = 100$ different vertical grid distributions (all with $K = 10$ layers); a) horizontal velocity u; b) eddy viscosity ν; c) turbulent kinetic energy k; d) dissipation rate ε. Reference solutions using $K = 1000$ layers are given by the thick black line with green square markers.

3
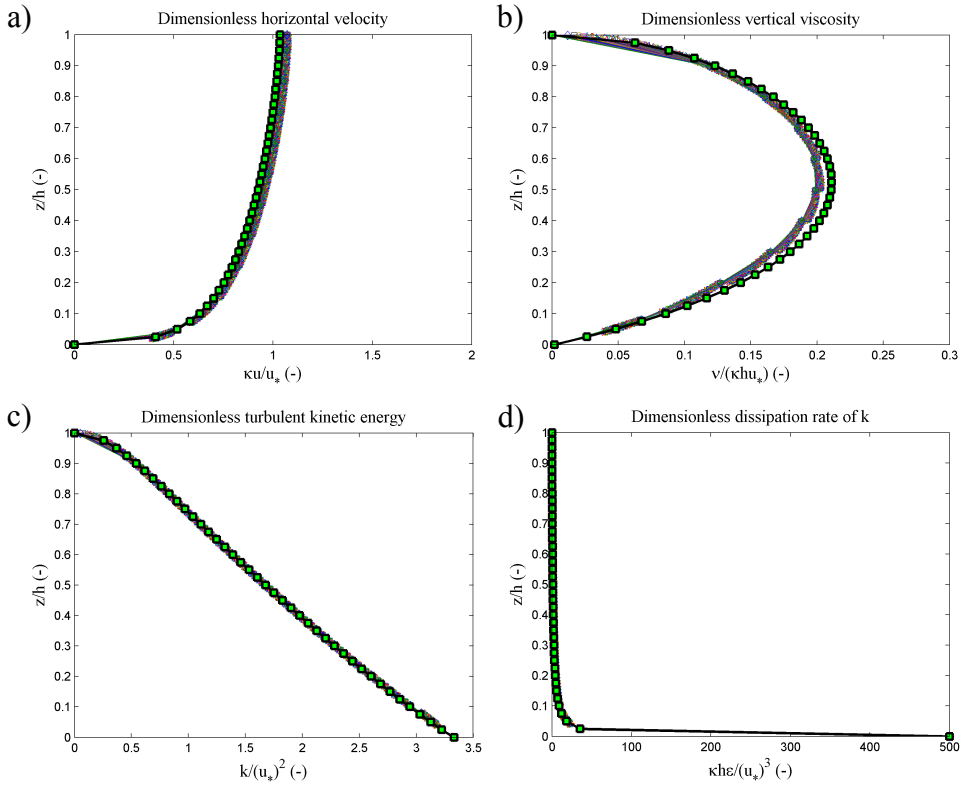
Figure 15: Dimensionless vertical profiles obtained for the uniform channel flow using the $k - \varepsilon$ turbulence model for the $I = 100$ different vertical grid distributions, using $\alpha = 0.5$ to modify the layering in the two-near bed cells (all with $K = 10$ layers); a) horizontal velocity u; b) eddy viscosity ν; c) turbulent kinetic energy k; d) dissipation rate ε. Reference solutions using $K = 1000$ layers are given by the thick black line with green square markers.

boundary conditions, e.g. Burchard and Petersen [35]. We like to maintain the Dirichlet conditions, but note that it is important that the computed near-bottom vertical diffusion fluxes in the k- and ε-equation have adequate values. This should also be the case for coarse vertical discretizations, where the boundary layer is only one cell thick (or less) and for non-equidistant grid layering.

Based on numerical experiments with our code, we modified the discretization of the vertical diffusion terms of k and ε near the bottom. This is necessary to achieve an accurate amount of diffusion in the near-bottom (and high-gradient) part of the water column. The following modifications are most accurate and least sensitive to the grid layering:

$$
\frac{\partial}{\partial z}\left(\frac{\nu}{\sigma_k}\frac{\partial k}{\partial z}\right)\Bigg|_{i,j,3/2}^{n+1} =
$$
$$
\frac{1}{\Delta z_{i,j,3/2}^n}\left(\frac{\nu_{i,j,2}^n}{\sigma_k}\frac{k_{i,j,5/2}^{n+1} - k_{i,j,3/2}^{n+1}}{\Delta z_{i,j,2}^n}\right.
$$
$$
\left. -\frac{\nu_{i,j,3/2}^n}{\sigma_k}\frac{k_{i,j,3/2}^{n+1} - k_{i,j,1/2}^{n+1}}{\Delta z_{i,j,1}^n}\right)
\tag{90}
$$

$$
\frac{\partial}{\partial z}\left(\frac{\nu}{\sigma_\varepsilon}\frac{\partial \varepsilon}{\partial z}\right)\Bigg|_{i,j,3/2}^{n+1} =
$$
$$
\frac{1}{\Delta z_{i,j,3/2}^n}\left(\frac{\nu_{i,j,2}^n}{\sigma_\varepsilon}\frac{\varepsilon_{i,j,5/2}^{n+1} - \varepsilon_{i,j,3/2}^{n+1}}{\Delta Z_{i,j,2}^n}\right.
$$
$$
\left. -\frac{\tilde{\nu}_{i,j,1}^n}{\sigma_\varepsilon}\frac{\varepsilon_{i,j,3/2}^{n+1} - \varepsilon_{i,j,1/2}^{n+1}}{\Delta z_{i,j,1}^n}\right)
\tag{91}
$$

where $\nu_{i,j,2}^n = \left(\nu_{i,j,3/2}^n + \nu_{i,j,5/2}^n\right)/2$ and where we defined:

$$
\tilde{\nu}_{i,1}^n = \frac{2\nu_{i,1/2}^n \nu_{i,3/2}^n}{\nu_{i,1/2}^n + \nu_{i,3/2}^n},
\tag{92}
$$

i.e. we modified the viscosities that are used in the computation of the near-bed diffusion fluxes for k and ε. For k, it is best to take its value at the first interface above the bottom. For ε we changed the vertical averaging of ν in the near-bottom part of the diffusion flux from a strictly arithmetic

average to a harmonic average, which was also used by Deubelbeiss and Kaus [70] for geodynamic simulations (Stokes equations) with strongly-varying viscosity.

Especially for ε, this is important to make sure the discretization results in an accurate near-bottom diffusion flux, also for coarse resolutions. Our numerical experiments confirmed that the combination of a locally-equidistant near-bed layering with the discretizations given in (90)-(92) provides the least sensitive near-bed diffusion fluxes for k and ε, and therefore the most accurate velocity profiles, for a large range of vertical layer distributions. The considerations presented here also apply to σ-models, as the standard near-bottom approximation of $\nu \partial \varepsilon / \partial z$ is also inaccurate for coarse (near-)equidistant grid layering.

We have illustrated that when aiming to resolve the vertical flow structure for a uniform channel flow situation using a model with $k - \varepsilon$ turbulence, two aspects are of key importance: applying an equidistant grid layering near the bottom and adequately computing the near-bottom vertical diffusion fluxes of k and ε.

This answers research question 4.

3.5 RESULTS

In this section we consider two models. Firstly, a reduced 2DV model, where we do not account for advection, horizontal diffusion, wind, buoyancy effects and Coriolis forcing, which we use to model the uniform channel flow. Secondly, we use the z-layer module of Delft3D (Deltares [69]), to model the flow over a sinusoidal bottom sill. We compare the results with those obtained using the Delft3D σ-model.

3.5.1 *Uniform channel flow*

We test the 2DV version of the schematic model described in section 3.3, including the $k - \varepsilon$ turbulence model. We prescribe a constant discharge per unit width $q = hu$ at inflow and apply a Sommerfeld (or linearized Riemann) condition for the water level at the outflow boundary, converging

to a steady state water level gradient at the boundary equal to the bed level gradient:

$$q|_{x=0} = q_{in} \tag{93}$$

$$\frac{\partial \zeta}{\partial t} + \sqrt{gh}\frac{\partial \zeta}{\partial x}\bigg|_{x=L} = -\sqrt{gh}i_b \tag{94}$$

where i_b is the bottom slope (positive downwards).

We consider a channel with length $L = 5000$m, $i_b = 0.0001$[-] and roughness height $z_0 = 0.0023$m.. As initial conditions, we set $\zeta = 0$m and $u = w = 0$m/s. For the $k - \varepsilon$ model, we initialize the model with some background turbulence, to make sure that division by zero is avoided in the sink terms: $k_{bg} = 1.0e^{-5}$m^2/s^2, $\varepsilon_{bg} = 9.0e^{-7}$m^2/s^3 and $\nu_{bg} = 1.0e^{-5}$m^2/s. As boundary conditions we apply $q_{in} = 50$m^2/s at inflow and (94) for the water level at the outflow boundary.

We discretize the channel using 100 cells in x-direction and 13 z-layers in z-direction. All layers have a $\Delta z = 0.4$m ($0.003 < \beta < 0.006$), except for the bottom and free-surface layers, which vary in thickness along the channel due to the sloping bottom and water level. Due to the channel slope and the specific layering, the bottom crosses a layer interface once, at $x = 2500$m, introducing a near-bed layer thickness ratio $\alpha = \Delta z_{min} / (\Delta z + \Delta z_{min}) = 0.0244$, where Δz_{min} is the smallest allowable layer thickness in the model, which we chose to be $\Delta z_{min} = 0.01$m (see also Section 3.6). This small α occurs when no layer remapping is applied.

In Figure 16, the profiles of u and v for all $I = 100$ cells along the channel are plotted in one location. We have shifted the profiles vertically, such that the bottom lies at $z = 0$m. The profiles (all with $K = 13$ layers) are shown for the original layering and for the modified near-bed layering ($\alpha = 0.5$), together with results obtained using $K = 1000$ vertical layers (thick black lines with green square markers). One can see that the velocity profiles with $K = 13$ match the $K = 1000$ profiles for both the original and the modified layering. The variation is now found only in the v-profiles.

The bottom shear stress $\tau_b = \rho(u_*)^2$ should be constant along the channel. In Figure 17 one can see that the large near-bed layer thickness ratio introduces a discontinuity in τ_b. Using the proposed remapping, the variation is greatly reduced and τ_b is close to the bottom shear stress obtained from the high-resolution run.

For the 2DV model, the errors due to large layer thickness ratios near the bottom express themselves differently than for the 1DV model. For the 1DV
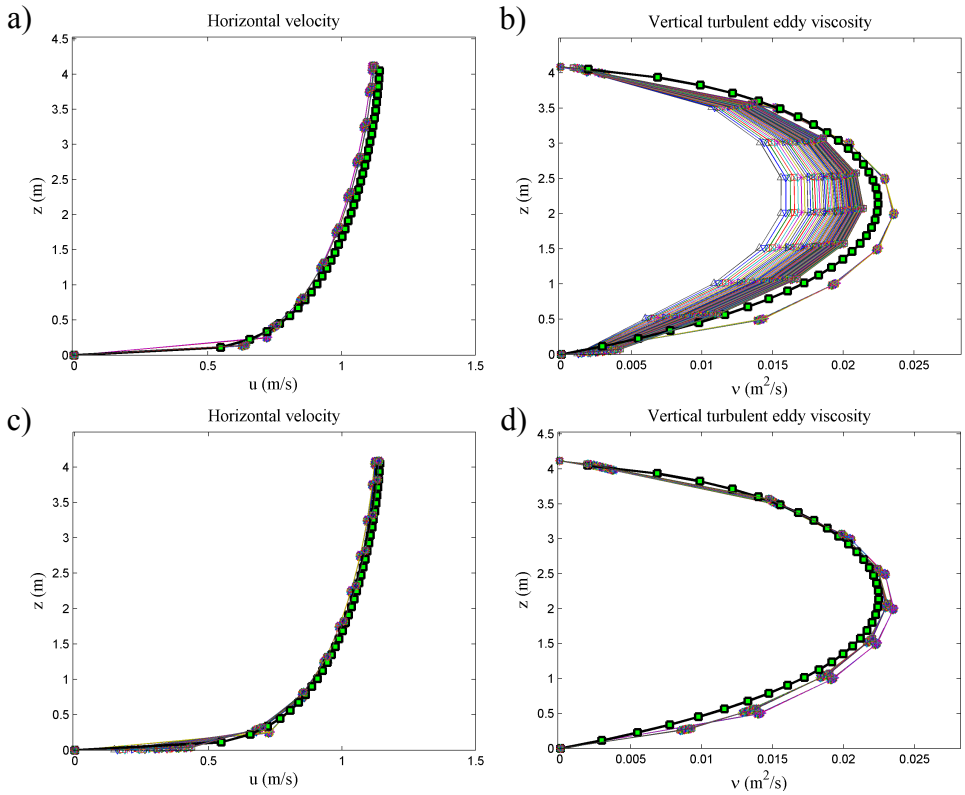
Figure 16: Vertical profiles for 2DV uniform channel flow (all with $K = 13$ layers); a) horizontal velocity u using original layering; b) vertical eddy viscosity ν using original layering; c) horizontal velocity u using modified near-bed layering; d) vertical eddy viscosity ν using modified near-bed layering. Results obtained with $K = 1000$ layers included as the thick black lines with green square markers. Profiles have been shifted vertically such that the bottom lies at $z = 0m$.
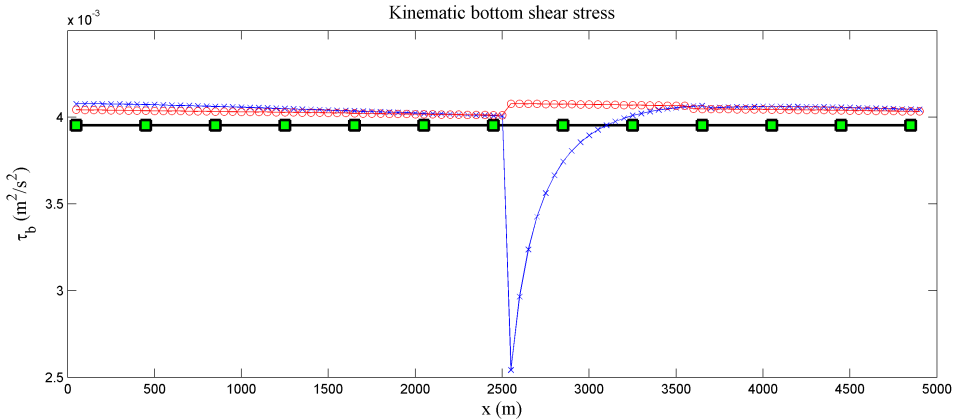
Figure 17: Bottom shear stress for uniform channel flow using the 2DV model with $K = 13$ layers; original layering (blue line with 'x'-markers), modified near-bed layering (red line with 'o'-markers) and results obtained with $K = 1000$ layers (thick black line with green square markers).

model, the pressure gradient is fixed and the truncation error manifests itself in the velocity profiles, whereas for the 2DV case, the discharge is specified from the inflow boundary condition and the truncation errors result in an erroneous bottom shear stress and equilibrium depth. The truncation error varies along the channel, growing in the direction of decreasing bottom layer thickness (upstream direction). From the downstream boundary upward, the truncation errors build up.

This can be recognized as follows: in the schematic 2DV model, the horizontal coupling is realized through the pressure gradient and the continuity equation. Each cell has a fixed inflow from the left (equal to q_{in}) and has a right water level which is influenced by the truncation error in the right neighbor cell and the resulting (slightly erroneous) equilibrium depth in that cell. This effect accumulates upstream, causing an artificial backwater effect. At $x = 2500$m, the truncation error changes sign, becomes small and then accumulates again in upstream direction.

3.5.2 *Flow over a bottom sill*

To test the method for use in more general flow situations, we implemented the approach in the *z*-layer module of the Delft3D modeling system and simulated the flow over a bottom sill passing through a number of *z*-layers.
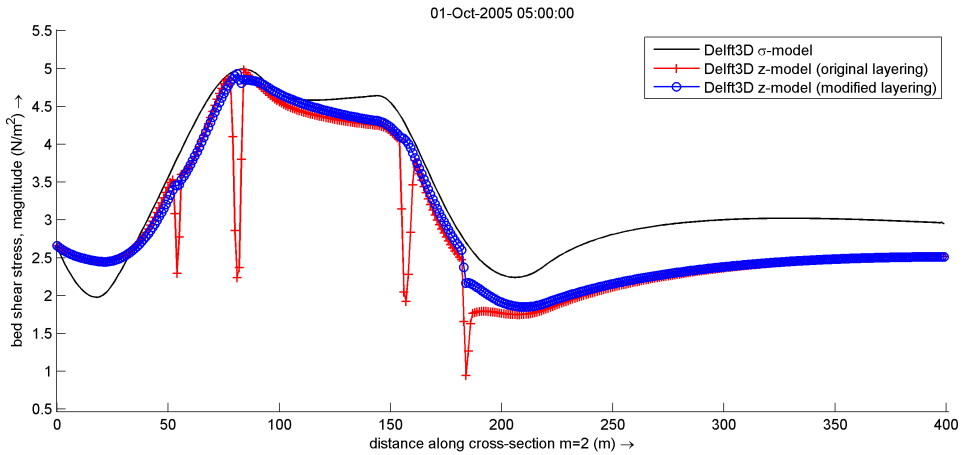
Figure 18: Bottom shear stress for the flow over a bottom sill using the Delft3D
σ-model (black line without markers), z-model with original layering
(red line with '+'-markers) and z-model with modified layering (blue
line with 'o'-markers).

We applied again the $k - \varepsilon$ turbulence model to compute ν. The test concerns a 400m long flume, with a bottom depth of 9m (excluding the bottom sill) and an initial water level of $\zeta = 0$m. The smooth bottom sill has a total length of 200m (75m sinuisoidal, 50m crest and again 75m sinuisoidal), extends from $x = 20$m to $x = 220$m and has a height of 1.92m. The grid is 2DV, has 400 cells in y-direction and 10 equidistant layers. At inflow a velocity of $v = 0.65$m/s is specified and at ouflow the water level is kept fixed at $\zeta = 0$m. We used a roughness height $z_0 = 0.002$m. The model was completed using the default settings of the Delft3D z-layer model.

In Figure 18 we have compared the bottom shear stress along the flume obtained with the Delft3D σ-model, the Delft3D z-model with original layering and the z-model with modified layering. One can see that using the modified layering, the shear stress distribution is much smoother than using the original layering. The z-layer results resemble the results obtained using the σ-model quite reasonably.

In this situation advection also plays a role. The effects are considered in section 3.6. Advection was not switched off in Delft3D for this test and no special measures were taken. The results obtained with the approach presented here are very encouraging. They suggest that the accurate rep-

resentation of near-bottom velocity and turbulence distributions in *z*-layer models for real life applications is within reach.

3.6 DISCUSSION

We demonstrated that the near-bed layer remapping and the modified discretizations for the vertical diffusion terms of k and ε provide significantly improved vertical profiles (1DV) and reduced erroneous variation and discontinuities in the bottom shear stress (2DV or 3D). The approaches are generally applicable to 3D *z*-layer models. Using the proposed approaches, the obtained velocity profiles and bottom shear stress distributions were very similar to those one (usually) obtains using a σ-model, allowing the direct use of the bottom shear stresses for morphodynamic computations.

As mentioned in the introduction, the presented considerations may also apply to immersed boundary methods (IBMs). When applying IBMs with a cut cell approach, the resulting grid has large jumps in cell size near the boundary, where a (logarithmic) boundary layer is supposed to be represented. For relatively coarse meshes (compared to the boundary layer thickness), we expect that such approaches suffer from the same problems and large discretization errors as presented here. Such methods may therefore benefit from the layer-remapping approach.

When ghost-cells are applied to approximate the boundary values and the distances from the points used for interpolation to the actual boundary point vary strongly, the interpolation may be inaccurate for the same reasons as illustrated in the paper. In this case, again (locally) equidistant grids will offer most accurate results, with the least dependency on the local grid structure or interpolation stencil.

An important effect of the near-bed layer remapping is that it causes neighbor cells to be shifted with respect to each other (see Figure 19). This should be taken into account in the computation of horizontal advection and in the possible transport of constituents. However, the remapping does not introduce problems with mass conservation, as each pair of cells uses the same cell interface area to compute the flux between the cells. The area is modified due to the remapping, but it is modified for both neighbor cells. We do not introduce multiple connectivity between cells, i.e. a cell always has only four horizontal neighbors (West, East, South and North),

Original layering

Remapped layering
$(\alpha = 0.5)$
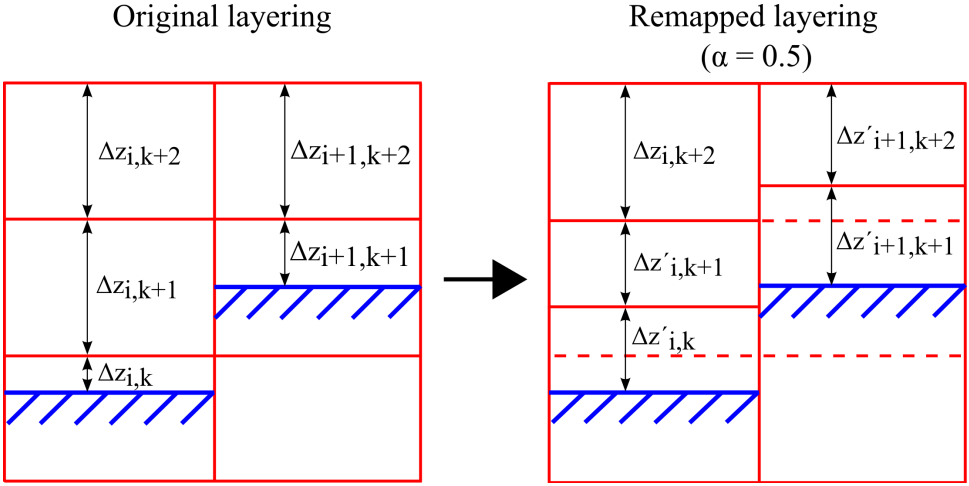
Figure 19: Remapping of the two near-bed layers to a locally equidistant layering ($\alpha = 0.5$) in a 2DV grid, for cells i and $i + 1$.

with which horizontal fluxes are exchanged. Discrete volume conservation still applies:

$$\Delta x \Delta y \Delta z_{i,j,k}^{n+1} = \Delta x \Delta y \Delta z_{i,j,k}^{n}$$
$$+ \Delta t \Delta y \left[\Delta z_{i-1/2,j,k}^{n} u_{i-1/2,j,k}^{n+1} - \Delta z_{i+1/2,j,k}^{n} u_{i+1/2,j,k}^{n+1} \right]$$
$$+ \Delta t \Delta x \left[\Delta z_{i,j-1/2,k}^{n} v_{i,j-1/2,k}^{n+1} - \Delta z_{i,j+1/2,k}^{n} v_{i,j+1/2,k}^{n+1} \right]$$
$$+ \Delta t \Delta x \Delta y \left[w_{i,j,k-1/2}^{n+1} - w_{i,j,k+1/2}^{n+1} \right] \tag{95}$$

even though $\Delta z_{i-1/2,j,k}$ and $\Delta z_{i,j-1/2,k}$ may not match $\Delta z_{i,j,k}$. This also applies to the transport equation.

In two specific situations, one must take special measures to maintain mass conservation. Firstly, when the water level enters the second cell from the bottom (drying/flooding) and secondly, when the bed level changes due to morphodynamics. In such situations, we added a vertical flux at the layer interface between the two bottom layers, to account for the volume change due to $\partial \zeta / \partial t$ and $\partial d / \partial t$. This causes some spurious mixing near the bottom.

We stress that we do not alter the baricenters of the cells involved in the remapping, i.e. the baricenters of horizontal neighbors are still at the same z-level. Therefore, the remapping does not introduce spurious barotropic/baroclinic pressure gradients.

With or without the remapping, the computation of advection over bottom steps requires attention, as e.g. illustrated in Kleptsova, Pietrzak, and Stelling [123] and Kleptsova, Stelling, and Pietrzak [124]. Otherwise, the solution may deteriorate due to spurious form drag. The combination of our layer-remapping with the remapping proposed by Kleptsova, Stelling, and Pietrzak [124] is therefore interesting to investigate. The latter remapping preserves an equidistant near-bed layering, so that no conflicts are expected in the combination. Applying an Eulerian-Lagrangian advection scheme could also be considered (e.g. Casulli and Cheng [49] and Ham, Pietrzak, and Stelling [94]). Adequate interpolation near the boundaries is then imperative.

We have inspected the vertical velocities near the bottom steps and found discontinuities, both with and without adaption of the near-bed layering. The vertical velocities in a hydrostatic model do not have an actual physical meaning, they merely serve to enforce continuity. We therefore believe that the jumps in vertical velocity might be reduced by applying a non-hydrostatic model, possibly with special care to balance the discontinuities in w near the bottom, induced by the way we commonly apply the continuity equation.

The discontinuities in vertical velocity w can probably also be reduced by applying a shaved- or cut-cell approach as e.g. proposed by Adcroft, Hill, and Marshall [2], Chen [60], Kirkpatrick, Armfield, and Kent [121], and Seo and Mittal [210]. Together with the layer-remapping approach and the modified near-bed discretizations in the $k - \varepsilon$ model, this may reduce the bottom-related problems in hydrodynamic z-layer models even further than shown in this paper. However, the implementation of such an approach in an existing finite difference or finite volume code is often not straightforward.

We incorporate the bottom boundary condition for the momentum equation via the law-of-the-wall approach. For a relatively smooth bed, physically, a no-slip boundary condition applies at the bottom, which should be sufficient to induce a logarithmic boundary layer profile. Unfortunately, this only holds for sufficiently high vertical resolution. Numerical experiments with the 1DV model from section 3.3 have shown that even with 500 layers the velocity profiles significantly differ from (80). Assuming a logarithmic velocity profile in the bottom layer as in (85), more accurate solutions can be obtained using only 5 layers.

3

The computation of u_* from (51) requires the evaluation of the velocity at a certain height above the bed, for which we know that it is located in the logarithmic boundary layer. Commonly, this is realized by using the velocity in the lowest active grid cell $u_{i+1/2,j,m}$. However, for velocity profiles that are not (perfectly) logarithmic in the bottom boundary layer, the resulting value of u_* may be strongly dependent on the local grid structure. The grid influence is often reduced by using e.g. the velocity in the second active layer from the bed $u_{i+1/2,j,m}$ or some weighted average of $u_{i+1/2,j,m}$ and $u_{i+1/2,j,m+1}$. By applying the equidistant near-bed layer remapping ($\alpha = 0.5$), the results become much less sensitive to which velocity is used for computing u_*.

Another important notice is related to the common use of a minimum layer thickness Δz_{min}. Such a parameter is often applied to avoid too thin layers in z-layer models. Both for the 2DV and the Delft3D model, we applied $\Delta z_{min} = 0.01$m, meaning that layers that would become thinner than 0.01m, are added to the layer above (for the bottom) or below (for the free surface). Using our layer remapping procedure, application of a Δz_{min} is strictly only necessary to avoid thin layers near the free surface, as thin layers near the bottom will get their thickness averaged with the layer above.

Applying a larger Δz_{min} would also partly relieve the problems considered in this paper. However, to obtain similar layer thickness ratios as with our remapping approach, one would have to apply $\Delta z_{min} = 0.5\Delta z$ (with Δz a uniform or average layer thickness), which would result in the fact that near the bottom a layer would have a thickness $0.5\Delta z \leq \Delta z_b \leq 1.5\Delta z$. This would lead to jumps in layer thickness from $1.5\Delta z$ to Δz for two horizontally-neighboring cells, at locations where the bottom crosses a layer interface, whereas our approach results in jumps in layer thickness from Δz to $0.5\Delta z$ for two neighbouring cells. Our approach thus retains a somewhat higher resolution near the bottom. When a $\Delta z_{min} < 0.5\Delta z$ is applied, the layer thickness ratios and discretization errors are larger than with the remapping approach.

We apply Dirichlet boundary conditions for k and ε at the bottom. Burchard and Petersen [35] and Burchard, Deleersnijder, and Stoyan [34] state that Neumann- or flux-type bottom boundary conditions perform better than Dirichlet boundary conditions in many flow situations. Burchard and Petersen [35] prescribe a zero diffusion flux for k at the bottom boundary:

$$\frac{\nu}{\sigma_k}\frac{\partial k}{\partial z} = 0 \tag{96}$$

and the following relation for ε:

$$\frac{\nu}{\sigma_\varepsilon}\frac{\partial \varepsilon}{\partial z} = -\left(c_\mu^0\right)^3 \frac{\nu}{\sigma_\varepsilon}\frac{k^{3/2}}{\kappa\left(z + z_0\right)^2} \tag{97}$$

where c_μ^0 is a constant. The question then remains at which height these conditions are evaluated, e.g. at the bottom interface, or at the first internal grid point, leaving an ambiguity and introducing grid dependency. The advantage of specifying Dirichlet conditions is that they are easy to implement, that the problem is well-posed and that k and ε are bounded.

3.7 CONCLUSIONS

Three-dimensional hydrodynamic z-layer models can provide erroneous velocity profiles and bottom shear stress distributions at positions where the bottom crosses a layer interface, introducing a large ratio in layer thickness near the bottom. We demonstrated this for the situation of uniform channel flow. The errors are caused by the inaccuracy of the discretization of the vertical diffusion term in the momentum equations for non-uniform vertical layering and can be avoided by performing a local remapping to an equidistant near-bed layering. The new approach works both in combination with an algebraic mixing length turbulence model and the $k - \varepsilon$ turbulence model.

Additionally, modifications in the near-bottom treatment of the vertical diffusion terms in the k- and ε-equations have been presented. The combination of these modifications with the layer-remapping approach allows the accurate and smooth representation of bottom shear stress and velocity profiles along sloping channels and rivers using z-layer models. We showed the applicability using a schematic 2D vertical model for uniform channel flow and by using the Delft3D modeling system to simulate the flow over a bottom sill. Using the new methods it is now feasible also for z-layer models to use the straightforwardly computed bottom shear stress as direct input for coupled morphodynamic models.

4

SUBGRID MODELLING, EFFICIENCY AND GRID CONVERGENCE

Wе present a new modelling strategy for improving the efficiency of computationally intensive flow problems in environmental free-surface flows. The approach combines a recently developed semi-implicit subgrid method with a hierarchical-grid solution strategy. The method allows the incorporation of high-resolution data on subgrid scale to obtain a more accurate and efficient hydrodynamic model. The subgrid method improves the efficiency of the hierarchical grid method by providing better solutions on coarse grids. The method is applicable to both steady and unsteady flows, but we particularly focus on river flows with steady boundary conditions. There, the combined hierarchical grid-subgrid method reduces the computational effort to obtain a steady state with factors up to 43. For unsteady models, the method can be used for efficiently generating accurate initial conditions on high-resolution grids. Additionally, the method provides automatic insight in grid convergence. We demonstrate the efficiency and applicability of the method using a schematic test for the vortex shedding around a circular cylinder and a real-world river case study.

4.1 INTRODUCTION

Many environmental free-surface flow problems involve dynamic systems which are close to an equilibrium state. The numerical models used for solving such problems generally apply constant boundary conditions. This

is particularly valid for large-scale river applications, where the quasi-steady state is mostly determined by the combination of fixed upstream discharges, downstream water levels and a global balance between pressure gradient and bottom friction, see for example Ge and Sotiropoulos [88], Jia, Xu, and Wang [111], Kang et al. [116], Paik, Escauriaza, and Sotiropoulos [177], and Patzwahl, Jankowski, and Lege [179]. Very often, however, a large spectrum of topographic scales – ranging from bends and meanders at larger scales, down to smaller scales with groynes, weirs, dunes and ripples – are present in the problem. To accurately represent the resistance effects and resulting flow patterns emerging from such topographic features, (locally) high-resolution models are required.

Two aspects are always important: computational efficiency and accuracy. Efficiency requires efficient solvers and parallel computing. For quasi-steady state computations efficiency also implies minimizing the spin-up time. For the second issue, accuracy, an approach where solutions are obtained on different grids will offer insight in the grid dependency or convergence and as such in the accuracy of the solution.

Over the past decades, much effort was invested in the development of methods applying multiple resolutions. Multigrid methods Hackbusch [91] and Trottenberg, Oosterlee, and Schüller [232], multiscale methods Lamby, Müller, and Stiriba [128] and Müller and Stiriba [163], (adaptive) local grid refinement Berger, LeVeque, and Mandli [15], Berger and Colella [16], Brandt [27], and Liang et al. [141], coarse-grid projection Lentine, Zheng, and Fedkiw [138], nested-grid modelling Baranya, Olsen, and Józsa [10], coupling of models with different resolutions Fringer, McWilliams, and Street [83], or *hp*-adaptivity in finite element methods Kubatko, Westerink, and Dawson [126] are all based on this basic idea. All of these approaches involve coarse approximations of a problem that contains finer scales. Within these coarse approximations, an inherent step in the algorithm is averaging or interpolation of fine grid quantities, commonly resulting in some loss of accuracy.

Full Multigrid (FMG) (e.g. Trottenberg, Oosterlee, and Schüller [232]), is a particular variant of multigrid, that is mostly applied to boundary-value problems. In FMG, the solution to a problem is progressively improved on a sequence of finer grids. A first solution is computed using a coarse-grid approximation of the fine-grid problem, after which the solution is interpolated to a finer grid. Then a new solution is computed using multigrid cycles. This process is repeated recursively, until the finest resolution

is reached. The method is known for its excellent theoretical convergence, but in practice the efficiency of the method depends on how well the coarse-grid problems represent the underlying fine-grid problem.

Independently, subgrid methods were developed to significantly improve the accuracy of low-resolution models, by accounting for high-resolution data and/or processes. The availability and quality of such data has greatly increased. In particular, advances in remote sensing (e.g. Li-DAR) and other measurement techniques have improved the quality of high-resolution topography and land-use data. With the advent of these new data sources, there is a need to incorporate these high-resolution data in numerical models (e.g. Dottori, Baldassarre, and Todini [72] and Forzieri et al. [81]).

Many subgrid methods apply an approach based on averaging of available data over computational cells and/or determining a porosity value per grid cell, thereby improving the quality of coarse-grid numerical models, e.g. Bates et al. [12], Cea and Vázquez-Cendón [55], Defina [67], Lane et al. [131], McMillan and Brasington [153], Olsen and Stokseth [172], Sanders, Schubert, and Gallegos [205], and Yu and Lane [262]. Recently, a new subgrid method was developed, where high-resolution data is incorporated into the model by integrating over computational cells Casulli [46] and Casulli and Stelling [51]. An important difference between this subgrid method and previous ones, is that it results in a nonlinear equation for the free surface. To the authors' knowledge, this is the first method to do so. This method significantly improves the quality of numerical models, reduces the grid dependency of the model and in many cases allows the application of (very) coarse grids using subgrid data, with limited loss of accuracy. In particular for simulations with wetting and drying, the method has clear advantages, both in two-dimensional (2D) and three-dimensional (3D) models Casulli [46] and Casulli and Stelling [51].

The method is under continuous development in terms of accuracy, efficiency and practical applicability. It was extended to accurately include the effect of subgrid variability on bottom friction and advection in shallow flows in a finite volume concept and it was combined with local grid refinement using quadtree grids Stelling [219] and Volp, Prooijen, and Stelling [240]. The subgrid method has been implemented in the unstructured grid UnTRIM^2 model Casulli [46] and Casulli and Stelling [51] and it has been reported that a significant reduction in computational effort Sehili, Lang, and Lippert [209] can be obtained with respect to the conventional UnTRIM

model without subgrid Casulli and Walters [52] and Casulli and Zanolli [53]. Tools for pre- and post-processing have been successfully adapted to accommodate the subgrid method, making it mature enough for practical application Sehili, Lang, and Lippert [209].

Building on these developments, we constructed a new approach for efficient quasi-steady flow modelling that combines the new subgrid method Casulli [46], Casulli and Stelling [51], and Stelling [219] (discussed in section 4.2.1) with a hierarchical grid approach applying some multigrid concepts to efficiently solve the flow problem on a sequence of finer grids (presented in section 4.2.2). Instead of performing multigrid iterations (within a time step), we simply perform time stepping and evolve the solution towards the (possible) steady state, but then on a sequence of grids. This allows possible instationary processes to develop with increasing grid resolution. The method effectively deals with the different spatial and temporal scales that are present in free-surface flow problems with complex geometries and therefore allows considerable savings in computational times. Additionally, it provides automatic insight in grid convergence. It can also be used for efficiently generating initial conditions for high-resolution, unsteady computations.

In section 4.3 we describe two test cases: (1) the problem of vortex shedding and (2) a real-world case study of the Elbe River in Germany. In section 4.4 we present the results obtained for the two test cases, demonstrating the efficiency of the combined approach and the resulting insight in grid convergence and numerical diffusion. We discuss the new method and the obtained results in section 4.5 and end with the conclusions in section 4.6.

4.2   THE COMBINED HIERARCHICAL GRID-SUBGRID METHOD

We present a new modelling approach in which we extend the subgrid method Casulli [46], Casulli and Stelling [51], Stelling [219], and Volp, Prooijen, and Stelling [240] to a solution strategy on hierarchical grids. The subgrid method forms the hydrodynamic core of our approach and the hierarchical grid approach is a solution strategy built around that core to effectively deal with the different spatial and temporal scales that are present in the problems we aim to solve. Before we consider the details of the combined approach in section 4.2.2, we discuss some general properties of the applied subgrid method.

4.2.1 *The subgrid method*

Subgrid methods are applied to account for data or processes that act at a scale smaller than the grid resolution, e.g. topographical variation, turbulence, hydraulic structures, vegetation and precipitation. Many existing subgrid methods are based on a statistical or empirical representation of these subgrid processes, e.g. Bates et al. [12], Cea and Vázquez-Cendón [55], Defina [67], Lane et al. [131], McMillan and Brasington [153], Olsen and Stokseth [172], Sanders, Schubert, and Gallegos [205], and Yu and Lane [262]. These methods have been shown to improve the accuracy and applicability of coarse-grid models.

To the authors' knowledge, Casulli Casulli [46] was the first to account for subgrid effects using an integral approach: integrating known subgrid data over computational cells and edges. Casulli applies a (semi-)implicit method for the shallow water equations, in which the momentum equations are substituted in the continuity equation. For conventional methods, this results in a linear equation for the unknown water level. The subgrid method Casulli [46], however, by the same procedure of substitution, yields a nonlinear equation for the water level.

The momentum equations for the subgrid method can be derived in a number of ways: (a) as strictly depth-averaged and edge-averaged as in Casulli [46], (b) using subgrid velocities as in Casulli and Stelling [51], or (c) as volume-averaged velocities as in Stelling [219] and Volp, Prooijen, and Stelling [240]. When applied on regular, structured grids, the method presented in Casulli and Stelling [51], particularly lends itself for a combination with a hierarchical grid approach (section 4.2.2). For simplicity, we apply the 3D method from Casulli and Stelling [51] in 2D depth-averaged mode. Neglecting wind and Coriolis effects, the governing equations are:

$$\frac{\partial u}{\partial t} + u\frac{\partial u}{\partial x} + v\frac{\partial u}{\partial y} = -g\frac{\partial \zeta}{\partial x} + \frac{\partial}{\partial x}\left(v_h\frac{\partial u}{\partial x}\right) + \frac{\partial}{\partial y}\left(v_h\frac{\partial u}{\partial y}\right) - \frac{\gamma\,|U|\,u}{H} \quad (98)$$

$$\frac{\partial v}{\partial t} + u\frac{\partial v}{\partial x} + v\frac{\partial v}{\partial y} = -g\frac{\partial \zeta}{\partial y} + \frac{\partial}{\partial x}\left(v_h\frac{\partial v}{\partial x}\right) + \frac{\partial}{\partial y}\left(v_h\frac{\partial v}{\partial y}\right) - \frac{\gamma\,|U|\,v}{H} \quad (99)$$

$$\frac{\partial \zeta}{\partial t} + \frac{\partial\,(Hu)}{\partial x} + \frac{\partial\,(Hv)}{\partial y} = 0 \quad (100)$$

where u and v are the depth-averaged velocities in x- and y-direction, respectively; ζ is the free-surface position; H is the total water depth defined as $H = \zeta + h$, where h is the bottom depth (positive downwards);
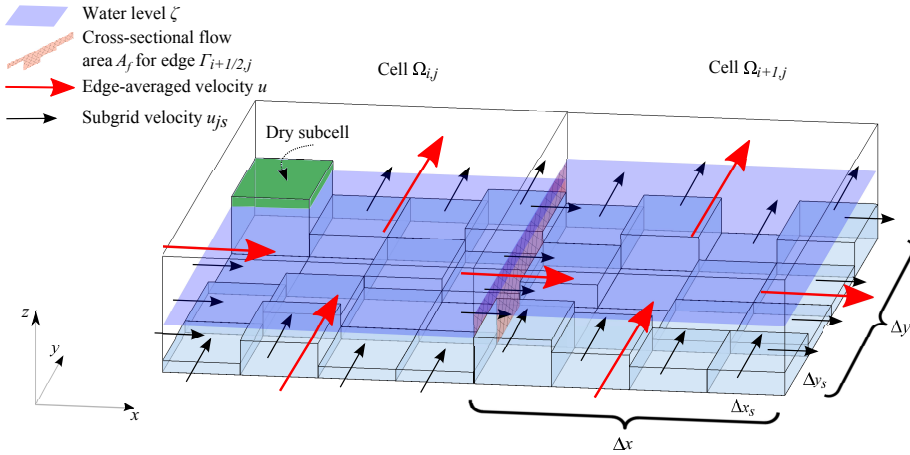
Figure 20: Illustration of two computational cells with topography defined on sub-grid level, using in this case 4x4 subgrid cells per computational cell. The water level is defined on computational grid level. The topography can vary on subgrid level, allowing the occurrence of dry subcells as shown in cell $\Omega_{i,j}$. Computational grid velocities are indicated by the thick red arrows and subgrid velocities along the computational edges are indicated by the thin black arrows (their relationship is given by (108)). The cross-sectional flow area A_f on edge $\Gamma_{i+1/2,j}$ between the two computational cells is hatched. The cell sizes Δx and Δy and the subcell sizes Δx_s and Δy_s are also indicated.

t represents time; g is the gravitational acceleration; γ is the bottom friction coefficient, computed using e.g. a Chézy or Manning formulation; $|U| = (u^2 + v^2)^{1/2}$; and ν_h is the horizontal eddy viscosity.

We discretize the equations on a rectangular grid in Cartesian coordinates with constant grid sizes Δx and Δy. The grid has I cells in the x-direction and J cells in the y-direction. We use a C-grid administration (staggered positioning of variables), i.e. water level ζ and horizontal viscosity ν_h are specified in cell centres and velocity components u and v at cell edges. $\Omega_{i,j}$ is the cell at position (i, j), where i and j are the indices in x and y-direction, respectively, with $i = 1, 2, \ldots, I$; $j = 1, 2, \ldots, J$.

In conventional methods, variables such as depth, roughness coefficients and velocity are constant within computational cells and/or along computational edges. Within the subgrid context, only the water level (and associated volume) is assumed to have a single value within a computational cell (for a certain point in time), thereby also fixing the pressure gradient

over a computational edge to a single value for each edge. Other variables are allowed to vary within cells (bottom topography, horizontal eddy viscosity) and along cell edges (bottom topography, roughness coefficients, velocity). This concept is illustrated in Figure 20 for two computational cells with subgrid topography. In the figure, one subcell in the left cell is dry. The edge-averaged velocity vectors and the subgrid velocities along the cell edges are displayed. Additionally, the cross-sectional flow area A_f between the two computational cells is indicated. Instead of computing the edge-averaged velocity $u_{i+1/2,j}$ as in conventional methods, we now compute the subgrid velocities, defined as $(u_{j_s})_{i+1/2,j}$, where j_s is a subgrid edge along computational edge $\Gamma_{i+1/2,j}$ between cells $\Omega_{i,j}$ and $\Omega_{i+1,j}$. Applying the subgrid approach with these definitions, we discretize the momentum equations (1) and (2) for all subgrid edges along a cell edge Γ as in Casulli and Stelling [51], but with a slightly different notation:

$$
\begin{aligned}
(u_{j_s})_{i+1/2,j}^{n+1} &= (Fu_{j_s})_{i+1/2,j}^{n} - g\frac{\Delta t^n}{\Delta x}\left(\zeta_{i+1,j}^{n+1} - \zeta_{i,j}^{n+1}\right) \\
&\quad -\Delta t^n \frac{(\gamma_{j_s})_{i+1/2,j}^{n}}{(H_{j_s})_{i+1/2,j}^{n}}\left|(U_{j_s})_{i+1/2,j}^{n}\right|(u_{j_s})_{i+1/2,j}^{n+1} \\
&\qquad \forall j_s \in \Gamma_{i+1/2,j}
\end{aligned}
\tag{101}
$$

$$
\begin{aligned}
(v_{i_s})_{i,j+1/2}^{n+1} &= (Fv_{i_s})_{i,j+1/2}^{n} - g\frac{\Delta t^n}{\Delta y}\left(\zeta_{i,j+1}^{n+1} - \zeta_{i,j}^{n+1}\right) \\
&\quad -\Delta t^n \frac{(\gamma_{i_s})_{i,j+1/2}^{n}}{(H_{i_s})_{i,j+1/2}^{n}}\left|(U_{i_s})_{i,j+1/2}^{n}\right|(v_{i_s})_{i,j+1/2}^{n+1} \\
&\qquad \forall i_s \in \Gamma_{i,j+1/2}
\end{aligned}
\tag{102}
$$

where n is the time level and Δt^n is the time step size at level n. Fu and Fv contain the explicitly discretized horizontal advection and diffusion terms. For the advective part we apply the following first-order upwind scheme:

$$
\begin{aligned}
(Fu_{j_s})_{i+1/2,j}^{n}\Big|^{\text{Adv}} &= -\frac{\Delta t^n}{\Delta x}\left[u^-\left(u_{i+3/2,j}^{n} - (u_{j_s})_{i+1/2,j}^{n}\right)\right. \\
&\qquad\qquad \left. + u^+\left((u_{j_s})_{i+1/2,j}^{n} - u_{i-1/2,j}^{n}\right)\right] \\
&\quad -\frac{\Delta t^n}{\Delta y}\left[v^-\left(u_{i+1/2,j+1}^{n} - (u_{j_s})_{i+1/2,j}^{n}\right)\right. \\
&\qquad\qquad \left. + v^+\left((u_{j_s})_{i+1/2,j}^{n} - u_{i+1/2,j-1}^{n}\right)\right] \\
&\qquad \forall j_s \in \Gamma_{i+1/2,j}
\end{aligned}
\tag{103}
$$

where the advective velocities are computed using the following upwind definitions:

$$u^- = \frac{1}{4}\left(u^n_{i+1/2,j} + u^n_{i+3/2,j} - \left|u^n_{i+1/2,j} + u^n_{i+3/2,j}\right|\right) \tag{104}$$

$$u^+ = \frac{1}{4}\left(u^n_{i-1/2,j} + u^n_{i+1/2,j} + \left|u^n_{i-1/2,j} + u^n_{i+1/2,j}\right|\right) \tag{105}$$

$$v^- = \frac{1}{4}\left(v^n_{i,j+1/2} + v^n_{i+1,j+1/2} - \left|v^n_{i,j+1/2} + v^n_{i+1,j+1/2}\right|\right) \tag{106}$$

$$v^+ = \frac{1}{4}\left(v^n_{i,j-1/2} + v^n_{i+1,j-1/2} + \left|v^n_{i,j-1/2} + v^n_{i+1,j-1/2}\right|\right) \tag{107}$$

A similar expression holds for the discretization of Fv. Note that the advective velocities u^-, u^+, v^- and v^+, as well as the upwind velocities in the velocity gradient are based on the edge-integrated velocities, whereas the velocities on the considered subgrid edge in the velocity gradients are taken as the local subgrid velocities $\left(u_{j_s}\right)^n_{i+1/2,j}$. It can be verified that after integration along a computational edge, one obtains a consistent discretization of the advection term in this way. Instead of discretizing the advection term using finite differences, one could apply a finite volume discretization as in Stelling [219], where the advection operator only depends on edge-integrated quantities.

The edge-averaged velocity of edge $\Gamma_{i+1/2,j}$ is obtained from the subgrid velocities as follows:

$$u_{i+1/2,j} = \frac{1}{A^f_{i+1/2,j}} \sum_{j_s \in \Gamma_{i+1/2,j}} \left(u_{j_s}\right)_{i+1/2,j} \left(H_{j_s}\right)_{i+1/2,j} \Delta y_s \tag{108}$$

where Δy_s is the subedge length and where the cross-sectional flow area $A^f_{i+1/2,j}$ is computed as:

$$A^f_{i+1/2,j} = \sum_{j_s \in \Gamma_{i+1/2,j}} \left(H_{j_s}\right)_{i+1/2,j} \Delta y_s \tag{109}$$

The explicit upwind scheme is stable when the Courant-Friedrichs-Lewy (CFL) condition for horizontal flow velocity is satisfied. One could also apply a partly implicit scheme, e.g. Piacsek and Williams [183] or an Eulerian-Lagrangian scheme, e.g Casulli and Cheng [50], Ham, Pietrzak, and Stelling [94], and Wang, Zhao, and Fringer [245] to avoid the CFL condition on the time step.

We discretize the diffusion term in (101) using central differences (similarly for the term in (102)):

$$
\begin{aligned}
\left(Fu_{j_s}\right)^n_{i+1/2,j}\Big|^{\text{Diff}} &= \frac{\Delta t^n}{\Delta x^2}\left[(v_h)^n_{i+1,j}\left(u^n_{i+3/2,j}-u^n_{i+1/2,j}\right)\right.\\
&\quad\left.-(v_h)^n_{i,j}\left(u^n_{i+1/2,j}-u^n_{i-1/2,j}\right)\right]\\
&\quad+\frac{\Delta t^n}{\Delta y^2}\left[(\bar{v}_h)^n_{i+1/2,j+1/2}\left(u^n_{i+1/2,j+1}-u^n_{i+1/2,j}\right)\right.\\
&\quad\left.-(\bar{v}_h)^n_{i+1/2,j-1/2}\left(u^n_{i+1/2,j}-u^n_{i+1/2,j-1}\right)\right]\\
&\quad\forall\,j_s\in\Gamma_{i+1/2,j}
\end{aligned}
\tag{110}
$$

where $\bar{v}_h$ is the viscosity v_h (defined in the cell centre) averaged to the cell corner. We note that the discretized diffusion operator only depends on the edge-integrated velocities and not on the subgrid velocities. For simplicity, we did not investigate the use of subgrid viscosities and velocity gradients in the computation of the horizontal diffusion. The discretization of the horizontal diffusion operator also poses a stability restriction on the time step, but this restriction is commonly much less severe than that from the advection term Casulli and Cheng [50]. Together with the velocity at time level n, we obtain the explicit operator Fu (and similarly Fv):

$$
\left(Fu_{j_s}\right)^n_{i+1/2,j}=\left(u_{j_s}\right)^n_{i+1/2,j}+\left(Fu_{j_s}\right)^n_{i+1/2,j}\Big|^{\text{Adv}}+\left(Fu_{j_s}\right)^n_{i+1/2,j}\Big|^{\text{Diff}}
$$
$$
\forall\,j_s\in\Gamma_{i+1/2,j}\tag{111}
$$

The continuity equation (100) is discretized as usual for each computational cell $\Omega_{i,j}$, but the fluxes are now summations over the subedges along each computational edge Γ of the cell. When integrating (100) over the cell area, we obtain a volume conservation equation:

$$V_{i,j}^{n+1}(\zeta_{i,j}^{n+1}) = V_{i,j}^{n}(\zeta_{i,j}^{n})$$

$$-\Delta t^n \left\{ \sum_{j_s \in \Gamma_{i+1/2,j}} \left[(H_{j_s})_{i+1/2,j}^{n} (u_{j_s})_{i+1/2,j}^{n+1} \Delta y_s \right] \right.$$

$$- \sum_{j_s \in \Gamma_{i-1/2,j}} \left[(H_{j_s})_{i-1/2,j}^{n} (u_{j_s})_{i-1/2,j}^{n+1} \Delta y_s \right]$$

$$+ \sum_{i_s \in \Gamma_{i,j+1/2}} \left[(H_{i_s})_{i,j+1/2}^{n} (v_{i_s})_{i,j+1/2}^{n+1} \Delta x_s \right]$$

$$\left. - \sum_{i_s \in \Gamma_{i,j-1/2}} \left[(H_{i_s})_{i,j-1/2}^{n} (v_{i_s})_{i,j-1/2}^{n+1} \Delta x_s \right] \right\} \quad (112)$$

where Δx_s and Δy_s are the subgrid cell sizes (taken constant for simplicity, but the subgrid method allows variable subgrid resolution per cell); and V is the water volume in a cell.

The water volume and wet area in a cell depend on the local bathymetry and water level. As the bathymetry can vary on subgrid level, the volume and wet area are computed using integrals over the cell, allowing possible dry subcells, as illustrated in Figure 20. Following Casulli [46] and replacing the integrals by summations over subgrid cells, the wet area A and volume V for a cell $\Omega_{i,j}$ are computed through:

$$A_{i,j}(\zeta_{i,j}) = \sum_{p \in \Omega_{i,j}} \left(\Theta \left(h_p + \zeta_{i,j} \right) \Delta x_s \Delta y_s \right) \quad (113)$$

where p is the index of a subgrid cell within $\Omega_{i,j}$ and Θ is the Heaviside step function:

$$\Theta \left(h_p + \zeta_{i,j} \right) = \begin{cases} 1 & \text{if} \quad h_p + \zeta_{i,j} > 0 \\ 0 & \text{otherwise} \end{cases} \quad \text{for} \quad -\infty < \zeta_{i,j} < \infty \quad (114)$$

The volume function $V_{i,j}$ is related to $A_{i,j}$ by:

$$V_{i,j}(\zeta_{i,j}) = \sum_{p \in \Omega_{i,j}} \max \left(0, h_p + \zeta_{i,j} \right) \Delta x_s \Delta y_s \quad (115)$$

or:

$$V_{i,j}(\zeta_{i,j}) = \int_{-\infty}^{\zeta_{i,j}} A_{i,j} \left(\zeta_{i,j} \right) dz \quad (116)$$

Examining (112), one can see that the volume of cell $\Omega_{i,j}$ is altered by the sum of all fluxes across its cell faces. Using the subgrid approach, the fluxes are integrals along the edges of the cell, accounting for possible variations in depth, roughness, horizontal eddy viscosity and velocity along these edges.

The momentum and volume conservation equations (101), (102) and (112) together form a system of equations for the unknown flow velocities u and v across all cell (sub)edges and the unknown free-surface levels ζ in all cell centres. After formal substitution of (101) and (102) in (112), we obtain a discrete equation for the volume of water in each cell $\Omega_{i,j}$:

$$
V_{i,j}^{n+1}\left(\zeta_{i,j}^{n+1}\right) - g\left(\Delta t^{n}\right)^{2}\left(\psi_{i+1/2,j}^{n}\frac{\zeta_{i+1,j}^{n+1}-\zeta_{i,j}^{n+1}}{\Delta x} - \psi_{i-1/2,j}^{n}\frac{\zeta_{i,j}^{n+1}-\zeta_{i-1,j}^{n+1}}{\Delta x}\right.
$$

$$
\left. +\psi_{i,j+1/2}^{n}\frac{\zeta_{i,j+1}^{n+1}-\zeta_{i,j}^{n+1}}{\Delta y} - \psi_{i,j-1/2}^{n}\frac{\zeta_{i,j}^{n+1}-\zeta_{i,j-1}^{n+1}}{\Delta y}\right) = b_{i,j}^{n} \quad (117)
$$

where $\psi_{i+1/2,j}^{n}$ is a scalar quantity that is part of the coefficient that couples cells $\Omega_{i+1,j}$ and $\Omega_{i,j}$ and $b_{i,j}^{n}$ is a scalar quantity that contains all explicit contributions from the momentum and volume conservation equations. They are given by:

$$
\psi_{i+1/2,j}^{n} = \sum_{j_s\in\Gamma_{i+1/2,j}}\left[\frac{\left(\left(H_{j_s}\right)_{i+1/2,j}^{n}\right)^{2}\Delta y_s}{\left(H_{j_s}\right)_{i+1/2,j}^{n}+\Delta t^{n}\left(\gamma_{j_s}\right)_{i+1/2,j}^{n}\left|\left(U_{j_s}\right)_{i+1/2,j}^{n}\right|}\right] \quad (118)
$$

and

$$
\begin{aligned}
b_{i,j}^n \;=\; & V_{i,j}^n\left(\zeta_{i,j}^n\right) \\
& -\Delta t^n \left\{ \sum_{j_s \in \Gamma_{i+1/2,j}} \left[\frac{\left(\left(H_{j_s}\right)_{i+1/2,j}^n\right)^2 \left(Fu_{j_s}\right)_{i+1/2,j}^n \Delta y_s}{\left(H_{j_s}\right)_{i+1/2,j}^n + \Delta t^n \left(\gamma_{j_s}\right)_{i+1/2,j}^n \left|\left(U_{j_s}\right)_{i+1/2,j}^n\right|} \right] \right. \\
& - \sum_{j_s \in \Gamma_{i-1/2,j}} \left[\frac{\left(\left(H_{j_s}\right)_{i-1/2,j}^n\right)^2 \left(Fu_{j_s}\right)_{i-1/2,j}^n \Delta y_s}{\left(H_{j_s}\right)_{i-1/2,j}^n + \Delta t^n \left(\gamma_{j_s}\right)_{i-1/2,j}^n \left|\left(U_{j_s}\right)_{i-1/2,j}^n\right|} \right] \\
& + \sum_{i_s \in \Gamma_{i,j+1/2}} \left[\frac{\left(\left(H_{i_s}\right)_{i,j+1/2}^n\right)^2 \left(Fv_{i_s}\right)_{i,j+1/2}^n \Delta x_s}{\left(H_{i_s}\right)_{i,j+1/2}^n + \Delta t^n \left(\gamma_{i_s}\right)_{i,j+1/2}^n \left|\left(U_{i_s}\right)_{i,j+1/2}^n\right|} \right] \\
& \left. - \sum_{i_s \in \Gamma_{i,j-1/2}} \left[\frac{\left(\left(H_{i_s}\right)_{i,j-1/2}^n\right)^2 \left(Fv_{i_s}\right)_{i,j-1/2}^n \Delta x_s}{\left(H_{i_s}\right)_{i,j-1/2}^n + \Delta t^n \left(\gamma_{i_s}\right)_{i,j-1/2}^n \left|\left(U_{i_s}\right)_{i,j-1/2}^n\right|} \right] \right\}
\end{aligned}
\tag{119}
$$

Assembling (117) for all cells into a system of equations, we obtain:

$$
\mathbf{V}\left(\zeta\right) + \mathbf{T}\zeta = \mathbf{b}
\tag{120}
$$

where $\mathbf{T}$ is a sparse, symmetric, at least semi positive-definite coefficient matrix. Matrix $\mathbf{T}$ is penta-diagonal, where the main diagonal is the negative sum of the four nonpositive off-diagonals $t_{i-1,j}$, $t_{i+1,j}$, $t_{i,j-1}$ and $t_{i,j+1}$:

$$
t_{i,j} \;=\; g\left(\Delta t^n\right)^2 \left(-\frac{\psi_{i-1/2,j}^n}{\Delta x} - \frac{\psi_{i+1/2,j}^n}{\Delta x} - \frac{\psi_{i,j-1/2}^n}{\Delta y} - \frac{\psi_{i,j+1/2}^n}{\Delta y} \right)
\tag{121}
$$

System (120) is sparse, as all cells are only coupled to direct neighbours and it is symmetric, as all fluxes from one cell flow into another cell. The system is also mildly nonlinear due to the fact that the volume function $\mathbf{V}\left(\zeta\right)$ is piecewise-linear in the case of dry cells ($\zeta \leq -h$), as can be seen in Figure 21 (top). In the case that the volume is computed using subgrid bathymetry, the volume function can be nonlinear also for the situation of (partly) wet cells, see Figure 21 (bottom). According to Casulli [46], the equation is piecewise linear and the nonlinearity is only on the main diagonal, allowing an efficient solution strategy.
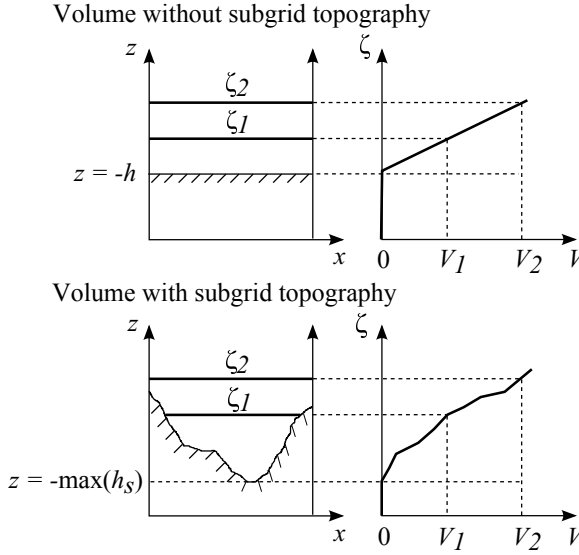
Figure 21: One-dimensional illustration of the volume V in a cell as a nonlinear function of the free-surface level ζ. Top: no subgrid bathymetry variation. Bottom: subgrid bathymetry variation within the cell.

As proposed in Casulli [46], the mild nonlinearity is resolved by using the Newton method. Rewriting (120) in canonical form and following the classical steps within the Newton method, we obtain:

$$\mathbf{f} = \mathbf{V}(\zeta^m) + \mathbf{T}\zeta^m - \mathbf{b} \;,\; \frac{\partial \mathbf{f}}{\partial \zeta^m} \;=\; \frac{\partial \mathbf{V}(\zeta^m)}{\partial \zeta^m} + \mathbf{T} \;,\; \zeta^{m+1} = \zeta^m - \Delta\zeta^m \tag{122}$$

$$\Delta\zeta^m \;=\; \left[\frac{\partial \mathbf{f}}{\partial \zeta^m} \right]^{-1} \mathbf{f} \tag{123}$$

where $\partial \mathbf{V}(\zeta^m)/\partial \zeta^m = \mathbf{A}$ as follows from (116). System (123) can also be written as:

$$\frac{\partial \mathbf{f}}{\partial \zeta^m}\Delta\zeta^m \;=\; \mathbf{f}$$
$$[\mathbf{A} + \mathbf{T}]\,\Delta\zeta^m \;=\; \mathbf{f} \tag{124}$$

This linear system that needs to be solved for each Newton iteration m, is inverted using a preconditioned conjugate gradient method. When no wetting and drying is present, the volume function (115) is linear and the Newton algorithm converges in one iteration.

We note here, that the size of the linear system that is to be solved does not depend on the subgrid discretization. Only the number of computational cells (which equals the number of unknown water levels) determines the system size. Once the new water levels have been obtained from the Newton iteration loop, the subgrid velocities can be directly obtained from the momentum equations (101) and (102), that have been setup for each subedge j_s along a computational edge $\Gamma_{i+1/2,j}$. The edge-integrated velocity $u_{i+1/2,j}$ of edge $\Gamma_{i+1/2,j}$ is then obtained from the subgrid velocities using (108).

The total number of algebraic equations for the velocity depends on the subgrid discretization. If no subgrid is used, the number of equations is $(I+1)J + I(J+1) \approx 2IJ$. If the subgrid method is used, this number needs to be multiplied with the subgrid refinement. These equations are independent and therefore their solution could be accelerated using parallel computing.

Numerous examples Casulli [46], Casulli and Stelling [51], Sehili, Lang, and Lippert [209], Stelling [219], and Volp, Prooijen, and Stelling [240] show that using the described subgrid method, the results from coarse-grid computations for e.g. water levels and discharge distributions are close to the high-resolution results, but with significantly less computational time. Moreover, due to the inclusion of the high-resolution topography, the computational volume, wet area and cross-sectional flow area are defined with higher accuracy than in conventional models with the same resolution. This results in a more accurate representation of wetting and drying, allowing also flow in small (subgrid) channels, without having to increase the computational grid resolution. Effectively, the subgrid method introduces an automatic 'cut-cell' method Rosatti, Cesari, and Bonaventura [202] for subgrid-scale topography, as was illustrated for the flow in a curved channel Stelling [219] and Volp, Prooijen, and Stelling [240]. The subgrid method was applied within the UnTRIM² model Casulli [46] and Casulli and Stelling [51] and a reduction in computational times with respect to the conventional UnTRIM model without subgrid Casulli and Walters [52] and Casulli and Zanolli [53] of a factor 15 to 20 was obtained Sehili, Lang, and Lippert [209], by coarsening the computional grid and including topography on subgrid level.

4.2.2 *The hierarchical-grid approach*

We aim to accurately and efficiently solve flow problems with steady boundary conditions. We then wish to know two things. First, the solution to our problem and second, whether our initially-chosen grid resolution was sufficient, too coarse or perhaps too fine. The conventional way of answering these two questions, would be to run computations on different grid resolutions coarser and finer than the one we had in mind. For computations with large computational grids, the spin-up phase of the model may take a considerable amount of time, due to the fact that initial waves have to travel over many grid cells, often with small time steps due to stability or accuracy limitations. On coarser grids, this process of model spin-up goes much faster.

The subgrid method described in section 4.2.1 allows the incorporation of high-resolution data for e.g. topography and friction parameters on coarser grids, using integral representations of the different terms in the momentum and continuity equations. The subgrid method, however, is only sufficiently accurate when small-scale topographical features – which are on subgrid scale in coarse models – do not cause significant local energy losses or flow-blocking. When this occurs, the subgrid method may not suffice and a higher grid resolution required.

Combining these two notions, we developed a combined hierarchical grid-subgrid (HGSG) method to speed up (quasi-)steady computations, which is particularly applicable to river models. There are different approaches to obtain a steady-state solution to a problem. In conventional computations, a steady-state solution on a certain (fine) grid is obtained by evolving the solution on that grid, until the solution shows less variation over a time step than a certain threshold. We refer to this approach as *Conventional Time Stepping* (CTS). Instead of directly computing on a fine grid, we apply an approach schematically shown in Figure 22, for a computation using six hierarchical grids. We start by coarsening (*C*) the original fine-grid problem $P1$, to a resolution that is coarse enough to perform a quick computation (using time stepping (*TS*) to a steady-state on that grid. In our implementation, a steady state is reached when e.g. the maximum water level and velocity change over a time step is smaller than a certain stationarity criterion ϵ_{stat}. After this, the solution (*S6* in the example) is interpolated (*I*) on to a finer grid and the computation is re-initialized from the interpolated solution, now being problem $P5$ on the finer grid. This process
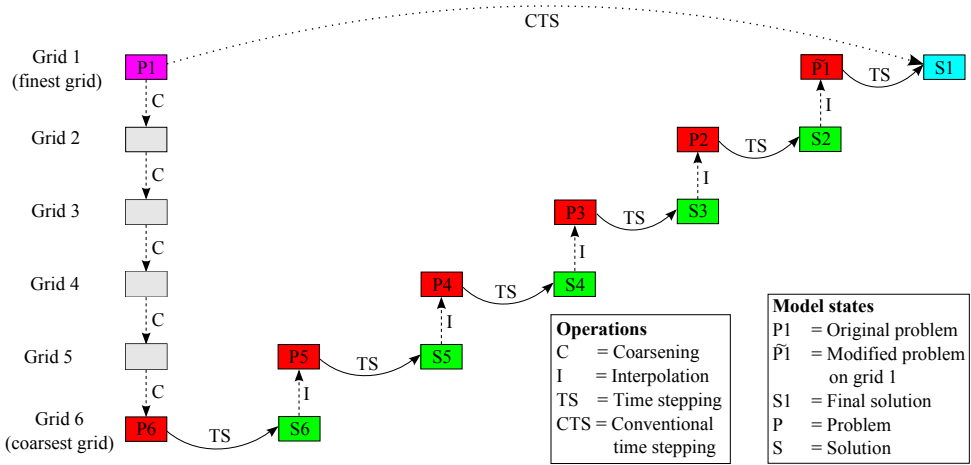
Figure 22: The hierarchical grid algorithm showing the coarsening (*C*) of the original problem (*P*1), the time stepping (*TS*) on the series of hierarchical grids and the interpolation (*I*) of the solution to the next finer grid, to generate the new problem (*P*) for that grid, until the finest grid is reached. The modified problem $\tilde{P}$1 obtained from the hierarchical-grid algorithm provides much better initial conditions for the computation on grid 1 than the original problem *P*1. After time stepping on grid 1, the final solution (*S*1) on the finest grid is obtained. The dotted arrow shows the conventional time stepping (*CTS*) algorithm on a single grid.

is repeated recursively, until the grid-resolution of the original problem *P*1 is obtained or until the solution shows no significant changes after grid refinement. In the latter case, one may assume that grid convergence has been achieved. After interpolating solution *S*2 to grid 1, we obtain a modified problem $\tilde{P}$1. It can be seen as an improved starting condition for the computation on grid 1, compared to the original problem *P*1. It will be shown in section 4.4 that this modelling strategy considerably reduces the computational effort and gives insight in grid convergence by providing results on a sequence of hierarchical grids.

The efficiency of the hierarchical-grid approach can be understood by noting that a computation on a four (2×2) times coarser grid, can generally be run with a twice larger time step. In total this computation would then be eight times faster than the computation on the next finer grid. This notion holds recursively for the coarser grids. From this it can be concluded that an efficient modelling strategy is to perform as much of the total com-

putation on the coarser grids as possible. This is also confirmed by the numerical experiments in section 4.4.

Within the hierarchical-grid algorithm, the coarsest grid level l^{max} is a parameter which can be chosen freely. Additionally, the modeller can choose whether a solution is advanced to the next finer grid, based upon a stationarity condition or simply after a certain time period on a certain grid. Three aspects are important in the algorithm: the setup of the coarse-grid problems, the interpolation of the coarse-grid results to the next finer grid, and the specification of the boundary conditions.

4.2.2.1 *Coarsening*

The setup of the coarse-grid problems is different from conventional hierarchical-grid approaches. With the subgrid method, our numerical representation of topography and roughness parameters on all grid resolutions are integrals/summations of these quantities on subgrid level. This is particularly important for the topography, since it makes sure that the total water volumes on all grid levels are very similar (as demonstrated in section 4.4), and it enables capturing the effects of small-scale topographic variability (e.g. flow blocking) on the coarser grids (see Figure 23). Similarly, for the roughness – being a nonlinear term – taking into account variations in subgrid depth and velocity, results in a much more accurate representation of the total friction, see e.g. Casulli and Stelling [51], Stelling [219], and Volp, Prooijen, and Stelling [240]. This makes the model much less sensitive to the computational grid resolution.

Coarsening of the problem within the HGSG approach, only involves a shift in resolution from the computational grid to the subgrid level. When the computational grid is diadically coarsened (2 × 2), the absolute subgrid resolution and the topography remain unchanged. Only the relative subgrid resolution per cell increases (see also Figures 23 and 24).

The extent to which small-scale topographic and roughness features are captured by the subgrid method, depends on whether the cross-sectional flow areas on computational cell edges are affected. When this is the case, the effect of the subgrid topography and roughness is directly present in the momentum equations (101)-(102) and the continuity equation (112) in the form of reduced (sub)edge depths and cross-sectional flow areas, increased friction in shallow subcells, possible flow blocking by dry sub-

a) Conventional grid coarsening
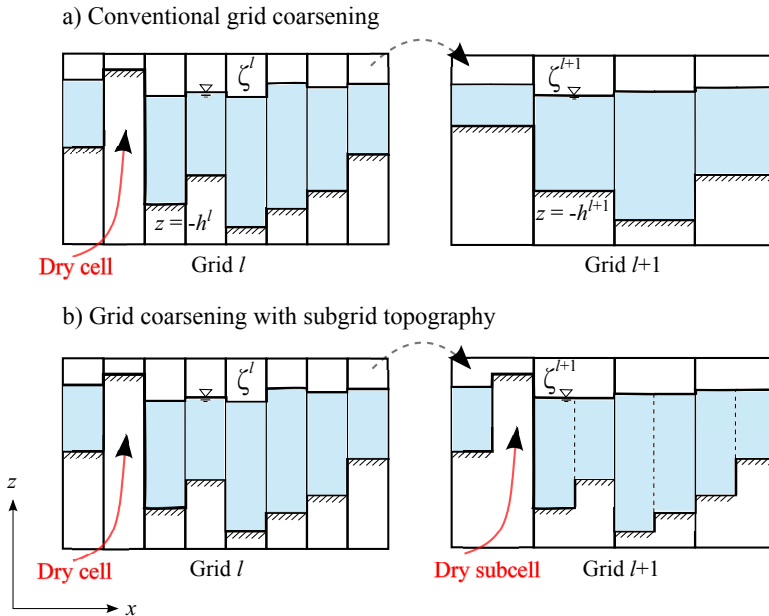
Figure 23: Illustration of 1D grid coarsening of an 8-cell grid (level l) to a 4-cell grid (level $l+1$); a) conventional grid coarsening; b) coarsening with (2-cell) subgrid topography.

cells and therefore an automatic 'cut-cell' approach Stelling [219] and Volp, Prooijen, and Stelling [240].

However, subgrid features, may also be positioned inside computational cells, without touching the computational cell edges. Such features only have a limited effect in the subgrid method, due to the reduced cell volumes and due to a modified friction term when the friction term is integrated over the complete wet area of the cell Stelling [219] and Volp, Prooijen, and Stelling [240]. In these situations, however, the subgrid method may not be sufficiently accurate and a higher computational grid resolution may be required. Modification of the grid generation algorithm is possible to avoid such situations, also applying unstructured grids Sehili, Lang, and Lippert [209]. However, within the hierarchical grid algorithm, the small-scale topographical features are actually resolved on the finer grids. The hierarchical grid algorithm will automatically correctly handle also small-scale topographic features and provide insight in grid convergence related to such features, as we will show in section 4.4.

4.2.2.2 *Interpolation*

The second important aspect in the hierarchical grid algorithm is the interpolation of the solution from a grid to the next finer one. Here we must distinguish between interpolation of water levels (cell-centered) and velocities (edge-based). After having computed a solution on a certain (coarser) grid level, we wish to transfer the water levels to the next finer grid, without introducing large disturbances. Since the water level or pressure gradient is a key forcing for the flow velocity, we chose a linear interpolation method that exactly preserves these gradients.

For the four fine cells in a coarse cell, we alternate between two interpolation types, depending on the position in the grid. The values in the southwest and northeast cells are interpolated linearly between the two coarser cells that are on the southwest-northeast diagonal of the cell: interpolation type 1 in the top left part of Figure 24. The values in the northwest and southeast cells are obtained through linear interpolation between the three coarse cells forming a triangle: interpolation type 2 in the top left part of Figure 24. The interpolation formulas for the water levels on the finer grid are (when no dry cells are present):

$$\zeta^f_{SW} = \frac{3}{4}\zeta^c_{SW} + \frac{1}{4}\zeta^c_{NE} \tag{125}$$

$$\zeta^f_{NE} = \frac{3}{4}\zeta^c_{NE} + \frac{1}{4}\zeta^c_{SW} \tag{126}$$

$$\zeta^f_{SE} = \frac{1}{2}\zeta^c_{SE} + \frac{1}{4}\zeta^c_{SW} + \frac{1}{4}\zeta^c_{NE} \tag{127}$$

$$\zeta^f_{NW} = \frac{1}{2}\zeta^c_{NW} + \frac{1}{4}\zeta^c_{SW} + \frac{1}{4}\zeta^c_{NE} \tag{128}$$

It can be verified that this interpolation scheme – in contrast to e.g. bilinear interpolation – preserves water level (or pressure) gradients in the interpolation from the coarse grid to the next finer one.

After having transferred the water levels from a coarser to a finer grid as described above, we interpolate the velocities to the finer grid. First, velocities along edges that coincide on the coarse and fine grids, are already known on subgrid resolution from (101) and (102). The fine grid velocities along these edges therefore only involve integration of subgrid velocities along a computational edge on the fine grid (half a coarse edge). No interpolation is required (interpolation type 1 in the top right part of Figure 24).

For the fine-grid velocities that are positioned on edges that do not coincide with the coarser grid, we apply bilinear interpolation between

Water level interpolation

Velocity interpolation

Subgrid velocity interpolation
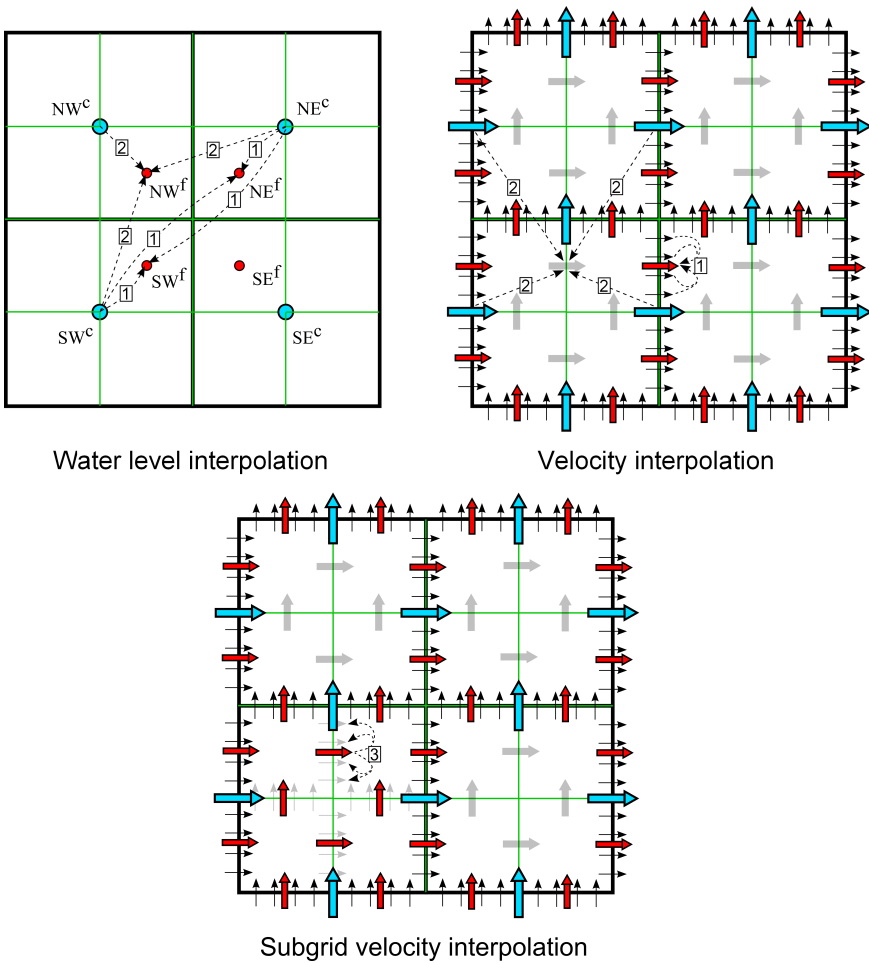
Figure 24: Top left: interpolation of water levels: southwest and northeast cells on finer grids are linearly interpolated between the two coarse cells on the southwest-to-northeast line (interpolation type 1). Northwest and southeast cells on finer grids are interpolated from the surrounding triangle of coarse cells (interpolation type 2); Top right: interpolation of cell-edge velocities: fine grid velocities along edges coinciding with the coarse grid (thick red arrows) are obtained from integrating subgrid velocities along the edge (velocity interpolation type 1). Fine grid velocities on non-coinciding edges (thick grey arrows) are obtained from bilinear interpolation between four surrounding coarse grid velocities (velocity interpolation type 2). Bottom: subgrid velocities along non-coinciding edges (thin grey arrows) are obtained via a conveyance distribution of the fine-grid velocities (velocity interpolation type 3, eq. (129)).

coarse-grid velocities, thereby automatically satisfying the maximum principle. Dry edges (having zero velocity) are not included in the interpolation stencil (interpolation type 2 in the top right part of Figure 24). This interpolation, does not introduce any large disturbances to the computed flow field. The effect of possible subgrid obstacles that cause flow acceleration or deceleration will be 'felt' by the flow in the first time step on the next finer grid.

From these fine-grid velocities, we then obtain the subgrid velocities along these edges by distributing the flux along the computational edge (interpolation type 3 in the bottom part of Figure 24). This distribution is done based on the concept of *conveyance* (e.g. Chow [61] and Volp, Prooijen, and Stelling [240]) as is common practice in one-dimensional models where a flux needs to be distributed over a cross-sectional profile, to accurately represent the total friction contribution of the cross-section. The subgrid velocities are then computed as follows:

$$
\left(u_{j_s}\right)_{i+1/2,j} = \frac{1}{K_{i+1/2,j}} u_{i+1/2,j} \frac{\left(H_{j_s}\right)_{i+1/2,j}^{3/2}}{\left(\gamma_{j_s}\right)_{i+1/2,j}^{1/2}} \Delta y_s \tag{129}
$$

where $K_{i+1/2,j}$ is computed as:

$$
K_{i+1/2,j} = \sum_{j_s \in \Gamma_{i+1/2,j}} \frac{\left(H_{j_s}\right)_{i+1/2,j}^{3/2}}{\left(\gamma_{j_s}\right)_{i+1/2,j}^{1/2}} \Delta y_s \tag{130}
$$

Based on continuity of half coarse cells (summing subgrid fluxes) one could also reconstruct the fine grid velocities without interpolation, instead of interpolation type 2. This, however, only works when no large jumps in cross-sectional flow area occur inside the coarse cell. Numerical experiments (not shown here) have demonstrated that in the latter situation, this velocity reconstruction introduces large velocities due to the fact that (large) fluxes are 'squeezed' through small cross-sectional flow areas. The cause of this problem is that the (subgrid) total water depths are based on the coarse-grid water levels (possibly after interpolation), but that they are not yet influenced by the possible backwater effect due to energy losses generated by the topographical obstruction on subgrid level (see also section 4.5).

4.2.2.3 *Boundary conditions*

The specification of water level or pressure boundary conditions in the hierarchical grid algorithm requires some special attention. Because the grid resolution changes over the sequence of grids, boundary values that are specified in ghost cells – as is often the case for water level boundary conditions – would shift position. Therefore, we prescribe our water level boundary values not in the ghost-cell using $\zeta_{I+1,j} = \zeta_{ghost}$, but at the outer edge of the domain applying $\zeta_{I+1/2,j} = \zeta_{out}$. We then use the water level gradient over half a grid cell distance in (101) and (102). For the eastern boundary edge of boundary cell with index $i = I$, the momentum equation for a subgrid edge j_s becomes:

$$
\begin{aligned}
\left(u_{j_s}\right)^{n+1}_{I+1/2,j} &= \left(Fu_{j_s}\right)^{n}_{I+1/2,j} - g\frac{2\Delta t^n}{\Delta x}\left(\zeta_{out} - \zeta^{n+1}_{I,j}\right) \\
&\quad -\Delta t^n \frac{\left(\gamma_{j_s}\right)^{n}_{I+1/2,j}}{\left(H_{j_s}\right)^{n}_{I+1/2,j}}\left|\left(U_{j_s}\right)^{n}_{I+1/2,j}\right|\left(u_{j_s}\right)^{n+1}_{I+1/2,j}
\end{aligned}
$$

$$\forall\, j_s \in \Gamma_{I+1/2,j} \tag{131}$$

where $\zeta_{out} = \zeta_{I+1/2,j}$ is prescribed by the modeller. Flux or discharge boundary conditions specified on cell edges do not require any special treatment.

In the interpolation of water levels from coarser to finer grids, the boundary values (in case of water level boundary conditions) also need to be adequately taken into account. In this case the ghost cell values $\zeta_{ghost} = \zeta_{I+1,j}$ are needed in the interpolation. Since we assume to be in or close to a steady state at the time of the grid transition we can use the latest known value of the water level in the last internal grid cell at the boundary, to compute the ghost-cell value. Again, for the eastern boundary this becomes:

$$\zeta_{ghost} = 2\zeta_{out} - \zeta_{I,j} \tag{132}$$

4.3   NUMERICAL EXPERIMENTS

We apply the hierarchical grid-subgrid (HGSG) method, described in section 4.2 to two quasi-steady flow examples. Although the boundary conditions are steady, the two examples both show unsteady flow behavior. We note that our numerical model is relatively simple, being 2D depth-averaged, applying a first-order upwind advection scheme and lacking an

advanced turbulence model. Our aim, at this point in the development of the HGSG model, is not to obtain the most accurate solutions for the examples presented in this section, but to investigate the performance and grid convergence properties of the method. We are aware of the fact that to obtain better approximations, we probably require a more advanced advection scheme and an adequate turbulence model. This is, however, beyond the scope of the present work.

To investigate the accuracy and efficiency of the method and its two components, namely the subgrid method and the hierarchical grid approach, we compare different configurations of the algorithm described in section 4.2.2. Each run uses the same 2D, depth-averaged computational core, as described in section 4.2.1. The differences are found in the number of applied hierarchical grid levels l^{max}, and the way subgrid data is included on the coarser grids. One configuration is a reference run on a single grid, corresponding to the conventional time stepping (CTS) in Figure 22. A second configuration is a hierarchical grid computation named HGSG applying the subgrid method in the setup of the coarse grid problems and in the interpolation from coarse to fine grids. Third, we perform a hierarchical grid computation named HG that applies the hierarchical grid approach, but does not use the subgrid method on the coarser grids. Instead, for this run an averaged topography is applied on the coarser grids in the hierarchical grid algorithm, as would be the conventional way of coarsening data to a coarser grid (upscaling).

The hierarchical grid tests for both examples are run with a maximum of l^{max} = 6 grid levels. Additionally, grid level 1 is always chosen identical to the subgrid resolution. Both of these choices are not strictly necessary. Both for the HGSG and the HG computation, we obtain results on all six grid levels (solutions $S6$–$S1$ in Figure 22). For all computations, the time step Δt^n is computed based on a fixed Courant criterion, using the maximum velocity in the domain for each time step n:

$$\Delta t^n = C \cdot \min \left(\frac{\Delta x^l}{\max (|u^n|)}, \frac{\Delta y^l}{\max (|v^n|)} \right) \tag{133}$$

where C is the Courant number and Δx^l and Δy^l are the grid dimensions on grid level l. To maintain stable solutions for all tests, we chose $C = 0.7$ in our experiments. This holds for all grids within the sequence of hierarchical grids, i.e. on the coarser grids a larger time step is applied (when flow velocities are comparable for all grids).

4.3.1 *Vortex shedding behind a circular cylinder*

First we simulate the well-known vortex shedding behind a circular cylinder, which finds an application in river modelling, for instance in the flow around bridge pillars or at groyne tips. The initial flow situation is completely symmetric, so since we do not have an advanced turbulence model, any unsteadiness must come from round-off errors introducing asymmetry. Despite the fact that one could suspect that a model with a simple advection scheme, lacking a turbulence model, is not able to accurately compute the complex vortex shedding patterns, we apply our model on increasingly finer grids within the hierarchical-grid algorithm to see what the refinement yields.

For river applications at higher Reynolds numbers, often the available grid resolution is insufficient for computing the detailed flow dynamics around bridge pillars or groyne tips. The aim of our approach is, therefore, not to investigate how well our model can simulate the flow dynamics around the cylinder, but to demonstrate how the combined HGSG approach can provide insight in grid convergence and grid-size dependent numerical diffusion. Additionally, we show that the approach significantly reduces the computational effort required and how the subgrid method improves the approximations on the coarser grids in the hierarchical grid approach.

Our model domain is a 100 x 100 m square, with a circular cylinder with a diameter $D = 4$ m at $x = 20$ m, $y = 50$ m. Between $y = 25$ m and $y = 75$ m, the channel has a constant depth of $h = 4$ m. Outside that centre part, the bottom increases linearly over a distance of 25 m to a height of 1 m above the initial water level which is at $\zeta^0 = 0$ m, giving the channel a trapezoidal cross-section with dry areas along the south and north boundaries. This setup reduces reflections of waves on the south and north boundaries and therefore provides us with a clearer picture of the vortex-shedding frequency.

On the west side, we have specified an inflow discharge of $Q_{in} = 250$ m^3/s (resulting in an inflow velocity $u_{in} \approx 1$ m/s in the middle of the channel) and on the east side, we prescribe a fixed water level boundary condition of $\zeta_{out} = 0$ m, see (131). A uniform Chézy coefficient $C_z = 65$ m$^{1/2}$/s was specified $\left(\gamma = g/C_z^2\right)$ and a constant horizontal eddy viscosity of $\nu_h = 1 \times 10^{-4}$ m^2/s was applied. We start all computations with stagnant flow conditions. The flow velocity of $u \approx 1$ m/s results in a

Table 3: Vortex shedding behind a circular cylinder: Number of computational cells (and rectangular base grid dimensions), subgrid resolution per cell, end time T, and average time step Δt per grid level l for the hierarchical grid computations.

Grid l	Computational cells N	Subgrid resolution	Grid size $\Delta x, \Delta y$ [m]	End time T [s]	Time step Δt [s]
6 (coarsest)	1150 (32×32)	32 × 32	3.125	700	≈ 2
5	4346 (64×64)	16 × 16	1.562	1200	≈ 1
4	16884 (128×128)	8 × 8	0.781	1600	≈ 0.5
3	66534 (256×256)	4 × 4	0.391	1800	≈ 0.25
2	264138 (512×512)	2 × 2	0.195	1900	≈ 0.12
1 (finest)	1052564 (1024×1024)	1 × 1	0.098	2000	≈ 0.06

4

flow-through time $T_f = L/u \approx 100$ s. Using the diameter of the cylinder, we obtain a (theoretical) Reynolds number $Re = uD/v \approx 4 \times 10^4$, which puts this flow in the turbulent range. However, we will see that for several reasons, the *numerical* Reynolds number will be much lower. We chose a relatively low value for v_h because we aim to investigate the effect of numerical diffusion on the different grids. As noted among others by Roshko [203], the flow character around a cylinder does not change strongly over the range from $Re \approx 3 \times 10^2$ to $Re \approx 10^5$. In section 4.4.1, we will demonstrate that the hierarchical grid strategy gives us insight in the effective Reynolds number per grid. We will see that the results on the finer grids are in the aforementioned and targeted Reynolds number range.

We specify the topography on a 1024×1024 grid, resulting in grid sizes of $\Delta x = \Delta y = 0.098$ m. This resolution is our subgrid level and also the finest resolution at which we wish to obtain our final results (solution $S1$ on grid 1, as in Figure 22). We note here that since the circular cylinder is mapped to a rectangular grid, it is not a round object anymore. The effects of this simplification and the dependency on the grid resolution is demonstrated in section 4.4. The five coarser grids used in the hierarchical grid algorithm, are obtained through 2×2 coarsening of the next finer one. The respective resolutions are presented in Table 3. For the subcells lying directly adjacent to the cylinder, we have raised the bottom level by 20 cm (≈ 5 % of the total water depth) to simulate the effect of wall roughness within our 2D model.

For this test, we perform two separate reference runs (*CTS*) on grids 1 and 2, where we simulate a time period of $T_{CTS} = 750$ s ($T_{CTS} \approx 7.5 T_f$). Vortex shedding was found to start after approximately 500 s of simulated time for grid 1 (spin up time $\approx 5 T_f$) and after 550 s for grid 2 (spin up time $\approx 5.5 T_f$). For the hierarchical grid computations, we used a total simulated time of $T = 2000$ s ($T \approx 20 T_f$). On each of the six grids a part of the total period was simulated as presented in Table 3. We stress that only a period of 100 s ($\approx T_f$) was simulated on the finest grid. We used fixed end times, instead of a stationarity condition (ϵ_{stat}), to determine when to switch to a finer grid, because of the dynamic vortex shedding that starts at a certain grid level (no steady state). The results for this test are presented in section 4.4.1.
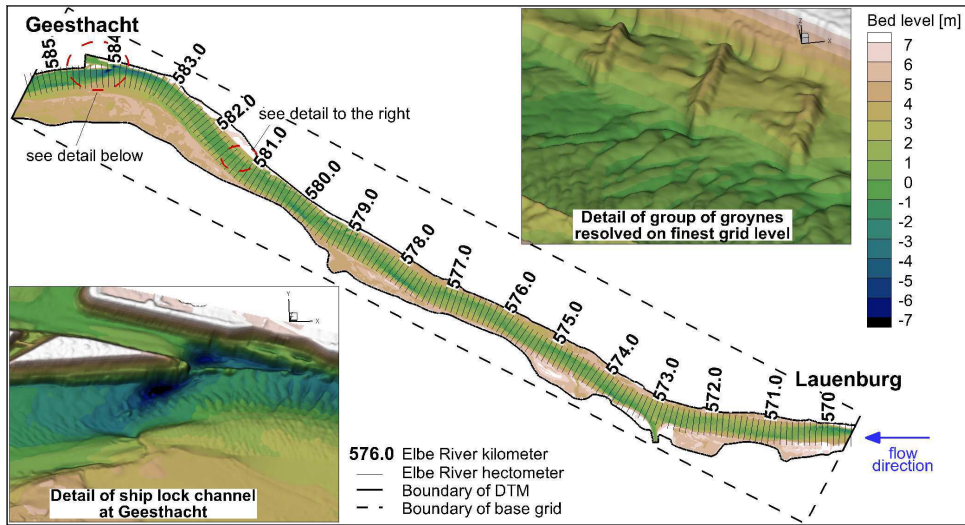
Figure 25: The Elbe River model: Digital Terrain Model (DTM) on subgrid resolution (2x2m) for the Elbe River between the city of Lauenburg and the weir at Geesthacht. The 3D detail figures of the topography are ten times vertically exaggerated, compared to the horizontal scale.

4.3.2 *Case study: Elbe River from Lauenburg to Geesthacht*

As a second application, we consider a reach of the Elbe River between the cities of Lauenburg and Geesthacht in Germany, which is approximately 17 km long and, including the floodplains, 2.5 km wide (see Figure 25). Near the harbour of Geesthacht, at the inlet of the ship lock channel, an area has been identified showing vortex shedding and formation of deep scour holes. For this area, we compare computed velocity patterns with measurements. We illustrate that results on a fine grid are obtained with significant reductions in computational effort and that also for this case the HGSG method provides insight in grid convergence over the sequence of grids.

At the eastern inflow boundary at the city of Lauenburg we prescribe a constant discharge of Q_{in} = 1710 m^3/s (average velocity $|\bar{u}| \approx 1.5$ m/s and flow-through time $T_f = L/|\bar{u}| \approx 3$ hours). For this discharge, we have measurements available to validate our results. At the western outflow boundary, near the weir of Geesthacht, the water level is kept fixed at ζ_{out} = 4.3 m, matching the measurements for the given discharge. For the bottom friction, we set a fixed value for Manning's roughness coeffi-

Table 4: The Elbe River model: Number of computational cells (and rectangular base grid dimensions), subgrid resolution per cell, end time T, and average time step Δt per grid level l for the HGSG computation.
[a] For the HG computation, only the end times for the two finest grids are different: $T^2 = 52.8$ h and $T^1 = 61.1$ h, to obtain (quasi-)stationary solutions.

Grid l	Computational cells N	Subgrid resolution	Grid size $\Delta x, \Delta y$ [m]	End time T [h]	Time step Δt [s]
6 (coarsest)	2958 (213×33)	32 × 32	64	13.9	≈ 31
5	11185 (426×66)	16 × 16	32	25.0	≈ 18
4	43484 (852×132)	8 × 8	16	36.1	≈ 7.7
3	171477 (1904×264)	4 × 4	8	44.4	≈ 3.4
2	681012 (3808×528)	2 × 2	4	50.0[a]	≈ 1.5
1 (finest)	2714156 (7616×1056)	1 × 1	2	55.6[a]	≈ 0.6

cient $n = 0.03$ m$^{1/3}$/s $\left(\gamma = gn^2/H^{1/3}\right)$ and for the horizontal viscosity we choose a value of $\nu_h = 1 \times 10^{-4}$ m^2/s. We start with an initial water level ζ^0, linearly-sloped downward from Lauenburg (5.7 m) to Geesthacht (4.2 m), globally matching the slope in the measured water levels. The initial velocity is taken zero.

We interpolated a Digital Terrain Model (DTM) with a resolution of 2×2 m (almost 3 million data points), onto a rectangular base grid of 7616×1056 cells that envelopes the model domain (see Figure 25). The 2×2 m resolution is taken as the subgrid resolution, at which the topography and the roughness parameters are prescribed, and it is again also used as the reference grid and as the finest grid in the hierarchical grid algorithm. In Figure 25 one can see that topographic features such as groynes and bed forms are resolved on the finest resolution.

For the reference run (*CTS*) we simulated a period of $T = 16.7$ h ($T \approx 5.5T_f$), which was chosen based on preliminary runs. For the hierarchical grid computations, we simulated a total time of $T = 55.6$ h ($T \approx 18.5T_f$). As with the previous test, different partial periods were simulated on the six grids as listed in Table 4. Cells that have no subgrid cells that can be flooded, are eliminated from the grid in a preprocessing step. The number of active (wet or partially dry) cells for each grid level are also given in Table 4, together with the average time step Δt for each grid. On the finer grid levels, the flow shows dynamic eddies. Therefore – as with the vortex shedding test –, the transition to the next finer grid was not based on a stationarity condition, but using fixed end times per grid level. The results for this example are presented in section 4.4.2.

4.4 RESULTS

We compared the results of the reference run with the HG and HGSG computations. All tests were run without parallelization on one core of an Intel Xeon E5-2670 (2.6GHz) CPU with 20 MB L2 cache. We compare both the accuracy of the results, the grid dependency and the performance of the different approaches.

4.4.1   *Vortex shedding behind a circular cylinder*

For this example, we inspect the flow patterns, the resistance due to the cylinder, the shedding frequencies and finally the CPU times. In Figure 26 the *u*-velocity in the *x*-direction is shown at the end times of all six grids in the hierarchical-grid solution algorithm. The left column shows results for computation HG and the right column contains the results for computation HGSG. As an indication of the grid resolution and of the way the cylinder is represented on the grid, the grid cells that are positioned inside the cylinder (inactive cells) are displayed. The main difference between the HGSG and the HG run, is that for the latter the topography changes over the sequence of grids. This results in a number of interesting aspects, as can be seen from Figure 26.

On the coarsest grid ($l = 6$) the solutions are very different. For the HG approach, the topography of the cylinder is averaged to the computational grid, making it a rectangle of two cells and leading to the emergence of a large stationary wake behind and a large setup before the obstacle. For the HGSG run, the cylinder does not block any computational cell completely. It makes four cells partially dry, but the flow can still pass without actual blocking. No real wake and stagnation zone are formed.

On grid 5, the representation of the cylinder for the HG computation changes to a dry rectangle of 2×3 cells, i.e. an obstacle more slender than the actual cylinder. The strength of the wake and the setup before the obstacle are strongly reduced. For the HGSG run, two cells are now dry and all surrounding cells are partially dry, having reduced volumes and cross-sectional flow areas. A wake emerges, that is stationary due to the high numerical diffusion (and a correspondingly low effective Reynolds number).

On grid 4, the HG result shows vortex shedding, due to the fact that the cylinder is still represented by a blunt obstacle, and the numerical diffusion has sufficiently reduced. The velocity field for the HGSG run is at the point where asymmetry of the wake starts developing.

On grid 3, vortex shedding is present for both runs. The results of the two computations are similar, but closer inspection shows that the wave length of the vortices in the HGSG run is sligthly shorter than in the HG run (and closer to the results on grids 2 and 1).

On grids 2 and 1 the results are very similar. It appears that on these resolutions the topography is captured sufficiently accurate and the numerical
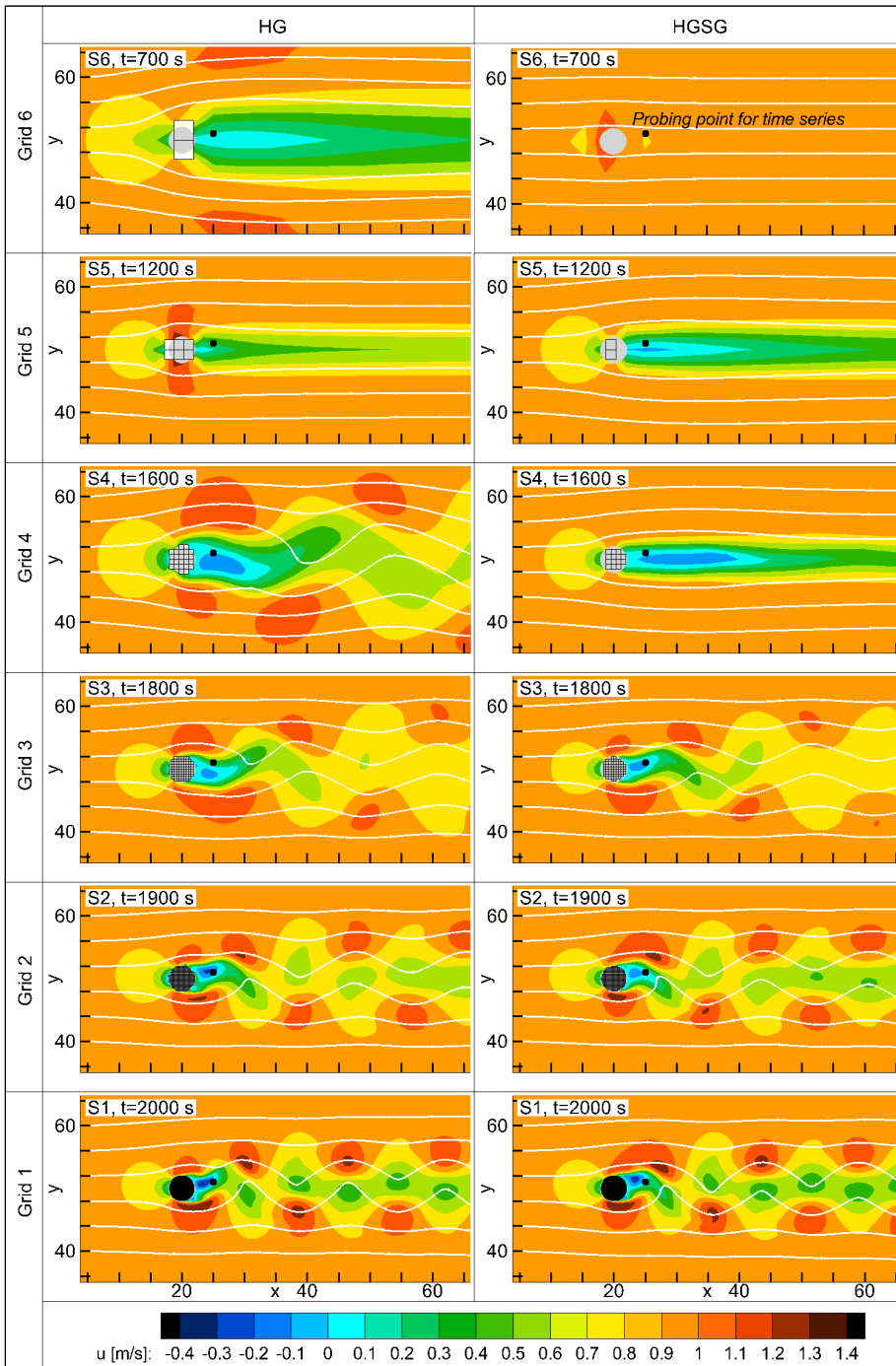
Figure 26: Vortex shedding behind a circular cylinder: Solutions *S*6 to *S*1 for the *u*-velocity on the six grid levels in the hierarchical grid algorithm, without subgrid topography (left), with subgrid topography (right). We indicated the point (at position $x = 25$ m, $y = 51$ m) where the time series of *u*-velocity was probed for the frequency analysis (see Figure 27).

diffusion is low enough to allow vortex shedding at an effective Reynolds number in the range $Re \approx 3 \times 10^2$ to $Re \approx 10^5$, where the flow characteristics do not change much with increasing Reynolds number Roshko [203].

If one aims to include the effect of an obstacle (round or any other shape) in a conventional model, with a resolution on which the obstacle can not be represented sufficiently accurate, one can expect excessive resistance from this obstacle. Applying the subgrid method, the resistance will be approximated more accurately, or at most be underestimated. It is, however, always possible to add some extra resistance (e.g. increased bottom friction) to a model. Reducing the resistance is much more difficult.

To inspect the vortex-shedding frequency of our results, we generated a time series of the u-velocity, in a point in the wake of the cylinder ($x = 25$ m, $y = 51$m). From this time series, we generated a frequency spectrum per grid level by Fourier transformation using commercial software. The time series and spectrum are given in Figure 27. From the time series in the top figure, one can see that on the two coarsest grids (grids 6 and 5), the solution shows no periodic behaviour, matching Figure 26.

The figure also shows that on grid 3 a peak in the spectrum can be found around a frequency $f = 0.04$ Hz. In particular the HG run shows nicely developed characteristics, even containing higher harmonics. However, the hierarchical grid strategy reveals that upon further grid refinement the solution changes to a shedding frequency $f = 0.05$ Hz for the two finest grids (grids 2 and 1), with higher harmonics at $f = 0.10$ Hz and $f = 0.15$ Hz. It appears that the effective Reynolds numbers of grid 1 and 2 are in the range we aimed for and result in very similar flow patterns, yielding both grid resolutions sufficiently fine for practical purposes.

At the bottom of Figure 27 one can see that the dominant frequencies of the hierarchical grid computations match those of the reference runs on grids 1 and 2. Additionally, it can be seen that only for the reference run on the finest grid, the higher harmonics have developed.

Based on the Strouhal number St, the dominant vortex-shedding frequency f is related to the main flow parameters by (see e.g. Roshko [203] and Tai and Zhao [227] and the references therein):

$$St = \frac{fD}{U} \qquad\qquad (134)$$

where U is the free-stream velocity and D is the cylinder diameter.

Inserting the dominant vortex shedding frequency $f = 0.05$ Hz in (134), gives us a Strouhal number of $St = 0.2$, which matches the values found in

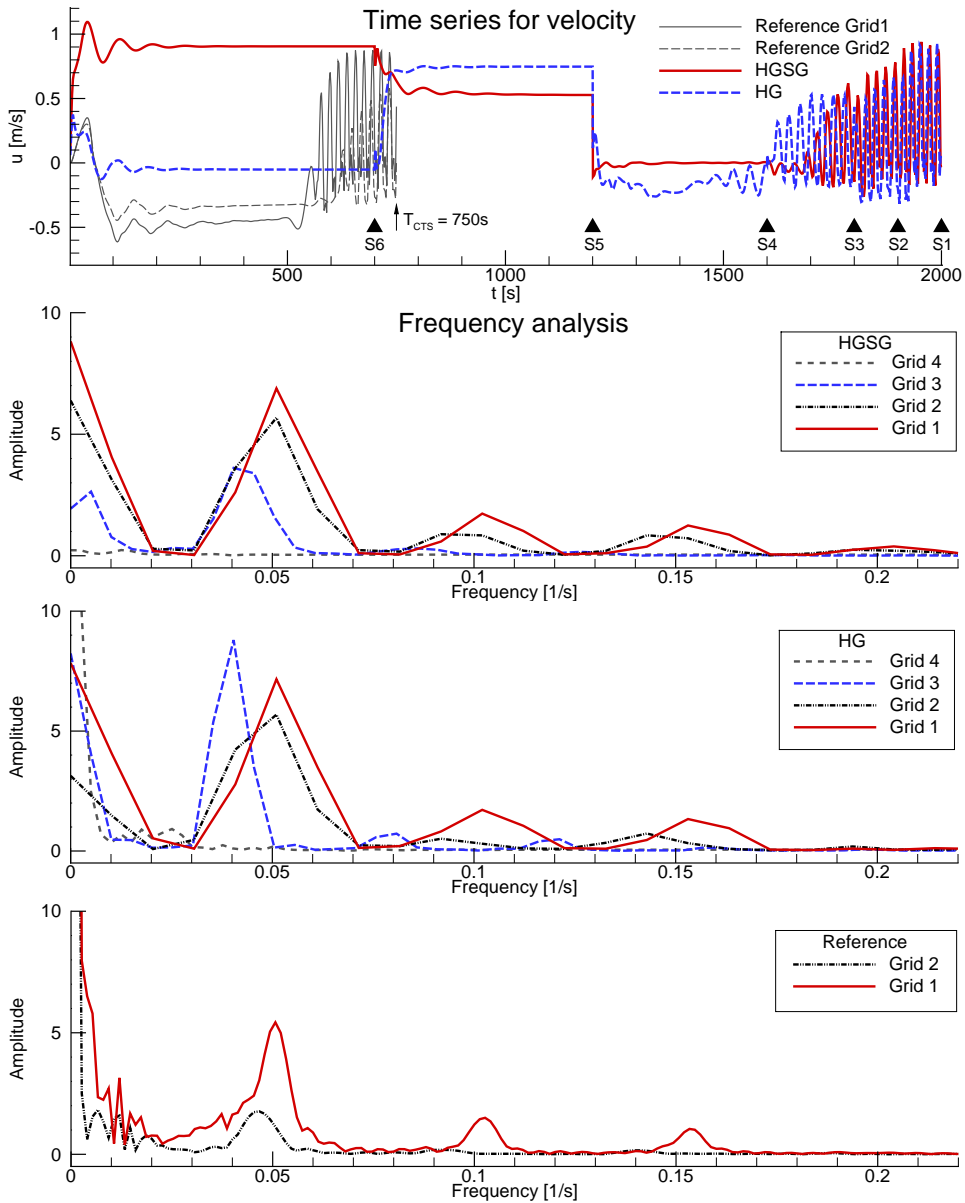Figure 27: Vortex shedding behind a circular cylinder. Top: time series of u-velocity in point (x=25m, y=51m) for the HG and HGSG computations. Middle two figures: frequency spectrum of u-velocity in point (x=25m, y=51m), for the HG and HGSG computations (four finest grid levels (grids 4 to 1)), respectively. Bottom: frequency spectrum for the two reference computations on grids 1 and 2.

e.g. Roshko [203] and Tai and Zhao [227], for the Reynolds number range we are considering.

From these results (and Figure 26), one can conclude that a computation applying grid 2 as the finest grid (with grid 1 as subgrid resolution) suffices to obtain an accurate and converged solution. These results – after 1900 s of simulated time on grid 2 – are obtained after only 0.2 h of CPU time, instead of the 1.5 h required to obtain the solution on grid 1 after 2000 s of simulated time.

The CPU times for the different computations are given in Table 5. The reference (single-grid) run, simulating only 750 s, instead of 2000 s, is significantly less efficient than the hierarchical-grid computations. The vortex-shedding was found to start after approximately 500 s, for the reference computation, resulting in the fact that 2/3 of the simulated time is occupied by the model spin-up for this test. Computation HG, without the subgrid method is found to be most efficient for this test. Considering solution $S2$ to be sufficiently accurate, we obtain this solution 43.3 times faster than the reference run (disregarding the different simulated times and final resolution).

The HG computation is more computationally efficient than the HGSG run for this example, since application of the subgrid method results in an increase in the number of Newton iterations per time step, from 1 for the HG method to 2 or 3 for the HGSG method. This is due to the subgrid wetting and drying that takes place near the north and south domain boundaries. The overhead of the subgrid method makes the HGSG computation 'only' 36.7 times faster than the reference run.

4.4.2   *Case study: Elbe River from Lauenburg to Geesthacht*

For the Elbe model, we also compared the results of the different runs with each other and with the available measurements. The chosen Manning value was found to result in water levels along the river axis that satisfactorily matched the available water level data.

We inspected the velocity patterns at some of the higher grid resolutions we ran. In Figure 28, one can see the resulting streamlines from the measured and computed velocity fields near the ship lock channel entrance. We indicated the areas where three recirculations zones (RZ) and an acceleration zone (AZ) are identified in the measurements. Near the acceleration zone a large scour hole was found. In the figure, we compare the results

4

Table 5: Vortex shedding behind a circular cylinder: simulated time T, CPU time and speed-up factor with respect to the reference run, for the different computations.

Computational setup		Simulated time T [s]	CPU time T_{CPU} [h]	Speed up S
Reference run		750	9.2	1
HG	S1	2000	1.2	7.5
	S2	1900	0.2	43.3
HGSG	S1	2000	1.5	6.2
	S2	1900	0.3	36.7

4
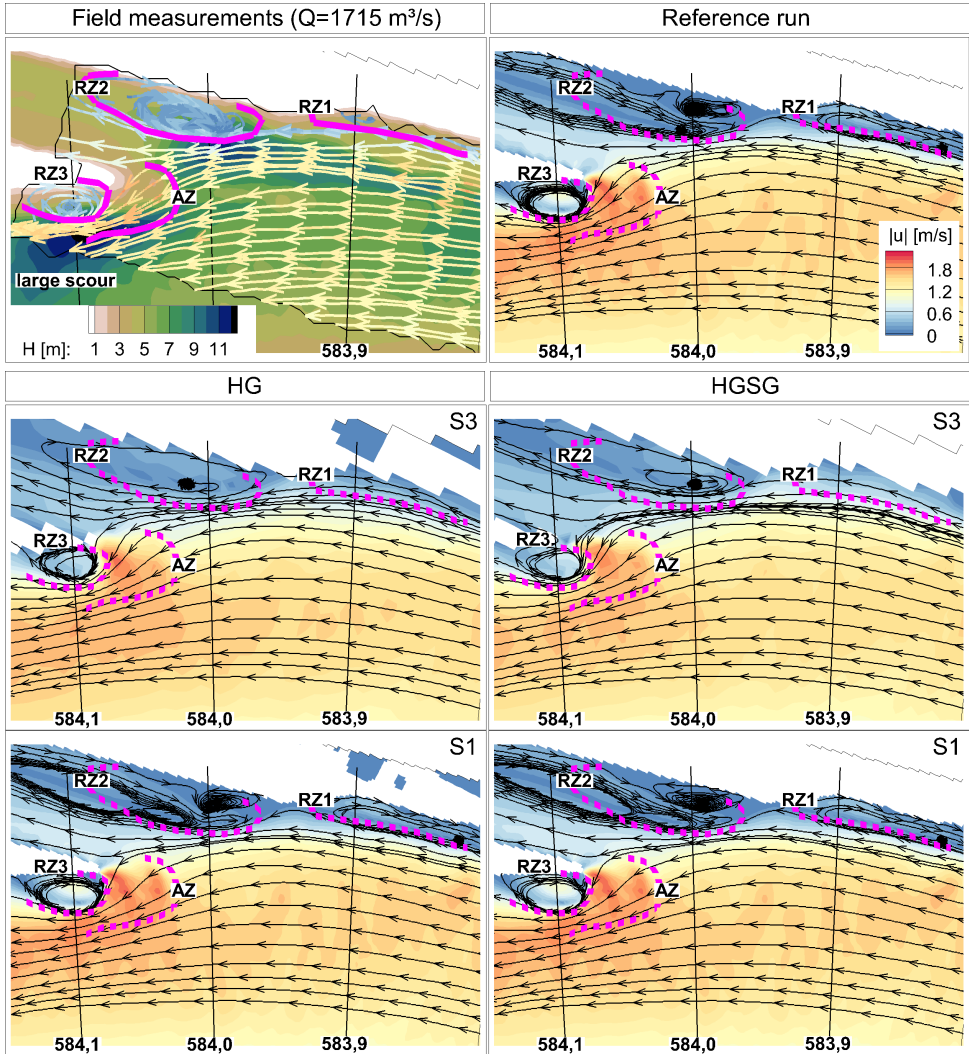
Figure 28: The Elbe River model: streamlines derived from the velocity field. Top left: measured streamlines (the background depicts the topography). Top right: results of the reference computation after at T = 16.7 h of simulated time; Middle and bottom row: solutions $S3$ and $S1$ for the HG (left column) and HGSG runs (right column) on grids 3 and 1. Recirculation (RZ) and acceleration zones (AZ) are indicated as identified in the field measurements.
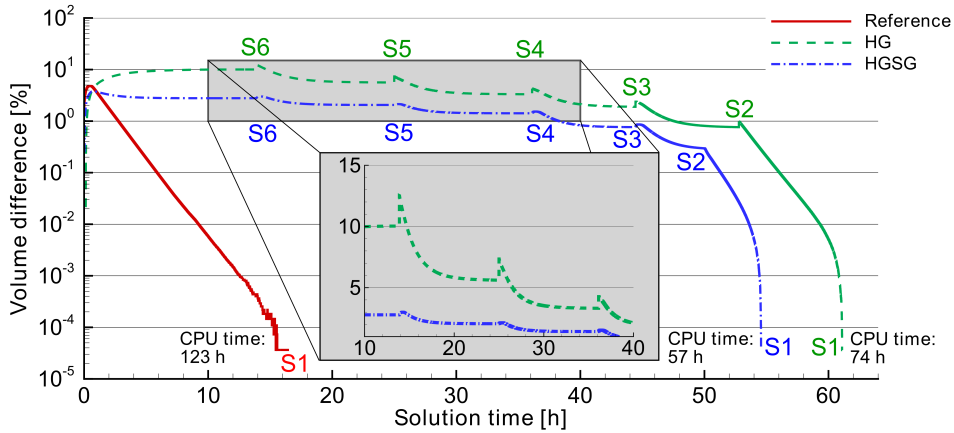
Figure 29: The Elbe River model: Percentual volume difference ΔV [%] with the total steady state volume in the river. Indicated are the CPU times at the end times of the computations. Note the logarithmic scale on the vertical axis.

of the reference run on a single grid (top right), with the results from the HG (left column; middle and bottom row) and the HGSG (right column; middle and bottom row) runs. The results depicted in the middle row are the solutions $S3$ at the end of the simulation period on grid 3, with grid resolution 8×8 m. The bottom figures show the results on the finest grid 1, with resolution 2×2 m. Comparing the results with the measured velocity patterns (top left), no large differences can be distinguished, even for the results on grid 3. It appears that the dominant topographical scales determining the flow patterns, are also represented adequately on this grid, for which the results are obtained with considerably less computational effort than on the finest grid.

For all three computations we determined the total steady state volume in the domain: for the reference run $V^{ref} = 2.7455 \times 10^7$ m^3, for the HG run $V^{HG} = 2.7594 \times 10^7$ m^3 and for the HGSG run $V^{HGSG} = 2.7449 \times 10^7$ m^3. The volume for the HG and the HGSG computation thus differed 0.5 % and 0.023 % from the reference run, respectively. Figure 29 shows the time history of the volume difference for the three computations with their respective steady state volumes. One can see that the convergence for the reference run follows an exponential decay (the figure has a logarithmic vertical scaling). Towards the end fluctuations are visible, due to dynamic wetting and drying of cells. This dynamic behaviour is not present for the

4

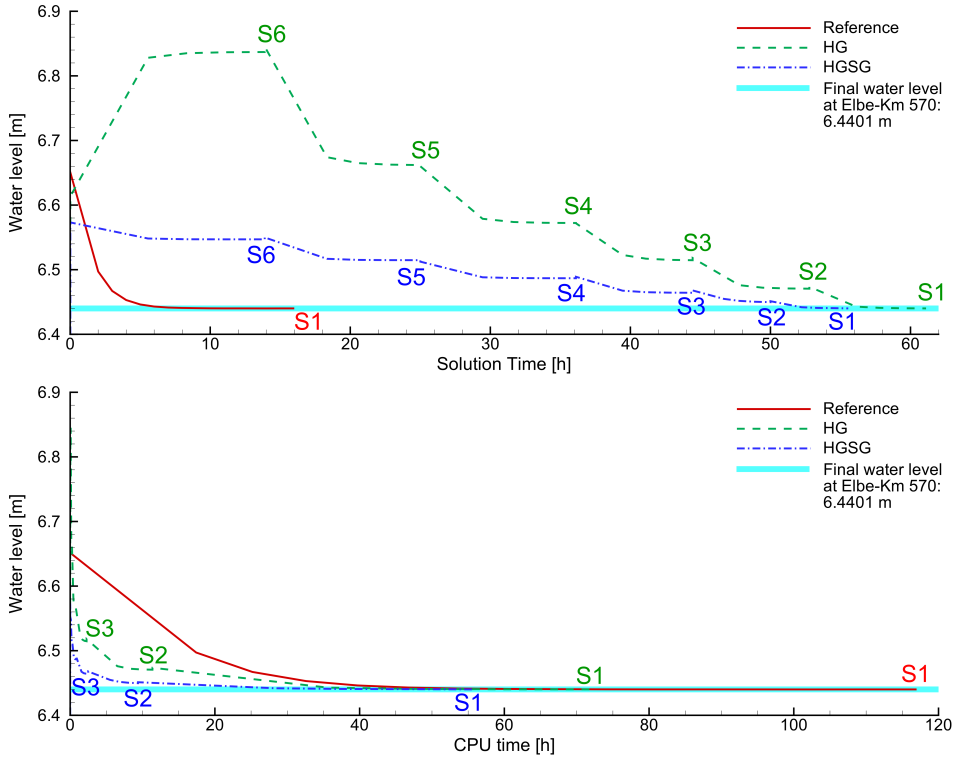Figure 30: The Elbe River model: Time series of water level at Elbe kilometer (Elbe-km) 570. Top: water level versus simulated time. Bottom: water level versus CPU time. Indicated by the thick cyan line is the final steady state water level of $\zeta = 6.4401$ m, which is reached by all three computations.

HG and HGSG runs, near the steady state. A possible explanation could be that after the relatively short simulation period for the reference run, certain long-period, low-amplitude waves are still in the system. In the detail picture in Figure 29, one can see the differences in the size of the disturbances introduced by the interpolation from a coarse grid to a finer one, between the HG and HGSG method. The advantage of the subgrid method is evident. With different interpolation methods than those described in section 4.2.2, the disturbances were significantly larger, requiring more time to be damped out again.

Also for this example we compared the CPU times for the hierarchical grid runs with the reference computation. The simulated times, CPU times and speed-up factors with respect to the reference run are shown in Table 6. Based on the convergence towards the final volume in the model domain, we listed the times the different computations took to attain a certain volume difference with respect to the total volume belonging to its steady state. We considered four percentual volume differences: $\Delta V = 1$ %, $\Delta V =$ 0.1 %, $\Delta V = 0.01$ % and $\Delta V = 0.001$ %. For the 2.7 million cells 2 $\times$ 2 m grid, a volume difference $\Delta V = 0.01$ % corresponds to an average water level difference of 0.25 mm per cell with the reference run.

Figure 30 shows the time series of the water level for the different computations at Elbe-km 570 (near the upstream boundary, see Figure 25. The water levels are plotted both against the simulated time and against the CPU time. One can clearly see that the HG and HGSG computations achieve the (identical) final water level $\zeta = 6.4401$ m much faster than the reference computation. Additionally, the solutions obtained on the different grids within the HG computation, differ much more from the reference solution, than those from the HGSG computation. This clearly illustrates the advantage of applying the subgrid method to resolve the topography on the coarser grids.

As can be seen in Table 6, the reference computation took respectively 23, 46, 69 and 90 hours of CPU time to reach the aforementioned volume differences ΔV, with its steady state volume. The other runs achieve these differences significantly faster, with the lowest CPU times for the HGSG run, which reached the 1 % volume difference already on grid level 3, after 1.3 h of CPU time, i.e. 17.7 times faster than the reference run. The HG model reached the same volume difference at grid level 2 after 6.2 h of CPU time, making it 3.8 times faster than the reference run. In Figure 28 one can see that the resulting velocity field on grid 3 does not differ significantly

Table 6: The Elbe River model: simulated time T, CPU time T_{CPU}, and speed up factor S with respect to the reference run, for three different values of the difference ΔV in total volume in the river with respect to the final steady state volume.
[a] For the HGSG computation, $\Delta V = 1$ % is reached on grid 3.
[b] For the HG computation, $\Delta V = 1$ % is reached on grid 2.

| Model setup | Difference in volume ΔV w.r.t. steady state of reference run | | | |
	$\Delta V = 1$ %	$\Delta V = 0.1$ %	$\Delta V = 0.01$ %	$\Delta V = 0.001$ %
Simulated time T [h]				
CPU time T_{CPU} [h]				
Speed up S w.r.t. reference run				
Reference run	$T = 2.8$	$T = 5.9$	$T = 9.2$	$T = 12.5$
	$T_{CPU} = 23.3$	$T_{CPU} = 46.0$	$T_{CPU} = 69.0$	$T_{CPU} = 90.5$
HG	$T = 47.5$	$T = 56.1$	$T = 59.3$	$T = 60.8$
	$T_{CPU} = 6.2$	$T_{CPU} = 35.2$	$T_{CPU} = 59.2$	$T_{CPU} = 70.5$
	$S = 3.8$	$S = 1.3$	$S = 1.2$	$S = 1.3$
	(ΔV reached on grid 2)[b]		(ΔV reached on grid 1)	
HGSG	$T = 38.3$	$T = 51.3$	$T = 53.6$	$T = 54.4$
	$T_{CPU} = 1.3$	$T_{CPU} = 20.5$	$T_{CPU} = 39.8$	$T_{CPU} = 46.6$
	$S = 17.7$	$S = 2.2$	$S = 1.7$	$S = 1.9$
	(ΔV reached on grid 3)[a]		(ΔV reached on grid 1)	

4

from that on the finest grid, both for the HG and the HGSG computation. The smaller volume differences of 0.1 to 0.001 % are attained at the finest grid for both the HG and the HGSG run, with speed up factor $S \approx 1.3$ for the HG run and $S \approx 1.9$ for the HGSG run.

In this way, the hierarchical grid approach can be used for deciding which grid resolution is appropriate for a certain application. For this example, the subgrid method greatly improves the coarse-grid approximations and therefore accelerates the overall performance of the approach.

This answers research question 5.

4.5 DISCUSSION

The results presented in section 4.4 show that considerable reductions in computational effort can be obtained by applying the combined hierarchical grid-subgrid method, without loss of accuracy. We demonstrated that applying the subgrid method, the coarser-grid solutions within the hierarchical grid approach show much less deviations from the fine-grid solution, than without the subgrid method.

For the problem of vortex-shedding around a circular cylinder, we are actually solving different problems, with and without the subgrid method. Without the subgrid topography, the problems on the coarser grids involve flow around a rough staircased-boundary obstacle, instead of a circular cylinder. Therefore, the size of the wake is dependent on the grid resolution, vortex-shedding occurs earlier, and the vortices have a lower shedding frequency. With subgrid, the coarse-grid problems losely resemble the fine grid problem. However, on the coarser grids, the resolution is insufficient for vortex shedding develop.

For the Elbe River application, we found that by applying the combined HGSG approach we can achieve a nearly steady-state solution that has less than 1 % volume difference compared to the single-grid reference run, while using almost 18 times less computational time. The result was obtained on a 16 times coarser grid, but with the high-resolution subgrid topography underneath the computational grid. The velocity fields on the coarser grids, do not differ much from the fine-grid solution. The similarity of the coarse-grid solutions to the fine-grid solution was much better using the subgrid method, as shown in Figures 29 and 30.

For unsteady computations on grids with many computational points, the HGSG approach can be used for efficiently generating accurate initial conditions using steady boundary conditions, before continuing with the

unsteady part of the simulation. In this way, one can efficiently pass the spin-up phase of the computation.

The interpolation between the grids in the hierarchical grid algorithm, makes use of the subgrid information that is available, without assuming constant velocity and depth along computational edges. However, a number of algorithms based on the reconstruction of local velocity fields are worthwhile investigating to improve the interpolation algorithms from a coarse to a finer grid Ham, Pietrzak, and Stelling [94] and Volp, Prooijen, and Stelling [240]. A key issue here is the fact that the interpolation adequately handles subgrid-scale flow contractions. The interpolation scheme presented in this work was found to introduce the smallest disturbances (see the zoomed area in Figure 29).

As mentioned before, we note the similarity of the hierarchical grid approach with the Full Multigrid (FMG) method discussed among others by Trottenberg, Oosterlee, and Schüller [232] for boundary-value problems. Within multigrid, the different grid resolutions are used in grid cycles for efficiently damping all error modes in the residual within each time step (for initial-value problems). We have tested the application of multigrid V- and W-cycles within time steps to accelerate the linear solver (applying multigrid as preconditioner for our Conjugate Gradient solver), but we found that often the problems per time step are too simple (too few distinct error modes to be damped), for multigrid to have improved efficiency. This particularly holds when approximating a steady state. For transient problems with more dynamics and for advection schemes with no/less limitation on the time step, the multigrid method may be more efficient. Another idea from multigrid that may be worth investigating, is the *restriction* of the solution back to a coarser grid. This may be useful in dynamic computations, in situations where temporarily less resolution is required, e.g. during slack water in tidal flows. Only the water levels would have to be interpolated. The velocities can be computed exactly from the already available subgrid velocities.

A possible future development could be to use local grid refinement within the hierarchical grid algorithm. Based on spatial and temporal gradients of the solution, geometry and/or forcing, the grid can be refined locally to improve the resolution only in those areas where it is needed. For example, the use of a quadtree approach as done by e.g. Stelling [219] may result in an even more efficient method. In this context, for example, it

may be interesting to combine the Multi-Level Adaptive Technique (MLAT) Brandt [27] with the subgrid approach.

The presented method was applied to the 2D depth-averaged shallow water equations. However, an extension to 3D and/or e.g. the Navier-Stokes equations, is in general possible. For three-dimensional models, care would have to be taken in the interpolations in the vertical, when transferring solutions from one grid to a next finer one. Again, besides conservation, a key issue is avoiding the introduction of disturbances in the solution. Additionally, we applied the HGSG method on structured rectangular grids. The subgrid method has been applied succesfully on unstructured grids Casulli [46], Casulli and Stelling [51], and Sehili, Lang, and Lippert [209]. The extension of the hierarchical grid algorithm to unstructured grids, would require testing of existing coarsening techniques such as *agglomeration* known from the fields of grid partitioning and Algebraic Multigrid (AMG). The interpolations from coarse to finer grids would have to be revisited, specifically when grid sequences become non-nested.

With the development of the subgrid method, certain difficulties associated with structured grids may need to be re-evaluated. The topography can be represented on subgrid resolution, possibly in combination with local grid refinement around topographic features such as groynes and levees. The applicability of this approach is still to be examined in more detail and could be compared with cut-cell approaches and unstructured grid methods. The advantages of structured grids, e.g. use of higher order approximations, simple grid generation, ease of implementation, and suitability for vectorization and parallelization, may then render such methods competitive with unstructured grid models, for certain applications.

4.6 CONCLUSIONS

A new method was presented that considerably improves the efficiency of quasi-steady computations on high-resolution grids, with a particular application for river computations. The method is an extension of the subgrid method that integrates high-resolution subgrid data for topography and roughness on coarser computational grids. Applying a sequence of hierarchical grids to effectively deal with the different spatial and temporal scales in common environmental flow problems, the approach exploits the advantages of the subgrid method and proves to be very efficient. The subgrid method improves the coarse-grid solutions in the hierarchical

grid approach, thereby increasing the overall accuracy and efficiency of the combined method. Compared to conventional computations on a high-resolution grid, the computational effort was reduced with factors up to 43 for a vortex-shedding flow problem and up to 18 for a case study of the Elbe River in Germany, on a grid with 2.7 million computational cells.

A convenient by-product of the approach is that – by providing the modeller with results on a sequence of hierarchical grids – the method offers direct insight in grid convergence and assists in the selection of the appropriate grid resolution. The approach can also be used for efficiently generating accurate initial conditions for unsteady simulations on large grids. The method can be extended with local grid refinements using e.g. quadtree grids for further optimization.

CONCLUSIONS AND OUTLOOK

5.1 CONCLUSIONS

In this thesis, several aspects were investigated concerning the accuracy and efficiency of numerical river modelling. At presently-applied grid resolutions, where a part of the river geometry is resolved on the grid, the momentum advection scheme and turbulence model have a strong influence on the model results. It was demonstrated that seemingly small choices in these model components and their implementation can have a large impact.

First, the advection scheme for momentum transport was investigated for its artificial/numerical contribution to the backwater in 2D computations. Next, the bottom shear stress computation and the turbulence model were considered in 3D computations, concerning the accuracy with which the vertical profiles of flow and turbulent quantities are represented. Finally, efficiency and convergence aspects were addressed and a new method was proposed to improve the accuracy and efficiency of quasi-steady river computations by combining the subgrid method from Casulli [46], Casulli and Stelling [51], and Stelling [219] with a hierarchical-grid solution strategy. This approach also provides the modeller with automatic insight in grid convergence. In this way, an effective modelling stategy was developed for simulating quasi-steady river flows, aiding the river engineer in model setup.

The research questions formulated in section *Research questions* have been answered. The answers are summarized here, with their corresponding questions.

The first research question was whether numerical (discretization) errors generate an artificial backwater effect in river computations. It has been demonstrated that at grid resolutions where geometrical variations are represented, an artificial backwater contribution can result from such numerical errors coming from the momentum advection scheme. Depending on

the properties of the advection scheme, this contribution can be of the same order as the contribution from bottom friction (see page 57).

This brings us to the second research question, addressing the properties of an appropriate advection scheme for simulating river flow. It was found that advection schemes that adhere to physical principles, such as momentum conservation or energy-head constancy along streamlines, give less artificial backwater than schemes that do not adhere to such principles. The size of the artificial backwater contribution is largely determined by these conservation/constancy properties of the scheme and to a lesser extent by the order of the scheme (see page 57).

The next research question addressed the problem of distorted vertical profiles and discontinuities in bed shear stress in z-layer models. It has been found that these are caused by the inaccuracy of the discretization of the vertical diffusion term in the momentum equations and in the $(k - \varepsilon)$ turbulence model, for non-uniform vertical layering (see page 76). These problems cannot easily be completely resolved, but are at least considerably reduced by performing a local remapping to an equidistant near-bed layering and by modifying the near-bottom treatment of the vertical diffusion terms in the k- and ε-equations (see page 82).

The final two research questions concern the application of the subgrid method, developed by Casulli [46], Casulli and Stelling [51], and Stelling [219], for improving the efficiency of quasi-steady river computations. Indeed, using the proposed combination of a hierarchical-grid solution strategy and the subgrid method, the computational effort could be reduced with factors up to 43 for a vortex-shedding flow problem and up to 18 for a case study of the Elbe River in Germany, on a grid with 2.7 million computational cells, compared to conventional computations on a single high-resolution grid (see page 133).

By providing the modeller with results on a sequence of hierarchical grids, this method offers direct insight in grid convergence, in the amount of numerical diffusion and assists in the selection of the appropriate grid resolution and in setting up a numerical model, answering the final research question (see page 126).

In the following sections, the general conclusions are summarized for the three different combinations of numerical choices and related physical aspects, considered in the present work.

5.1.1 *The advection scheme and the backwater*

An important finding from this work is that when applying moderate-grid river models, aiming foremost at determining water levels (i.e. the backwater), first-order advection schemes may provide less artificial/numerical backwater than higher-order methods, depending on the conservation/constancy properties of the scheme.

It was demonstrated that the artificial backwater due to errors in the momentum advection discretization can be quite substantial in river computations. The backwater effect was quantified for three first-order advection schemes using a 1D analysis and verified using a sequence of 1D and 2D numerical experiments for these schemes and for two second-order accurate extensions.

A scheme designed for maintaining constant energy head, can indeed compute the flow over variable topography with minimal energy losses. It was also shown that – in agreement with the conclusions from Kramer and Stelling [125] and Stelling and Duinmeijer [220] – the artificial backwater for a momentum-conservative scheme cannot be controlled. The scheme gives an energy loss (positive backwater contribution) at expansions and an energy gain (negative backwater contribution) for contractions. However, the momentum-conservative scheme yields a smaller artificial backwater than the non-conservative (standard) first-order upwind scheme.

These findings are confirmed by the numerical experiments, where the contributions to the global backwater from bottom friction and from the advection scheme have been computed. The scheme with energy-head constancy indeed shows very little to no backwater, but unfortunately shows this property also for flows where losses might be expected, such as for the flow over groynes. The non-conservative first-order upwind scheme was found to cause an artificial backwater effect that could be as high as 35% of the backwater due to bottom friction. In agreement with the 1D analysis, the momentum-conservative scheme shows less backwater than the non-conservative first-order upwind scheme.

Tests with the second-order extensions of both the non-conservative and the conservative first-order upwind schemes showed that the non-conservative second-order upwind scheme does show faster convergence than the first-order scheme, but on coarser grids the backwater is even larger than with the first-order scheme. It was shown that first-order advection schemes that adhere to physical principles, such as momentum

5

conservation or energy-head constancy along streamlines, give less artificial backwater than a higher-order scheme that does not adhere to such principles.

It was found that, for quasi-steady river flow over variable topography, the *local balance* in the momentum equation is dominated by the pressure gradient and advection term and not by the pressure gradient and bottom friction. Due to the discretization errors in the advection scheme, even the contribution to the *global balance* may be substantial, depending on the chosen advection scheme and grid resolution. Therefore, the common consensus that rivers are dominated by a balance between pressure (or free-surface) gradient and bottom friction is often invalid when considering a numerical model. Already for relatively small bottom variations, the global contribution to the backwater due to inaccuracies of the advection scheme may be of the same order of magnitude as that from bottom friction.

For the flow over and around groynes, the total head loss for the different advection schemes and resolutions varies with as much as a factor two, corresponding to several decimeters of water level difference. The lowering of the groynes resulted in a decrease in water levels in the range of 9–23 cm, depending on the advection scheme and the grid resolution, rendering these choices very relevant in engineering projects.

In particular for 'moderate-grid' computations – where the topography is represented with limited resolution – the differences in artificial backwater can be considerable. Unfortunately, most river computations commonly employ grids where the topography is coarsely resolved. From the advection schemes investigated in the present work – for such low- to moderate-resolution computations – it is recommended to use the momentum-conservative first-order scheme or energy-head constancy scheme, for their efficiency and insensitivity to the grid resolution. For higher resolutions – where accurate flow patterns need to be resolved (e.g. including vortex shedding) – the second order (slope-limited) momentum-conservative scheme is recommended.

5.1.2   *The turbulence model and the vertical flow structure*

For applications with bends (with secondary-flow development), or for the flow over and around obstacles, such as weirs and groynes, the use of a three-dimensional model is required to accurately represent the vertical flow structure. For a number of reasons – e.g. efficiency, simplicity of the

discretization, reduced numerical mixing –, hydrodynamic z-layer models might be preferred over σ- or other layering approaches. In particular for applications with significant shallow areas (e.g. floodplains), a z-layer discretization may provide a very efficient approach.

However, z-layer models can provide erroneous velocity profiles and bottom shear stress distributions at positions where the bottom crosses a layer interface, introducing a large ratio in layer thickness near the bottom. We demonstrated this for the situation of uniform channel flow. The errors are caused by the inaccuracy of the discretization of the vertical diffusion term in the momentum equations for non-uniform vertical layering and not by the so-called 'staircase bottom'. The errors can be avoided by performing a local remapping to an equidistant near-bed layering. The new approach works both in combination with an algebraic mixing length turbulence model and the $k - \varepsilon$ turbulence model.

Additionally, modifications in the near-bottom treatment of the vertical diffusion terms in the k- and ε-equations have been presented. The combination of these modifications with the layer-remapping approach allows the accurate and smooth representation of bottom shear stress and velocity profiles along sloping channels and rivers using z-layer models. The applicability of the method was shown using a schematic 2D vertical model for uniform channel flow and using the Delft3D modeling system to simulate the flow over a bottom sill. With the new approach, it is now feasible also for z-layer models to use the straightforwardly-computed bottom shear stress as direct input for coupled morphodynamic models.

5.1.3 *Subgrid modelling, efficiency and grid convergence*

A new method was presented that considerably improves the efficiency of quasi-steady computations on high-resolution grids, with a particular application for river computations. The method is an extension of the subgrid method by Casulli [46], Casulli and Stelling [51], and Stelling [219] that integrates high-resolution subgrid data for topography and roughness on coarser computational grids. Applying a sequence of hierarchical grids to effectively deal with the different spatial and temporal scales in common environmental flow problems, the approach exploits the advantages of the subgrid method and proves to be very efficient. The subgrid method improves the coarse-grid solutions in the hierarchical grid approach, thereby increasing the overall accuracy and efficiency of the

combined method. Compared to conventional computations on a high-resolution grid, the computational effort was reduced with factors up to 43 for a vortex-shedding flow problem and up to 18 for a case study of the Elbe River in Germany, on a grid with 2.7 million computational cells.

Using the combined method, a computation was performed of a river reach at a moderate resolution, but with high-resolution topography underneath. In this way, similar results were obtained as from a computation on the higher resolution grid, but with a considerable performance increase. This increases the bandwidth of feasible grid resolutions as presented in Figure 2 or in Appendix A.

A convenient by-product of the approach is that – by providing the modeller with results on a sequence of hierarchical grids – the method offers direct insight in grid convergence and assists in the selection of the appropriate grid resolution. The approach can also be used for efficiently generating accurate initial conditions for unsteady simulations on large grids. The method can be extended with local grid refinements using e.g. quadtree grids for further optimization.

5.2   OUTLOOK

The investigations in this thesis were performed on structured, rectangular grids. A preliminary assessment (not included in the work) was initiated to follow up on the work from chapter 2 concerning the accuracy of the horizontal advection discretization on (horizontally) unstructured grids. Similar experiments could be performed for the accuracy of the discretization of the horizontal diffusion term on unstructured grids. Due to the fact that the term involves a second derivative and therefore a larger stencil, it could be expected that the accuracy is very sensitive to the grid structure.

The considerations on momentum advection from Chapter 2 and additional experiments aiming at understanding the interaction between the horizontal turbulence model and numerical diffusion might raise the question whether a horizontal turbulence model is really worth the effort for river applications at moderate resolutions. The numerical diffusion from the advection scheme is often too large on the applied grid resolutions, for the contribution of a turbulence model like that of Smagorinsky [214] to have an effect (see also Cea et al. [56]). Our findings are that only at small enough grid resolution, with $\Delta x < H$ (H being the total water depth), the numerical diffusion is 'small enough'. However, at such fine resolutions,

the applicability of the common turbulence models may be debatable. Turbulence models where the transport of turbulent quantities is taken in to account may offer an improvement here, see e.g. Cea et al. [56]. For this purpose, the numerical diffusion from the advection scheme needs to be better understood and where possible reduced, in particular on unstructured grids. Works like those from Holleman, Fringer, and Stacey [104] may form the basis for further research in this direction. Advances in the field of Implicit LES methods (Boris et al. [26], Grinstein, Fureby, and DeVore [90], and Rodi, Constantinescu, and Stoesser [200]) also find their application here. Rodi [199] and Uijttewaal [234] have recently presented nice overviews of the current status of turbulence modelling in rivers and other shallow flows.

The subgrid method as developed by Casulli [46], Casulli and Stelling [51], and Stelling [219] allows the incorporation of high-resolution data (such as topography) in coarser resolution models. However, the method does not yet accurately handle flow blocking and energy losses due to subgrid obstacles, i.e. obstacles that do not 'touch' any grid cell edges and therefore only modify the volume of a cell, but no cross-sectional areas of computational cell edges. Different approaches with exactly this aim have been recently proposed, see e.g. Casas et al. [42], Fu and Hodges [85], Hodges [101], Neal, Schumann, and Bates [166], Sanders, Schubert, and Gallegos [205], and Yu and Lane [262] or Milzow and Kinzelbach [157] for similar considerations in groundwater flow models or work from meteorology related to *orographic drag*, e.g. Lott and Miller [143], Trossman et al. [231], and Zadra et al. [263]. Such approaches may be 'combined' with the subgrid method considered in this thesis. Another approach for dealing with such fine-scale obstacles is the local increase of the computational grid resolution either using e.g. quadtree refinement as in Stelling [219] or by applying unstructured grids.

An interesting property of the subgrid method developed by Casulli [46], Casulli and Stelling [51], and Stelling [219] is the following. In conventional methods (without such a subgrid approach), there has been a long-lasting discussion how to compute the total water depth in positions where it is not defined, e.g. in a velocity point (cell faces). Often, such a quantity is computed by taking the minimum or mean value of surrounding cell centre values. With the subgrid method – since the topography or depth is available on subgrid-scale – such a discussion is rendered obsolete.

Volp et al. [241] and Volp [242] investigated the combination of the same subgrid method as in the present thesis with sediment transport and morphodynamics. It was shown that using the subgrid method and an appropriate subgrid velocity reconstruction (Volp, Prooijen, and Stelling [240]), the computational times for large-scale, long-term morphodynamic computations in tidal areas could be greatly reduced. It is to be expected that the broad applicability of the subgrid method is far from fully exploited.

An interesting extension based on the subgrid method may be possible in Implicit LES methods, by performing a subgrid velocity reconstruction, including the effect of subgrid topography (see already Volp, Prooijen, and Stelling [240] and using this reconstructed velocity both in the computation of the momentum advection term and in the approximation of the Reynolds stresses $\rho\overline{u'v'}$. Adequate velocity reconstructions may be developed based on voriticity considerations, where e.g. a vorticity transport equation is used for capturing the effect of the transport of vorticity generated by subgrid topography.

As already proposed by Kleptsova [122], it may be interesting to investigate the combination of the layer-remapping in z-layers proposed in the present thesis for the accurate representation of the vertical diffusion term with the remapping strategy from Kleptsova [122] and Kleptsova, Stelling, and Pietrzak [124] for advection in three-dimensional computations.

A possibility to circumvent some of the performance or efficiency issues of 3D computations might be to consider a 2D–3D coupling, where a 2D (depth-averaged) discretization is applied on the floodplains (saving computational time) and a 3D model is applied in the main channel, allowing the resolution of e.g. secondary flow patterns and vertical recirculation zones behind e.g. submerged groynes and weirs.

The combined hierarchical-grid-subgrid method (HGSG) as proposed in Chapter 4, could be extended by using (adaptive) local grid refinement within the hierarchical grid algorithm. Based on spatial and temporal gradients of the solution, geometry and/or forcing, the grid can be refined locally to improve the resolution only in those areas where it is needed. For example, the use of a quadtree approach as done by e.g. Stelling [219] may result in an even more efficient method. In this context, for example, it may be interesting to combine the Multi-Level Adaptive Technique (MLAT) (Brandt [27]) with the subgrid approach.

In its present form, the HGSG method is only applicable for quasi-steady applications. A further development of the method for dynamic problems,

might be to allow the transition both from coarser to finer grids and vice versa. One could then perform parts of the simulation with little dynamics on coarser grids, saving computational time. In particular, in combination with the aforementioned local grid refinement, this may prove most efficient. One would end up with possible, dynamic, local grid refinement and local grid coarsening. The difficulty with such methods is choosing the appropriate coarsening and refinement criteria.

Finally, the application of the hierarchical grid algorithm to obtain insight in grid convergence, can be used in studies aiming at the modelling of turbulent flow structures, to estimate the amount of numerical diffusion. Varying the eddy viscosity or the turbulence model, one can automatically detect at which grid resolution (globally/locally), the numerical diffusion (globally/locally) is small enough for the turbulence model to have an effect on the flow.

5.3 FINAL REMARKS

At first sight, the issues considered in this thesis may appear to be of secondary importance in river computations. However, it is shown that the effect of certain modelling choices related to these issues (the advection scheme, the vertical layering/discretization type, the turbulence model) made by the river modeller, or discretization/implementation choices (momentum-conservative implementation, near-bed diffusion discretization, use of subgrid data) made by the developer, can considerably influence the model results.

Modellers, project managers and model developers are strongly encouraged to have a critical look at model input, implementation and results to avoid situations where important engineering conclusions are drawn from erroneous model results. However, before one knows where to look, one should know where the most decisive errors might be. For this reason, this work has aimed at highlighting a number of important issues that might introduce errors or discrepancies in a hydrodynamic river model. The idea was to create awareness by the reader (modeller, manager, developer or a different kind), that certain commonly-accepted modelling building blocks are not to be taken for granted. May this general idea be an incentive for others to continue this line of investigations.

A

ESTIMATING FEASIBLE GRID RESOLUTIONS FOR RIVER COMPUTATIONS

What grid resolutions are presently feasible for river computations can be estimated based on a number of assumptions for the extent of the model domain, the simulation period and the efficiency of the applied modelling system. Based on these assumptions the computational (CPU) time will be estimated, both for serial and parallel computations. The present analysis is restricted to two-dimensional (2D) computations.

A.1 ASSUMPTIONS ON DOMAIN EXTENT

To estimate the required computational time for modelling a complete rivers or at least a longer reach, we consider a river with characteristic dimensions:

Length $L = N_x \Delta x$ = 100 km
Width $W = N_y \Delta x$ = 1 km,

where we have assumed for simplicity that a constant grid size Δx is applied over the whole domain.

A.2 ASSUMPTIONS ON THE SIMULATION PERIOD

One can consider two different classes of computations, leading to two different characteristic simulation periods. The first class concerns stationary or quasi-stationary computations, often aiming at determining water levels and average flow patterns. Such computations often require simulated times expressed in the number of *through-flow times* $T_f = L/\overline{u}$, where L is the river/channel length and $\overline{u}$ is the average velocity over the domain. For such computations, we assume that a simulated time of $T = N_f T_f$, with N_f = 10 is sufficient for obtaining (quasi-)stationary conditions.

The second class concerns long-term dynamic computations, e.g. aimed at determining flooding frequency and extent or river morphodynamics. For this class of computations, we assume that – irrespective of the domain size – the simulated time amounts to one year. In summary, we have:

Short-term stationary computations: Simulated time $T = 10L/\overline{u}$ or $N_f = 10$. Long-term dynamic computations: Simulated time $T = 365 \cdot 24 \cdot 3600$ s or $N_f = 365 \cdot 24 \cdot 3600\overline{u}/L (\approx 3 \times 10^7 \overline{u}/L)$.

To finish the temporal definitions, we need to assume a time step size Δt. This can be estimated based on the fact that most simulation systems have at least an explicit treatment of the advection term, thereby introducing the need to adhere to the CFL condition $C = |\overline{u}|\Delta t/\Delta x \leq 1$ (actually a maximum velocity $|u|^{max}$ should be used here). Assuming a Courant number of $C = 0.7$ as is common in 2D computations one obtains a characteristic time step of:

$$\Delta t = C\Delta x/|\overline{u}|$$

Models that also discretize the pressure/wave part of the equations explicitly often suffer from a much stricter Courant criterion, because $\sqrt{gH} >> |\overline{u}|$:

$$\Delta t = C\Delta x/(|\overline{u}| + \sqrt{gH}).$$

A.3 ASSUMPTIONS ON MODEL EFFICIENCY

The efficiency η of a numerical model is often computed as:

$$\eta = T_{CPU}/(N * N_T) \tag{135}$$

where T_{CPU} is the total CPU time, N is the number of computational cells and N_T is the number of time steps. Using this relation and the assumptions made above, one can relate the CPU time T_{CPU} to the grid size Δx:

$$T_{CPU} = \eta NN_T \tag{136}$$

$$= \frac{\eta LWT}{\Delta x^2 \Delta t} \tag{137}$$

$$= \frac{\eta L^2 WN_f}{|\overline{u}|\Delta x^2 \Delta t} \tag{138}$$

$$= \frac{\eta L^2 WN_f}{C\Delta x^3} \tag{139}$$

For most numerical modelling systems the efficiency is in the range of $\eta = 5 \times 10^{-7}$ to $\eta = 5 \times 10^{-6}$, where the former refers to a more efficient model than the latter. For the two different classes of river computations introduced above, we can now evaluate these expressions and obtain direct relations between the CPU time and the grid size.

Class I : short-term (quasi-)stationary computations with N_f = 10, we obtain $T_{CPU} = \frac{\eta 1 \times 10^{14}}{0.7\Delta x^3}$.

Class II : long-term dynamic computations (using T directly given), we get $T_{CPU} = \frac{\eta 3 \times 10^{20}}{0.7\Delta x^3}$.

Figure 31 shows a plot of these two relations on a double logarithmic scale, where the range of model efficiency is represented by the shaded area. As an indication of feasible grid resolutions, two characteristic CPU times have been chosen: the first for a one-day computation, below which all computations are feasible without parallel high-performance computing (HPC) and one for a 1000-day CPU time, indicating the range of computations that is feasible when HPC resources are available, assuming a maximum parallel speed-up of 1000 (resulting again in a CPU times of one day or less). It can be seen that – depending on the model efficiency – there is an overlap of the different regions. For clarity, four regions have been indicated:

Region I : (hatched southwest-northeast) indicates the most performant range of short-term computations, where computational times up to 1000 days are accelerated using parallel HPC to around one day (parallel speed-up factors of up to 1000 required).

These computations are not feasible without HPC. The region is bounded approximately between grid sizes $1 < \Delta x < 10$ m, where the bandwidth of short-term computations then indicates the computational times without parallel speed up.

Region II : (hatched southeast-northwest) indicates the range of short-term computations feasible also without HPC. Simulations in this region are feasible using grid sizes of approximately $\Delta x > 10$ m, where the bandwidth of short-term computations then indicates the computational times corresponding to a certain grid size.

Region III : (hatched vertically) indicates the range of long-term computations feasible only with HPC (serial CPU times up to 1000 days). The region lies between $3 < \Delta x < 65$ m, where now the bandwidth of long-term computations indicates the computational times without parallel speed up.

Region IV : (hatched horizontally) indicates the range of long-term computations feasible also without HPC. These simulations are feasible with grid sizes of approximately $\Delta x > 30$ m, where the bandwidth of short-term computations again indicates the computational times corresponding to a certain grid size.

It can be seen from the figure that not all characteristic length scales, such as those for bed forms and hydraulic structures, can be resolved on the computational grid in present-day river modelling. The figure indicates that all computations with grid sizes $\Delta x < 1$ m (termed LES computations in the figure) are not feasible yet for large-scale river computations, even with parallel computing. In particular for dynamic, long-term computations, this will most likely remain so for quite some time in the future, unless there is considerable increase in computational performance or a change in the way rivers are modelled/discretized (e.g. using the subgrid method by Casulli [46], Casulli and Stelling [51], and Stelling [219]).

The above analysis holds for depth-averaged computations. It can easily be verified that for 3D computations the CPU times will generally increase with a factor depending mainly on the number of vertical layers applied in the 3D model. Of course, this factor is different for σ-layer than for z-layer models. For the former, the CPU times will approximately linearly scale with the number of layers, i.e. a 10 layer computation will increase the CPU times also by a factor of 10. For z-layer models, the factor depends
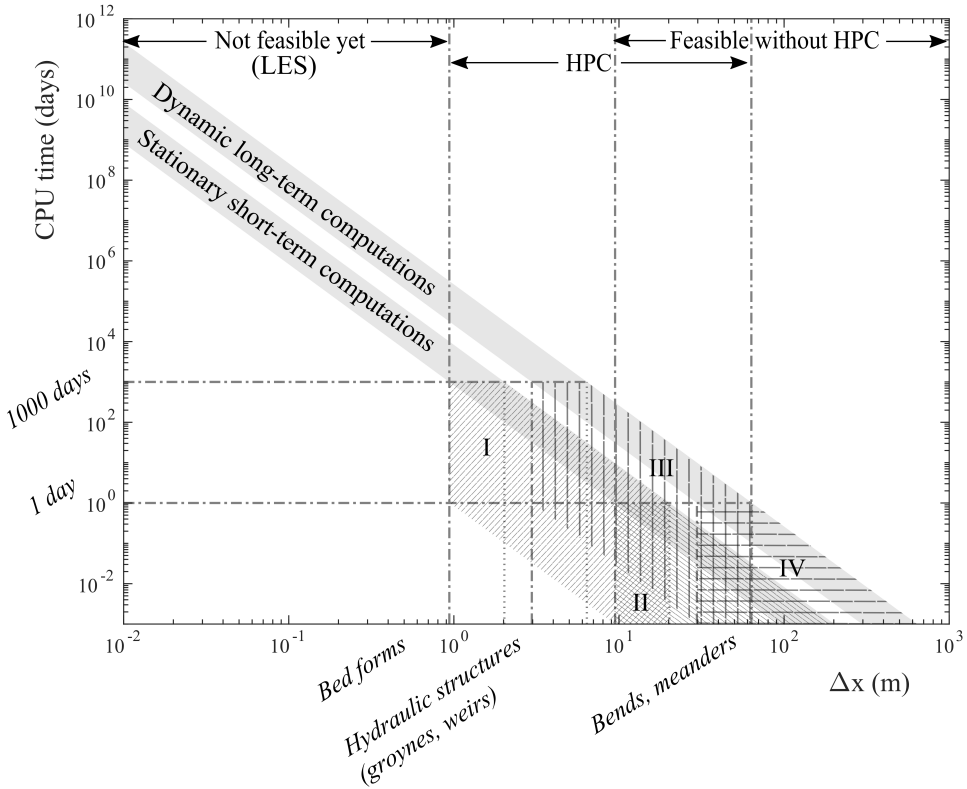
Figure 31: Schematic representation of the increase in CPU time with increasing resolution. The shaded area represents a representative bandwidth of model efficiency. The hatched regions I–IV indicate the ranges of feasible computations with and without parallel High Performance Computing (HPC).

on the relative horizontal extent of the main channel versus the floodplain. If one assumes both parts to be of equal contribution, the CPU times will scale with half of the number of layers, i.e. a 10 layer computation will increase the CPU times by a factor of 5.

A

[1] J. D. Abad, B. L. Rhoads, I. Güneralp, and M. H. García. „Flow Structure at Different Stages in a Meander-Bend with Bendway Weirs." In: *Journal of Hydraulic Engineering* 134.8 (2008), pp. 1052–1063. DOI: 10.1061/(ASCE)0733-9429(2008)134:8(1052) (cit. on pp. 8, 15).

[2] A. Adcroft, C. Hill, and J. Marshall. „Representation of Topography by Shaved Cells in a Height Coordinate Ocean Model." In: *Monthly Weather Review* 125.9 (1997), pp. 2293–2315. DOI: {10.1175/1520-0493(1997)125$<$2293:ROTBSC$>$2.0.CO;2} (cit. on pp. 61, 89).

[3] C.-f. Ai and S. Jin. „Three-Dimensional Non-Hydrostatic Model for Free-Surface Flows With Unstructured Grid." In: *Journal of Hydrodynamics* 20.1 (2008), pp. 108–116. ISSN: 1001-6058. DOI: DOI:10.1016/S1001-6058(08)60035-9 (cit. on p. 16).

[4] S. Ali. „Flow over weir-like structures." PhD thesis. Delft University of Technology, 2013 (cit. on p. 16).

[5] M. S. Altinakar, E. Miglio, and C. Leupi. „Free-surface flows solver with nonhydrostatic pressure and modified $k - \epsilon$ turbulence model : simulation of the curved open channel." In: *Submitted for publication in J. Hydr. Engrg., ASCE.* (2004) (cit. on p. 16).

[6] A. Atzeni, A. Balzano, R. A. Falconer, B. L. Lin, and Y. Wu. „Comparison of shallow water models with accurate treatment of flooding and drying." In: *Proceedings XXIX IAHR Congress*. Beijing, China, 2001, pp. 350–357 (cit. on p. 14).

[7] A. Balzano. „Evaluation of methods for numerical simulation of wetting and drying in shallow water flow models." In: *Coastal Engineering* 34.1-2 (1998), pp. 83–107. ISSN: 0378-3839. DOI: DOI:10.1016/S0378-3839(98)00015-5 (cit. on p. 14).

[8] M. J. Baptist, C. Babovic, J. R. Uthurburu, A. Mynett, and A. Verwey. „On inducing equations for vegetation resistance." In: *J. Hydraul. Eng.* 45.4 (2007), pp. 435–450 (cit. on p. 16).

[9]   S. Baranya and J. Jozsa. „Flow analysis in river Danube by field measurements and 3D CFD turbulence modelling." In: *Periodica Polytechnica Ser. Civ. Eng.* 50.(1) (2006), pp. 57–68 (cit. on pp. 8, 15).

[10]   S. Baranya, N.R.B. Olsen, and J. Józsa. „Flow analysis of a river confluence with field measurements and RANS model with nested grid approach." In: *River Research and Applications* 31.1 (2013), pp. 28–41. DOI: 10.1002/rra.2718 (cit. on pp. 5, 94).

[11]   P. D. Bates and A. P. J. de Roo. „A simple raster-based model for flood inundation simulation." In: *Journal of Hydrology* 236.1–2 (2000), pp. 54–77 (cit. on p. 8).

[12]   P. D. Bates, M. D. Wilson, M. S. Horritt, D. C. Mason, N. Holden, and A. Currie. „Reach scale floodplain inundation dynamics observed using airborne synthetic aperture radar imagery: Data analysis and modelling." In: *Journal of Hydrology* 328.1-2 (2006), pp. 306–318. ISSN: 0022-1694. DOI: DOI:10.1016/j.jhydrol.2005.12.028 (cit. on pp. 8, 95, 97).

[13]   A. Beckmann and R. Döscher. „A Method for Improved Representation of Dense Water Spreading over Topography in Geopotential-Coordinate Models." In: *J. Phys. Oceanogr.* 27 (1997), pp. 581–591. DOI: {10.1175/1520-0485(1997)027$<$581:AMFIRO$>$2.0.CO;2} (cit. on p. 61).

[14]   L. Begnudelli and B. F. Sanders. „Unstructured Grid Finite-Volume Algorithm for Shallow-Water Flow and Scalar Transport with Wetting and Drying." In: *Journal of Hydraulic Engineering* 132.4 (2006), pp. 371–384. DOI: 10.1061/(ASCE)0733-9429(2006)132:4(371) (cit. on p. 14).

[15]   D.L. Berger M.J. and. George, R.J. LeVeque, and K.T. Mandli. „The GeoClaw software for depth-averaged flows with adaptive refinement." In: *Advances in Water Resources* 34.9 (2011), pp. 1195–1206. DOI: 10,1016/j.advwatres.2011.02.016 (cit. on pp. 5, 94).

[16]   M.J. Berger and P. Colella. „Local adaptive mesh refinement for shock hydrodynamics." In: *Journal of Computational Physics* 82.1 (1989), pp. 64–84. DOI: 10.1016/0021-9991(89)90035-1 (cit. on pp. 5, 94).

[17]   E. Bernsen. „A new approach to the Spin-up Problem in ocean-climate models." PhD thesis. Utrecht University, 2010 (cit. on p. 6).

[18] M. D. J. P. Bijvelds. „Numerical modelling of estuarine flow over steep topography." PhD thesis. Delft University of Technology, 2001 (cit. on pp. 15, 22, 24, 61, 65, 70).

[19] M. D. J. P. Bijvelds, C. Kranenburg, and G. S. Stelling. „3D numerical simulation of turbulent shallow-water flow in square harbor." In: *Journal of Hydraulic Engineering* 125.1 (1999), pp. 26–31 (cit. on p. 22).

[20] P. M. Biron, T. W. Haltigin, R. J. Hardy, and M. F. Lapointe. „Assessing different methods of generating a three-dimensional numerical model mesh for a complex stream bed topography." In: *Int. J. Comput. Fluid Dyn.* 21 (1 2007), pp. 37–47. ISSN: 1061-8562. DOI: 10.1080/10618560701374411 (cit. on pp. 7, 8).

[21] K. Blanckaert. „Topographic steering, flow recirculation, velocity redistribution, and bed topography in sharp meander bends." In: *Water Resources Research* 46.9 (2010), pp. 1–23. ISSN: 1944-7973 (cit. on p. 56).

[22] K. Blanckaert and W. H. Graf. „Momentum Transport in Sharp Open-Channel Bends." In: *Journal of Hydraulic Engineering* 130.3 (2004), pp. 186–198 (cit. on pp. 16, 56).

[23] K. Blanckaert, I. Schnauder, A. Sukhodolov, W. van Balen, and W. S. J. Uijttewaal. „Meandering: field experiments, laboratory experiments and numerical modeling." In: *River, Coastal and Estuarine Morphodynamics (RCEM)*. [695]. 2009 (cit. on p. 16).

[24] A. F. Blumberg and G. L. Mellor. „A Description of a Three-Dimensional Coastal Ocean Circulation Model." In: *Three-Dimensional Coastal Ocean Models*. Ed. by N.S. Heaps. American Geophysical Union, 1987, pp. 1–16. ISBN: 9781118665046. DOI: 10.1029/CO004p0001 (cit. on pp. 31, 59).

[25] J. P. Boris and D. L. Book. „Flux-Corrected Transport. I. SHASTA, A fluid transport algorithm that works." In: *Journal of Computational Physics* 11 (1973), pp. 38–69 (cit. on p. 12).

[26] J. P. Boris, F. F. Grinstein, E. S. Oran, and R. L. Kolbe. „New insights into large eddy simulation." In: *Fluid Dynamics Research* 10 (1992), pp. 199–228 (cit. on pp. 11, 13, 23, 143).

[27] A. Brandt. „Multi-level adaptive solutions to boundary value problems." In: *Math. Comp.* 31.138 (1977), pp. 333–390 (cit. on pp. 5, 94, 135, 144).

[28]   A. Brandt. *Multigrid Techniques: 1984 Guide with Applications to Fluid Dynamics*. Tech. rep. 85. GMD, 1984 (cit. on p. 5).

[29]   D. Bresch, R. Klein, and C. Lucas. „Multiscale analyses for the shallow water equations." In: ed. by E. Krause, Y. Shokin, M. Resch, D. Kröner, and N. Shokina. Computational Science and High Performance Computing IV: the 4th Russian-German Advanced Research Workshop. Spinger Berlin Heidelberg, 2011, pp. 194–164 (cit. on p. 5).

[30]   P. Brufau and P. García-Navarro. „Unsteady free surface flow simulation over complex topography with a multidimensional upwind technique." In: *Journal of Computational Physics* 186.2 (2003), pp. 503 –526. ISSN: 0021-9991. DOI: DOI:10.1016/S0021-9991(03)00072-X (cit. on p. 14).

[31]   G.W. Brunner. *HEC-RAS River Analysis System, Hydraulic Reference Manual 5.0*. US Army Corps of Engineers, Davis, CA, USA. 538 pp. 2016 (cit. on p. 31).

[32]   M. Bruwier, P. Archambeau, S. Erpicum, M. Pirotton, and B. Dewals. „Discretization of the divergence formulation of the bed slope term in the shallow-water equations and consequences in terms of energy balance." In: *Applied Mathematical Modelling* 40 (2016), pp. 7532–7544 (cit. on p. 56).

[33]   S. Bunya, E. J. Kubatko, J. J. Westerink, and C. Dawson. „A wetting and drying treatment for the Runge–Kutta discontinuous Galerkin solutions to the shallow water equations." In: *Comput. Methods Appl. Mech. Engrg.* 198 (2009), pp. 1548–1562 (cit. on p. 14).

[34]   H. Burchard, E. Deleersnijder, and G. Stoyan. „Marine turbulence: theories, observations, and models." In: Cambridge: Cambridge University Press, 2005. Chap. Some numerical aspects of turbulence-closure models, pp. 197–206 (cit. on pp. 65, 90).

[35]   H. Burchard and O. Petersen. „Models of turbulence in the marine environment - a comparative study of two-equation turbulence models." In: *Journal of Marine Systems* 21.1-4 (1999), pp. 29–53. ISSN: 0924-7963. DOI: {10.1016/S0924-7963(99)00004-4} (cit. on pp. 65, 81, 90).

[36] M. M. Busnelli. „Numerical simulation of free surface flows with steep gradients." Ph.D. thesis. PhD Thesis. Delft University of Technology, Faculty of Civil Engineering and Geosciences, Department of Hydraulic Engineering, 2001 (cit. on p. 16).

[37] M. M. Busnelli, F. Schuurman, A. Sieben, M. van der Wal, and H. Hector. „Morphodynamic responds of groyne fields to the lowering of crest level of the groynes in the Waal River, The Netherlands." In: *River, Coastal and Estuarine Morphodynamics: RCEM2011*. The 7th IAHR Symposium on River, Coastal and Estuarine Morphodynamics, Sept. 6-8. Tsinghua University Press, Beijing, 2011, pp. 1450–1463 (cit. on pp. 2, 46, 54).

[38] V. Caleffi and A. Valiani. „Well-Balanced Bottom Discontinuities Treatment for High-Order Shallow Water Equations WENO Scheme." In: *Journal of Engineering Mechanics* 135.7 (2009), pp. 684–696 (cit. on pp. 13, 30).

[39] V. Caleffi, A. Valiani, and G. Li. „A comparison between bottom-discontinuity numerical treatments in the DG framework." In: *Applied Mathematical Modelling* 40 (2016), pp. 7516–7531 (cit. on pp. 13, 30).

[40] A. Canestrelli and E.F. Toro. „Restoration of the contact surface in FORCE-type centred schemes II: Non-conservative one- and two-layer two-dimensional shallow water equations." In: *Advances in Water Resources* 47 (2012), pp. 76–87 (cit. on p. 30).

[41] H. Capart, T. I. Eldho, S. Y. Huang, D. L. Young, and Y. Zech. „Treatment of Natural Geometry in Finite Volume River Flow Computations." In: *Journal of Hydraulic Engineering* 129.5 (2003), pp. 385–393. DOI: 10.1061/(ASCE)0733-9429(2003)129:5(385) (cit. on pp. 8, 14).

[42] A. Casas, S. N. Lane, D. Yu, and G. Benito. „A method for parameterising roughness and topographic sub-grid scale effects in hydraulic modelling from LiDAR data." In: *Hydrology and Earth System Sciences* 14 (2010), pp. 1567–1579. DOI: 10.5194/hess-14-1567-2010 (cit. on pp. 8, 143).

[43] M. A. Casas, S. N. Lane, Gerardo Benito, and P. J. Whiting. „Reconstruction of subgrid-scale topographic variability and its effect upon the spatial structure of three-dimensional river flow." In: *Wa-*

ter Resources Research 46.3 (2010), 17 p. DOI: 10.1029/2009WR007756 (cit. on p. 8).

[44]   V. Casulli. „Semi-implicit finite difference methods for the two-dimensional shallow water equations." In: *J. Comput. Phys.* 86.1 (1990), pp. 56–74. ISSN: 0021-9991 (cit. on pp. 5, 27, 33).

[45]   V. Casulli. „A semi-implicit finite difference method for non-hydrostatic, free-surface flows." In: *International Journal for Numerical Methods in Fluids* 30 (1999), pp. 425–440. DOI: 10.1002/(SICI)1097-0363(19990630)30:4$<$425::AID-FLD847$>$3.3.CO;2-4 (cit. on p. 16).

[46]   V. Casulli. „A high-resolution wetting and drying algorithm for free-surface hydrodynamics." In: *International Journal for Numerical Methods in Fluids* 60.4 (2009), pp. 391–408 (cit. on pp. viii, xii, xvii, xxxiii, 5, 9, 14, 18, 21, 25, 27, 95–97, 102, 104–106, 135, 137, 138, 141, 143, 150).

[47]   V. Casulli. „A semi-implicit numerical method for the free-surface NavierStokes equations." In: *International Journal for Numerical Methods in Fluids* 74.8 (2014), pp. 605–622. ISSN: 1097-0363. DOI: 10.1002/fld.3867 (cit. on p. 5).

[48]   V. Casulli and E. Cattani. „Stability, Accuracy and Efficiency of a semi-implicit method for three-dimensional shallow water flow." In: *Computers Math. Applic* 27.4 (1994), pp. 99–112 (cit. on pp. 27, 33).

[49]   V. Casulli and R. T. Cheng. „Stability analysis of Eulerian-Lagrangian methods for the one-dimensional shallow-water equations." In: *Applied Mathematical Modelling* 14 (1990), pp. 122–131 (cit. on pp. 67, 89).

[50]   V. Casulli and R. T. Cheng. „Semi-implicit finite difference methods for three-dimensional shallow water flow." In: *Int. J. Numer. Meth. Fluids* 15.6 (1992), pp. 629–648 (cit. on pp. 12, 100, 101).

[51]   V. Casulli and G. S. Stelling. „Semi-implicit subgrid modelling of three-dimensional free-surface flows." In: *International Journal for Numerical Methods in Fluids* 67.4 (2011), pp. 441–449 (cit. on pp. viii, xii, xvi, xvii, xxxiii, 5, 9, 14, 18, 21, 25, 27, 95–97, 99, 106, 109, 135, 137, 138, 141, 143, 150).

[52] V. Casulli and R. Walters. „An unstructured grid, three-dimensional model based on the shallow water equations." In: *International Journal for Numerical Methods in Fluids* 32.3 (2000), pp. 331–348. DOI: {10.1002/(SICI)1097-0363(20000215)32:3$<$331::AID-FLD941$>$3.0.CO;2-C} (cit. on pp. 8, 31, 59, 62, 96, 106).

[53] V. Casulli and P. Zanolli. „Semi-implicit numerical modeling of nonhydrostatic free-surface flows for environmental problems." In: *Math. Comput. Model* 36.9-10 (2002), pp. 1131–1149 (cit. on pp. 8, 16, 96, 106).

[54] L. Cea, G. Stelling, and M. Zijlema. „Non-hydrostatic 3D free surface layer-structured finite volume model for short wave propagation." In: *International Journal for Numerical Methods in Fluids* 61.4 (2009), pp. 382–410 (cit. on p. 16).

[55] L. Cea and M. E. Vázquez-Cendón. „Unstructured finite volume discretization of two-dimensional depth-averaged shallow water equations with porosity." In: *International Journal for Numerical Methods in Fluids* 63.8 (2010), pp. 903–930. ISSN: 1097-0363. DOI: 10.1002/fld.2107 (cit. on pp. 8, 95, 97).

[56] L. Cea, L. Pena, J. Puertas, M. E. Vázquez-Cendón, and E. Peña. „Application of several depth-averaged turbulence models to simulate flow in vertical slot fishways." In: *Journal of Hydraulic Engineering* 133.2 (2007), pp. 160–172. DOI: 10.1061/(ASCE)0733-9429(2007)133:2(160) (cit. on pp. 142, 143).

[57] M. Cevheri, R. McSherry, and T. Stoesser. „A local mesh refinement approach for large-eddy simulations of turbulent flows." In: *International Journal for Numerical Methods in Fluids* 82.5 (2016), pp. 261–285. ISSN: 1097-0363. DOI: 10.1002/fld.4217 (cit. on pp. 4, 10).

[58] Hubert Chanson. *The hydraulics of open channel flow*. English. 2nd. Butterworth-Heinemann, Oxford, 2004, 544 p. ISBN: 0750659785 (cit. on pp. 31, 39, 54).

[59] Hubert Chanson. „Development of the Bélanger Equation and Backwater Equation by Jean-Baptiste Bélanger (1828)." In: *Journal of Hydraulic Engineering* 135.3 (2009), pp. 159–163 (cit. on p. 31).

[60]   X. Chen. „Using a piecewise linear bottom to fit the bed variation in a laterally averaged, *z*-co-ordinate hydrodynamic model." In: *International Journal for Numerical Methods in Fluids* 44.11 (2004), pp. 1185–1205. DOI: {10.1002/fld.680} (cit. on pp. 61, 89).

[61]   V. T. Chow. *Open Channel Hydraulics*. New York, USA: McGraw-Hill Book Co., 1959 (cit. on p. 113).

[62]   D. M. Cobby, D. C. Mason, and I. J. Davenport. „Image processing of airborne scanning laser altimetry data for improved river flood modelling." In: *ISPRS Journal of Photogrammetry and Remote Sensing* 56.2 (2001), pp. 121–138 (cit. on p. 7).

[63]   C. J. Conroy, E. J. Kubatko, and D. W. West. „ADMESH: An advanced, automatic unstructured mesh generator for shallow water models." In: *Ocean Dynamics* 62 (2012), pp. 1503–1517 (cit. on p. 7).

[64]   S. G. Constantinescu. „On the use of eddy resolving techniques to simulate river transport processes and flow around hydraulic structures." In: *US-China Workshop on Advanced Computational Modeling in Hydroscience and Engineering*. University of Mississippi, USA, 2005 (cit. on pp. 8, 10, 16).

[65]   J. A. Cunge, F. M. Holly, and A. Verwey. *Practical aspects of computational river hydraulics*. London, UK: Pitman Publishing, 1980 (cit. on p. 3).

[66]   DHI. *MIKE 21 C Curvilinear Model, Scientific Documentation. Mike by DHI*. 112 pp. Hørsholm, Denmark, 2011 (cit. on p. 31).

[67]   A. Defina. „Two-dimensional shallow flow equations for partially dry areas." In: *Water Resources Research* 36.11 (2000), pp. 3251–3264. ISSN: 0043-1397 (cit. on pp. 8, 14, 95, 97).

[68]   A. Defina and A. C. Bixio. „Mean flow and turbulence in vegetated open channel flow." In: *Water Resources Research* 41.7 (2005), pp. 1–12. ISSN: 0043-1397. DOI: 10.1029/2004WR003475 (cit. on p. 16).

[69]   Deltares. *Delft3D-FLOW: Simulation of multi-dimensional hydrodynamic flows and transport phenomena, including sediments. User Manual*. 672 pp. Delft, the Netherlands, 2011 (cit. on pp. viii, xii, xvi, 31, 59, 62, 82).

[70]   Y. Deubelbeiss and B.J.P. Kaus. „Comparison of Eulerian and La-grangian numerical techniques for the Stokes equations in the presence of strongly varying viscosity." In: *Physics of the Earth and Planetary Interiors* 171.1-4 (2008), pp. 92–111. DOI: {10.1016/j.pepi.2008.06.023} (cit. on p. 82).

[71]   J.C. Dietrich, S. Tanaka, J.J. Westerink, C.N. Dawson, R.A. Luettich Jr., M. Zijlema, L.H. Holthuijsen, J.M. Smith, L.G. Westerink, and H.J. Westerink. „Performance of the unstructured-mesh, SWAN+ADCIRC model in computing hurricane waves and surge." In: *J Sci Comput* 52 (2012), pp. 468–497 (cit. on p. 6).

[72]   F. Dottori, G. Di Baldassarre, and E. Todini. „Detailed data is welcome, but with a pinch of salt: Accuracy, precision, and uncertainty in flood inundation modeling," in: *Water Resour. Res.* 49 (2013), pp. 6079–6085. DOI: doi:10.1002/wrcr.20406 (cit. on pp. 7, 95).

[73]   M. Dumbser and V. Casulli. „A staggered semi-implicit spectral discontinuous Galerkin scheme for the shallow water equations." In: *Applied Mathematics and Computation* 219 (2013), pp. 8057–8077 (cit. on pp. 4, 13).

[74]   D. R. Durran. *Numerical Methods for Wave Equations in Geophysical Fluid Dynamics*. Springer-Verlag New York, 1999 (cit. on p. 13).

[75]   J.W. Elder. „The dispersion of a marked fluid in turbulent shear flow." In: *Journal of Fluid Mechanics* 5.4 (1959), pp. 544–560 (cit. on p. 10).

[76]   T. Ezer and G. L. Mellor. „A generalized coordinate ocean model and a comparison of the bottom boundary layer dynamics in terrain-following and in *z*-level grids." In: *Ocean Modelling* 6.3 (2004), pp. 379–403. DOI: {10.1016/s1463-5003(03)00026-x} (cit. on p. 61).

[77]   J. H. Ferziger and M. Perić. *Computational methods for fluid dynamics*. 3rd edition. Springer, 2002 (cit. on pp. 7, 13, 17).

[78]   T. Fischer-Antze, N. Ruether, N. R. B Olsen, and D. Gutknecht. „3D modeling of non-uniform sediment transport in a channel bend with unsteady flow." In: *Journal of Hydraulic Engineering and Research* 47.5 (2009), pp. 670–675 (cit. on pp. 15, 16).

[79]   U.S. Fjordholm, S. Mishra, and E. Tadmor. „Well-balanced and en-
        ergy stable schemes for the shallow water equations with discontin-
        uous topography." In: *Journal of Computational Physics* 230.14 (2011),
        pp. 5587–5609 (cit. on p. 56).

[80]   C.K. Forester. „Higher Order Monotonic Convective Difference
        Schemes." In: *Journal of Computational Physics* 23 (1977), pp. 1–22
        (cit. on p. 12).

[81]   G. Forzieri, M. Degetto, M. Righetti, F. Castelli, and F. Preti. „Satel-
        lite multispectral data for improved floodplain roughness mod-
        elling." In: *Journal of Hydrology* 407.1-4 (2011), pp. 41–57. DOI: 10 .
        1016/j.jhydrol.2011.07.009 (cit. on p. 95).

[82]   O. B. Fringer, M. Gerritsen, and R. L. Street. „An unstructured-grid,
        finite-volume, nonhydrostatic, parallel coastal ocean simulator." In:
        Ocean Modelling 14 (2006), pp. 139–173. DOI: 10.1016/j.ocemod.
        2006.03.006 (cit. on pp. 16, 31, 59, 62).

[83]   O. B. Fringer, J. C. McWilliams, and R. L. Street. „A new hy-
        brid model for coastal simulations." In: *Oceanography* 19.1 (2006),
        pp. 46–59 (cit. on pp. 5, 94).

[84]   J. E. Fromm. „A method for reducing dispersion in convective differ-
        ence schemes." In: *Journal of Computational Physics* 3 (1968), pp. 176–
        189 (cit. on p. 12).

[85]   S. Fu and B.R. Hodges. „An Integration Of Subgrid Physics Into
        Coarse Grid Simulations Of River Models." In: *AGU Fall Meeting
        Abstracts* (2007), A171+ (cit. on pp. 8, 143).

[86]   A. A. Galema. „Vegetation resistance - Evaluation of vegetation re-
        sistance descriptors for flood management." MA thesis. University
        of Twente, 2009 (cit. on p. 16).

[87]   A. Gassmann. „Inspection of hexagonal and triangular C-grid dis-
        cretizations of the shallow water equations." In: *Journal of Computa-
        tional Physics* 230.7 (2011), pp. 2706–2721. ISSN: 0021-9991. DOI: http:
        //dx.doi.org/10.1016/j.jcp.2011.01.014 (cit. on p. 7).

[88]   L. Ge and F. Sotiropoulos. „3D Unsteady RANS Modeling of Com-
        plex Hydraulic Engineering Flows. I: Numerical Model." In: *Journal
        of Hydraulic Engineering* 131.9 (2005), pp. 800–808. DOI: 10.1061/
        (ASCE)0733-9429(2005)131:9(800) (cit. on p. 94).

[89] S. K. Godunov. „A difference method for numerical calculation of discontinuous solutions of the equations of hydrodynamics." In: *Mat. Sb. (N.S.)* 47(89).3 (1959). Translated by I. Bohachevsky, pp. 271–306 (cit. on p. 12).

[90] F. F. Grinstein, C. Fureby, and C. R. DeVore. „On MILES based on flux-limiting algorithms." In: *International Journal for Numerical Methods in Fluids* 47 (2005), pp. 1043–1051 (cit. on pp. 11, 13, 23, 143).

[91] W. Hackbusch. *Multi-grid methods and applications*. Heidelberg, Germany: Springer-Verlag, 1985 (cit. on pp. 5, 94).

[92] A. T. Haile and T. H. M. Rientjes. „Uncertainty issues in hydrodynamic flood modeling." In: *Proceedings of the 5th International symposium on Spatial Data Quality*. ITC. Enschede, The Netherlands, 2007, 6 p. (Cit. on p. 4).

[93] D. A. Ham, J. D. Pietrzak, and G. S. Stelling. „A scalable unstructured grid 3-dimensional finite volume model for the shallow water equations." In: *Ocean Modelling* 10.1-2 (2005), pp. 153–169. ISSN: 1463-5003. DOI: 10.1016/j.ocemod.2004.08.004 (cit. on pp. 59, 62).

[94] D. A. Ham, J. D. Pietrzak, and G. S. Stelling. „A streamline tracking algorithm for semi-Lagrangian advection schemes based on the analytic integration of the velocity field." In: *J. Comput. Appl. Math.* 192.1 (2006), pp. 168–174. ISSN: 0377-0427. DOI: 10.1016/j.cam.2005.04.055 (cit. on pp. 12, 67, 89, 100, 134).

[95] R.L. Haney. „On the pressure gradient force over steep topography in sigma coordinate ocean models." In: *Journal of Physical Oceanography* 21 (1991), pp. 610–619. DOI: {10.1175/1520-0485(1991)021$<$0610:OTPGFO$>$2.0.CO;2} (cit. on pp. 15, 60).

[96] R. J. Hardy, S. N. Lane, M. R. Lawless, J. L. Best, L. Elliott, and D. B. Ingham. „Development and testing of a numerical code for treatment of complex river channel topography in three-dimensional CFD models with structured grids." In: *Journal of Hydraulic Research* 43.5 (2005) (cit. on p. 8).

[97] R.J. Hardy, D.R. Parsons, J.L. Best, S.N. Lane, R. Kostaschuck, and O. Orfeo. „Three-dimensional numerical modelling of flows over a natural dune field." In: *River Flow 2006*. Ed. by Rui M.L Ferreira, Elsa C.T.L. Alves, Joao G.A.B. Leal, and Antonio H. Cardoso. London, UK: Taylor and Francis, 2006, pp. 1077–1083 (cit. on pp. 15, 60).

[98]   J.-M. Hervouet and J.A. Jankowski. „Comparing numerical simula-
       tions of free surface flows using non-hydrostatic Navier-Stokes and
       Boussinesq equations." In: *Proceedings of the 4th Conference on Hy-
       droinformatics*. Iowa City, Iowa (USA), 2000 (cit. on p. 16).

[99]   R. Hess. „Dynamically Adaptive Multigrid on Parallel Computers
       for a Semi-Implicit Discretization of the Shallow Water Equations."
       Sankt Augustin: GMD Forschungszentrum Informationstechnik,
       133 pp. Zugl.: Köln, Univ., Diss., GMD research series, No. 9. Köln
       University, 1999 (cit. on p. 5).

[100] C. Hirsch. *Numerical Computation of Internal and External Flows: The
       Fundamentals of Computational Fluid Dynamics*. 2nd edition. John Wi-
       ley & Sons Ltd., 2007 (cit. on pp. 7, 11, 13).

[101] B. R. Hodges. „Representing hydrodynamically important blocking
       features in coastal or riverine lidar topography." In: *Nat. Hazards
       Earth Syst. Sci.* 15 (2015), pp. 1011–1023 (cit. on pp. 8, 143).

[102] B. van 't Hof and E. A. H. Vollebregt. „Modelling of wetting and
       drying of shallow water using artificial porosity." In: *International
       Journal for Numerical Methods in Fluids* 48 (2005), pp. 1199–1217. DOI:
       10.1002/fld.959 (cit. on p. 14).

[103] J. D. Hoffman. „Relationship between the truncation Errors of Cen-
       tered Finite-Difference Approximations on Uniform and Nonuni-
       form Meshes." In: *Journal of Computational Physics* 46 (1982), pp. 469–
       474. DOI: 10.1016/0021-9991(82)90028-6 (cit. on p. 77).

[104] R. Holleman, O. Fringer, and M. Stacey. „Numerical diffusion for
       flow-aligned unstructured grids with application to estuarine mod-
       eling." In: *International Journal for Numerical Methods in Fluids* 72.11
       (2013), pp. 1117–1145. ISSN: 1097-0363 (cit. on pp. 7, 143).

[105] M. S. Horritt, P. D. Bates, and M. J. Mattinson. „Effects of mesh res-
       olution and topographic representation in 2D finite volume models
       of shallow water fluvial flow." In: *Journal of Hydrology* 329.1-2 (2006),
       pp. 306–314. ISSN: 0022-1694. DOI: DOI:10.1016/j.jhydrol.2006.
       02.016 (cit. on p. 8).

[106] N. M. Hunter, P. D. Bates, M. S. Horritt, and M. D. Wilson. „Sim-
       ple spatially-distributed models for predicting flood inundation: A
       review." In: *Geomorphology* 90.3-4 (2007). Reduced-Complexity Ge-
       omorphological Modelling for River and Catchment Management,

pp. 208–225. ISSN: 0169-555X. DOI: DOI:10.1016/j.geomorph.2006.10.021 (cit. on p. 8).

[107] F. Huthoff. „Modeling hydraulic resistance of floodplain vegetation." PhD thesis. Enschede, The Netherlands: University of Twente, 2007 (cit. on p. 16).

[108] S. Ii and F. Xiao. „A global shallow water model using high order multi-moment constrained finite volume method and icosahedral grid." In: *Journal of Computational Physics* 229.5 (2010), pp. 1774–1796. ISSN: 0021-9991. DOI: DOI:10.1016/j.jcp.2009.11.008 (cit. on p. 7).

[109] J.A. Jankowski. „A Non-Hydrostatic Model for Free Surface Flows." Bericht Nr. 56. Institut fuer Stroemungsmechanik, 1999 (cit. on p. 16).

[110] J.A. Jankowski. „Parallel implementation of a non-hydrostatic model for free surface flows with semi-Lagrangian advection treatment." In: *International Journal for Numerical Methods in Fluids* 59 (2009), pp. 1157–1179. DOI: 10.1002/fld.1859 (cit. on pp. 8, 12, 16).

[111] Y. Jia, Y. Xu, and S. S. Y. Wang. „Numerical Study of Flow Affected by Bendway Weirs in Victoria Bendway, the Mississippi River." In: *Journal of Hydraulic Engineering* 135.11 (2009), pp. 902–916. DOI: 10.1061/(ASCE)0733-9429(2009)135:11(902) (cit. on pp. 8, 15, 94).

[112] Y. Jia, S. Scott, Y. Xu, S. Huang, and S. S. Y. Wang. „Three-Dimensional Numerical Simulation and Analysis of Flows around a Submerged Weir in a Channel Bendway." In: *Journal of Hydraulic Engineering* 131.8 (2005), pp. 682–693. DOI: 10.1061/(ASCE)0733-9429(2005)131:8(682) (cit. on p. 16).

[113] G.-S. Jiang and C.-W. Shu. „Efficient Implementation of Weighted ENO Schemes." In: *Journal of Computational Physics* 126.1 (1996), pp. 202–228. ISSN: 0021-9991. DOI: http://dx.doi.org/10.1006/jcph.1996.0130 (cit. on p. 4).

[114] W.P. Jones and B. E. Launder. „The prediction of laminarisation with a two-equation model of turbulence." In: *International Journal of Heat and Mass Transfer* 15 (1972), pp. 301–314. DOI: 10.1016/0016/0017-9310(72)90076-2 (cit. on pp. 10, 22, 64).

[115] S. Kang, I. Borazjani, and F. Sotiropoulos. „Curvilinear immersed-boundary method for simulating unsteady flows in shallow natural streams with arbitrarily complex obstacles." In: *APS Meeting Abstracts* (2008), A3+ (cit. on p. 7).

[116] S. Kang, A. Lightbody, C. Hill, and F. Sotiropoulos. „High-resolution numerical simulation of turbulence in natural waterways." In: *Advances in Water Resources* 34.1 (2011), pp. 98–113. ISSN: 0309-1708. DOI: `10.1016/j.advwatres.2010.09.018` (cit. on pp. 4, 6, 8, 10, 94).

[117] S. Kashyap, C. D. Rennie, R. Townsend, G. Constantinescu, and T. E. Tokyay. „Flow around submerged groynes in a sharp bend using a 3D LES model." In: *River Flow 2010*. Ed. by Aberle Dittrich Koll and Geisenhainer. Bundesanstalt für Wasserbau. 2010 (cit. on pp. 6, 10, 15).

[118] J. Kent, C. Jablonowski, J. P. Whitehead, and R. B. Rood. „Determining the effective resolution of advection schemes. Part II: Numerical testing." In: *Journal of Computational Phys* 278 (2014), pp. 497–508 (cit. on p. 12).

[119] H. W. J. Kernkamp, A. van Dam, G. S. Stelling, and E. D. de Goede. „Efficient scheme for the shallow water equations on unstructured grids with application to the Continental Shelf." In: *Ocean Dynamics* 61.8 (2011), pp. 1175–1188. ISSN: 1616-7228 (cit. on p. 34).

[120] J. A. Th. M. Van Kester. *Validatie Delft3D voor menglaag proef*. Tech. rep. WL|Delft Hydraulics, 1994 (cit. on p. 65).

[121] M. P. Kirkpatrick, S. W. Armfield, and J. H. Kent. „A representation of curved boundaries for the solution of the Navier-Stokes equations on a staggered three-dimensional Cartesian grid." In: *Journal of Computational Physics* 184.1 (2003), pp. 1 –36. ISSN: 0021-9991. DOI: `10.1016/S0021-9991(02)00013-X` (cit. on pp. 7, 61, 89).

[122] O. Kleptsova. „Unstructured Orthogonal Meshes for Modeling Coastal and Ocean Flows." PhD thesis. Delft University of Technology, 2013 (cit. on p. 144).

[123] O. Kleptsova, J. D. Pietrzak, and G. S. Stelling. „On a momentum conservative z-layer unstructured C-grid ocean model with flooding." In: *Ocean Dynamics* 54-55 (2012), pp. 18–36 (cit. on pp. 27, 34, 89).

[124]   O. Kleptsova, G. .S Stelling, and J. D. Pietrzak. „An accurate momen-
        tum advection scheme for a Z-level coordinate models." In: *Ocean
        Dynamics* 60.6 (2010), pp. 1447–1461. ISSN: 1616-7341 (cit. on pp. 27,
        61, 67, 89, 144).

[125]   S. C. Kramer and G. S. Stelling. „A conservative unstructured
        scheme for rapidly varied flows." In: *International Journal for Numer-
        ical Methods in Fluids* 58.2 (2008), pp. 183–212 (cit. on pp. 34, 36, 40,
        57, 139).

[126]   E. J. Kubatko, J. J. Westerink, and C. Dawson. „hp Discontinu-
        ous Galerkin methods for advection dominated problems in shal-
        low water flow." In: *Comput. Methods Appl. Mech. Engrg.* 196 (2006),
        pp. 437–451. DOI: `10.1016/j.cma.2006.05.002` (cit. on pp. 4, 5, 13,
        94).

[127]   Z. W. Kundzewicz, N. Legeri, R. Dankers, Y. Hirabayashi, P. Döll,
        I. Pińskwar, T. Dysarz, S. Hochrainer, and P. Matczak. „Assessing
        river flood risk and adaptation in Europe – review of projections for
        the future." In: *Mitigation and Adaptation Strategies for Global Change*
        15.7 (2010), pp. 641–656. DOI: `10.1007/s11027-010-9213-6` (cit. on
        p. 1).

[128]   P. Lamby, S. Müller, and Y. Stiriba. „Solution of shallow water equa-
        tions using fully adaptive multiscale schemes." In: *Int. J. Numer.
        Meth. Fluids* 49.4 (2005), pp. 417–437. DOI: `10.1002/fld.1004` (cit.
        on pp. 5, 94).

[129]   S. N. Lane, K. F. Bradbrook, K. S. Richards, P. A. Biron, and A.
        G. Roy. „The application of computational fluid dynamics to nat-
        ural river channels: three-dimensional versus two-dimensional ap-
        proaches." In: *Geomorphology* 29.1-2 (1999), pp. 1–20. ISSN: 0169-555X.
        DOI: `10.1016/S0169-555X(99)00003-3` (cit. on pp. 3, 8, 14, 15, 60).

[130]   S. N. Lane, R. J. Hardy, L. Elliott, and D. B. Ingham. „High-
        resolution numerical modelling of three-dimensional flows over
        complex river bed topography." In: *Hydrological Processes* 16.11
        (2002), pp. 2261–2272 (cit. on p. 8).

[131]   S. N. Lane, R. J. Hardy, L. Elliott, and D. B. Ingham. „Numerical
        modeling of flow processes over gravelly-surfaces using structured
        grids and a numerical porosity treatment." In: *Water Resources Re-
        search* 40, W01302 (2004), pp. 1–18 (cit. on pp. 8, 95, 97).

[132]   P. Lax and B. Wendroff. „Systems of Conservation Laws." In: *Communications on Pu* XIII (1960), pp. 217–237 (cit. on p. 12).

[133]   R.J. LeVeque. *Finite Volume Methods for Hyperbolic Problems*. Cambridge, 2002 (cit. on p. 13).

[134]   S. H. Lee, H. Zhou, and H. A. Tchelepi. „Adaptive multiscale finite-volume method for nonlinear multiphase transport in heterogeneous formations." In: *Journal of Computational Physics* 228 (2009), pp. 9036–9058. DOI: 10.1016/j.jcp.2009.09.009 (cit. on p. 5).

[135]   J.J. Leendertse. *Aspects of a computational model for long-period water-wave propagation*. Memorandum RM-5294-PR. Santa Monica, USA: Rand Corporation, 1967 (cit. on p. 5).

[136]   T. Lege, M. Alexy, and J. Kellermann. „Three-dimensional flow fields as a prerequisite for sediment transport modelling in low land rivers." In: *5th International Symposium on Environmental Hydraulics (ISEH V)*. Tempe, Arizona, USA, 2007 (cit. on pp. 15, 60).

[137]   M. Lentine, J. T. Grétarsson, and R. Fedkiw. „An unconditionally stable fully conservative semi-Lagrangian method." In: *J. Comput. Phys.* 230.8 (2011), pp. 2857–2879. ISSN: 0021-9991. DOI: 10.1016/j.jcp.2010.12.036 (cit. on p. 12).

[138]   M. Lentine, W. Zheng, and R. Fedkiw. „A novel algorithm for incompressible flow using only a coarse grid projection." In: *ACM Trans. Graph.* 29.4 (2010), 114:1–114:9. DOI: 10.1145/1778765.1778851 (cit. on pp. 5, 6, 94).

[139]   B.P. Leonard. „A stable and accurate convective modelling procedure based on quadratic upstream interpolation." In: *Computer Methods in Applied Mechanics and Engineering* 19 (1979), pp. 59–98 (cit. on p. 12).

[140]   Q. Liang and A. G. L. Borthwick. „Adaptive quadtree simulation of shallow flows with wet-dry fronts over complex topography." In: *Computers & Fluids* 38.2 (2009), pp. 221–234. ISSN: 0045-7930. DOI: http://dx.doi.org/10.1016/j.compfluid.2008.02.008 (cit. on pp. 7, 14).

[141] Q. Liang, G. Du, J. W. Hall, and A. G. L. Borthwick. „Flood In-
       undation Modeling with an Adaptive Quadtree Grid Shallow Wa-
       ter Equation Solver." In: *Journal of Hydraulic Engineering* 134 (2008),
       pp. 1603–1610. DOI: 10.1061/(ASCE)0733-9429(2008)134:11(1603)
       (cit. on pp. 5, 94).

[142] S.-J. Lin and R. B. Rood. „Multidimensional Flux-form semi-
       lagrangian transport schemes." In: *Monthly Weather Review* 124
       (1996), pp. 2046–2070 (cit. on pp. 12, 13).

[143] F. Lott and M. J. Miller. „A new subgrid-scale orographic drag
       parametrization: Its formulation and testing." In: *Quarterly Journal
       of the Royal Meteorological Society* 123.537 (1997), pp. 101–127. ISSN:
       1477-870X. DOI: 10.1002/qj.49712353704 (cit. on p. 143).

[144] X. Lv, Y. Zhao, X.Y. Huang, G.H. Xia, and Z.J. Wang. „An efficient
       parallel/unstructured-multigrid preconditioned implicit method
       for simulating 3D unsteady compressible flows with moving ob-
       jects." In: *Journal of Computational Physics* 215.2 (2006), pp. 661–690.
       ISSN: 0021-9991. DOI: DOI:10.1016/j.jcp.2005.11.012 (cit. on p. 6).

[145] M. L. MacWilliams. „Three-dimensional hydrodynamic simulation
       of river channels and floodplains." 222 p. PhD thesis. Stanford CA,
       USA: Stanford University, 2004 (cit. on p. 8).

[146] P. A. Madsen, M. Rugbjerg, and I. R. Warren. „Subgrid modelling
       in depth integrated flows." In: *Coastal Engineering 1988*. Vol. 1. 21.
       1988. Chap. 35, pp. 505–511. DOI: 10.1061/9780872626874.036 (cit.
       on p. 10).

[147] K. Marks and P.D. Bates. „Integration of high-resolution topo-
       graphic data with floodplain flow models." In: *Hydrological Processes*
       14.11-12 (2000), pp. 2109–2122. ISSN: 1099-1085. DOI: 10.1002/1099-
       1085(20000815/30)14:11/12<2109::AID-HYP58>3.0.CO;2-1 (cit.
       on p. 8).

[148] A. McAdams, E. Sifakis, and J. Teran. „A parallel multigrid Poisson
       solver for fluids simulation on large grids." In: *Eurographics/ ACM
       SIGGRAPH Symposium on Computer Animation*. Ed. by M. Otaduy
       and Z. Popovic. Madrid, Spain: Eurographics Association, 2010,
       pp. 65–74 (cit. on p. 6).

[149]   A. W. McCoy. „Numerical investigations using LES: exploring flow physics and mass exchange processes near groynes." PhD thesis. University of Iowa, 2006 (cit. on p. 8).

[150]   A. McCoy, G. Constantinescu, and L. Weber. „Coherent structures and mass exchange processes in channel flow with spanwise obstructions." English. In: *ERCOFTAC International Symposium on Engineering Turbulence Modeling and Measurements*. Vol. 6. Sardinia, Italy, 2005, pp. 277–286. ISBN: 0-08-044544-6 (cit. on p. 21).

[151]   A. McCoy, L. J. Weber, and G. Constantinescu. „Numerical investigation of flow hydrodynamics in a channel with a series of groynes." English. In: *Journal of Hydraulic Engineering-ASCE* 134.2 (2008), pp. 157–172. ISSN: 0733-9429. DOI: 10.1061/(ASCE)0733-9429(2008)134:2(157) (cit. on p. 10).

[152]   C. McGahey, P. G. Samuels, and D. W. Knight. „A practical approach to estimating the flow capacity of rivers – Application and analysis." In: *River Flow 2006*. Ed. by Rui M.L Ferreira, Elsa C.T.L. Alves, Joao G.A.B. Leal, and Antonio H. Cardoso. Taylor and Francis, 2006, pp. 303–312 (cit. on p. 9).

[153]   H. K. McMillan and J. Brasington. „Reduced complexity strategies for modelling urban floodplain inundation." In: *Geomorphology* 90.3-4 (2007), pp. 226–243. ISSN: 0169-555X. DOI: DOI:10.1016/j.geomorph.2006.10.031 (cit. on pp. 8, 95, 97).

[154]   F. Mesinger. „On the convergence and error problems of the calculation of the pressure gradient force in sigma coordinate models." In: *Geophys. & Astrophys. Fluid Dyn.* 19 (1982), pp. 105–117. DOI: 10.1080/03091928208208949 (cit. on pp. 15, 60).

[155]   P. Mewis. *Morphodynamisch-numerische Modellierung von Flußkurven*. Heft 126. Institut für Wasserbau und Wasserwirtschaft, Technische Universität Darmstadt, 2002 (cit. on p. 16).

[156]   P. C. D. Milly, R. T. Wetherald, K. A. Dunne, and T. L. Delworth. „Increasing risk of great floods in a changing climate." In: *Nature* 415 (2002), pp. 514–517 (cit. on p. 1).

[157]   C. Milzow and W. Kinzelbach. „Accounting for subgrid scale topographic variations in flood propagation modeling using MODFLOW." In: *Water Resources Research* 46.W10521 (2010), pp. 1–14. DOI: doi:10.1029/2009WR008088 (cit. on p. 143).

[158]   B. L. Mitchell and S. R. Fulton. *Adaptive Multigrid Solution of the Shallow Water Equations*. Technical Report 2000-02. Potsdam, New York: Dep. of Math. and Comp. Science, Clarkson Univ., 2000 (cit. on p. 5).

[159]   R. Mittal and G. Iaccarino. „Immersed Boundary Methods." In: *Annual Review of Fluid Mechanics* 37 (2005), pp. 239–261. DOI: 10.1146/annurev.fluid.37.061903.175743 (cit. on p. 61).

[160]   M. Mohammadi-Aragh, K. Klingbeil, N. Brügemann, C. Eden, and H. Burchard. „The impact of advection schemes on restratifiction due to lateral shear and baroclinic instabilities." In: *Ocean Modelling* 94 (2015), pp. 112–127. ISSN: 1463-5003. DOI: http://dx.doi.org/10.1016/j.ocemod.2015.07.021 (cit. on p. 13).

[161]   B. Mohammadi and O. Pironneau. *Analysis of the $k - \varepsilon$ turbulence model*. Wiley-Masson Series Research in Applied Mathematics. J. Wiley & Sons, 1994, 194 p. (Cit. on p. 64).

[162]   P. Molinaro, A. Di Fillippo, and F. Ferrari. „Modelling of flood wave propagation over flat dry areas of complex topography in presence of different infrastructures." In: *Modelling of flood propagation over initially dry areas*. Vol. 1. New York, USA, 1994, pp. 209–228 (cit. on p. 14).

[163]   S. Müller and Y. Stiriba. „A multilevel finite volume method with multiscale-based grid adaptation for steady compressible flows." In: *Journal of Computational and Applied Mathematics* 227.2 (2009). Special Issue on Emergent Applications of Fractals and Wavelets in Biology and Biomedicine, pp. 223–233. DOI: 10.1016/j.cam.2008.03.035 (cit. on pp. 5, 94).

[164]   J. Murillo and P. García-Navarro. „Energy balance numerical schemes for shallow water equations with discontinuous topography." In: *Journal of Computational Physics* 236 (2013), pp. 119–142 (cit. on p. 56).

[165]   M. Nabi, H. J. de Vriend, E. Mosselman, C. J. Sloff, and Y. Shimizu. „Detailed simulation of morphodynamics: 1. Hydrodynamic model." In: *Water Resources Research* 48.12 (2012). W12523, pp. 1–19. ISSN: 1944-7973. DOI: 10.1029/2012WR011911 (cit. on pp. 5, 16).

[166] J. Neal, G. Schumann, and P. Bates. „A subgrid channel model for simulating river hydraulics and floodplain inundation over large and data sparse areas." In: *Water Resour. Res.* 48, W11506 (2012), pp. 1–16. DOI: 10.1029/2012WR012514 (cit. on pp. 8, 9, 143).

[167] H.M. Nepf. „Flow and Transport in Regions with Aquatic Vegetation." In: *Annual Review of Fluid Mechanics* 44.1 (2012), pp. 123–142. DOI: 10.1146/annurev-fluid-120710-101048. eprint: http://dx.doi.org/10.1146/annurev-fluid-120710-101048 (cit. on p. 16).

[168] A. P. Nicholas and C. A. Mitchell. „Numerical simulation of overbank processes in topographically complex floodplain environments." In: *Hydrological Processes* 17.4 (2003), pp. 727–746. ISSN: 1099-1085. DOI: 10.1002/hyp.1162 (cit. on p. 8).

[169] F. Nieuwstadt. *Turbulentie*. Epsilon Uitgaven, 1998 (cit. on p. 11).

[170] Y. Nihei, Y. Kato, and K. Sato. „A three-dimensional numerical model for large-scale river flow with a new mode-splitting technique." In: *Paper presented at the 32nd Congress of the International Association of Hydraulic Engineering and Research*. Venice, Italy, 2007 (cit. on pp. 15, 60).

[171] S. Noelle, Y. Xing, and C.-W. Shu. „High-order well-balanced finite volume WENO schemes for shallow water equation with moving water." In: *Journal of Computational Physics* 226.1 (2007), pp. 29–58. ISSN: 0021-9991. DOI: http://dx.doi.org/10.1016/j.jcp.2007.03.031 (cit. on pp. 4, 13, 30).

[172] N.R.B. Olsen and S. Stokseth. „Three-dimensional Numerical Modelling of Water Flow in a River with Large Bed Roughness." In: *Journal of Hydraulic Research* 33.4 (1995), pp. 571–581 (cit. on pp. 8, 95, 97).

[173] W. Ottevanger. „Modelling and parameterizing the hydro- and morphodynamics of curved open channels." PhD thesis. Department of Hydraulic Engineering, Faculty of Civil Engineering and Geosciences, Delft University of Technology, 2013 (cit. on p. 16).

[174] W. Ottevanger and W. Van Balen. „Challenges in modeling river bends." In: *NCR Days 2008*. Ed. by A.G. van Os. Poster. Dalfsen, The Netherlands, 2008 (cit. on p. 16).

[175] S. J. Owen. „A survey of unstructured mesh generation technology." unpublished. 2000 (cit. on p. 7).

[176]   R. C. Pacanowski and A. Gnanadesikan. „Transient response in a Z-level ocean model that resolves topography with partial cells." In: *Monthly Weather Review* 126 (1998), pp. 3248–3270. DOI: {10.1175/1520-0493(1998)126\$<\$3248:TRIAZL\$>\$2.0.CO;2} (cit. on p. 61).

[177]   J. Paik, C. Escauriaza, and F. Sotiropoulos. „Coherent Structure Dynamics in Turbulent Flows past In-Stream Structures: Some Insights Gained via Numerical Simulation." In: *Journal of Hydraulic Engineering* 1.1 (2010). SPECIAL ISSUE: Special Issue on River Flow Hydrodynamics: Physical and Ecological Aspects, pp. 1–53. DOI: 10.1061/(ASCE)HY.1943-7900.0000089 (cit. on p. 94).

[178]   S. V. Patankar. *Numerical heat transfer and fluid flow.* New York, USA: Hemisphere Publishing Co., 1980 (cit. on p. 69).

[179]   R. Patzwahl, J. A. Jankowski, and T. Lege. „Very high resolution numerical modelling for inland waterway design." In: *International Conference on Fluvial Hydraulics (River Flow 2008).* Izmir, Turkey, 2008 (cit. on pp. 15, 60, 94).

[180]   A. R. Paz, J. M. Bravo, D. Allasia, W. Collischonn, and C. E. M. Tucci. „Large-Scale Hydrodynamic Modeling of a Complex River Network and Floodplains." In: *Journal of Hydrologic Engineering* 15.2 (2010), pp. 152–165. DOI: 10.1061/(ASCE)HE.1943-5584.0000162 (cit. on p. 8).

[181]   B. Perot. „Conservation properties of unstructured staggered mesh schemes." In: *J. Comp. Phys.* 159 (2000), pp. 58–89 (cit. on p. 34).

[182]   N. A. Phillips. „A coordinate system having some special advantages for numerical forecasting." In: *Journal of Meteorology* 14 (1957), pp. 184–185. DOI: {10.1175/1520-0469(1957)014\$<\$0184:ACSHSS\$>\$2.0.CO;2} (cit. on p. 60).

[183]   S. A. Piacsek and G. P. Williams. „Conservation properties of convection difference schemes." In: *Journal of Computational Physics* 6 (1970), pp. 392–405 (cit. on p. 100).

[184]   J. D. Pietrzak, J. B. Jakobson, H. Burchard, H. J. Vested, and O. Petersen. „A three-dimensional hydrostatic model for coastal and ocean modelling using a generalised topography following coordinate system." In: *Ocean Modelling* 4 (2002), pp. 173–205 (cit. on p. 15).

[185]   F. W. Platzek, G. S. Stelling, J. A. Jankowski, and R. Patzwahl. „On the representation of bottom shear stress in z-layer models." In: *Hydroinformatics 2012*. Hamburg, Germany, 2012 (cit. on p. xix).

[186]   F. W. Platzek, G. S. Stelling, J. A. Jankowski, and J. D. Pietrzak. „Accurate vertical profiles of turbulent flow in z-layer models." In: *Water Resour. Res.* 50 (2014), pp. 2191–2211. DOI: 10.1002/2013WR014411 (cit. on pp. xix, 59).

[187]   F. W. Platzek, G. S. Stelling, J. A. Jankowski, R. Patzwahl, and J. D. Pietrzak. „An efficient semi-implicit subgrid method for free-surface flow on hierarchical grids." In: *Int. J. Numer. Meth. Fluids* 80.12 (2016), pp. 715–741 (cit. on pp. xix, 32, 36, 40, 46, 47, 93).

[188]   F. W. Platzek, G. S. Stelling, J. A. Jankowski, R. Patzwahl, and J. D. Pietrzak. „River computations: artificial backwater from the momentum advection scheme." In: *Journal of Hydraulic Research* (2017), pp. 1–21 (cit. on pp. xix, 29).

[189]   S. B. Pope. *Turbulent Flows*. Cambridge University Press, 2000 (cit. on p. 11).

[190]   L. Prandtl. „Bericht über Untersuchungen zur ausgebildeten Turbulenz." In: *Z. Angew. Math. und Mech.* 5 (1925), pp. 136–139 (cit. on pp. 10, 71).

[191]   B. C. van Prooijen, R. Booij, and W. S. J. Uijttewaal. „Measurement and analysis methods of large scale coherent structures in a wide shallow channel." In: *Proc. 10th Int. Symp. Appl. Laser Tech. Fluid Mech.* Lissabon, Portugal, 2000 (cit. on p. 21).

[192]   B. Rabus, M. Eineder, A. Roth, and R. Bamler. „The shuttle radar topography mission – a new class of digital elevation models acquired by spaceborne radar." In: *ISPRS Journal of Photogrammetry and Remote Sensing* 57.4 (2003), pp. 241–262 (cit. on pp. 7, 8).

[193]   A. K. Rastogi and W. Rodi. „Predictions of Heat and Mass Transfer in Open Channels." In: *Journal of the Hydraulics Division, ASCE* 104.3 (1978), pp. 397–420 (cit. on p. 22).

[194]   M. Ricchiuto. „An explicit residual based approach for shallow water flows." In: *Journal of Computational Physics* 280 (2015), pp. 306–344. ISSN: 0021-9991 (cit. on pp. 13, 14, 30, 45).

[195] R. D. Richtmyer and K. W. Morton. *Difference methods for initial value problems*. New York, London: Interscience Publishers, 1967 (cit. on pp. 3, 4, 12).

[196] T.D. Ringler, J. Thuburn, J.B. Klemp, and W.C. Skamarock. „A unified approach to energy conservation and potential vorticity dynamics for arbitrarily-structured C-grids." In: *Journal of Computational Physics* 229 (2010), pp. 3065–3090 (cit. on pp. 4, 13).

[197] P. J. Roache. *Computational Fluid Dynamics*. Hermosa Publishers, 1972, 434 p. (Cit. on p. 12).

[198] W. Rodi. *Turbulence models and their application in hydraulics*. Delft, The Netherlands: International Association for Hydraulic Research, 1984, 104 p. (Cit. on pp. 10, 22, 65).

[199] W. Rodi. „Turbulence Modeling and Simulation in Hydraulics: A Historical Review." In: *Journal of Hydraulic Engineering* 143.5 (2017), pp. 1–20 (cit. on pp. 10, 11, 143).

[200] W. Rodi, G. Constantinescu, and T. Stoesser. *Large-Eddy Simulation in Hydraulics, CRC Press, Taylor & Francis Group (2013)*. Ed. by Peter A. Davies (IAHR). IAHR Monograph. CRC Press, Taylor & Francis Group, 2013 (cit. on pp. 4, 10, 11, 13, 23, 143).

[201] R.B. Rood. „Numerical advection algorithms and their role in atmospheric transport and chemistry models." In: *Reviews of Geophysics* 25.1 (1987), pp. 71–100 (cit. on p. 12).

[202] G. Rosatti, D. Cesari, and L. Bonaventura. „Semi-implicit, semi-Lagrangian modelling for environmental problems on staggered Cartesian grids with cut cells." In: *Journal of Computational Physics* 204 (2005), pp. 353–377 (cit. on pp. 7, 12, 13, 106).

[203] A. Roshko. *On the development of turbulent wakes from vortex streets*. NACA Report 1191. National Advisory Committee for Aeronautics, 1954 (cit. on pp. 118, 124, 126).

[204] P. Sagout, S. Deck, and M. Terracol. *Multiscale and Multiresolution Approaches in Turbulence, LES, DES and Hybrid RANS/LES Methods: Applications and Guidelines*. Imperial College Press, London, 2013 (cit. on pp. 5, 10).

[205]   B. F. Sanders, J. E. Schubert, and H. A. Gallegos. „Integral formula-
        tion of shallow-water equations with anisotropic porosity for urban
        flood modeling." In: *Journal of Hydrology* 362 (2008), pp. 19–38 (cit.
        on pp. 8, 95, 97, 143).

[206]   R. Schneiders. 2016. URL: {www . robertschneiders . de /
        meshgeneration/software.html} (cit. on p. 7).

[207]   G. Schroeder, K.H. Schlünzen, and F. Schimmel. „Use of (weighted)
        essentially non-oscillatory advection schemes in a mesoscale
        model." In: *Q. J. R. Meteorol. Soc.* 132 (2006), pp. 1509–1526 (cit. on
        p. 13).

[208]   G. J.-P. Schumann, K. M. Andreadis, and P. D. Bates. „Downscaling
        coarse grid hydrodynamic model simulations over large domains."
        In: *Journal of Hydrology* 508.0 (2014), pp. 289–298. ISSN: 0022-1694.
        DOI: 10.1016/j.jhydrol.2013.08.051 (cit. on p. 8).

[209]   A. Sehili, G. Lang, and C. Lippert. „High-resolution subgrid mod-
        els: background, grid generation, and implementation." English. In:
        Ocean Dynamics 64.4 (2014), pp. 519–535. ISSN: 1616-7341. DOI: 10.
        1007/s10236-014-0693-x (cit. on pp. 14, 95, 96, 106, 110, 135).

[210]   J. H. Seo and R. Mittal. „A sharp-interface immersed boundary
        method with improved mass conservation and reduced spurious
        pressure oscillations." In: *Journal of Computational Physics* 230 (2011),
        pp. 7347–7363. DOI: 10.1016/j.jcp.2011.06.003 (cit. on pp. 61, 89).

[211]   F.D. Shields, K.G. Coulton, and H. Nepf. „Representation of Vegeta-
        tion in Two-Dimensional Hydrodynamic Models." In: *Journal of Hy-
        draulic Engineering* 143 (2017), pp. 1–9. DOI: 10.1061/(ASCE)HY.1943-
        7900.0001320 (cit. on p. 16).

[212]   C.-W. Shu. „High-order Finite Difference and Finite Volume WENO
        Schemes and Discontinuous Galerkin Methods for CFD." In: *Inter-
        national Journal of Computational Fluid Dynamics* 17.2 (2003), pp. 107–
        118. DOI: 10.1080/1061856031000104851. eprint: http://dx.doi.
        org/10.1080/1061856031000104851 (cit. on p. 4).

[213]   S. K. Sinha. „An algebraic grid generation technique for three-
        dimensional natural river reaches." In: *Communications in Numerical
        Methods in Engineering* 13 (1997), pp. 475–485 (cit. on p. 7).

[214]   J. Smagorinsky. „General circulation experiments with the primitive equations." In: *Mon. Weather Rev* 91.3 (1963), pp. 99–164 (cit. on pp. 10, 22, 142).

[215]   Y. T. Song and Y. Chao. „An embedded bottom boundary layer formulation for z-coordinate ocean models." In: *Journal of Atmospheric and Oceanic Technology* 17 (2000), pp. 546–560. DOI: `{10.1175/1520-0426(2000)017$<$0546:AEBBLF$>$2.0.CO;2}` (cit. on p. 61).

[216]   A. Staniforth and J. Côté. „Semi-Lagrangian integration schemes for atmospheric models - A review." In: *Monthly Weather Review* 119 (1991), pp. 2206–2223 (cit. on pp. 12, 13).

[217]   G. S. Stelling. „On the construction of computational methods for shallow water flow problems." PhD thesis. Delft, Netherlands: Technische Hogeschool Delft, 1983. DOI: `http://repository.tudelft.nl/view/ir/uuid%3Ad3b818cb-9f91-4369-a03e-d90c8c175a96/` (cit. on pp. 5, 12).

[218]   G. S. Stelling. „Compact differencing for stratified free surface flow." In: *Advances in Hydro-Science and Engineering*. Vol. II Part A. Bejing, China, 1995, pp. 378–386 (cit. on p. 61).

[219]   G. S. Stelling. „Quadtree flood simulations with sub-grid digital elevation models." In: *Proceedings of the ICE - Water Management* 165.WM10 (2012), pp. 567–580 (cit. on pp. viii, xii, xvi, xvii, xxxiii, 5, 9, 14, 18, 21, 25, 27, 35, 56, 95–97, 100, 106, 109, 110, 134, 137, 138, 141, 143, 144, 150).

[220]   G. S. Stelling and S. P. A. Duinmeijer. „A staggered conservative scheme for every Froude number in rapidly varied shallow water flows." In: *International Journal for Numerical Methods in Fluids* 43 (2003), pp. 1329–1354 (cit. on pp. 30, 34–37, 40, 57, 139).

[221]   G. S. Stelling and J. A. Th. M. Van Kester. „On the approximation of horizontal gradients in sigma coordinates for bathymettry with steep bottom slope." In: *Int. J. Numer. Methods Fluids* 18 (1994), pp. 915—935. DOI: `10.1002/fld.1650181003` (cit. on pp. 15, 60).

[222]   T. Stoesser, C. A. M. E. Wilson, P. D. Bates, and A. Dittrich. „Application of a 3D numerical model to a river with vegetated floodplains." In: *Journal of Hydroinformatics* 5 (2003), pp. 99–112 (cit. on p. 8).

[223] B. H. Strauss, S. Kulp, and A. Levermann. *Mapping Choices: Carbon, Climate and Rising Seas, Our Global Legacy*. Research Report. 1–38. Climate Central, 2015 (cit. on p. 1).

[224] A. Sukhodolov, W. S. J. Uijttewaal, and C. Engelhardt. „On the correspondence between morphological and hydrodynamical patterns of groyne fields." English. In: *Earth Surface Processes and Landforms* 27.3 (2002), pp. 289–305. ISSN: 0197-9337. DOI: 10.1002/esp.319 (cit. on p. 16).

[225] W.J. Syme. „Modelling of bends and hydraulic structures in a two-dimensional scheme." In: *Conference on Hydraulics in Civil Engineering*. Ed. by A.C.T Barton. Vol. 6. The Institution of Engineers. Hobart, Australia, 2001, pp. 127–136 (cit. on p. 16).

[226] E. Tadmor and W. Zhong. „Energy-preserving and stable approximations for the two-dimensional shallow water equations." In: *Mathematics and Computation, a Contemporary View*. 2008 (cit. on p. 56).

[227] C.H. Tai and Y. Zhao. „Parallel unsteady incompressible viscous flow computations using an unstructured multigrid method." In: *Journal of Computational Physics* 192.1 (2003), pp. 277–311. ISSN: 0021-9991. DOI: DOI:10.1016/j.jcp.2003.07.005 (cit. on pp. 6, 124, 126).

[228] J.F. Thompson. *Convection schemes for use with curvilinear coordinate systems – A survey*. Miscellaneous Paper E-84-4. prepared for the US Army Engineer Waterways Experiment Station. Vicksburg, Mississippi: Mississippi State University, 1984 (cit. on p. 12).

[229] E. F. Toro and P. Garcia-Navarro. „Godunov-type methods for free-surface shallow flows: A review." In: *Journal of Hydraulic Research* 45.6 (2007), pp. 736–751 (cit. on pp. 13, 30).

[230] M. Tritthart and D. Gutknecht. „3-D computation of flood processes in sharp river bends." In: *Water Management* 160.WM4 (2007), pp. 233–247 (cit. on pp. 8, 16).

[231] D. S. Trossman, B. K. Arbica, J. G. Richman, S. T. Garner, S. R. Jayne, and A. J.Wallcraft. „Impact of topographic internal lee wave drag on an eddying global ocean model." In: *Ocean Modelling* 97 (2016), pp. 109–128 (cit. on p. 143).

[232] U. Trottenberg, C. Oosterlee, and A. Schüller. *Multigrid*. London, UK: Academic Press, 2001 (cit. on pp. 5, 94, 134).

[233] Y.-H. Tseng and J. H. Ferziger. „A ghost-cell immersed boundary method for flow in complex geometry." In: *J. Comput. Phys.* 192.2 (2003), pp. 593–623. ISSN: 0021-9991. DOI: 10.1016/j.jcp.2003.07.024 (cit. on p. 61).

[234] W. S. J. Uijttewaal. „Hydrodynamics of shallow flows: application to rivers." In: *Journal of Hydraulic Research* 52.2 (2014), pp. 157–172 (cit. on pp. 3, 21, 143).

[235] W. S. J. Uijttewaal, D. Lehmann, and A. van Mazijk. „Exchange processes between a river and its groyne fields: Model experiments." English. In: *Journal of Hydraulic Engineering-ASCE* 127.11 (2001), pp. 928–936. ISSN: 0733-9429 (cit. on p. 21).

[236] S. Ullmann. „Three-dimensional computation of non-hydrostatic free-surface flows." MA thesis. Delft University of Technology, Faculty of Electrical Engineering, Mathematics and Computer Science, Delft Institute of Applied Mathematics, 2008 (cit. on p. 16).

[237] W. Van Balen, W. S. J. Uijttewaal, and K. Blanckaert. „Large-eddy simulation of a curved open-channel flow over topography." In: *Physics of Fluids* 22.7, 075108 (2010), p. 18. DOI: 10.1063/1.3459152 (cit. on pp. 10, 15, 16, 56).

[238] B. Van Leer. „Towards the Ultimate Conservative Difference Scheme. II. Monotonicity and Conservation Combined in a Second-Order Scheme." In: *Journal of Computational Phy* 14 (1974), pp. 361–370 (cit. on p. 12).

[239] H.K. Versteeg and W. Malalasekera. *An Introduction to Computational Fluid Dynamics: The Finite Volume Method*. second edition. Pearson Prentice Hall, 2007 (cit. on pp. 7, 13).

[240] N. D. Volp, B. C. Van Prooijen, and G. S. Stelling. „A finite volume approach for shallow water flow accounting for high-resolution bathymetry and roughness data." In: *Water Resour. Res.* 49.7 (2013), pp. 4126–4135 (cit. on pp. 5, 14, 18, 35, 95–97, 106, 109, 110, 113, 134, 144).

[241]   N. D. Volp, B. C. Van Prooijen, J. D. Pietrzak, and G. S. Stelling. „A subgrid based approach for morphodynamic modelling.“ In: *Advances in Water Resources* 93, Part A (2016), pp. 105–117 (cit. on pp. 16, 144).

[242]   N.D. Volp. „Subgrid is Dancing with Sediment: A Full Subgrid Approach for Morphodynamic Modelling.“ PhD thesis. Delft University of Technology, Faculty of Civil Engineering and Geosciences, 2017 (cit. on pp. 16, 144).

[243]   C.B. Vreugdenhil. „Accuracy and reliability of numerical river models.“ In: *Journal of the American Water Resources Association* 38.4 (2002), pp. 1083–1095 (cit. on p. 4).

[244]   C.B. Vreugdenhil. „Appropriate models and uncertainties.“ In: *Coastal Engineering* 53.2-3 (2006). Coastal Hydrodynamics and Morphodynamics, pp. 303–310. ISSN: 0378-3839. DOI: DOI:10.1016/j.coastaleng.2005.10.017 (cit. on p. 4).

[245]   B. Wang, G. Zhao, and O. B. Fringer. „Reconstruction of vector fields for semi-Lagrangian advection on unstructured, staggered grids.“ In: *Ocean Modelling* 40.1 (2011), pp. 52–71. DOI: 10.1016/j.ocemod.2011.06.003 (cit. on pp. 12, 13, 100).

[246]   N.P. Waterson and H. Deconinck. „Design principles for bounded higher-order convection schemes – a unified approach.“ In: *Journal of Computational Physics* 224.1 (2007), pp. 182–207. ISSN: 0021-9991. DOI: https://doi.org/10.1016/j.jcp.2007.01.021 (cit. on p. 12).

[247]   V. Weitbrecht, S. A. Socolofsky, and G. H. Jirka. „Experiments on mass exchange between groin fields and main stream in rivers.“ English. In: *Journal of Hydraulic Engineering-ASCE* 134.2 (2008), pp. 173–183. ISSN: 0733-9429. DOI: 10.1061/(ASCE)0733-9429(2008)134:2(173) (cit. on p. 21).

[248]   I. Wenneker. „Computation of flows using unstructured staggered grids.“ PhD thesis. Delft, The Netherlands: Delft University of Technology, 2002 (cit. on p. 7).

[249]   R. M. Westaway, S. N. Lane, and D. M. Hicks. „Remote survey of large-scale braided, gravel-bed rivers using digital photogrammetry and image analysis.“ In: *International Journal of Remote Sensing* 24.4 (2003), pp. 795–815. DOI: 10.1080/01431160110113070. eprint: http://dx.doi.org/10.1080/01431160110113070 (cit. on pp. 7, 8).

[250]   D.C. Wilcox. *Turbulence modeling for CFD*. DCW Industries, Inc., 1993 (cit. on pp. 10, 61).

[251]   R. D. Williams, J. Brasington, M. Hicks, R. Measures, C. D.Rennie, and D.Vericat. „Hydraulic validation of two-dimensional simulations of braided river flow with spatially continuous aDcp data." In: *Water Resour. Res.* 49 (2013), 51835205. DOI: 10.1002/wrcr.20391 (cit. on p. 8).

[252]   B.A. Wols. „Undular hydraulic jumps." MA thesis. Delft University of Technology, Faculty of Civil Engineering and Geosciences, Section of Environmental Fluid Mechanics, 2005 (cit. on p. 16).

[253]   W. Wu. *Computational river dynamics*. Taylor & Francis Ltd, 2007 (cit. on p. 16).

[254]   W. Wu, W. Rodi, and T. Wenka. „3D numerical modeling of flow and sediment transport in open channels." In: *Journal of Hydraulic Engineering* 126.1 (2000), pp. 4–15. DOI: 10.1061/(ASCE)0733-9429(2000) 126:1(4) (cit. on pp. 15, 60).

[255]   W. Wu, P. Wang, and N. Chiba. „Comparison of Five Depth-Averaged 2-D Turbulence Models for River Flows." In: *Archives of Hydro-Engineering and Environmental Mechanics* 51.2 (2004), pp. 183–200 (cit. on pp. 10, 22).

[256]   X. Xing. „High order finite volume WENO schemes for the shallow water flows through channels with irregular geometry." In: *Journal of Computational and Applied Mathematics* 299 (2016), pp. 229–244 (cit. on pp. 4, 13).

[257]   X. Xing and C.-W. Shu. „High-order finite volume WENO schemes for the shallow water equations with dry states." In: *Advances in Water Resources* 34 (2011), pp. 1026–1038 (cit. on pp. 4, 13).

[258]   Y. Xing and C.-W. Shu. „A Survey of High Order Schemes for the Shallow Water Equations." In: *J. Math. Study* 47.3 (2014), pp. 221–249. DOI: 10.4208/jms.v47n3.14.01 (cit. on pp. 4, 13).

[259]   M. F. M. Yossef. „Morphodynamics of rivers with groynes." PhD thesis. Delft, The Netherlands: Delft University of Technology, 2005 (cit. on p. 16).

[260]   M. F. M. Yossef and H. J. de Vriend. „Sediment exchange between a river and Its groyne fields: mobile-bed experiment." In: *Journal of Hydraulic Engineering* 136.9 (2010), pp. 610–625. DOI: 10.1061/(ASCE)HY.1943-7900.0000226 (cit. on p. 16).

[261]   D. Yu and S.N. Lane. „Urban fluvial flood modelling using a two-dimensional diffusion-wave treatment, part 2 : development of a sub-grid-scale treatment." In: *Hydrological Processes* 20.7 (2006), pp. 1567–1583 (cit. on pp. 8, 14).

[262]   D. Yu and S.N. Lane. „Interactions between subgrid-scale resolution, feature representation and grid-scale resolution in flood inundation modelling." In: *Hydrological Processes* 25 (2011), pp. 36–53 (cit. on pp. 8, 95, 97, 143).

[263]   A. Zadra, M. Roch, S. Laroche, and M. Charron. „The subgrid-scale orographic blocking parametrization of the GEM Model." In: *Atmosphere-Ocean* 41.2 (2003), pp. 155–170. DOI: 10.3137/ao.410204. eprint: http://dx.doi.org/10.3137/ao.410204 (cit. on p. 143).

[264]   D. de Zelicourt, L. Ge, F. Sotiropoulos, and A. Yoganathan. „Efficient unstructured cartesian/immersed-boundary method with local mesh refinement to simulate flows in complex 3D geometries." In: *APS Meeting Abstracts* (2008), A5+ (cit. on p. 7).

[265]   D. Zhang, C. Jiang, D. Liang, and L. Cheng. „A review on TVD schemes and a refined flux-limiter for steady-state calculations." In: *Journal of Computational Physics* 302 (2015), pp. 114–154 (cit. on p. 38).

[266]   G. Zhao. „Numerical simulation of complex channel flows." PhD thesis. Stanford, USA: Department of Civil and Environmental Engineering, Stanford University, 2007 (cit. on pp. 12, 13, 16).

[267]   F. Zhou, G. Chen, S. Noelle, and H. Guo. „A well-balanced stable generalized Riemann problem scheme for shallow water equations using adaptive moving unstructured triangular meshes." In: *International Journal for Numerical Methods in Fluids* 73.3 (2013), pp. 266–283. ISSN: 1097-0363. DOI: 10.1002/fld.3800 (cit. on p. 5).

[268]   M. Zijlema and G. S. Stelling. „Efficient computation of surf zone waves using the nonlinear shallow water equations with non-hydrostatic pressure." In: *Coastal Engineering* 55.10 (2008), pp. 780–790. ISSN: 0378-3839. DOI: DOI:10.1016/j.coastaleng.2008.02.020 (cit. on p. 16).

CURRICULUM VITÆ

Frank Platzek was born in The Hague, the Netherlands, in 1981. He lived in Delft during his primary and secondary school years, where he attended the Grotius College. After finishing secondary school, Frank started studying Aerospace Engineering at Delft University of Technology, where he graduated in 2007 at the chair of Aerodynamics, with a thesis entitled: "Modeling of shallow water flow over a non-flat bottom".

After graduation, Frank started working at Deltares (at that time WL | Delft Hydraulics) in Delft, the Netherlands. There, he joined the software department and worked on the maintenance and development of the modelling system Delft3D.

In 2010, Frank commenced his PhD in a joint cooperation between Deltares, the Department of Civil Engineering and Geosciences of Delft University of Technology and the Federal Waterways Engineering and Research Institute or *Bundesanstalt für Wasserbau (BAW)* in Karlsruhe, Germany. The result of this cooperation is this thesis. During the six years that Frank worked on the PhD, he spent half of the time in Karlsruhe, exchanging knowledge and experience between Dutch and German river modellers, numerical mathematicians and high-performance computing specialists.

During his school years and studies and later alongside his scientific work, Frank was active both as a field hockey player and youth trainer for many years.